Direct Laser Sintering of Stainless Steel: Thermal Experiments and Numerical Modelling

Christopher Martin Taylor

Submitted in accordance with the requirements for the degree of PhD

The University of Leeds

School of Mechanical Engineering

February 2004

ACKNOWLEDGEMENTS

My greatest appreciation to my supervisors Doctor Kenny Dalgarno and Professor Tom Childs, for their guidance throughout my project. Thanks to Carl Hauser for his training in use of various equipment. Also thanks to Abbas Ismail and Phil Woods for realisation of my powder bed tray and vacuum feed-through designs. Thanks to Peter Anthony and the EPSRC loan pool for the use of their thermal imaging system.

Thanks to Ma and Pa, for forwarding my mail and being on hand with some decent food.

ABSTRACT

SLS is a commercial solid freeform fabrication process. Layers of powder material are bonded by a laser beam to rapidly manufacture three dimensional freeform models. In this work, the direct SLS of room temperature single-phase steel powder beds is researched.

Two approaches are adopted:

- Experimental analysis of heat transfer in the process;
- Numerical modelling of the process.

Experimental work involves the use of analytical equations to calculate the thermal conductivity and laser energy absorptance of the SLS powder bed. Experiments take place in a range of representative situations. Two temperature measurement systems are used, requiring some custom-designed elements. Conductivity values in the range 0.07 to 0.25 W/(m.K) are found, dependent on atmospheric gas and powder particle size. Absorptance varies from 0.08 to 0.21, dependent on atmosphere and material type. Measurements are made to learn more about temperature variation in the bed with position and time. It is found that processed material melts and solidifies in under 4 seconds in studied cases.

Numerical modelling involves developing and testing an existing Fortran model of the SLS process. A method is devised to visualise modelled parts in 3D. Pre-processing is simplified, and more status information is communicated during execution. The effect on modelled parts of changes made to the program are tested. The stability of part depth is improved. The nature of parts is categorised against input parameters. The area, relative density and morphology of manufactured and modelled single layer parts are compared. Manufactured scans are found to have a variable cross-sectional shape, whereas the cross-sectional shape of modelled scans does not change. Modelled parts are found to be significantly smaller than manufactured parts. Reasons for these two differences are suggested.

TABLE OF CONTENTS

LIST OF FIGURES

LIST OF TABLES

NOTATION

A_N	Andrew number or energy density (J/ m^2)
C	specific heat (J/ (kg.K))
d	laser beam diameter (m)
d_p	powder particle diameter (m)
dT	temperature rise (°C)
dT_{max}	maximum temperature rise (°C)
E	Young's modulus (Pa)
E_L	energy per unit length (J/ m)
E_{LOSS}	energy lost by vaporisation (J)
E_M	energy contributing to melting, per unit length (J/ m)
I	laser beam irradiance (W/ m^2)
k	thermal conductivity (W/ (m.K))
L	scan length (m)
L_M	latent heat of melting (J/ kg)
L_V	latent heat of vaporisation (J/ kg)
m	mass (kg)
N	number of rescans of an area of material
P	laser power (W)
Q	strength of line heat source (m^2.K)
Q'	strength of plane heat source (m.K)
r	radial position (m)
R	laser power reflectance
Ra	surface roughness (m)
s	scan spacing (m)
t	time (s)
t_{Tmax}	time to maximum temperature (s)
t_s	time between successive scans (s)
T	temperature (°C are the default; in K if stated)
T_m	melting temperature (°C)
U	beam speed (m/ s)
V	volume (m^3)

x	axis in laser scanning direction (modelling and experiments)
	distance in x direction (m)
y	axis in powder bed depth direction (modelling and experiments)
	distance in y direction (m)
z	axis in scan spacing direction (modelling and experiments)
	distance in z direction (m)
Z	distance in powder bed depth direction, in Chapter 2 (m)
Z_l	powder layer thickness (m)
Z_p	laser penetration depth (m)

GREEK NOTATION

α	powder bed laser absorptance
α_s	solid material laser absorptance
χ	solid fraction (in material latent phase)
ε_r	emissivity
φ	powder bed porosity
κ	thermal diffusivity (m^2/ s)
λ	laser beam wavelength (m)
μ	viscosity (kg/ (m.s))
ρ	density (kg/ m^3)
ρ_{MAX}	maximum (solid) density (kg/ m^3)
ρ_r	relative density
σ	surface tension (J/ m^2)
σ_y	yield stress (MPa)

COMMON TERMS USED

Modelled part	Virtual part, a visualisation of density data output by program stmet3d
Manufactured part	Physical part, created by direct SLS

STMET3D PROGRAM VARIABLES AND FILES

CONDO	constant used to evaluate conductivity as function of temperature
CONDV	constant used to evaluate conductivity as function of temperature
DTIME	FE calculation time increment
J	incrementing heat step number within a scan
NLIMIT	number of heat steps required for current scan
Rhoplot	output file, of density and coordinates for the powder bed
SIGV1	constant used to evaluate conductivity as function of porosity
SIGV2	constant used to evaluate conductivity as function of porosity
stmet3d	Fortran-based finite element model of direct SLS
stme3dat	input parameter file, containing mesh, material and scan data
TDEG0	initial powder bed temperature
TDWELL	solidification temperature, at which marching cool down may end
TMAX	maximum temperature found within thermal mesh
TSOL	solidification temperature (material property)

ABBREVIATIONS

1D, 2D, 3D	one-dimensional, two dimensional, three dimensional respectively
CAD	Computer Aided Design
CL	Closed Loop (control)
CW	Constant Wave (non-pulsed, referring to lasers)
DMLR	Direct Metal Laser Re-Melting (SFF process)
DMLS	Direct Metal Laser Sintering (SFF process)
FE	Finite Element (computer numerical modelling)
FFPC	Feed Forward Process Control
FLS	First Line Scan (feature of SLS generated parts)
HAZ	Heat Affected Zone (in the powder bed)
IR	Infra Red (frequency range of thermal camera)
LPS	Liquid Phase Sintering
PBM	Powder Bed Mesh, in finite element program
RP	Rapid Prototyping (group of manufacturing processes)
RT	Rapid Tooling (group of manufacturing processes)
SFF	Solid Freeform Fabrication (group of manufacturing processes)
SLS	Selective Laser Sintering (type of SFF process)
SPS	Solid Phase Sintering
STL	StereoLithography file format (for geometrical data)
TM	Thermal Mesh, in finite element program

CHAPTER ONE

1 INTRODUCTION

This chapter summarises the need for the work undertaken in this PhD project, and describes the nature of that work. The layout of the following document is then explained.

1.1 Outline of Research Situation

To reduce the amount of time required in the development of new products, manufacturing industry has adopted a group of technologies collectively known as solid freeform fabrication (SFF) systems. SFF machines can be used for rapid prototyping (RP) or rapid tooling (RT) applications. RP systems allow prototype parts of any geometry (within size limits) to be built in a matter of hours. RT is used to quickly fabricate metallic tools which are then used to make many parts having production-standard mechanical properties.

One such SFF process is known as Selective Laser Sintering (SLS). SLS takes powdered material as its input. Before processing, the powder is spread flat to form a thin layer. A scanning laser beam selectively heats and bonds the powder particles in a layer, to form solid sections of a specified shape. More powder is spread on top of the processed layer: more laser scanning and bonding takes place. Adjacent layers bond to each other through the laser's heating effect, building up to form a solid part. Once it is built, an SLS part can then be treated with post processes to improve quality: however, this increases the overall duration required to complete a prototype.

It is desired to selectively laser sinter metal powders without post processing, to create short run tools or parts. The potential combination of speed, geometrical flexibility and low cost compares favourably against traditional manufacturing methods: casting, spark erosion and machining for example. A number of approaches are already available to create metallic parts directly via SFF, however the requirements of finished parts are hard to meet: high dimensional accuracy, high strength and low residual stresses are examples. In order to meet such requirements, attention must be paid to SFF process control. The thermal and

mechanical properties of the processed metal should be understood and taken into account.

1.2 This Thesis

In this thesis, two thermal characteristics of metals which relate to direct SLS are investigated. The material focussed on for study is stainless steel 314HS powder, of various particle sizes. Another type of tool steel and a polymer-bound steel powder are also tested. The heat transfer process when a constant wave carbon dioxide laser scans metal powder is examined, using contact and non-contact temperature measurements. Methods are developed to evaluate the effective thermal conductivity of powders, and the absorptance of laser radiation energy by powders as they are processed. The effect of laser parameters and scanning strategy on absorptance is considered.

An existing finite element model of direct metal SLS (written in Fortran) is developed in several ways. Generation of input files is simplified, and feedback during run-time is increased. The size of output files is reduced, and visualisation of output data is improved. The scope and nature of the model is assessed via process mapping.

The model output is compared to experimental output for verification, based on the cross-sectional dimensions of modelled and manufactured layers. The application of modelling work to better process control is considered.

1.3 Organisation of Thesis

The following document is split into chapters, with content as described below.

- Chapter 2 is the Literature Review. It begins with a discussion of the need for Solid Freeform Fabrication in manufacturing industry. SFF and popular SFF systems are detailed, then from these Selective Laser Sintering is chosen for a more in-depth discussion. Direct SLS of metal is analysed: the effect of process parameters and finished part characteristics are investigated. Previous work regarding heat transfer, material densification and numerical modelling

for SLS are reviewed. The future direction of SFF is considered. Findings are then summarised. The chapter ends with a statement of the aims of this PhD project.

- Chapter 3 is called Heat Transfer Experiments. The theory underlying the calculation of conductivity and absorptance is explained. Experimental apparatus (pre-existing and custom-made) and powders tested are described, with reasons for their selection or design. The procedure followed during experiments is explained. Experiments include measurement of thermal properties and the creation of single layer stainless steel parts for dimensional analysis and comparison against numerical model output. There is also a measurement of powder density and a study of material evaporation.

- Chapter 4 is about Numerical Model Development. It explains changes made to an existing numerical model, and pre-/ post-processing aids which were developed. These relate to ease of use, efficiency and communication of output. Chapter 4 also details activity undertaken to assess the scope and validity of the model for recreating direct SLS of metallic single layer parts.

- Chapter 5 describes Processing of Results. Raw data from thermal experiments and numerical modelling are converted into a useful format. Processing of experimental temperature data is done to determine material thermal properties (conductivity and laser absorptance) under various conditions. Calculations are made in order to measure powder density and the level of material evaporation. Sectional and 3D visualisation of modelled parts was made possible, via post-processing. This is undertaken using two software packages. Images of modelled parts are used to create process maps, showing the range of input parameters which would lead to parts of acceptable quality. Images are also created for morphology and area comparisons between modelled and manufactured single layer parts.

- Chapter 6 contains Results and Discussion: Thermal Experiments. Material absorptance and conductivity as measured under different circumstances are

presented. Observations are made concerning the laser-induced thermal field in direct metal SLS. Powder density and evaporation study results are presented. Stainless steel single layer cross-sections are displayed. All presented results are discussed. Possibilities for future experiments are identified.

- Chapter 7 is Results and Discussion: Numerical Modelling. Elementary modelled shapes are presented, with an explanation of generic features. Changes made to the program are validated by comparison of modelled parts. Process maps are presented. Modelled single layers are compared dimensionally and morphologically with the manufactured (real) equivalent. All items presented are discussed, and observations made during use of the model are detailed. Suggestions are made for future modelling work.

- Chapter 8 contains Conclusions. The contents of the thesis are condensed into a few statements.

- References and Appendices follow on from Chapter 8.

CHAPTER TWO

2 LITERATURE REVIEW

In this chapter, the work of others relating to the direct selective laser sintering (SLS) of metal is reviewed, leading to a statement of aims for this PhD project. Section 2.1 provides background information to explain the importance of the SLS process for rapid manufacturing applications. SLS is discussed alongside other processes used in rapid manufacturing.

Section 2.2 focuses on SLS in its different forms. The process is described with reference to hardware, materials and the manufacture of freeform structures. Machine parameters and the characteristics of parts are discussed. Section 2.3 concentrates on modes of heat transfer in the SLS process. Equations describing heat transfer mechanisms are reviewed. The effect of laser heat on SLS materials is examined in Section 2.4. In Section 2.5, numerical models of relevance to direct SLS are investigated. Section 2.6 reflects the views of authors concerning the future direction of processes such as SLS. Section 2.7 summarises the chapter so far, and Section 2.8 provides a statement of what this PhD project aims to achieve.

2.1 Introduction

In this section, a discussion of the contemporary product design process identifies a need for rapid manufacturing technology. Some rapid manufacturing methods are described, and the nature of output parts is discussed.

2.1.1 Needs of Manufacturing Industry

New technology and new working practices have affected the contemporary industrial product design process in many ways. The integration of new technology and practices has helped manufacturing industry to meet its evolving needs. Described below is the current state of the product design process, which leads to an understanding of why technologies such as the type researched in this work have been so quickly adopted by manufacturing companies across the world.

From the scale of a single-piece child's toy to an automobile comprising thousands of parts, manufacturers are perpetually involved in the business of product development. A team of people is assigned a specific product development task to complete in a given time, using given resources. Teams are multi-disciplinary, consisting of engineers, industrial designers, purchasers and marketers amongst others. All groups must bring their specialised knowledge to bear on the product, in order to define the details of its form and function. The product is then brought to the manufacturing stage, before being released to market.

The constituent activities of this product design process according to Pahl and Beitz [Pahl 1999] are shown in Figure 2.1. The process begins with an assessment of the market situation, to identify potential needs. If a niche for a product is identified, then a series of activities follows to identify a solution, briefly outlined here:

- Planning and clarifying: allocating necessary resources to the project, and defining a list of requirements (specification) for the product to fulfil;
- Conceptual design: finding methods by which the needs of the specification now generated can be met;
- Embodiment design: assessing these methods, choosing the most suitable one. Defining the form of the product;
- Detail design: exact dimensions, materials and means of manufacture are specified.

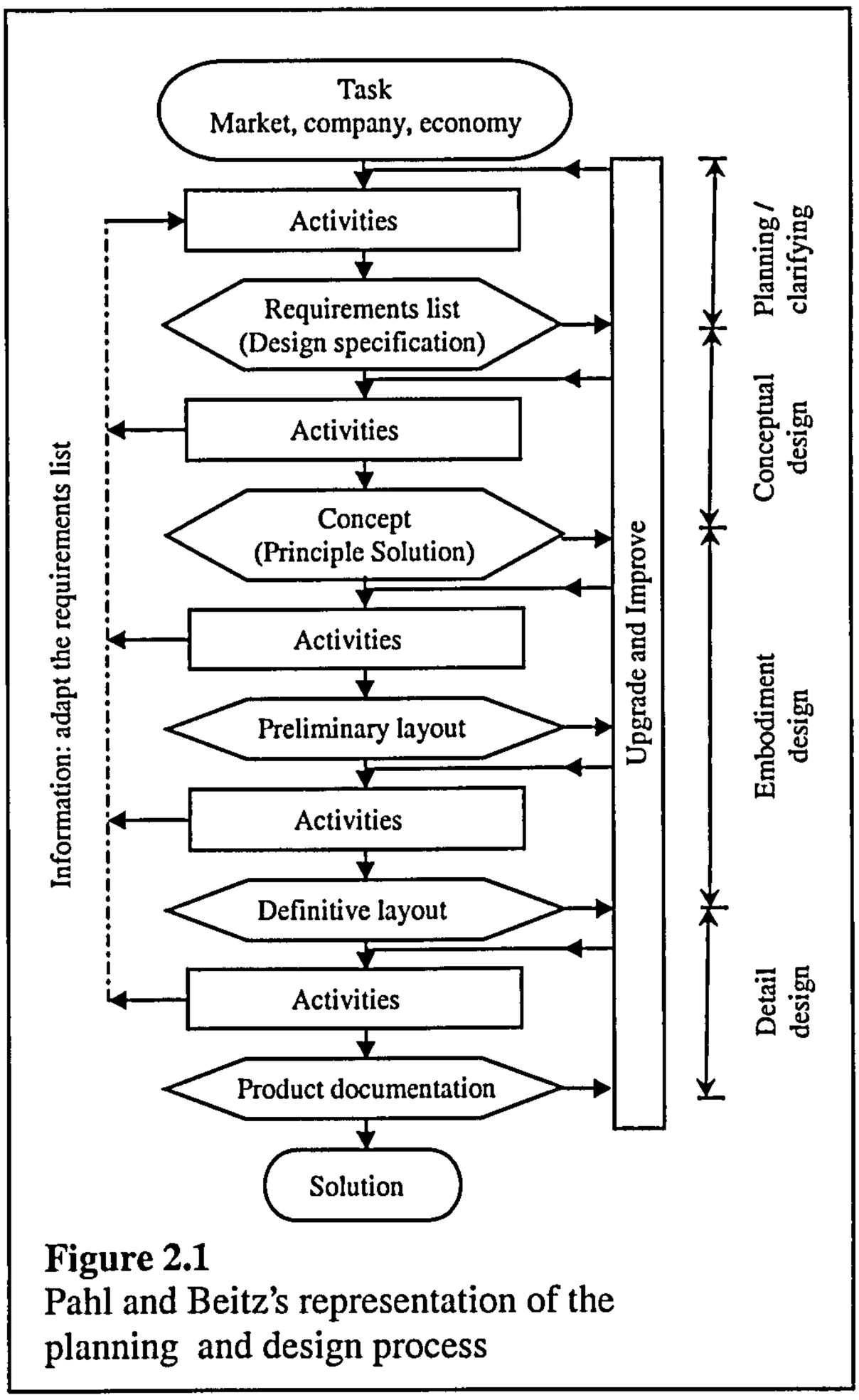

Figure 2.1
Pahl and Beitz's representation of the planning and design process

An alternative form of the design process is offered by [Ohsuga 1989]. Stages in the process are not ordered or named, but are generalised as a loop of analysis, evaluation then refinement. Both discussed forms of the design process suggest iteration from a vague to an explicit definition of the product. This model of design as an iterative process implies that the more iterations there are, the less flaws a product will have and the more fit for purpose it will be.

These iterations are more the result of brainstorming and critical discussion in the first instance, and more due to theoretical and practical testing in the later stages. A useful objective is that in the discussion stages the product concept is exposed to people having a wide pool of experience, including potential customers [Pham 1998], and that it is tested as widely as possible later on. Regular and specific communication of design details to the entire development

team not only facilitates feedback, but also allows individuals to start planning their up-and-coming tasks [Pham 1998]. This parallel, well-informed system of team working is known as concurrent engineering, and is vital to rapid development of high quality, complex products [Sohlenius 1992].

For the purposes of co-ordinating and communicating complex design information, computer-based tools have entered the product development process [McMahon 1998]. Computer aided design (CAD) allows a three-dimensional (3D) image of a product or part to be created using knowledge of geometry and set theory (using addition, union and so on). 3D models are quick to generate, easy to manipulate and can be stored or transmitted electronically with no degradation [Steen 1998]. Once a model's geometry and other explicit data have been defined, its in-service performance can be simulated by the computer in several ways: using finite element modelling to analyse mechanical or thermal scenarios [Livesley 1983], and using virtual reality [Kalpakjian 2001] to interact with the model.

The value of computers for visualisation and analysis has been identified, yet there is still a need for physical models in design verification and communication. The subtleties of ergonomic factors such as the comfort of a hand grip or the appearance of a textured surface in daylight may be impossible to assess in a CAD environment. Similarly, certain physical usage conditions may be too complex to be modelled accurately by numerical methods. A "real world" model or prototype is needed. Prototypes are unambiguous and an ideal focus point for non-technical personnel [Pham 1998].

A final dimension to add to the situation of new product development is that of time. IBM [Sohlenius 1992] have reported that over the period 1978-1994, the average life of a consumer product reduced from 7 to 2.5 years. Competition in a global market has increased pressure on manufacturers to accelerate their product life cycle. For fast-moving and forward-thinking companies, reduction of a new product's time to market increases the market share enjoyed as other companies work to develop competing products [Kalpakjian 2001].

With reference to their product design stage diagram Figure 2.1, Pahl and Beitz report that making a design modification at the concept stage will cost a tenth of making the same modification in the manufacturing engineering stage, and will only cost a hundredth of making the modification during mass production. This is because of the level of financial commitment made at the different stages. BAE Systems [Beaman 1997] have reported that once 5 percent of a design project's total cost has been spent, 85 percent of the total cost is committed.

The facts provided by IBM, Kalpakjian, Pahl and Beitz and BAE can be interpreted thus:

- The product development cycle should be as short as possible, in order to maximise product sales and income;
- Within this cycle, the product design should be modified repeatedly, with a rate of change which reduces over time in order to minimise the cost of changes.

What has been identified is that multiple, rapid repetitions of the early product development loop (analyse, evaluate and refine) are required. This loop may involve visualisation and testing in the computer environment, but will also require rapid realisation of 3D CAD geometry, i.e. physical model-making. This will facilitate communication of design developments to a broad range of people, and will allow limited product testing, both of which can drive future design iterations.

Such a group of methods for CAD data realisation has recently become available, collectively known as solid freeform fabrication (SFF) methods. Their ability to quickly create solid objects has attracted interest from people inside and outside manufacturing industry, leading to many novel applications. Discussed in the next section is the value to manufacturing industry of SFF technology not only for creating prototypes, but also for generating mass production forming tools.

2.1.2 Solid Freeform Fabrication in Manufacturing: RP and RT

Rapid prototyping (RP) refers to processes which create prototype parts, geometrically representing the final production part [Kalpakjian 2001]. Cheap and

simple machines which make "form and fit" type parts are often referred to as desktop RP systems. Machines also exist which can produce functional prototypes, with mechanical properties and accuracy close to those of a production part [Kruth 1998]. These are known as workshop RP systems [Pham 1998]. The rapid tooling (RT) group of processes involve the primary manufacture of a negative which serves as a tool in a secondary forming process. RT can create production-type parts which are equivalent to the final product, for testing purposes. In some cases RT tools are sufficient for mass production, for instance the injection moulding of 100,000 parts before tool wear became excessive [Radstok 1999].

The combination of RP and RT is referred to by the term solid freeform fabrication, or SFF. Whereas rapid prototyping and tooling describe the process in terms of a product development strategy, SFF describes the nature of the process output. The term SFF acknowledges the unrestrained geometrical properties of output parts, described further in Section 2.1.3.

Desktop RP, workshop RP and RT each have their own combination of qualities which are tailored to meet different needs. A production engineer may select them from amongst a large group of processes including more traditional material forming technologies. Three example scenarios are given below, in which a non-SFF and SFF process are compared for realising a 3D CAD design. More details on forming processes and any facts used below can be found in the work of [Kalpajkian 2001], [Swift 1997], [Pham 1998], [Shellabear 2001] and [Dickens 2000]. The SFF processes mentioned will be discussed further in Section 2.1.4.

Requirement 1: fast and cheap prototype part to verify a first design.

Non-SFF solution: desktop milling machine. Accuracy ±10μm. Machine cost £4,500. Maximum part size 120 x 100 x 120mm.

Best choice for: cost.

SFF solution: desktop RP, e.g. 3D printing. Accuracy ±130μm. Machine cost £25,000. Maximum part size 360 x 460 x 360mm.

Best choice for: reproduction of internal design features.

Requirement 2: rapidly-produced and functional prototype polymer part, strength and accuracy approaching that of production part.

Non-SFF solution: machined master, reproduced by reaction injection moulding. Appropriate accuracy and strength, can make up to 100 copies of master. Process is labour-intensive.

Best choice for: multiple prototypes.

SFF solution: workshop RP, e.g. selective laser sintering. Appropriate accuracy and strength. Production time about 1 day.

Best choice for: low skilled labour requirement.

Requirement 3: tool for plastic injection moulding.

Non-SFF solution: electrode discharge machining. Tool strength similar to that of cast material. Lead time 10 weeks, cost £6,000.

Best choice for: high production runs (100,000s of shots).

SFF solution: RT, e.g. DMLS. Tool strength approximately 75 percent of cast material. Lead time 2 weeks, cost £5,000.

Best choice for: fast tool production.

As has been illustrated, there are many factors to be considered when choosing a manufacturing process. These examples do not attempt to provide all the facts involved in a decision, but simply show that SFF processes are preferable in a variety of niche situations. In such a huge marketplace (the forming tool market alone being estimated at a value of £43 billion in 1999 [Wohlers 1999]), SFF technologies are thriving.

2.1.3 SFF Technology

2.1.3.1 Process Procedure and Part Features

Some of the advantages of solid freeform fabrication have already been demonstrated in the previous section. Commercial SFF technology is only 14

years old [Jacobs 1992], and has always been based on modern hardware and software technology. The procedure for converting a 3D CAD model into a physical model is largely automated, meaning a high process speed and minimal human intervention [Badrinarayan 1994]. This procedure by which an SFF part is made [Beaman 1997, Kalpakjian 2001] will be described with the aid of Figure 2.2. The influence of the process on the nature of parts is explained. Some example SFF processes are detailed in the next section, 2.1.4.

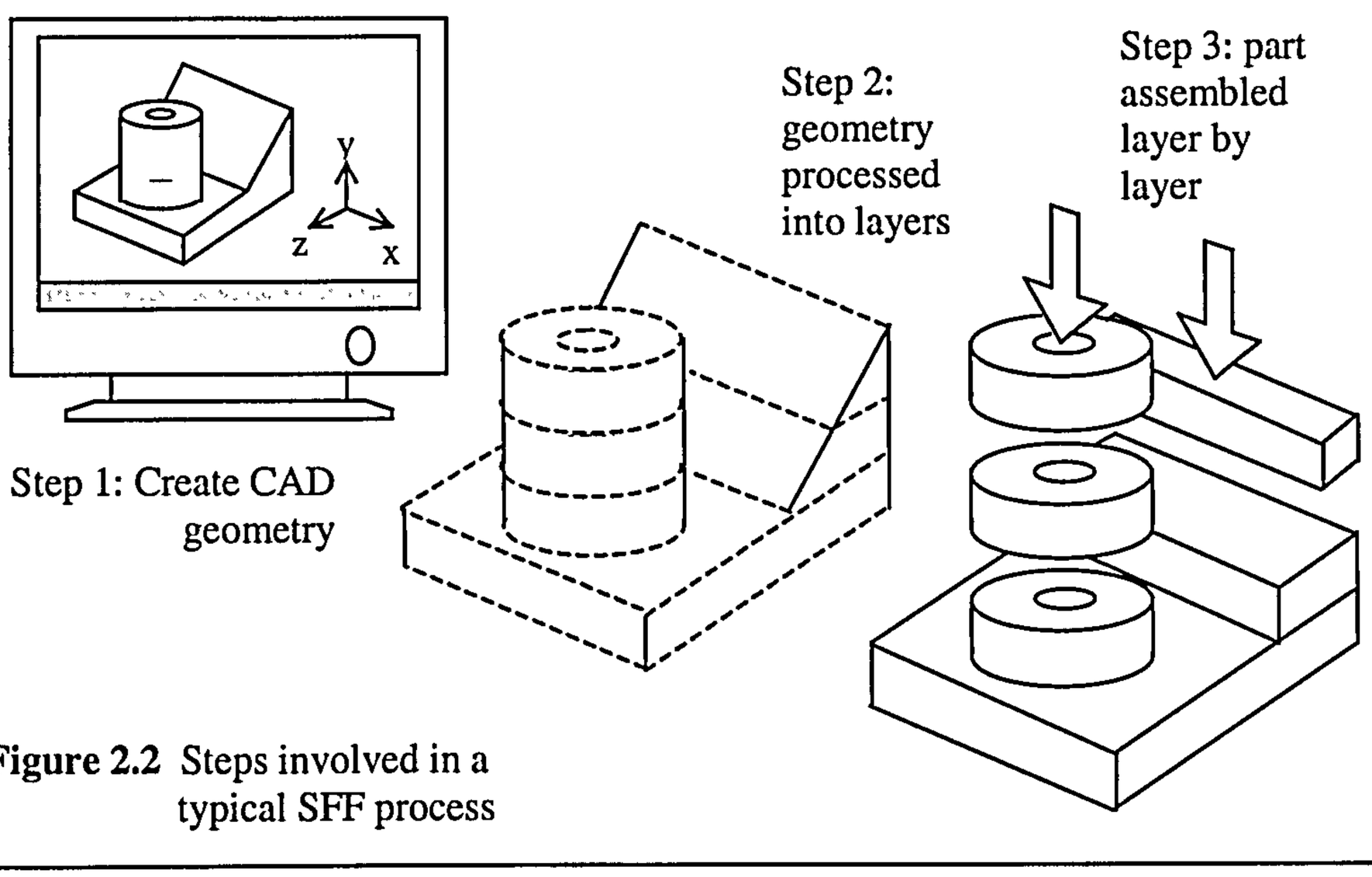

Figure 2.2 Steps involved in a typical SFF process

The input data required to make an SFF part are of three dimensional geometrical form (step 1, Figure 2.2). The most common way of creating 3D data is by assembling solids and surfaces using a CAD package. An alternative is to digitise the geometry of an existing object through laser or MRI scanning.

SFF systems have sometimes been termed "layer manufacture" systems. This is because the building of parts takes place one layer at a time, with each layer bonded on top of the last. Before a solid model can be realised, it is necessary to convert the 3D data into surface form, to be processed into tool paths. The most popular format to convert to is "stl" [Pham 1999], a de facto standard developed by 3D Systems which uses tesselating triangular elements to cover the full surface of the model. This leads to a diamond-like facetted appearance of curved surfaces, and reduces the accuracy of the model somewhat. Other formats exist, such as "slc" which generates polygonal contours around the model surface in parallel

planes. The value of the stl format though is that the triangle-based data make model processing fairly simple.

Once in stl format, the part data are usually transferred to the SFF equipment. The machine's software must now use the stl data to generate a scanning pattern for the processing tool (which may be a laser, polymer extrusion head or other device depending on the type of SFF process). A slicing algorithm calculates the intersection point between evenly-spaced parallel slicing planes and the stl surface triangles. The planes are trimmed to occupy the interior volume of the model (step 2 in Figure 2.2).

The method in which plane information is converted to a tool path is dependent on the SFF process. Some different forms of SFF are discussed in the next section. In the case of a raster-scanning laser used to form a solid structure where it contacts with raw material, the laser could simply be toggled on and off where it passes into and out of the area defined as solid by the layer plane.

Layers are built by the processing tool's interaction with the raw material as the tool follows the calculated paths. The layers are created and bonded together, to create the final part (step 3, Figure 2.2). Bonding of layers occurs either during the process or afterwards.

Note that no pre-fabricated part-specific tools are required in manufacture, a major advantage of SFF.

Using SFF-type processes, polymers, metals, ceramics and many composite materials can be transformed into bonded-layer parts. Raw material comes in powder, liquid, sheet or solid layer form. A part may be completely finished after SFF processing (known as a direct process), or in "green" form, ready for post-processing (which is discussed in Section 2.1.4.7). SFF parts can be recognised by certain features inherent in the process:

- Complex geometry, particularly in reproducing internal features. SFF tools have no "blind spots" such as found in machining, and corner radii are typically less than 0.5mm [Beaman 1997]. Figure 2.3 is an example of the detailed freeform output possible. A popular geometrical aspect of rapid tooling (RT) is the ability to create "conformal" cooling channels in mould

tools [Wohlers 1999]. Such channels run just below the cavity surface of the manufactured mould, carrying fluid which transfers heat away from the mould. Uniquely to RT, these channels can be fashioned to exactly follow the contour of the cavity surface. They provide the optimum result when molten material has been injected into the mould and must be cooled before ejection. The higher the cooling rate, the quicker the moulding process becomes [Sachs 1997].

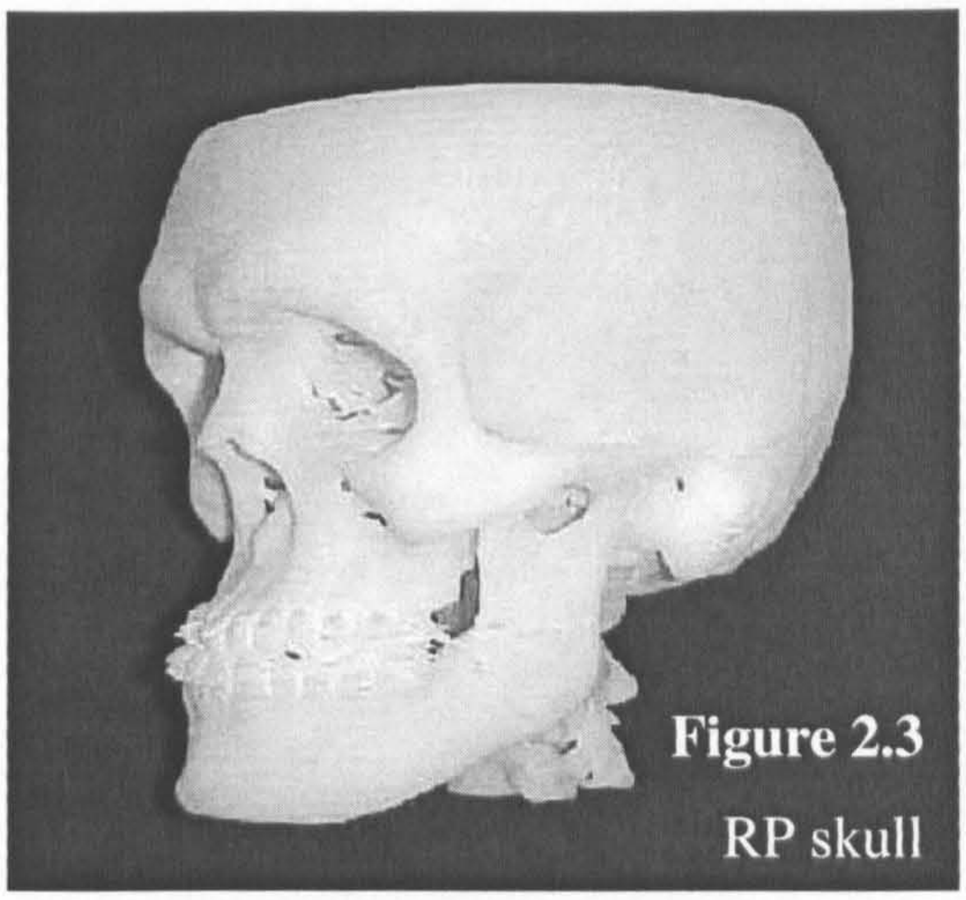

Figure 2.3
RP skull

- Use of supports. As a material additive process, not all SFF parts have the support structure needed to avoid in-process toppling, sinking or creeping of certain areas. Overhanging features in particular have been seen to distort under their own weight [Xu 1999, Matsumoto 2001]. To counter this effect, certain machines have software which provides further model processing, to calculate positions where extra part support structures should be built. These supports are either made of a wax-like material which does not bond to the part, or are designed to be broken off at special weak points.

- A rough "stepped" surface. Each layer is made with vertical walls, so curved surfaces are only approximated, shown in Figure 2.4 [Sabourin 1996]. The extent of the resulting inaccuracy is dependent on layer thickness and build orientation.

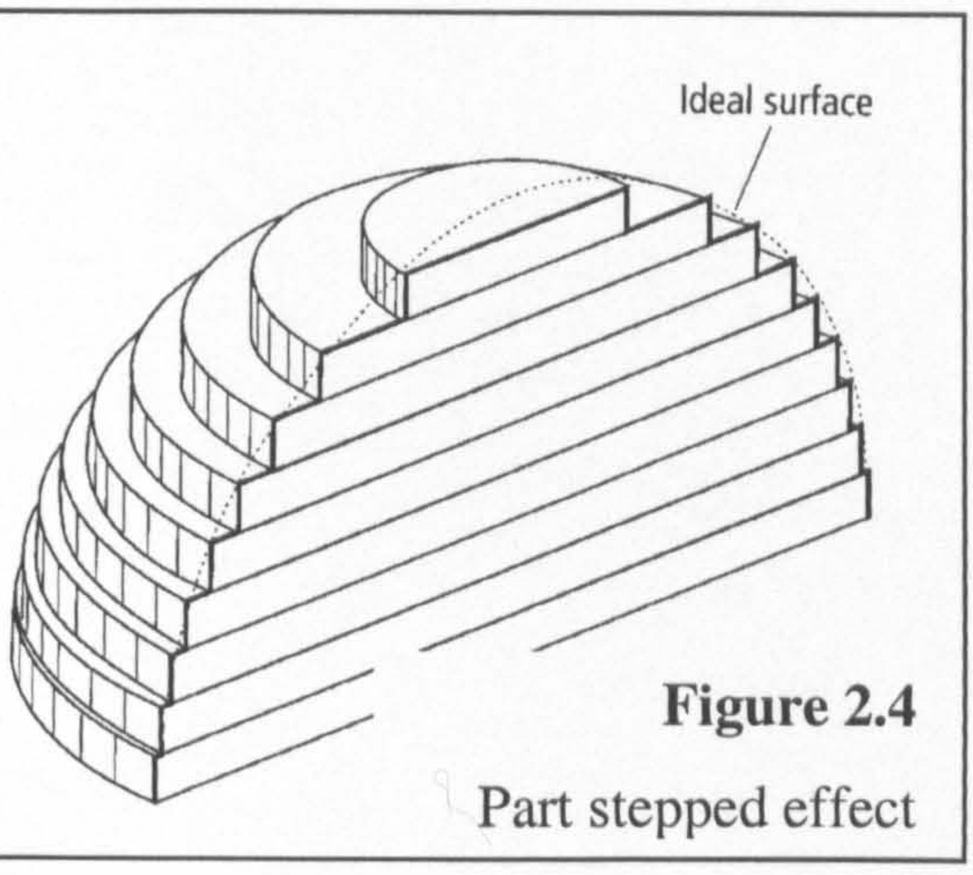

Figure 2.4
Part stepped effect

- Inaccuracy due to shrinkage and tool offset. Studies show [Wang 1999, Geiger 1996] that an effective way to remove en masse dimensional inaccuracies is through a feedback loop. A standard part is built, and a large number of dimensions are measured. Inaccuracy which varies linearly with position can be attributed to material shrinkage in forming, and any constant inaccuracy can be attributed to poor tool radius compensation, as is used when calculating machining toolpaths. SFF software can apply reverse values of shrinkage and tool offset to a CAD model, for dimensional control. This broad brush method can not however deal with the differential cooling and localised shrinkage/ warping inherent in truly freeform parts, discussed in Section 2.2.6.

- Non-isotropic mechanical properties. Parts have been found to be stronger when loaded in the build layer plane than when loaded orthogonally to this plane. This is because the layers themselves are generally stronger than the bonds between layers. Furthermore, SFF-processed materials tend to be more brittle, softer and less strong than if processed using standard production methods (e.g. casting for metals, injection moulding for plastics). There are applications where non-isotropic properties are advantageous: SFF can be used to deposit multiple materials alongside one another with a stepped or graded material transition. For instance, it is possible to incorporate internal wiring or high-strength zones into a manufactured object [Calder 2001].

- Porous (semi-dense) processed structure. This applies particularly to SFF processes involving powders. It is possible to induce necking between the powder particles, but leave interstitial channels as with sintering. Such open porosity can be useful when moving parts are intended to be self-lubricating (i.e. grease is held in the pores), or for medical applications [Wohlers 1999]. In most SFF applications a porous structure is accepted but is not desired, because a strong link exists between part porosity and low yield strength (discussed in Section 2.2.6.4). Solid (zero porosity) parts can be challenging to produce by SFF [Khaing 2001].

2.1.3.2 Machine Components

The majority of SFF machines fulfil similar functions:

- Raw material storage;
- Delivery and levelling of material for each layer;
- Means of processing material from raw to structural form;
- Movement of the processing tool relative to the work piece.

Different methods of fulfilling these functions will be seen in the examples provided, Section 2.1.4. Further consideration is given here to the most popular material processing tool used in SFF. This is the laser [Kruth 1998].

A laser's light is electromagnetic, but with the unusual property of being highly focussed (divergence a few milliradians) and of almost constant wavelength for a particular laser type [Luxon 1985]. The two most popular laser types for SFF are:

- Carbon dioxide (CO_2), up to 15kW CW power at 10.6μm wavelength;
- Neodymium YAG (Nd:YAG), up to 200W CW or 1.5kW pulsed power at 1.06μm wavelength.

The term "CW" is short for "continuous wave", meaning that the beam provides constant power over time. If a laser is pulsed, this means it is switched on and off rapidly, which can provides certain benefits. An Nd:YAG laser may be pulsed, a CO_2 laser may not. For their high power and relative low cost [Crafer 1993], CO_2 lasers have proven most popular for use in SFF machines. Nd:YAG lasers are growing in popularity for metals processing as their price decreases.

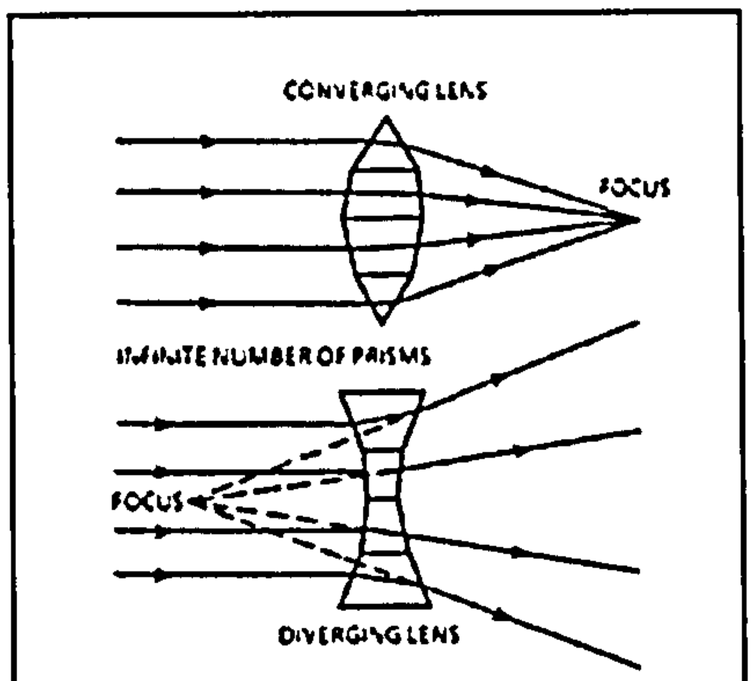

Figure 2.5 Lens types

Optical systems consisting of several lenses can expand, collimate and focus a laser beam as required. In Figure 2.5, two lenses are presented. A convex lens (top) causes the beam to converge by refraction; the concave lens (bottom) causes the beam to diverge. These two lenses are combined to form a beam expander, which improves focussing by reduction of beam diffraction effects. It is worth

bearing in mind that each optical component added to the beam delivery system reduces its efficiency, by absorbing the beam's energy.

Standard laser beams do not have a constant spatial distribution of power, rather a radial pattern of irradiance. Irradiance is strongest at the beam centre and reduces exponentially outwards. More detail will be provided in Section 2.3.1.

Laser light can be effectively redirected by mirrors, which are used in many SFF processes. Mounted on galvanometers [Tumer 1995], the mirrors redirect the beam when they are rotated. Certain lasers (including Nd:YAG) can be transmitted inside optical fibres, which are directed by an NC head [Kruth 1998b].

2.1.4 SFF Systems

There are now in excess of 58 types of SFF system being sold worldwide [Hunt 2001]. It is not proposed to describe them all here. In the next 5 sections, 5 popular SFF processes are detailed in terms of hardware features and performance. In a further 2 sections, other SFF technologies are summarised and post processes are considered. The variety of possible approaches becomes clear, as does the core concept of layered manufacturing. Prices quoted are for the most basic model. "RT part volume" refers to the number of parts which can be manufactured from a rapid tool made with the particular process. For further information on SFF processes, see [Kalpakjian 2001], [Dickens 2000], [Pham 1998] and [Castle Island 2002].

2.1.4.1 Stereolithography (SLA)

Material: liquid photocurable polymer.

Tool: laser.

Accuracy: ±100μm [Pham 1998].

Machine cost: £50,000 [CI 2002].

RT part volume: <1,000 [Radstok 1999].

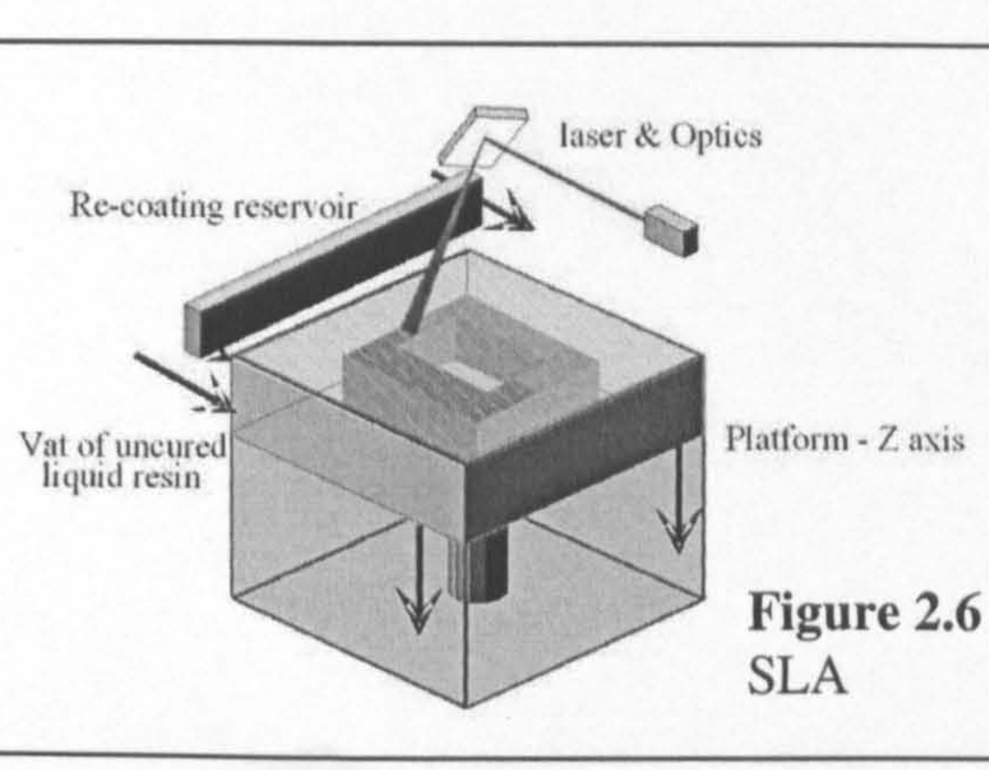

Figure 2.6 SLA

SLA is the first of the SFF processes, commercialised in 1988.

The apparatus is as in Figure 2.6. The part platform sits one layer thickness (as little as 0.025mm) below the surface of a liquid polymer bath, allowing a layer of the polymer to flow over it. A wiper blade is used to level the viscous liquid. The laser beam is then directed by rotating mirrors to contact chosen areas of the liquid polymer layer: where it does so, the polymer cures and solidifies. Once one solid layer structure has been completed, the laser switches off and the part platform lowers by one layer thickness. More polymer flows over the top of the solid layer and covers it. The laser scans again, building another layer on top of the previous one. The penetration of the laser is such that the new layer bonds to the previous one as it is cured. One by one, layers are added until a complete model is finished. The part platform raises from the bath allowing remaining liquid to drain from the model, then it is detached from the platform and may be post-cured to full density.

2.1.4.2 Selective Laser Sintering (SLS)

Material: powder form. Polymers, polymer-coated metals and ceramics, high/ low melting point metal mixtures and other composites.

Tool: laser.

Accuracy: ±51μm [Pham 1998].

Machine cost: £200,000 [CI 2002].

RT part volume: <100,000 [Radstok 1999].

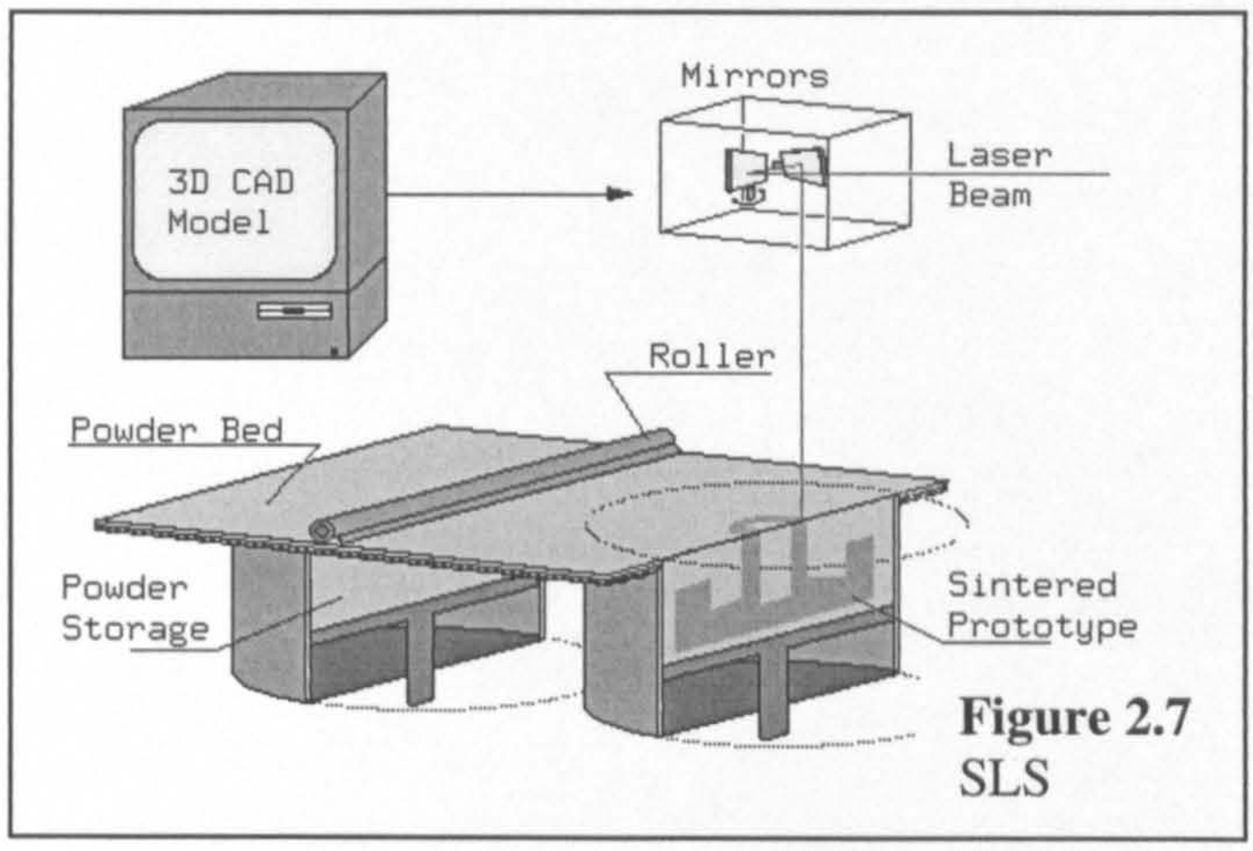

Figure 2.7 SLS

SLS is the most versatile SFF process. The materials used are cheaper than those used in SLA [Pham 1998].

Refer to Figure 2.7 to see the SLS apparatus. As in SLA, material is spread across the surface of a bed and processed by a laser. The major difference is that the material is in powder form, of typical particle diameter 50μm. The laser heats

material to approximately the melting point, causing adjacent powder particles to bond and form a solid structure. This requires higher laser power than for SLA. In the case of polymer or polymer-coated powders, sintering temperatures usually lie in the 100-200°C interval: the powder bed can be preheated to just below the melt temperature of the polymer, allowing tighter control of the sintering process.

The SLS process is discussed in greater detail in Section 2.2.

2.1.4.3 Laminated Object Manufacturing (LOM)

Material: sheet paper or plastic (may be ceramic-filled) with polymer binding underlayer.

Tool: laser or knife.

Accuracy: ±127μm [Pham 1998].

Machine cost: £80,000 [CI 2002].

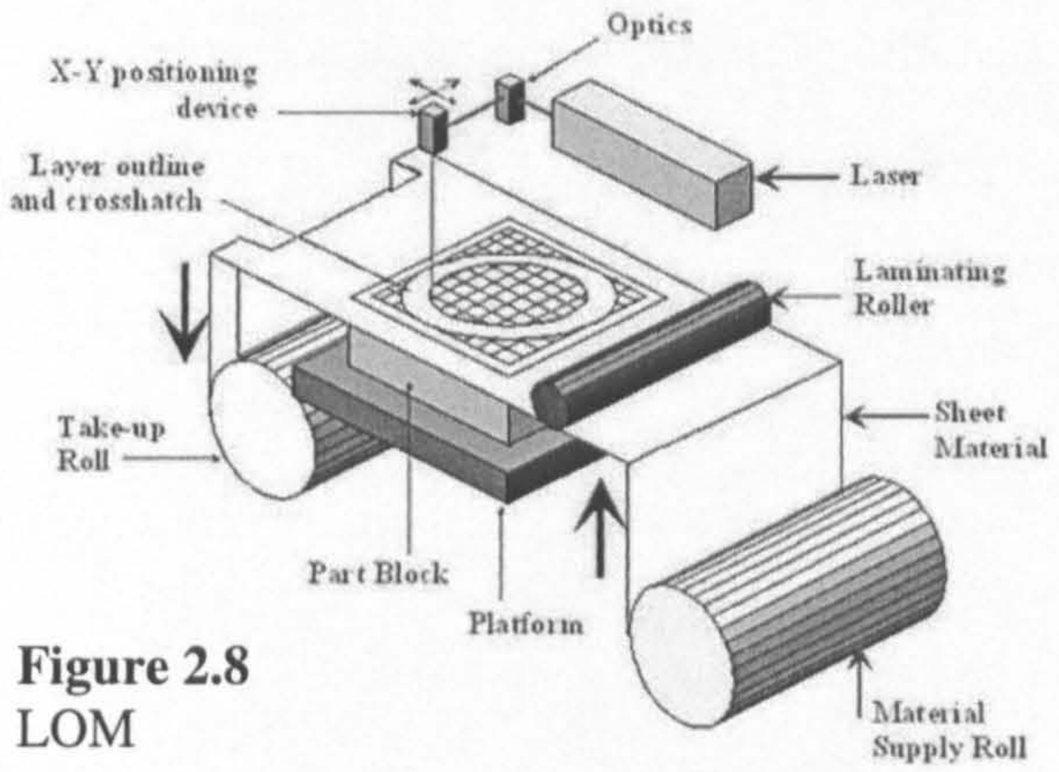

Figure 2.8
LOM

Refer to Figure 2.8 during the following description of the LOM process. A roll of flexible sheet is supplied to the part area, where a laser or knife cuts the pattern of a layer. The excess sheet around the pattern is cross-hatched for easy removal later. After cutting, a heated roller compresses the sheet layer. The heat of the roller activates the sheet's polymer undercoating, which bonds the current sheet to the previous one. Once the part is fully built, the bonded cross-hatched areas are removed from the interior and exterior. LOM is an example of a desktop RP process.

2.1.4.4 Fused Deposition Modelling (FDM)

Material: polymer or casting wax filaments.

Tool: heated extrusion head.

Accuracy: ±127μm [Stratasys 1998].

Machine cost: £20,000 [CI 2002].

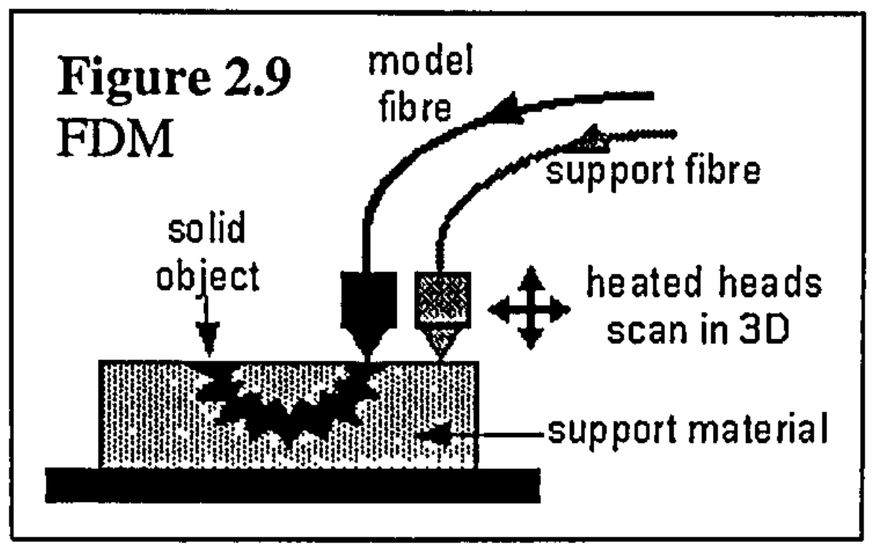

Figure 2.9
FDM

FDM has been the most popular SFF process on the market [Kruth 1998a].

As shown in Figure 2.9, input material comes in the form of reels of polymer fibre. An NC-directed extrusion head has rollers which feed the fibre onto the part. Inside the head are resistance heating elements which raise the temperature of the polymer to 0.5°C above its melting temperature. The soft polymer is then extruded through the head onto the part being built. The polymer solidifies 0.1 seconds after contact with the part, before creep occurs.

Two materials may be used at once: a hard model material and a soft, easily removed support material, as shown in the figure.

IJP (or ink jet printing), works in much the same way as FDM but forms a structure using molten thermoplastic droplets rather than a continuous feed.

2.1.4.5 Metal Powder Spraying by DirecTool

Material: mostly metals.

Tool: integrated laser beam and spraying head.

Accuracy: ±127μm [Knights 2001].

Machine cost: unknown.

RT part vol.: >100,000 [Radstok 1999].

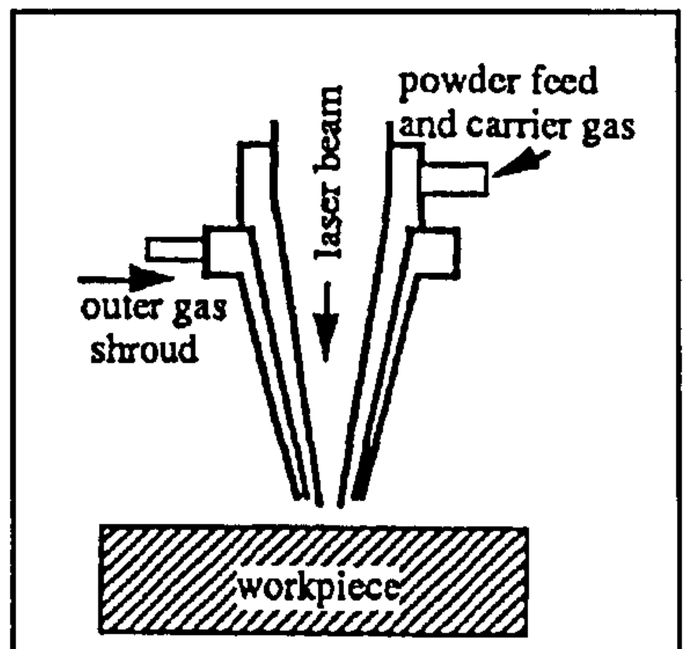

Figure 2.10
Powder spraying

Numerous powder spraying SFF methods exist, using a laser beam to melt a stream of particles which enter the beam's focal zone near the part surface. A material delivery head as shown in Figure 2.10 is moved by NC control. Spraying has the advantage over SLS that material supply to the processed area can be increased, to reduce part porosity. The DirecTool process can generate 100 percent dense parts from materials such as stainless steel. It is reckoned that a forming tool can be made in 1 week by DirecTool [Knights 2001].

2.1.4.6 Other SFF Technologies

In this section, some novel elements of other RP and RT processes are briefly considered.

Apart from the standard laser beam and heated extrusion head mentioned already, other processing tools have been used in SFF. These include:

- Geiger's [1996] dual-focussed laser. A beam is split into two concentric beams, using optics. One of these is of large diameter and low irradiance. In room temperature powder bed laser sintering (similar to SLS), where rapid heating and cooling can cause internal stresses in parts, the beam's outer ring slowly preheats and cools the processed material.
- A robot-controlled welding torch for metal SFF [Dickens 1992]. Dimensional accuracy was poor (±0.5mm) due to difficulty controlling the melt flow.
- A heated head which prints polymer binder into powder bed layers. The binder solidifies around the powder to form a structure [Kruth 1998a].
- An ultraviolet lamp, which shines through a custom-printed mask to solidify a layer of photocurable polymer. The entire layer is processed at once.
- A single- or multi-axis milling head. This is used to flatten the surface of layers as they are formed, or cut an angle on the vertical walls of each layer to reduce the stepped effect discussed in Section 2.1.3.1.

Some novel material schemes have been developed to overcome problems in SFF:

- Often it is desired to make parts from high melting temperature materials such as ceramics or steel. However, for good dimensional control in laser processing the peak temperature rise should be small, for reasons explained later in Section 2.2.6.3. [Kruth 1998a] and others have addressed this problem by using a dual-phase powder, with low temperature (binding) and high temperature (structural) constituents. The low temperature material melts on laser application, and flows by capillary force to form a bound part. The technique is known as liquid phase sintering (LPS) [Agarwala 1995b]. Low strength and high porosity result, which can be improved by post-processing.
- SFF materials tend to expand and shrink as they are processed. In the direct metal laser sintering (DMLS) process, metal blends have been developed

which undergo no overall shrinkage due to counteracting microstructural effects [Wilkening 1996]. Dimensional accuracy results are good. Liquid flow and particle rearrangement increase bulk density, then homogenisation causes diffusion, creating porosity and expansion to decrease bulk density. Processed parts are left less than 80 percent dense, however.

- In generating tools for drop forging and pressing, porosity is undesirable as it leads to lowered strength [Agarwala 1995a]. The Stratoconception SFF method [Poirier 2001] uses laminates cut from solid sheet material by laser or milling. These are stacked on top of one another and glued or brazed to form solid shapes. Metal tools made this way are very strong in compression.
- The benefits of powder spraying and LPS can be combined using selective area laser deposition vapour infiltration [Dai 2003a]. A powder bed is locally heated then infiltrated with vapour which fills pores, bonding the powder particles as it solidifies. High density and good dimensional control are seen in processed parts.

2.1.4.7 SFF Post Processes

If an SFF-generated part undergoes further processing, this is generally done to improve mechanical and geometrical qualities. Either the original part is enhanced, or its geometry is exploited by using it as a master to make new parts. Examples of "original part" post processes are furnace cycles, infiltration, machining/ polishing and painting. Examples of "master part" post-processes are rubber and resin moulding, electroplating and casting: these are usually used for rapid tooling (RT). Some post-processes are discussed below.

Furnace cycles offer longer and more consistent heating, for hours or tens of hours [Kruth 1998a]. Their function is to burn out SFF polymer binders, and to cause necking of the structural material which creates strength [Kruth 1996]. SLS furnace processes are discussed in more detail in Section 2.2.3. In 3D Keltool RT [Dickens 2000], core and cavity mould shapes are made by SLA equipment, then they are cast around with silicone rubber to create moulds. The mould is filled with polymer-bound metal powder, which is then cured. Firing in a furnace burns away the binder and sinters the metal particles. Infiltration can also occur in the furnace to produce tools with higher yield strength and hardness, and lower

roughness [Karapatis 1998a]. 1 million injection moulded parts have been made using a single copper-infiltrated Keltool tool [3D Systems]. Alternately, SFF parts may be coated with ceramic slurry, then burnt out in the furnace. The slurry is sintered to create an investment casting cavity [Pham 1997].

Other infiltrating materials include epoxy resin and solder. The surface or bulk of the part may be infiltrated, depending on the extent of porosity interconnection [Kruth 1997]. Infiltration of nickel-bronze SFF parts with tin solder by [Karapatis 1998a] increased their strength three times, and increased hardness five times.

Selective finishing (machining and polishing) of parts makes them smooth and flat, for interfacing with other parts and to reduce friction for moulding applications [Shellabear 2001].

Moulding using an SFF master part is done to produce parts of high and isotropic mechanical properties. An example process is room temperature vulcanising rubber (RTV) moulding [Dickens 2000]. Silicone rubber cast around an SFF master pattern is used as a cavity, to make urethane or epoxy parts. Material and labour costs make this method quite expensive.

In post-SFF electroplating, a master is sprayed with conductive laquer then electroplated with several millimetres' thickness of material such as nickel. External detail is very good, but holes cause difficulties [Dickens 2000].

There are numerous problems associated with post processing: for instance shrinkage in furnace cycles, 18 percent for some ceramics [Kruth 1998a]. Additional dimension changes accompany the use of geometrical negatives. In rapid tooling, tolerances need to be within ±50μm [Radstok 1999] so post-process control must be strong. Furnace cycles can add 5, 10 or more hours to lead times, and work such as polishing incurs high labour costs.

2.1.5 Summary of SFF in Manufacturing

SFF methods have become an integral part of the modern computer-driven design process. They help to reduce product development times, improving the communication and verification of product form. Different SFF processes have been developed to meet different needs. They compare favourably against more

traditional manufacturing processes not only in terms of speed, but also in terms of the complex internal detail which can be produced.

A processing tool creates a part from raw material in a layer-by-layer fashion, working from a 3D CAD design. A stepped surface, in-process shrinkage, non-isotropic properties and porosity are common qualities of SFF parts. Hardware, materials and post-processes have been developed to improve the qualities of parts. Post-processes add to the lead time required to obtain finished parts.

2.2 Selective Laser Sintering

In this section, different aspects of selective laser sintering (SLS) are considered. The original SLS process, as commercialised by DTM Corporation (now 3D Systems) is discussed in 2.2.1 and 2.2.2. Direct SLS processes are reviewed in 2.2.3.

The SLS equipment developed for the research undertaken in this work is the topic of Section 2.2.4. In 2.2.5, material properties are discussed. Section 2.2.6 discusses processing issues with a particular focus on direct SLS of steel powders.

2.2.1 The 3D Systems SLS Process in Detail

The 3D Systems SLS machine, also known as a SinterStation, was first devised in the 1980s [Deckard 1986]. It converts a CAD model in three dimensions to a solid object of the same geometry.

The data required to instruct an SLS machine how to build a part of certain geometry are in an stl format or equivalent. The creation of CAD geometry and conversion to stl has previously been discussed (Section 2.1.3.1). A model is draughted in 3D at actual size, and its interior/ exterior identified. The model's surface is automatically approximated by tesselated triangular patches, and this geometrical definition of the model is used to cut the internal volume into slices on parallel planes. The slice information is then converted to data controlling the

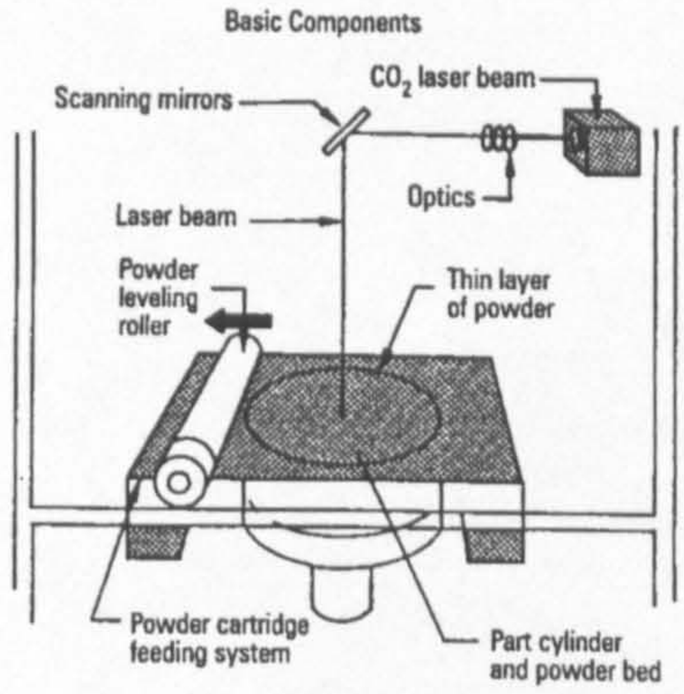

Figure 2.11 SLS Hardware

operation of the SLS laser beam [Beaman 1997]. The apparatus required for SLS is shown in Figure 2.11.

Materials used in SLS are polymers (which can be processed directly into a finished part), or polymer-bound metals and ceramics (made indirectly, requiring post-processes). All are in powder form. As an example of the particle diameter, the powder Rapid Steel 2 has a particle diameter range from 22 to 53μm [McAlea]. Fresh powder is entered into cartridges located on either side of the bed where the part is to be built. Underneath each cartridge is a feed piston which raises by a certain amount, presenting new powder to be moved to the part bed. The powder is moved by a roller, which rotates and moves to the left or right, depending on which powder cartridge is being used at the time. The roller moves the powder from the cartridge to the bed and spreads it flat across the bed's surface (on the next pass, it will serve the opposite cartridge moving in the opposite direction). The powder bed is preheated by radiant heaters, to a temperature just below the softening point of the binding material.

The laser, typically of 50W continuous wave CO_2 type, is activated. The laser beam is directed by two galvanometer-controlled mirrors, which rotate about perpendicular axes to deflect the beam left and right or up and down on the bed surface. The beam is switched on and off so that it selectively contacts with the powder surface. An automatic controller handles issues such as the timing of mirror movement against laser operation, and mirror velocity control [Deckard 1995].

As the laser beam makes contact with the powder surface, heat is absorbed locally by the powder particles, which increases their temperature. By a combination of sintering and melting, the particles in the beam's wake are bonded and cool to form lines of connected material on the bed's surface. Usually the laser moves in a "raster scan" pattern, drawing parallel lines with a degree of overlap to form a solid plane of material. Line scanning speeds can reach 7500mm/s [3D Systems 2002].

Once an entire solid layer has been formed, the part bed is lowered by one layer thickness. The powder feed piston and roller are activated to provide a new levelled powder layer on top of the previous one. Laser processing takes place

again, with laser power and layer thickness chosen so that temperature penetration is sufficient to bond the new layer to the previous one.

All unbonded powder is left in place during the process, which provides support for the structures created. More than one part may be made at once, for efficient use of the part bed volume and machine time. Thermally-induced shrinkage and residual stresses are minimised by preheating of the part bed and a slow cool-down after processing. Cooled parts are removed from the bed, and loose powder is extracted from them using brushes and compressed air. Unprocessed powder can be recycled after sieving [Pham 1998].

2.2.2 Optional Post-Processing Steps in 3D Systems SLS

SFF post processes have been mentioned in section 2.1.4.7. They are used to improve the mechanical and geometrical properties of parts. Most of the "original part" processes covered are used in SLS post-processing: furnace cycles, infiltration, machining and polishing [Beaman 1997]. Use of SLS for rapid tooling usually involves metallic or ceramic parts and as such, post processes are required. Materials have been specially designed for indirect RT applications, as will be seen below.

A key feature of specially-developed indirect SLS powders is the combination of a low melting temperature material and a high melting temperature material. The low temperature material is the binder, necking and bonding during SLS to create a continuous structure. The

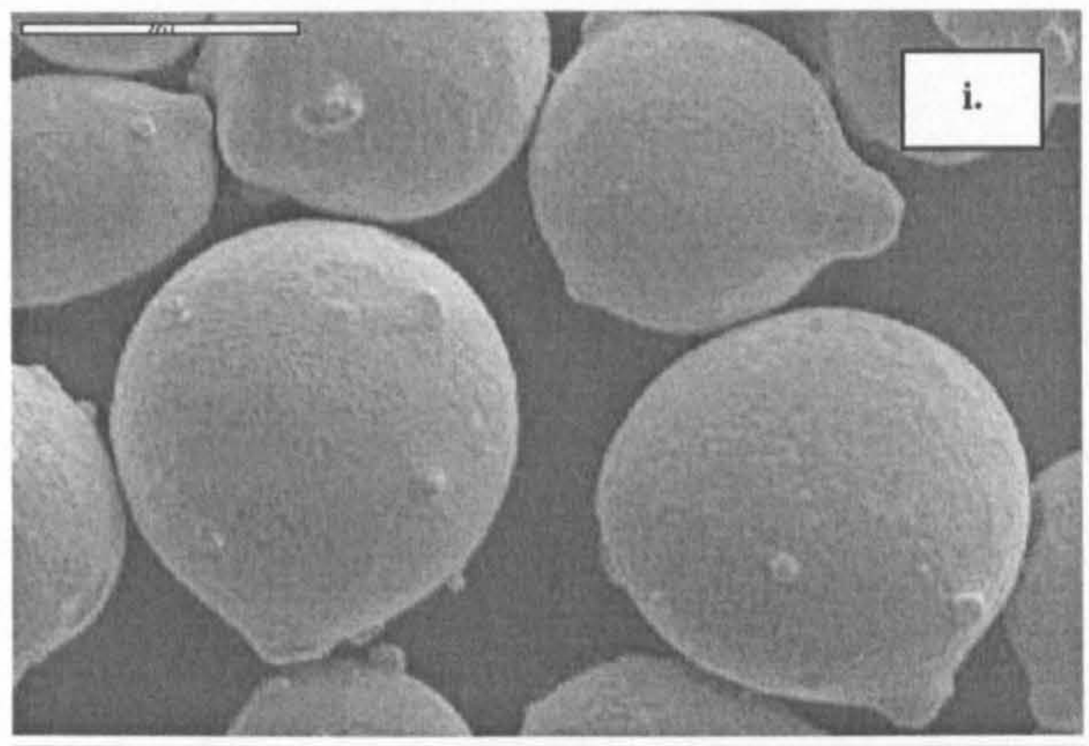

Figure 2.12 Magnified view of steel powder (i.); packing density range for spherical particles (ii.)

high temperature material provides properties looked for in the final part: temperature resistance, strength and stiffness. SLS-induced temperatures remain below the high temperature material's sintering point, to maximise dimensional accuracy [Pham 1999].

SLS of metals and ceramics is followed by furnace treatment. The polymer binder is burnt off, leaving a necked skeleton structure which is then sintered to full strength.

SLS parts are built from a powder bed which inherently contains voids, image (i.) in Figure 2.12. Although the sintering process incurs densification, green SLS parts are typically 70 percent dense, having a system of pores running throughout. This open-pored structure is unsuitable for an application such as plastic injection moulding or casting for several reasons:

- Cavity surfaces must be impermeable and smooth if formed parts are to be ejected easily and without causing wear;
- Hardness, strength and toughness of the structure are insufficient.

To improve the properties of parts after firing, infiltration is an option. A skeletal steel structure may be copper infiltrated as in the 3D Systems RapidTool process, or a ceramic structure may be polymer resin infiltrated. The infiltrant fills pores, improving strength and hardness and reducing surface roughness. An infiltrated yield strength of 300MPa has been reported for CastForm material [3D Systems 2002]. Infiltration also permits parts to be finished without damage. The infiltrant must not cause chemical reactions, which can lead to warping of parts.

Finishing processes include polishing to reduce roughness, and milling to improve surface planarity [Dalgarno 2000].

Investigations have been made into creation of short-run solid parts by SLS/ HIP processing [Das 1998]. The SLS part is built with gas-impermeable outer walls, and an interior of lesser-processed powder. The outer skin serves as an HIP (hot isostatic pressing) "can", to create fully dense parts. Normally a metal can must be specially formed for this purpose, so the HIP process is simplified. A titanium-based alloy part was made in this way, to 99.9 percent of full density.

To provide a real example of indirect part creation, consider a sand casting mould made in RT [Beaman 1997]. A polymer-coated silica powder is processed by SLS, so that the polymer coatings of adjacent particles bind to form a continuous structure of complex geometry. After SLS, colloidal silica in water is infiltrated into the part. The green polymer-silica part is transferred to an oven at 400°C which degrades the polymer binder and sets the colloid. The temperature is raised, and the silica mould is fired at 1000-1500°C for 17 hours, causing 1 percent shrinkage relative to the green part.

Indirect SLS is time-consuming, due to the number of stages involved: polymer burn-out and infiltration takes tens of hours [Kruth 1998a]. Part shrinkage and warping [Wang 1999, Pham 1999] accumulate with each process, making dimensional change difficult to predict.

2.2.3 Direct SLS-Type Technologies

As well as the original SLS equipment offered by 3D Systems, other similar machines are in development. The shared principle of the machines is as discussed above: the bonding of adjacent particles in a powder bed using a scanning laser beam. One similar machine is the subject of work reported in subsequent chapters of this document. The 3D Systems process can directly produce polymer parts, extensively investigated by [Beaman 1997] and [Childs 2001]. It is of interest to develop techniques for directly producing metal parts, because furnace cycles add many hours to SLS processing time as stated earlier. The techniques described below were designed for direct SLS of metals.

[O'Neill 1998] and [Morgan 2001b] report the results of a process called direct metal laser remelting (DMLR). An Nd:YAG laser of beam diameter d equal to 0.1mm is used to directly process room temperature stainless steel powder. It is reported that pulsing of the YAG laser causes vaporisation of surface material. Vaporisation pressure above the powder bed has the beneficial effect of flattening the melted material down, to produce a low-porosity structure. Coupled with an optimum building strategy, a part at 99.65 percent of solid density is achievable. The effect of machine parameters in DMLR is commented on in section 2.2.6.

Hauser [Hauser 1999a and 1999b] also uses a laser to directly process room temperature stainless steel powder. The laser in Hauser's arrangement is of continuous wave CO_2 type, with *d* equal to 1.1mm. Good bonding between adjacent scans is reported in an inert argon atmosphere, but processed part density is low at 50-60 percent. This process is discussed further in sections 2.2.4 and 2.2.6. The same machine used by Hauser has been used by [Lorrison 2002] to investigate direct laser sintering of bio-active glass ceramics.

[Wilkening 1996], [Shellabear 2001] and [Khaing 2001] describe the DMLS process already mentioned in section 2.1.4.6. Use of a particular material blend means that parts produced show no net shrinkage or warping. A CO_2 laser directly processes room-temperature steel-based powder to high density. With around 15 hours' processing and a few hours of post-processing a tensile strength of 500MPa, accuracy of ±0.1mm and skin porosity of 2 percent is achievable.

Further reading on direct SFF of metallic parts can be found in [Dickens 2000], [Tolochko 2003a], [Meiners 1999], [Griffith 1998], [Kaplan 2001], [Benda 1994].

2.2.4 Leeds Experimental SLS Station

The SLS machine based at the University of Leeds and described by [Hauser 1999a and 1999b] is instrumental in much of the experimental work reported in later chapters. Its function is the direct SLS processing of a room temperature powder bed. The powder bed is contained within a 460×260×250mm sealed chamber (Figure 2.13), allowing ambient air to be exchanged for an inert atmosphere via evacuation, backfill and purging. A continuous wave CO_2 laser beam of 250W capacity is guided by galvanometer-controlled mirrors, allowing the beam spot to move over a 70mm diameter build area on the surface of the powder bed. The beam scans at speeds of up to 100mm/s in reported experiments. The beam diameter at the powder bed surface is 1.1mm. The scanning beam is transmitted through a window into the chamber.

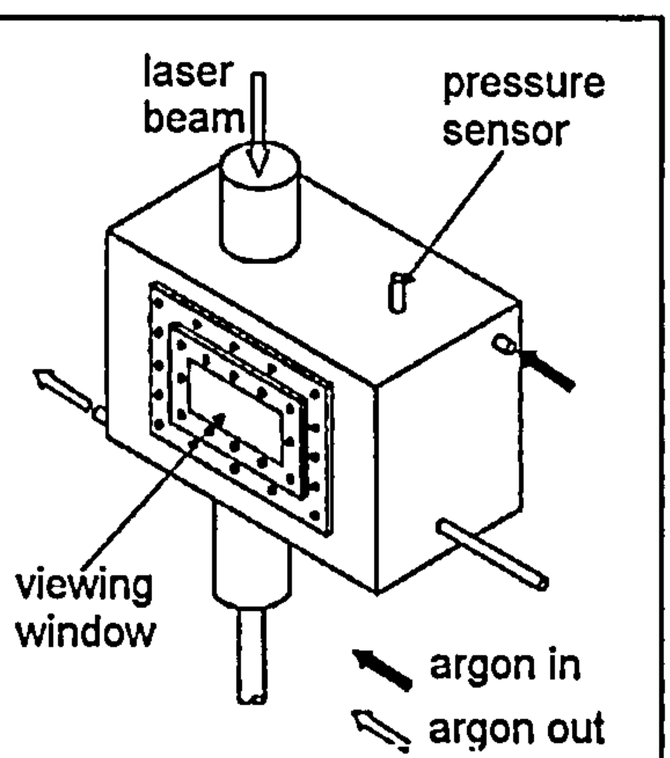

Figure 2.13
Processing chamber

In Hauser's work the powder used is gas-atomised stainless steel 314S, which has constituents as provided in Table 2.1.

Element	Fe	Ni	Cr	C	Si	P	Mn	S
Percent	Bal.	19.85	24.36	0.443	1.43	0.017	0.94	0.006

Table 2.1 Constituents of stainless steel powder used by [Hauser 1999a]

Four powder fractions are tested, from particle diameter d_p of 300μm down to less than 38μm.

In his work, Hauser tests the effect of atmosphere and process parameters on the qualities of output parts. Such studies on SLS-type processes are common in available literature: the observations of Hauser and others are disseminated in sections 2.2.6.3 and 2.2.6.4. Findings involving the Leeds machine are summarised below.

With regards to atmosphere, laser processing was carried out in ambient air, air/ argon and argon atmospheres. Oxygen in the air reacted with the molten steel to form surface oxides. Because argon is an inert gas, it did not react in such a way. It was reported that in an air atmosphere, the surface tension of the melt pool increased due to oxidation. The molten steel showed more tendency to form ball shapes, and bonding between adjacent melted tracks was poor. In an argon atmosphere, adjacent tracks bonded successfully over a much wider range of laser power and speed. The amount of material melted reduced relative to when processing in air, leading to the conclusion that oxidised samples had absorbed a higher proportion of laser energy. The final density of single layers processed in argon lay between 50 and 60 percent. In both air and argon atmospheres it was concluded that a reduction in powder particle size reduced the amount of energy required to melt the powder. More is said about this in the next section.

A variety of laser power, laser scanning speed and scan spacing combinations were tried to see their effect on the structural integrity of single layer and multiple layer parts. Some simple rules were established: a maximum scan length was found above which irregular shrinkage, warping and cracking began. It was

discovered that over the range of other parameters tested, a laser power to speed ratio above 1 J/mm was required to achieve bonding of adjacent scanned tracks.

The process requires that the laser heats the powder from room temperature to the melting temperature of stainless steel. The size of the resulting thermal gradients is thought to contribute to irregular shrinkage, warping and cracks in finished parts.

2.2.5 Powder Material Characteristics

This section introduces the properties of metals (and particularly steel) relating to the direct SLS process. Melting, balling and wetting of material during the process is discussed in the next section.

Selective laser sintering is a versatile process, suitable for processing polymers and polymer-bound ceramics or metals. All materials are supplied to the SLS machine in powder form. Material parameters stated to be important to SLS are [Agarwala 1995a]: viscosity μ, surface tension σ, particle size (d_p) distribution, particle shape, thermal conductivity k, specific heat C, melting temperature T_m, absorptance α and emissivity ε_r.

Material Name	Structure	Coefficient of Thermal Expansion (10^{-5} K^{-1})	Thermal Conductivity, k ($W.m^{-1}.K^{-1}$)	Specific Heat, C ($J.kg^{-1}.K^{-1}$)
Polyamide	Semi-cryst.	8.0	0.23	1800
Polycarb.	Amorphous	6.7		
Steel	Poly-cryst.	1.2	60.00	450
Silica	Poly-cryst.	-	0.02	1000

Table 2.2 Room temperature properties of SLS materials [Touloukian 1970].

Viscosity and surface tension become important when materials are in their softened or molten state. They affect material flow and densification, discussed in sections 2.2.6.2 and 2.4. Surface tension and viscosity have a more significant role

in direct SLS processing of metals than in direct SLS processing of polymers, accorded to [Agarwala 1995a].

Size distribution and shape of powder particles have an effect on the powder's bulk density ρ [Boivie 2003]. The density of a powder is less than that of the equivalent material in solid form, typically around 60 percent of solid density for steel [Niu 2000]. Transformation from powder to solid material state may be considered in terms of increasing density ρ, or in terms of reducing porosity φ in the powder bed. If bed density is considered as a fraction of solid density, equal to ρ_r, then the relationship between ρ_r and φ is such that:

$$\varphi = 1 - \rho_r \qquad (2.1)$$

The powder's density affects the relationship between heat input and changes of state [Childs 2000].

Specific heat, density and conductivity affect the magnitude and distribution of temperature in the powder bed over time. Some example k and C values for materials are provided in Table 2.2. The values tabulated suggest the need for special consideration of each material type. For instance, a unit of input energy would penetrate a steel sample more easily than a polymer sample (due to its higher thermal conductivity), and would raise the temperature of samples in proportion to the product of density and specific heat, or (ρ.C). C for steel is a quarter of C for polyamide, but ρ for steel is seven times that of polyamide. Therefore polyamide would reach a higher temperature.

To add complication, the thermal properties tabulated are only correct for solid material at room temperature. C and k change with temperature and k changes with density: these changes are detailed in sections 2.3.2 and 2.5.2.3. Around the material's melting point T_m, a change of state and latent heat become important.

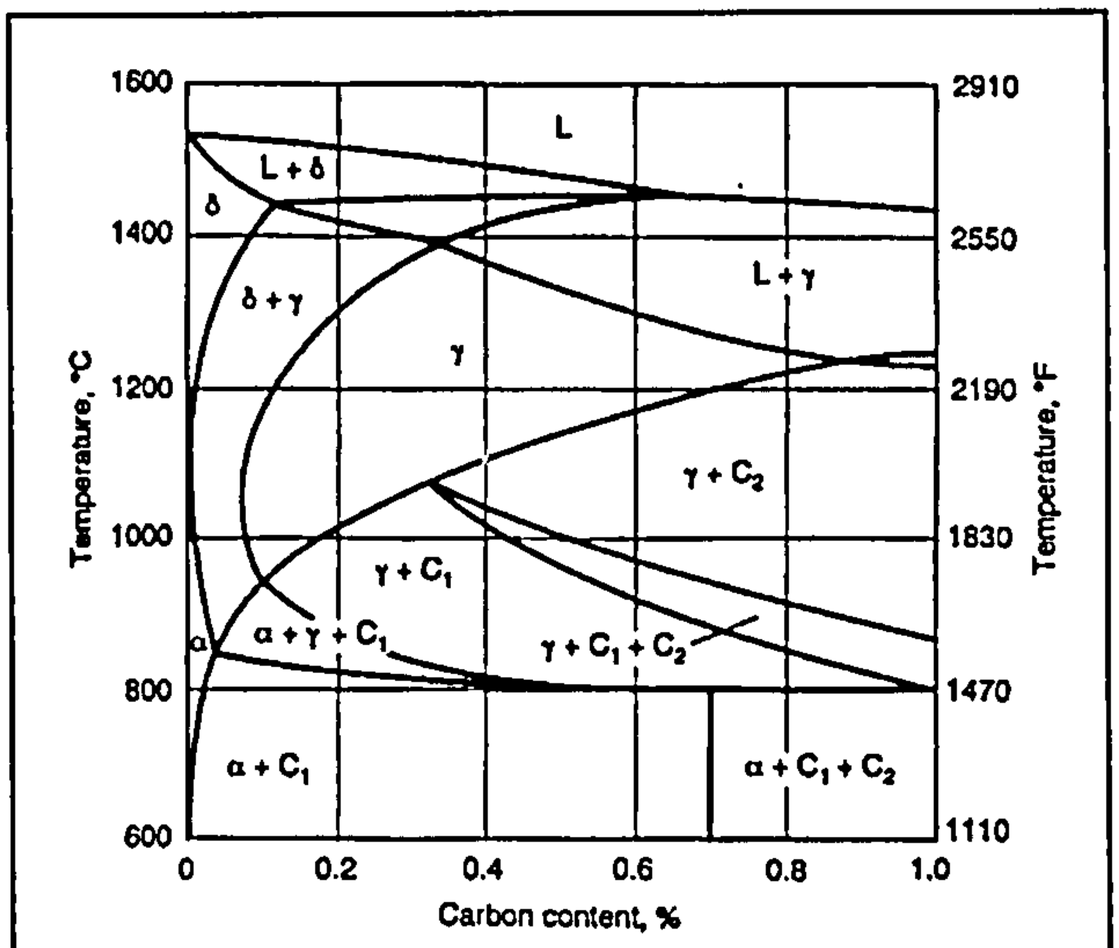

Figure 2.14 Equilibrium phase diagram, for stainless steel

In Figure 2.14, an equilibrium phase diagram for stainless steel is shown [Davis 1994]. The *x*-axis represents a changing percentage of carbon in the steel, the *y*-axis represents the steady-state temperature of the sample. Below 1200°C the steel is completely solid and at 1600°C it is entirely molten. The exact temperatures at which an alloy becomes completely solid or completely liquid are known as the solidus and liquidus respectively. Between these states there is a gradual phase change, accompanied by a heightened absorption (in heating) or evolution (in cooling) of heat. In the "L+δ" and "L+γ" regions near the top of the graph, liquid and solid phases co-exist. In these regions, wetting and bonding are very good in direct SLS as reported by [Hauser 1999a]. Processing resembles liquid phase sintering. However, the necessary temperature range would be hard to achieve consistently in direct SLS given the temporal and spatial temperature transience reported. 3D Systems SLS deals with high- T_m materials using post process furnace cycles, as discussed earlier.

Laser power absorption characteristics vary from material to material. They are affected by the surface condition of a material and also the laser wavelength used [Touloukian 1970]. Useful energy in SLS is that which is absorbed by the powder bed, raising its temperature. The remaining energy is lost to the bed's surroundings in various modes. Experiments have been carried out [Tolochko 2000] which find that the absorptance α (useful power/ laser input power) of

carbon dioxide laser radiation by silicon oxide powder (ceramic) is 0.96, by PTFE (polymer) is 0.73, and by iron (metal) is 0.45. The same study indicates that α does not depend on powder particle diameter d_p between 40 and 160μm, for an Nd:YAG laser sintering nickel alloy. This is logical, as particles in this interval are large relative to the laser beam wavelength yet small relative to the laser beam diameter. It is said that α tends to zero once d_p falls below the laser beam's wavelength [Karapatis 1998a]. As the powder material is processed by the laser its geometry and temperature change, both of which have an effect on absorptance [Tolochko 2000]. More is said about laser radiation in SLS in section 2.3.1.

Powder particle size can be important in other respects, such as material spreading and sintering rate. A typical layer thickness in SLS is 0.12mm [Nelson 1995], so in order to spread powder effectively a d_p value less than 0.12mm would be necessary. If a CO_2 laser at 10.6μm wavelength is used, d_p should be larger than 10.6μm to maximise absorptance. As was mentioned in the previous section, [Hauser 1999a] reported that steel powders required less power to form a melted structure as d_p reduced from the order of 200μm to 20μm. Smaller particles have a higher surface area (therefore surface energy) to volume ratio, and shorter inter-particle material diffusion path [Kaysser 1991]. These two facts may explain Hauser's findings. [O'Neill 1998] comments that reducing the mean powder particle diameter increases absorptance, although no size range is specified.

The shape of powder particles has an effect on their packing and processing characteristics. Spherical (low roughness) particles have a high packing density. They spread with low frictional shear stress and will bond well to adjacent particles when processed [Van der Schueren 1995a]. The roughness of particles is determined by a number of factors, including the way in which they are prepared. Gas atomised metal powders are less rough than water atomised metal powders for instance [Jenkins 1991, Niu 2000]. If spherical particles of constant size are assumed, then geometry dictates a packed density between $\pi/6$ and $\sqrt{3}\pi/8$, or 52 and 68 percent. See image (ii.) in Figure 2.12 for a 2D representation of minimum and maximum density arrangements.

The material stainless steel 314S HC was selected for the direct SLS research undertaken by Hauser. Constituents are as Table 2.1. This material is an austenitic stainless steel, having higher chromium, nickel and silicon content than typical 18-8 type stainless steel. Stainless steel's strength and corrosion resistance compare favourably with other metals. The extra percentage constituents give 314S HC a higher melting temperature than 18-8, meaning higher heat resistance [Davis 1994]. The crystal structure contains a relatively high proportion of carbides, providing creep resistance at high temperature. 314S HC is well suited to high-temperature superplastic forming of materials such as titanium alloy.

2.2.6 Process Characteristics and the Effect of Parameter Values

The type of SLS machine used, machine parameters and material properties all influence the qualities of finished parts. Many researchers have investigated the link between the above, and there is common ground between much of what is reported. Presented here is an introduction to process parameters (2.2.6.1), then a discussion of material melting (2.2.6.2). Unsteady effects inherent in the process (2.2.6.3) and the resulting part properties (2.2.6.4) are considered.

2.2.6.1 Introduction to Process Parameters

Parameters in SLS relating to materials have been discussed in section 2.2.5. Now the parameters of the machine processing the materials are considered. Machine parameters of importance in SLS accorded to [Agarwala 1995a] are: atmospheric control and air flow, bed heaters, laser type, power P, beam diameter d, scan vector length L, scanning system and powder spreading system. To add to this list are beam profile [Deng 1992], laser scanning parameters speed U and spacing s, and layer thickness Z_l [Gibson 1997]. See Figure 2.15 for an illustration of d, L, s and Z_l.

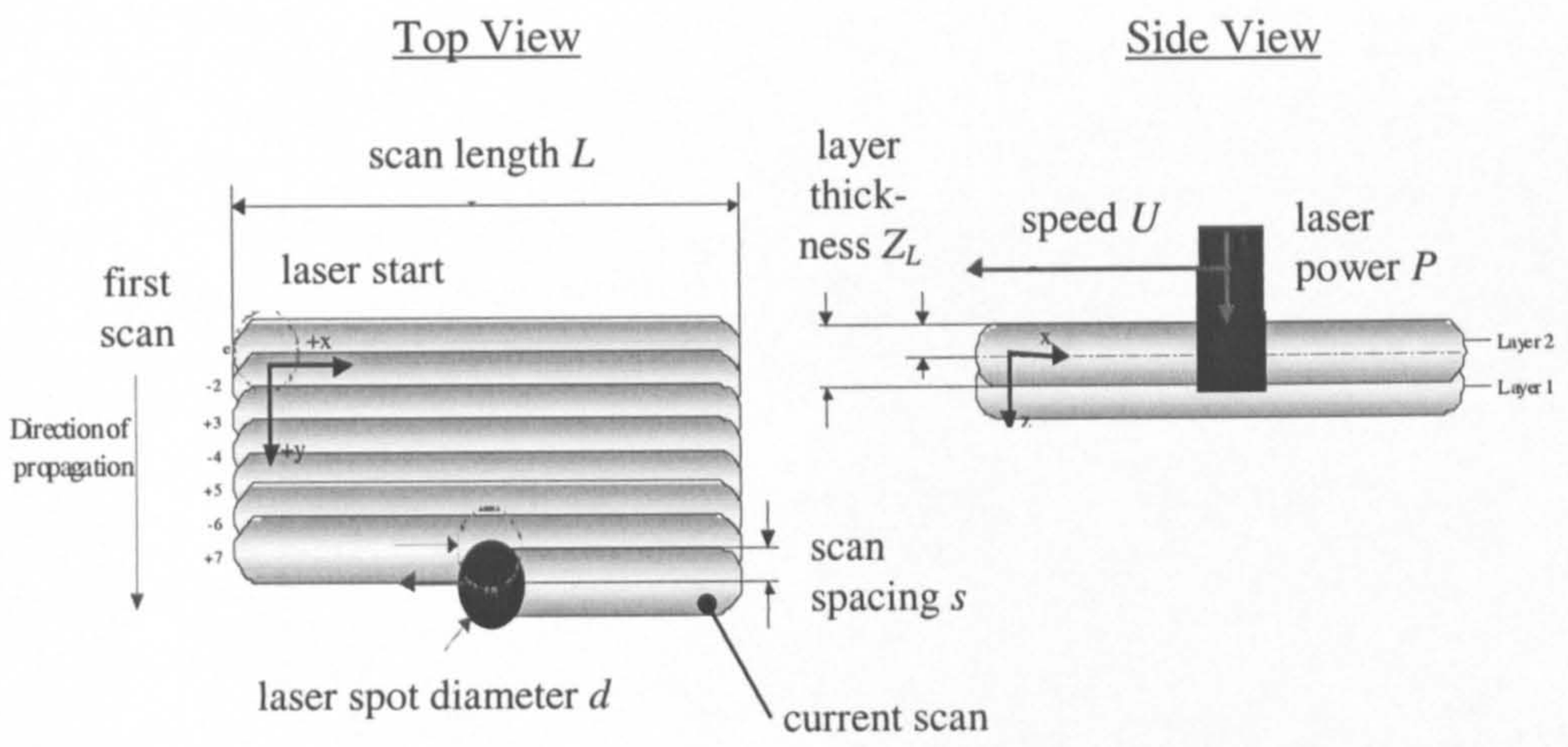

Figure 2.15 Layer scanning (adapted from [Hauser 1999b])

Use of an airtight sintering chamber allows the processing atmosphere to be modified by a through-flow of gas. Nitrogen [Deckard 1995] or argon [Yevko 1998] gases are popular due to their inert nature. Using inert gas as opposed to air means that oxidation and burning will not occur as the laser scans the material powder. It is vital to prevent surface oxides from forming on the melting material as this increases surface tension to hinder material flowing [Hauser 1999a]. The result of sintering in an air atmosphere is the formation of ball-like shapes, and poor bonding between sintered lines, leading to mechanically-weak parts [Karapatis 1998a]. Authors have reported that oxygen content in the order of hundreds of parts per million (in material powder and the sintering atmosphere) had a detrimental effect on manufactured structures [Niu 2000, Zong 1992].

If a protective gas is to be used, one must be selected which is appropriate to the material being processed; for instance it has been found that stainless steel absorbs nitrogen gas if present during sintering to form nitrides, which reduce the material's corrosion resistance [Tiziani 1989]. Therefore argon is often used when processing stainless steel. Polymer materials are not susceptible to this problem, so nitrogen is used in 3D Systems SLS machines because it is cheaper than argon.

It has been shown [Hauser 1999a] in experiments contrasting air- and argon-atmosphere sintering that when using argon, successful bonding may be achieved at lower powers and over a much wider range of power and scan speed.

Bed preheating is used in 3D Systems SLS machines where polymer or polymer-coated materials are being processed. Radiant heaters increase the powder bed temperature to a point just below the polymer material glass transition temperature. This means that a small power input from the laser will bring about sintering and bonding, with minimal residual stress and irregular shrinkage [Agarwala 1995a]. The bed temperature must be uniform: a variation of only a few degrees Celsius can affect part accuracy [Tontowi 2001].

To recreate the preheating method in direct sintering of metals or ceramics is difficult: for instance, all chamber components would have to be high-temperature rated [McWilliams 1992]. Also there is an issue of low-rate sintering taking place throughout the powder bed, which in metals begins at half the melting temperature [German 1996]. [Das 1998] and [Zong 1992] have directly processed metal powder mixtures to upwards of 80 percent relative density from preheated beds. Localised preheating methods [Geiger 1996, Benda 1994] are also possible, but most often no preheating is used in direct metal SLS.

Solid substrates are sometimes used in direct metal SLS, to anchor the processed structure in its early stages of building. Building onto a powder base provides little mechanical restraint [Agarwala 1995a], so initial scanned tracks may suffer from distortion and balling. [Morgan 2001b] and [Carter 1993] built metal parts onto substrates with resulting geometrical improvements.

Other SLS hardware issues include powder spreading system, laser type and laser scanning system. Some examples of SFF spreading systems have been shown in section 2.1.4 : the system used determines how flat each layer is, and may include compaction to increase the powder density. The laser type used in all reviewed cases of direct metal SLS was either CO_2 or Nd:YAG, the basic properties of which have been mentioned in 2.1.3.2. The CO_2 lasers reported provided up to 1.5kW of constant power at 10.6μm wavelength. Nd:YAG lasers reported provided up to 90W of constant power or as much as 100kW peak pulsed power, at up to 60kHz pulsing frequency. They operate at 1.06μm wavelength. Choice of laser affects the absorptance of laser power into the powder, and also therefore the attenuation of laser radiation with depth into the powder bed [Kruth 1998b].

The laser beam and powder bed are moved relative to each other either by NC motion or more popularly by two rotating mirrors (see Section 2.2.1). Mounted on galvanometers [Tumer 1995], the mirrors can achieve high angular acceleration. Momentary periods are required after each scan where the laser is switched off, allowing the mirrors to reach the required position and velocity for the next scan.

It is usual for a constant value of laser power P to be used in a particular build. P is measured at the powder bed surface position, and is expected to be less than the output of the laser unit because power is lost in the optical system [Luxon 1985]. P has a large effect on the density and depth of processed tracks [Deng 1992, Kruth 1996]. Nd:YAG lasers may operate in pulsed mode, where power is provided intermittently. Pulsing leads to greater peak power, and greater temperature gradients against position and time [Yevko 1998]. [Morgan 2001a] reports that pulsing an Nd:YAG laser increases the density of the generated metal structure in the DMLR process, mentioned in Section 2.2.3.

The laser beam diameter d is measured at the powder bed surface, like P. It is also known as the spot diameter. Reducing the value of d leads to greater beam intensity and narrower processed tracks [Eyerer 1994, Kandis 1999]. Values of d reported in direct metal SLS vary from below 45μm [Yevko 1998] to 1.1mm [Hauser 1999a]. In most cases reviewed the beam profile (distribution of intensity) was Gaussian, the meaning of which is explained in 2.3.1.

Scan speed U is the rate at which the laser spot moves over the powder bed surface during processing. SLS processing time is dependent on U. In the 3D Systems SLS process U reaches thousands of millimetres per second [3D Systems 2000], but in direct metal processes U in the order of 15mm/s is typical [Kahlen 2001, Hauser 1999b].

Scan length L and speed U allow the amount of time taken for a particular scan, t_s, to be calculated. Ignoring the short dwell period, t_s is equal to the time elapsed between successive scans, which affects the uniformity of cooling and can cause dimensional accuracy problems if its value is too high [Gibson 1997]. Uniformity of cooling and the effect on part properties are investigated in Sections 2.2.6.3 and 2.2.6.4. Typical values of L are in the order of millimetres [Morgan 2001b].

Scan spacing s is the distance perpendicular to the scanning direction by which the laser beam is displaced between adjacent scans, illustrated in Figure 2.15. Often s is chosen to be less than the beam diameter d so that scanned areas overlap. This means that the previously scanned material is reheated which helps in bonding it to the newly scanned material [Gibson 1997]. The number of times an area is exposed to laser radiation in scanning, N, can be calculated from the values d and s [Williams 1998]:

$$N = \left(\frac{d}{s}\right) - 1 \qquad (2.2)$$

If an area of a material is rescanned too many times, it can become warped and brittle. [Hauser 1999b] found direct SLS of room temperature steel powder worked best with $s < 0.3\ d$, or $N < 2.3$, for this reason.

Layer thickness Z_l is the depth of each newly-spread powder layer. Z_l affects the build time in SLS, and through the stepped effect described in Section 2.1.3.1 affects part accuracy. The chosen value of Z_l relates to powder particle size, as has been mentioned earlier. The laser must be able to penetrate a powder layer to melt it and bond it to the previous layer [Agarwala 1995a, Childs 2001]. Values of Z_l reported ranged from tens to hundreds of microns [Carter 1993, Morgan 2001b].

In sections 2.1.3.1 and 2.2.1, basic laser scanning strategies for SLS are discussed. In most cases, the strategy is to scan each material layer as a series of adjacent parallel lines with an amount of overlap, known as raster scanning. Parameters involved in the raster scanning method are shown in Figure 2.15. The laser supplies power P to the powder bed over a beam diameter d, scanning with speed U over a distance L and being indexed a distance s between scans (scan spacing). Ignoring the small dwell time between successive scans, the energy input into the bed is either directly or inversely proportional to the quantities P, U and s. The amount of input energy dictates the temperature rise in the powder bed, and so affects the volume and mechanical properties of the sintered material. A quantity known as energy density or the Andrew number A_N has been suggested to relate scanning parameters to aspects of sintered part quality [Nelson 1993]:

$$A_N = \frac{P}{U.s} \qquad (2.3)$$

It has been shown that SLS process success or failure can be related back to scanning parameters through A_N: too low a density of energy will not raise the powder to sintering temperature, and too high a density will cause material vaporisation [Kizaki 1992a, Yevko 1998]. Ideally then, one might manufacture parts at maximum levels of P and U (to minimise build time), whilst keeping A_N constant. However, [Williams 1998] states that the Andrew number can only be related to part properties within a range of the parameters P, U and s, with relationships breaking down at extreme values. For example, time-related energy loss from the part to the surroundings increases with part temperature in a non-linear fashion.

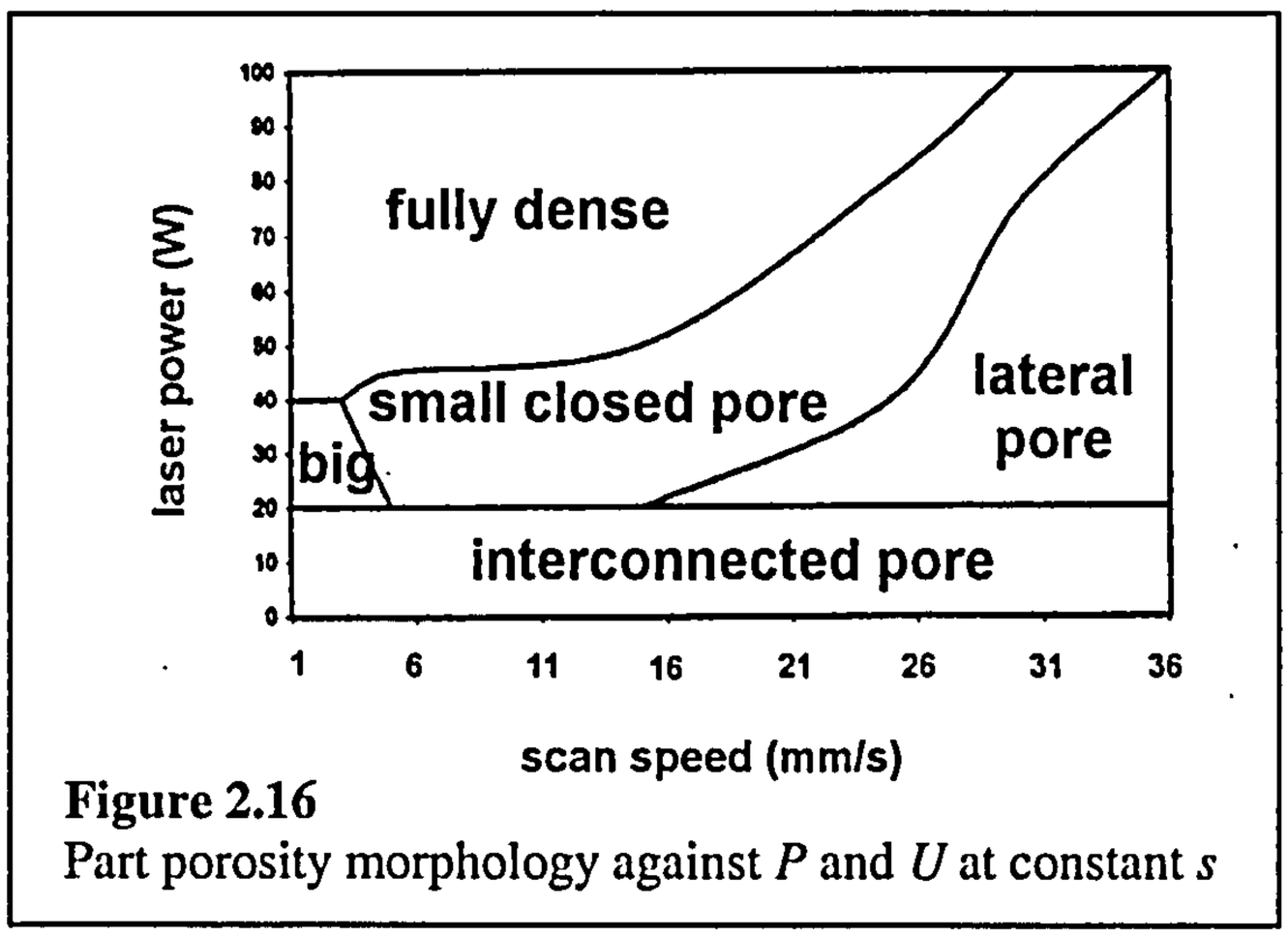

Figure 2.16
Part porosity morphology against P and U at constant s

Process mapping takes the practice of linking machine parameters to part quality one step further. [Hauser 1999a], [Nui 2000] and [Morgan 2001b] have constructed graphs of part morphology against combinations of P, U and s. An example of Niu's maps is provided, Figure 2.16. Examination of process maps reveals that a particular phenomenon such as poor bonding does not occur within an exclusive range of Andrew number values.

A statistical approach to parameter control was taken by [Prakash 2003], who conducted a Taguchi study on laser-aided processing of metals. See Section 2.6 for details.

Finally, the effect of scanning strategies is mentioned. For reasons already discussed, there are advantages to keeping scan lengths small, and yet large parts must be built. Methods of maximising part accuracy and density are required.

[Morgan 2001a] proposes processing each layer twice, and scanning each layer normal to the preceding one, to increase density. [Hauser 1999b] scanned triangular layers, which warp and crack less than rectangular ones.

2.2.6.2 Material Phase Change and Shape Change

Section 2.2.5 explains that metals, plastics and ceramics are significantly different in terms of their thermal and mechanical properties. It follows that different materials would behave in different ways when exposed to the laser beam in SLS. In the direct SLS of room-temperature single-phase metal powders, process issues are reported which are new or different compared to 3D Systems SLS. These issues mainly relate to the higher temperature rise required and the properties of pure metal powders.

In the 3D Systems process described in 2.2.1, material is preheated to a point just below its softening temperature then heated further by the laser beam. This lifts the material temperature just above the softening point for around 15 seconds [Childs 2001], allowing adjacent particles to bond. In contrast, shape change is reported to be complete in under 500ms in direct room-temperature metal SLS [Griffith 1998, Kizaki 1992a]. Laser beam exposure lasts less than 100ms [Wang 2002, Agarwala 1995a] and is followed by rapid cooling. The powder material must densify significantly in a short time, by an amount not possible at solid state sintering temperatures. The material must be able to flow, so melting must occur [Morgan 2001b]. See Section 2.4 for more on densification processes.

This indicates that a complex process occurs in under one second's duration. Temperature rises and falls due to laser application, during which time the metal material melts, changes shape and solidifies. Several phenomena are at work during this short time, which determine the size and shape of the processed geometry, also known as the heat-affected zone (HAZ). Parallels with laser cladding and laser welding phenomena exist.

When an area of powder is processed, adjacent particles merge with one another and porosity φ is reduced. In 3D Systems SLS a linear shrinkage of a few percent is typical [Childs 2001], causing modest densification. In direct metal SLS, the bed density increases by much larger amounts [Morgan 2001b]. φ

reduces, so any material properties which relate to φ will change continuously. The same is true of temperature. Thermal properties k and α decrease and increase with increasing φ respectively; k, C and α all increase with temperature [Yagi 1953, Tolochko 2000]. Mechanical properties μ and σ reduce with increasing temperature [Dowden 1983]. Reasons for these changes and related equations are provided in later sections.

Laser energy spreads into the powder bed as electromagnetic radiation and conducted heat. The amount of energy input has an important role to play in the material phase and shape change process. If the Andrew number A_N is too low, viscosity μ and surface tension σ are not low enough to allow adjacent particles to merge [Hauser 1999a]. However, too high a value of A_N leads to material evaporation [Tolochko 2000]. In metals processing, evaporation has two effects. One is the recoil pressure associated with vaporisation [O'Neill 1998, Dowden 1983]. This pressure from above has been observed to create a depression in the melted material [Cline 1977, Equilasers 2001]. The second is a vapour plasma cloud which blocks or scatters the laser beam to reduce energy absorbed into the melt [Dowden 1983, Steen 1998]. To avoid vaporisation effects at high A_N, a shield gas may be used to blow the vapour away from the processing area [Kahlen 2001, Steen 1998].

Once the metal powder melts, a number of things happen. Low viscosity allows particles to join together, forming a molten pool. Surface tension dominates gravity to drive the pool into a ball shape [Kaplan 2001]. If the pool is sitting on unprocessed powder, there will be little resistance to this reshaping. Surface tension gradients cause stirring inside the pool, known as Marangoni flow [Steen 1998, Anthony 1977]. Material convects from the hottest (low σ) to the coldest (high σ) regions. The pool rapidly solidifies to form a processed track. The volume of the track is less than that of the constituent powder due to densification. The track is reheated by the next pass of the laser, which reduces σ again so that the previous and current tracks can bond. At the boundary between melted material and the powder bed, partially-melted agglomerates are bonded to the tracks [Tolochko 2003b]. Surface oxides increase σ to reduce the quality of bonding, hence the need for an inert atmosphere [Hauser 1999a].

2.2.6.3 Manufacture of Multi-Layer Parts and Transient-State Effects

The line by line, layer by layer laser scanning procedure used in SLS means that adjacent areas in a part are heated and cooled asynchronously. Combined with material properties which change as the part is processed (detailed in the last section), this leads to the formation of characteristic features in direct metal SLS parts. Such features are illustrated in Figure 2.17 [Childs 1999] and described below.

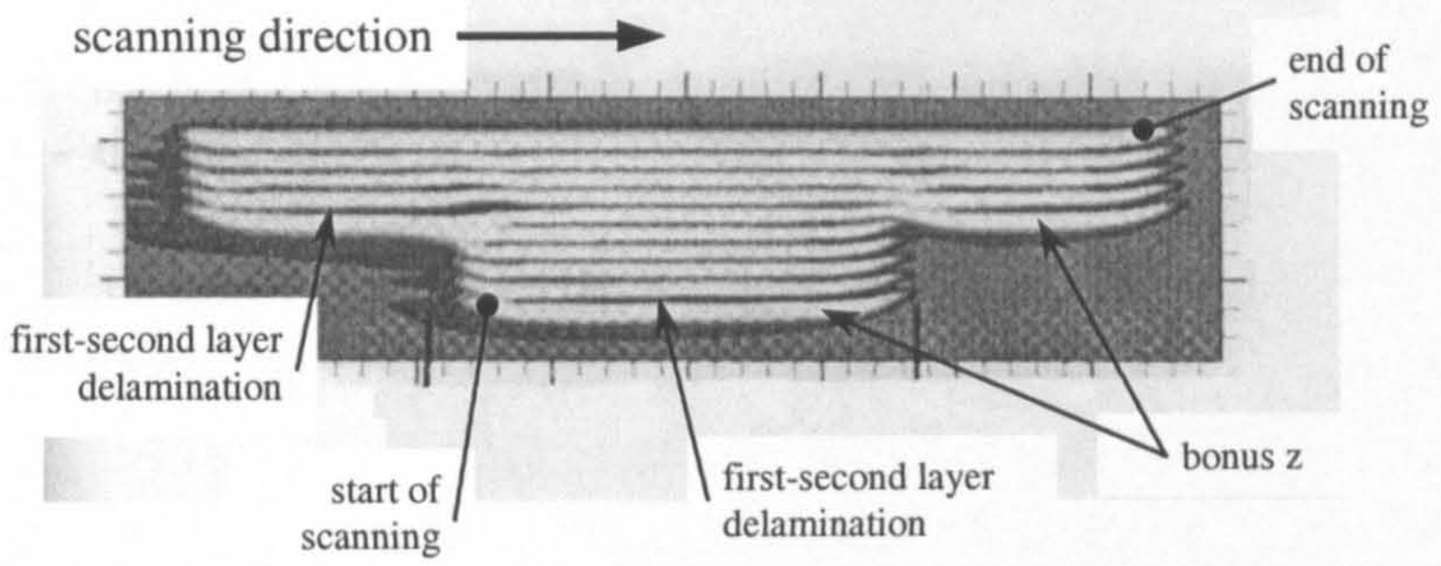

Figure 2.17
Sectional side view of part generated by model of SLS process

Each scanned track has a distinctive shape. Moving horizontally (Figure 2.17), the depth and width of a track increase from the edges to a steady state value. The edges form a "prow" shape rather than being square. One reason for this is that the first and last *d* of each scan receive less laser energy. The depth increase at the start of tracks (left hand side) is more rapid than the depth decrease at the end of tracks (right hand side), because the fresh powder has a higher α and lower k than processed material [Benda 1994].

The top surface of the track is more exposed to the laser beam and not insulated by the powder bed, so its heating and cooling cycle occurs faster than that at the bottom surface [Kathuria 1997]. This leads to a microstructure which changes with depth [Hauser 1999a], and in extreme cases causes scans to curl upwards [Carter 1993]. Microstructure is not featured in Figure 2.17.

When the second track in a layer is scanned next to the first, the amount of new material melted is less than the volume of the first track, observes [Song 1997]. See Figure 2.18. This relates to the higher α and lower k of unprocessed powder: if the first line is partially rescanned its lower absorptance will mean less energy is

delivered to the area. Some of the delivered energy will be lost into the first scan, which acts as a heat sink with its high *k* [Morgan 2001b]. [Benda 1994] reports that processing tungsten with a CO_2 laser, a second overlapping scan requires 20 percent more laser power to achieve the same material temperature as the first scan due to this effect. A third scan requires a further increase in *P* of less than 10 percent as the local *k* increases again.

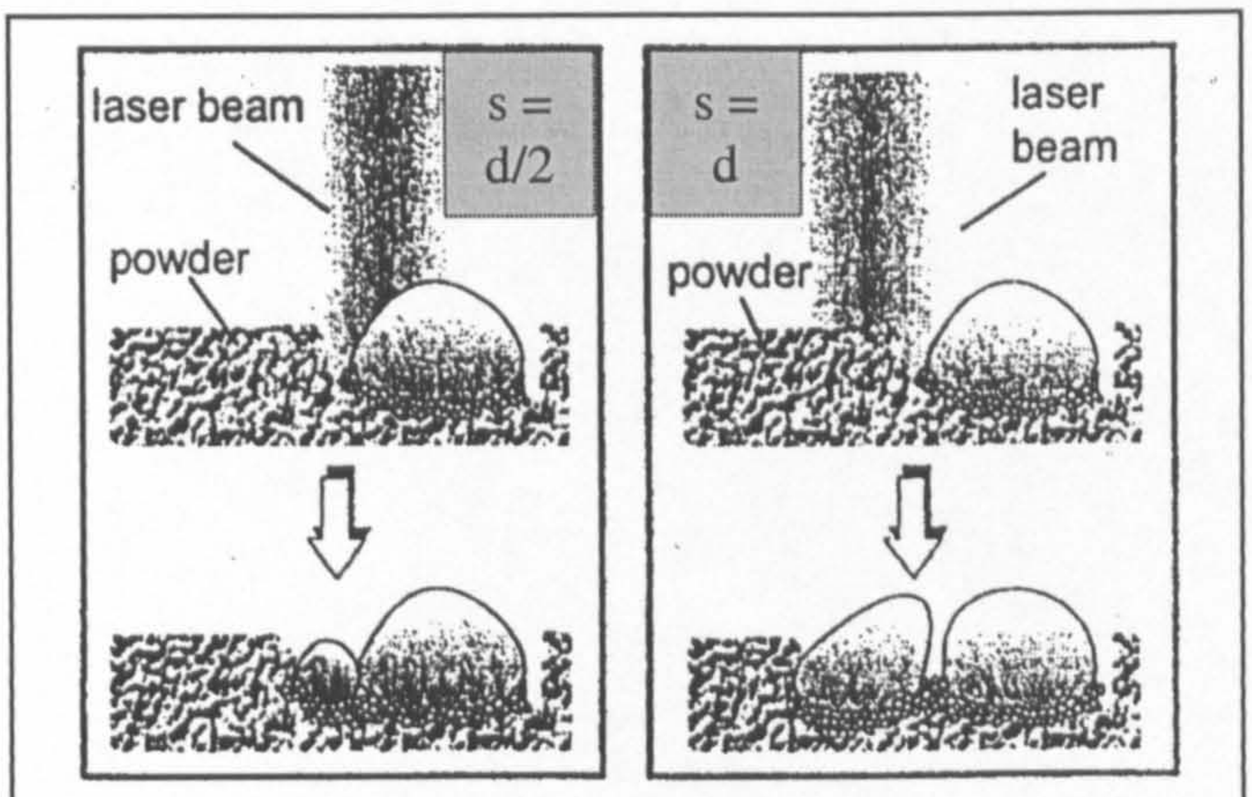

Figure 2.18 Evolution of first and second tracks

The phenomenon of previously-processed areas acting as a heat sink applies to whole layers as well as scans. If the first layer of a part is built onto unprocessed powder then a second layer is built on top, the conduction of heat from the second layer into the first is sufficient to cause it to be smaller [Pham 1999]. The first layer is larger than the others, a quality known as "bonus *Z*" [Dalgarno 1997]. [Papadatos 1997] reports that this is the biggest cause of inaccuracy in polycarbonate parts. Because the amount of densified material is greatest in the bottom layer, it is also the layer which shrinks the most. Therefore the gap between the first and second layers is large, and the bond between them is weak [Childs 1999]. In general, the bonding between layers is weaker than the bonding between adjacent scans [Agarwala 1995b, Gibson 1997].

The nature of raster scanning means that a time elapses between successive scans. The previous scanned track enters its cooling phase as the adjacent current track is being heated. The heat and cool cycle corresponds to thermal expansion and contraction of the track, so the previous track contracts as the current track is expanding. Each track bonds to the previous one at the end of the molten phase, so asynchronous cooling causes residual stress in tracks as they attempt to contract but are restrained by their colder neighbours [Matsumoto 2001]. This

differential shrinking mechanism can cause bending, warping and cracking of layers (see Figure 2.19). If the scan length L is limited, the asynchronicity reduces and layers become more dimensionally uniform [Gibson 1997, Hauser 1999b].

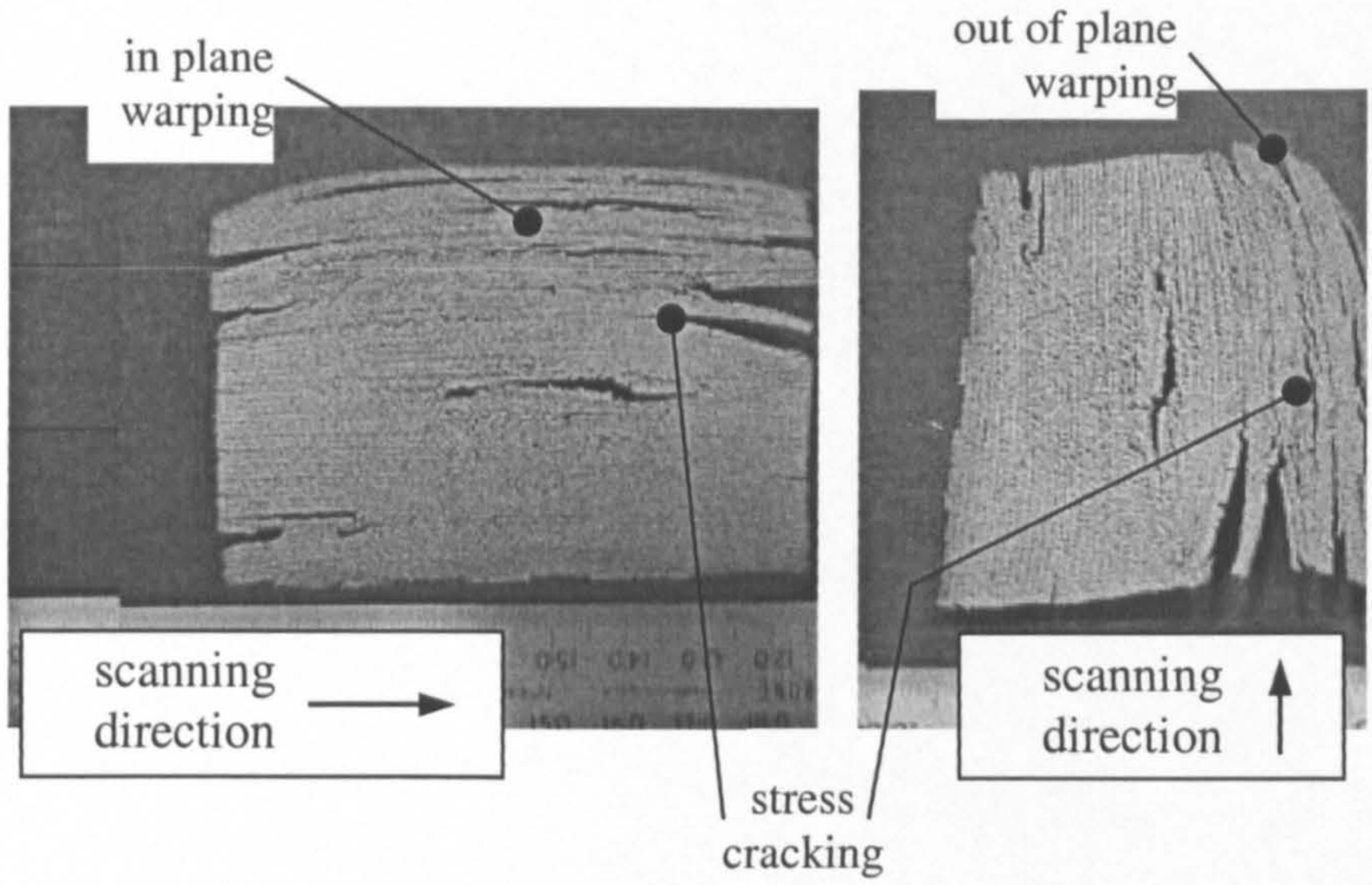

Figure 2.19 Layer scanning: distortion and cracks [Hauser 1999b]

The scanning pattern of the laser affects the cooling rate of processed regions. For instance, the centre of a part experiences slower cooling than its edges. Authors have reported that this causes higher hardness and lower ductility at the edges of parts [Dickens 1992, Gibson 1997, Karapatis 1998b and Griffith 1998]. In some cases, irregular temperature profiles cause bulk distortion of parts [Beaman 1997].

Some systems designed to counter transient-state effects are featured in 2.6.2.

[Hauser 2001] studied the cross-sectional morphology of individual stainless steel scanned tracks. Figure 2.20 demonstrates the marked difference in morphology which was found. Half-moon shaped cross sections were seen at very low U values, changing to a ball shaped section as U increased. The upper surface is either concave or convex.

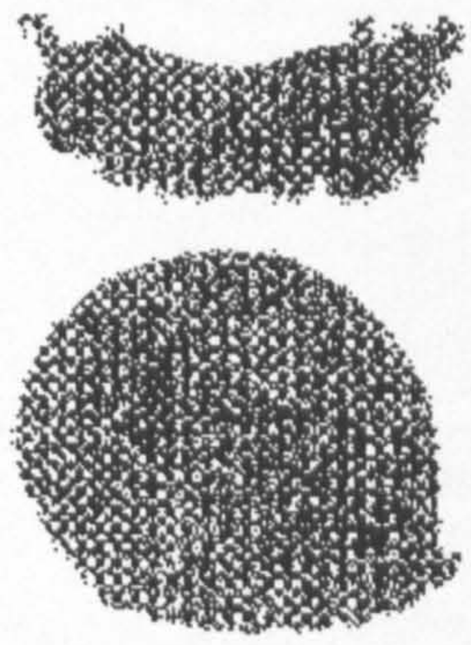

Figure 2.20 Scan cross-sections

Equation (2.3) earlier described how energy input per unit area can be assessed in layer scanning. In the case of scanning single tracks, the equivalent quantity is energy per unit length E_L, which is simple to evaluate:

$$E_L = P/U \qquad (2.4)$$

The scan shape change seen in Figure 2.20 is accompanied by a reverse in the change of the volume of material melted. In most cases, a reduction of E_L corresponds to a reduction in the melted volume of scans. However, the balled bottom scan in Figure 2.20 has a greater cross-sectional area than the top specimen, despite receiving only half as much energy (see the P and U values quoted). Testing over a range of P and U, the shape transition occurs at lower E_L as U increases. The underside of tracks is relatively rough, due to agglomerates (mentioned 2.2.6.2). Track width is anything up to 2.0mm, which is 1.8 times d and 1 to 3 times the track height. A typical track width is 1.5 times d.

2.2.6.4 Properties of Manufactured Parts

Direct metal SLS-processed parts must have good mechanical and geometrical properties, in order to compete effectively with material removal processes such as machining [Kalpakjian 2001]. For an example of the mechanical properties expected from a forming tool, consider P20 tool steel. The designation P20 signifies a σ_y of 830 MPa and a hardness 31 Rockwell C [Toolcraft 2000]. [Radstock 1999] contends that an accuracy of ±50μm and an $Ra \leq 1$μm are required for forming tools. In this section porosity φ, part relative density ρ_r, yield strength σ_y, Young's modulus E, surface roughness Ra, dimensional accuracy, hardness and microstructure are discussed in relation to processing conditions. The use of post-processes to enhance part properties has already been reviewed in Section 2.2.2 and will not be discussed further.

The first property considered is φ. Porosity in parts has a negative effect on mechanical properties. σ_y is reduced by stress concentrations: brittleness increases and fatigue life reduces because there are more possible crack initiation sites [Agarwala 1995a]. Surface hardness and therefore wear resistance is lower [Karapatis 1998b]. Porosity should ideally be eliminated in rapid tooling, that is to

say ρ_r brought close to 100 percent. Several processes now achieve $\rho_r > 99.5$ percent [Morgan 2001b, Knights 2001].

A relationship has been reported to link σ_y and ρ_r for tested parts [Badrinarayan 1994]:

$$\sigma_y = a(\rho_r)^n \qquad (2.5)$$

Where a and n are empirical constants. As ρ_r increases, so does σ_y. a and n are affected by factors such as oxide formation and residual stress [Karapatis 1998b, Kahlen 2001], which reduce σ_y for a given ρ_r.

In general, a high ρ_r is achieved by increasing the Andrew number A_N. However, too high a value of A_N can cause part distortion [Ryder 1996] and material evaporation. [Miller 1997] undertook a parametric study before modifying Badrinarayan's relationship:

$$\sigma_y = a_1.A_N - a_2.U.s \qquad (2.6)$$

The A_N term represents an approximate linear relationship between part strength and input laser energy. The extra terms in U and s are said to take into account time-based heat loss from the structure and the fact that A_N has a practical upper limit. Constants a_1 and a_2 would be expected to change as the scan length L changes: shorter time between scans means better bonds, as revealed in the last section and discussed by [Williams 1998].

Average porosity is anisotropic in SLS-processed parts, being lowest in the scanning direction, higher in the scan spacing direction and highest in the layering direction [Boivie 2003]. The relationship in equation (2.5) means that strength also changes with orientation, reducing as porosity increases [Agarwala 1995b, Gibson 1997].

[Kathuria 1997], [Hauser 1999a] and [Griffith 1998] examined the effect of direct laser processing on the microstructure of metal parts. Kathuria and Hauser report that microstructure changes between the top and bottom of a single scan. Kathuria describes a fine, hard structure near the top surface where cooling is fastest, and a coarse, softer structure near the underside where the material cools slower. On a larger scale, Griffith reports on the properties of a multi-layer H13 tool steel wall. The top of the wall is least insulated and so cools quickest, leading to a martensitic structure of hardness 59 Rockwell C. The body of the wall is

reheated with each laser pass, and so is softer at 50 Rockwell C. However, the temperature cycling of the body of the wall leads to ageing through carbide precipitation and so is not considered a positive effect.

Residual stresses in direct metal parts have been examined by [Griffith 1998] and [Vasinonta 2000]. Griffith found stress values of up to 25 percent of σ_y in steel parts. Vasinonta discovered that preheat could reduce residual stress by 40 percent, by reducing the σ_y of the material. The conclusion of these authors is as the last section, that rapid and asynchronous cooling cause the stress build-up. The structure being built can be caused to bend or warp: where stress exceeds the material strength, cracks are formed [Karapatis 1998a].

Dimensional requirements for forming tools include low roughness and high accuracy. A "counter tendency" can occur between part mechanical and dimensional requirements: [Song 1997] and [Ryder 1996] report that as A_N increases, σ_y of parts increases but they start to curl. [Niu 2000] and [Klocke 1996] comment that high ρ_r corresponds to high *Ra*. Compromises must be found, or post processes considered.

Part design [McCrum 1988] and powder bed preheat [Pham 1998, Benda 1994] can reduce dimensional distortion up to a point. Uniform shrinkage in a process can be compensated for by pre-processing CAD software [Wang 1999]. The transient state effects of the last section are hard to predict, and have a significant impact on part accuracy. They can be countered by build strategy, or simulation-driven machine control [Karapatis 1998b] which is explained in Section 2.6.2.

2.2.7 Summary of SLS Process Investigation

There are several types of SLS process under development. In all cases, a scanning laser converts powder material into a 3D structure. The material may be a polymer, ceramic or metal. Parts can be post-processed to enhance their properties: however, efforts are being made to generate metal parts directly in order to save time.

An example of a direct metal SLS machine can be found at Leeds University. A 1.1mm diameter CO_2 laser has been used to process stainless steel powder from

an ambient initial temperature. The effect of atmospheric gas and other machine parameters on part quality has been tested. The effect of material properties, and thermal properties in particular, on the SLS process has been considered. 12 machine parameters have been identified which can also affect the process. Criteria for selection of parameter values are presented. It is discovered that parameter changes may be beneficial in one way, but negative in another way. For instance, increased energy density leads to stronger but more curled parts.

It is found that material shape change takes place in under 1 second in direct metal SLS, and that material melting must occur. The porosity of the powder bed reduces with laser application. Material evaporation can occur, depressing the melted material or reducing laser energy absorption. Direct metal SLS parts have characteristic features, such as a reduction in scan depth from the first to the second and following scans in a layer. Hauser discovered that scan cross-sectional shape can change with laser power and speed, being either a circular or half-moon shape.

Various methods for predicting the relationship between SLS inputs and outputs are presented later in sections 2.3.4 and 2.5. Better control of machine parameters is discussed in 2.6.

2.3 Heat Transfer in SLS

As has been explained in Section 2.2, the heating effect of the scanning laser beam in SLS converts fresh powder into a coherent 3D structure. The laser leaves a heat-affected zone (HAZ) behind it: a common term for the volume in the powder bed within which the material has experienced a change of form. The size and shape of the HAZ depends on the interaction of heat transfer modes, and on the mechanical behaviour of molten materials.

When the laser beam interacts with the surface of the powder bed, its energy is divided into several forms: see Figure 2.21 [Williams 1998]. Firstly, a percentage of laser

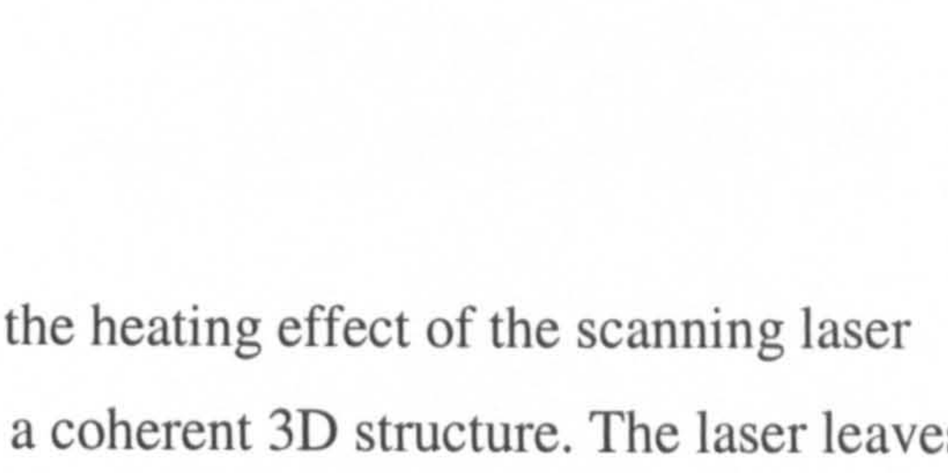

Figure 2.21 SLS heat transfer modes

energy is absorbed into the powder, the remainder is reflected away. This occurs almost instantaneously. The remaining heat contributes to material melting, or is dissipated in one of two ways: conduction into the wider powder bed, or loss from the bed's surface to the surroundings over time. All of these heat transfer modes are discussed below. The relative importance of each mode depends on the type of SLS process.

Methods of measuring powder bed thermal properties are reported, with advantages and disadvantages. Analytical models for predicting temperature change with position and time are also discussed.

2.3.1 Laser Radiation Interaction with Powder Bed

Laser beam energy absorption has been discussed several times previously in this chapter. CO_2 and Nd:YAG lasers have been compared, and the effect of powder diameter and atmosphere on absorptance α has been considered. The effect of α changing with material state was reported. Material vaporisation effects have been mentioned. In 2.3.1.1, a few paragraphs on the theory of lasers and radiation are followed by a review of radiation absorption measurement. Relevant equations are presented in 2.3.1.2. Theory information has been taken from books [Luxon 1985], [Steen 1998], [Ready 1997] and [Touloukian 1970].

2.3.1.1 Theory and Experiment

Laser radiation is electromagnetic, in the infra-red wavelength region for the types of laser used in direct metal SLS. The radiation is generated by stimulated emission from the atoms or molecules of the laser generating substance (carbon dioxide, for example). Absorption and emission of waves occur due to changes in either atomic electron levels, or in molecular vibration levels. A CO_2 laser relies on the changing vibration of molecules. Energy quanta or photons are transmitted in the emitted waves, with magnitude inversely proportional to the beam wavelength, λ.

When photon energy is absorbed by a molecule, its vibrations increase to higher levels (known as an "excited state"). Eventually they fall back to the

previous energy level, and in doing so they emit photon energy as a wave. Each type of molecule has unique vibration levels, so waves of a single characteristic λ are produced, hence the spectral coherence of laser sources. Another important effect is that when a photon passes sufficiently close to an excited molecule, the molecule emits a wave with the same direction of travel as the stimulating wave. This explains the unidirectional quality of laser light.

The absorption of laser radiation by opaque materials occurs in the following way. The electromagnetic waves incident on the material interact with the surface atoms, not penetrating the material more than 1μm in relevant reported cases [Tolochko 2000]. Two types of interactions are possible in the material: radiative and non-radiative. In a radiative interaction, energy levels are increased, then fall back with the release of another wave. In a non-radiative transition, heat is generated by energy transmission to the material's molecular structure (absorption). The proportion of radiative to non-radiative interactions decide the absorptivity of a smooth surface.

A "black body" is one which is said to absorb all incident radiation. It also has the property of emitting the maximum possible amount of energy at a given λ and temperature. Real materials exhibit lesser absorption and emission characteristics, so a quantity known as emissivity ε_r is used. ε_r is the ratio of radiant emission of a body to that of a black body at the same temperature. So long as Kirchoff's Law (which will not be entered into here) holds true, the ε_r value of a body is equal to absorptivity. In SLS the materials being tested do not have a smooth surface, so the term absorptance is used rather than the material property absorptivity.

For metals, the Drude free electron theory states that absorptance α is inversely proportional to the root of wavelength λ. Data compiled by Touloukian shows that metal powders absorb more power from lasers operating at lower λ. Radiation which is absorbed by the surface of a body may be held, or re-radiated by thermal radiation over time. Thermal radiation occurs in relation to the absolute temperature of the body and surroundings [Williams 1998]:

$$E_{TA} = \varepsilon_r . \sigma_{SB} . [(T_{SURFACE}^4) - (T_{ENVIRONMENT}^4)] \qquad (2.7)$$

Where E_{TA} is the energy radiated per unit time per unit area, ε_r is the material emissivity and σ_{SB} is the Stefan-Boltzmann constant, 5.7×10^{-8} W/(m^2.K^4). Temperature is in K. The effect of temperature on this heat transfer mode is large.

Some techniques for measuring α (or ε_r) of materials currently exist. These fall into the categories calometric (quantified through a heating effect) or radiometric (direct measurement of reflectivity). Four methods are discussed below. Results obtained using the four techniques are presented elsewhere in this chapter.

[Kizaki 1992a] used an integrating mirror arrangement to measure radiation reflected from a powder sample for the time interval 6-20ms from the application of a laser beam to the sample. The first test involved shining the laser through two flat mirrors, onto a parabolic mirror, and collecting at the focal point using a photon drag detector (Figure 2.22). The detector reading was taken to represent the case where no power was absorbed through the system. Next, one of the flat mirrors in the system was covered with a layer of a powder sample. Radiation reflected from the powder surface was again reflected from the parabolic mirror, onto the detector. An optical chopper acted as a switch by selectively blocking off the laser beam. Because of the high time definition, the response time of equipment had to be considered.

Figure 2.22 Kizaki's integrating mirror

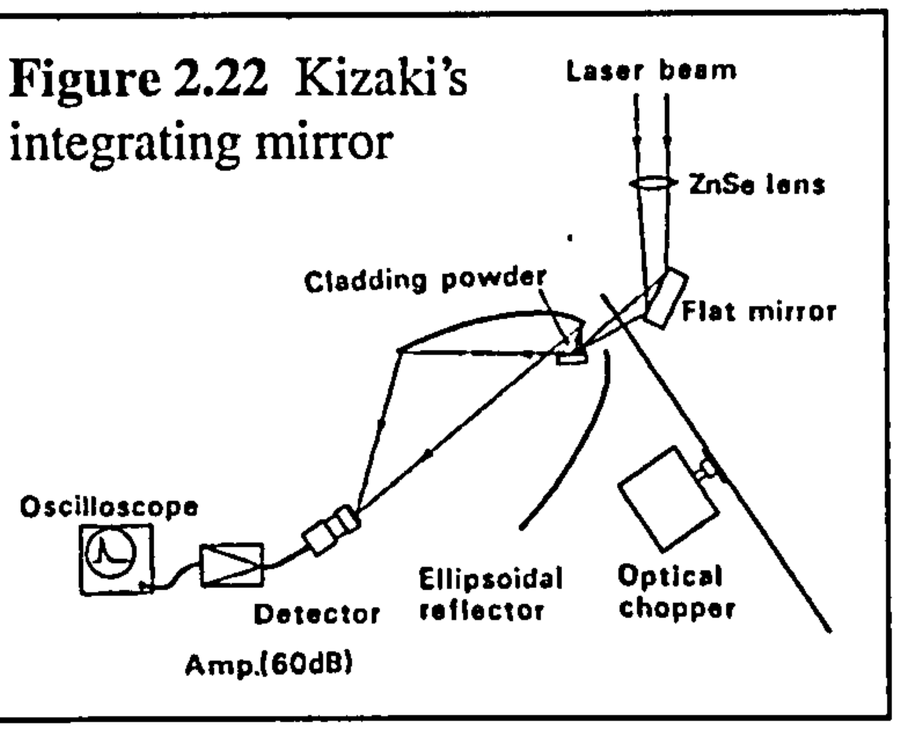

α of the powder sample was taken as:

α = 1- (detector reading with powder/ reading with no powder).

Figure 2.23 Tolochko's integrating sphere

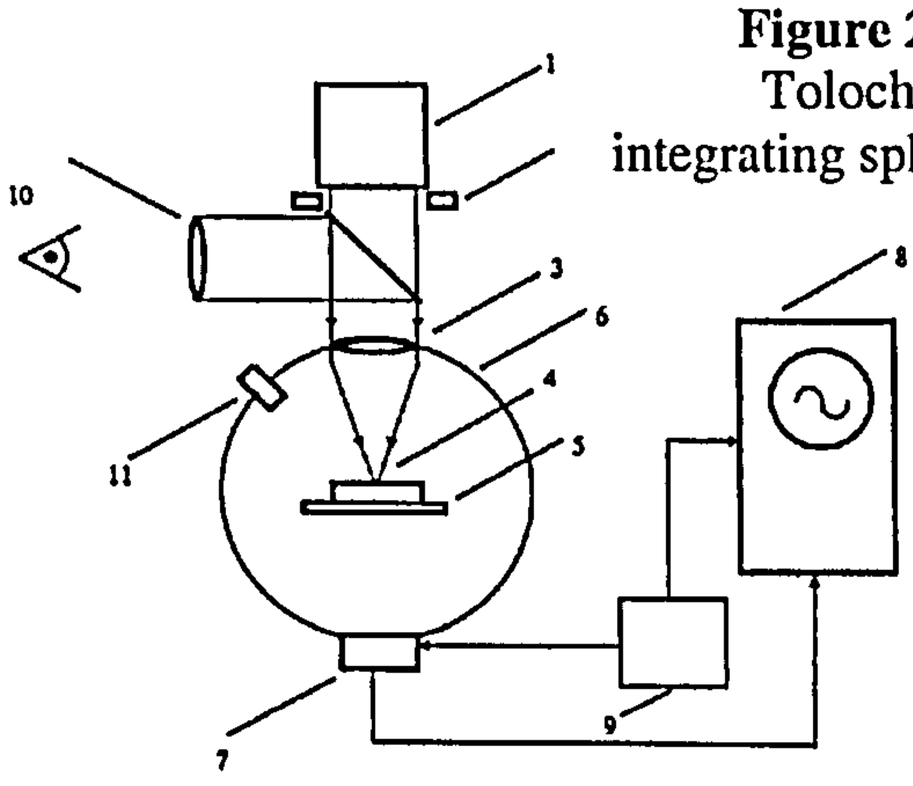

Key
(1) laser beam, (2) modulator, (3) optical system, (4) loose powder surface, (5) cuvette, (6) integrating sphere, (7) photo-receiver, (8) digital processing oscilloscope, (9) electronic unit, (10) optical microscope and (11) illuminating lamp.

[Tolochko 2000] used an integrating sphere to collect reflected laser radiation (Figure 2.23). The fundamental difference from Kizaki's approach was the diffusion of reflected laser radiation by the material covering the sphere wall, effectively distributing it evenly around the sphere. A photodetector viewed an area on the sphere wall, and took a reading proportional to the amount of reflected radiation. As in Kizaki's method, calibration of the system had to be carried out. Here a sample of known reflectivity was used and the corresponding reading taken.

Sih and Barlow [Sih 1993] used a calometric method. A laser was directed onto one end of a tube filled with powder, insulated around the curved surface (Figure 2.24). Using a coil heater wrapped around the tube, Sih and Barlow measured α at different bed temperatures. The laser power was kept small so that temperature rises were also small. This kept the powder thermal properties almost constant.

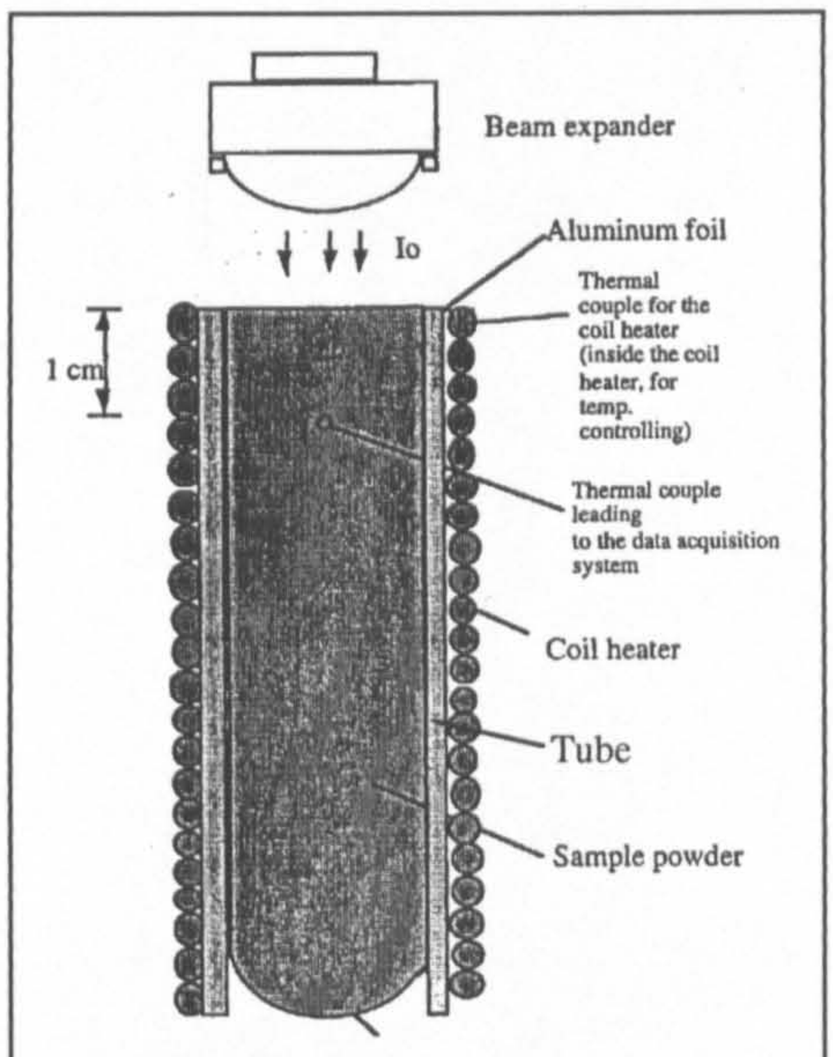

Figure 2.24 Sih and Barlow's unsteady state method

To calculate α for a powder sample, a solid heated by a surface source was considered, in two cases where α changes. It can be shown that:

$$I_S.\alpha_1.A = m.C.\left(dT/dt\right)_1 \qquad (2.8a)$$

$$I_S.\alpha_2.A = m.C.\left(dT/dt\right)_2 \qquad (2.8b)$$

Where (dT/dt) is the rate of temperature rise with time, I_S is the incident surface heat flux per unit area and A is the area over which the surface source acts. α, m and C are as previously defined. Subscripts *1* and *2* refer to the two cases. Equating C for the two cases and for the same I_S, A and m, it is found that:

$$C = \alpha_1.\left(dt/dT\right)_1 = \alpha_2.\left(dt/dT\right)_2 \qquad (2.8c)$$

When the laser was switched on, power absorbed at the bed's surface caused the powder temperature to increase. This unsteady-state temperature rise within the powder bed was recorded against time using a thermocouple to find $(dt/dT)_1$ for the powder of interest. The laser was switched off, then a thin layer of calibrating

material with a known α value (α_2) was applied to the surface of the powder bed. Once $(dt/dT)_2$ was found in a second experiment, the absorptance of the powder of interest (α_1) could be calculated using equation (2.8c). Powder 2 was carbon powder in Sih and Barlow's work (assumed 100 percent absorptive).

The experimental technique used by Sih and Barlow to measure powder α is also applicable to conductivity k. By measuring the temperature at different times for one position within the powder bed, k can be found. An equation exists to describe a semi-infinite solid with a constant heat source applied across its surface. The resulting heat flow through the solid is one-dimensional. By integrating this equation with appropriate boundary conditions, an expression for temperature rise against depth in the powder bed and time can be derived:

$$T(z,t) = \left(\frac{2\alpha.I_s}{k}\right)\left(\sqrt{\kappa.t}\right) ierfc\left(\frac{z}{2\sqrt{\kappa.t}}\right) \qquad (2.8d)$$

Where z is depth into the powder bed and κ is bed diffusivity equal to $k/(\rho.C)$. T, I_S, t, α, ρ, C and k are as previously defined. *ierfc* is an integrated complimentary error function, as described in Appendix II of [Carslaw 1959]. If measurements are made of T in two instances, a ratio can be established:

$$R_T = \frac{T(Z_1, 2t_1)}{T(Z_1, t_1)} \qquad (2.8e)$$

Where Z_1 is the depth position of the thermocouple (Figure 2.24) and t_1 is a chosen time interval. Examining equations (2.8d) and (2.8e), the relationship between temperature ratio R_T and κ is independent of material properties. Data from a thermocouple experiment can be used to obtain a value of R_T, from which κ is found. Measurement or knowledge of ρ and C allow k to be calculated.

By measuring the rate of temperature increase for a given input power, the specific heat C can be found.

[Hauser 2001] weighed single SLS-processed tracks made at different values of speed and power. A particular amount of energy is required to heat and melt a unit length of material, so α can be estimated through an energy balance:

$$E_M = \frac{P.\alpha}{U} = \frac{m}{L}(C.dT_{A-M} + L_M) \qquad (2.9)$$

Where P, α, U, L and C are as previously defined, E_M is the energy per unit length of track which contributes to melting material, m is the mass of the track (of length L), $dT_{A\text{-}M}$ is the temperature change from ambient to melting point and L_M is the latent heat of melting. Because some heat is conducted into the bed and does not contribute to melting, the value of α is expected to be an underestimate. The method's advantages are its simplicity and practicality given the situation at hand.

With regards to the atmosphere during experiments, Tolochko used an inert atmosphere, Sih used a vacuum. Hauser used air and argon. Kizaki used vacuum, argon and xenon gas. He reported that in argon and xenon a plasma was formed near the irradiation zone, causing absorption to increase with time where in vacuum it had decreased. Experiments carried out in vacuum would not be considered representative of processing carried out in an inert atmosphere.

In the experiments of Kizaki, Tolochko and Hauser, sintering occurred. In Sih's experiments it did not.

Calometric methods have the practical advantage that only heat actually remaining in the bed is measured. Radiometric methods measure reflected radiation: no account can be made of heat lost through convection or mass transfer if evaporation occurs. The advantage of radiometric methods is their definition against time, providing snapshot readings in the early milliseconds of laser application. Tolochko and Kizaki's short application of laser energy is approximately representative of the exposure provided to a point by a scanning laser. Irradiation time typically amounts to less than 1s in direct metal SLS [Kruth 1996].

There is a lack of heat transfer experimentation which closely recreates the processing conditions found in direct metal SLS. The atmospheric gas, laser and powder types used should correspond to the situation investigated, in order to generate representative results.

Of particular interest would be to see how laser absorption varies in the SLS process. There is expected to be a difference between heat absorbed into a first

scanned track and subsequent overlapping tracks, for instance. SLS could be recreated even more closely by testing a moving laser source.

The use of carbon as a simulated black body by Sih must be looked upon as not ideal; Touloukian [1970] writes: "All real materials reflect part of the radiant energy incident upon them".

Tolochko found that for iron powder exposed to a CO_2 laser, α was 0.45. [Kahlen 2001] uses an α of 0.4 for stainless steel powder processed by a CO_2 laser, saying that of this amount, 12 to 35 percent does not contribute to material melting. [Vasinonta 2000] uses α of 0.35 for steel powder processed with an Nd:YAG laser, a value derived from thermal imaging.

2.3.1.2 Models

Laser beams such as that used by [Hauser 1999a] have an irradiance which reduces radially from the beam centre (see Figure 2.25). The irradiance distribution is known as Gaussian, changing with radial position as described by the equation:

$$I(r) = I_C.e^{\left[-2r^2/w_0^2\right]} \qquad (2.10)$$

Where $I(r)$ is the beam irradiance at a radial position r, I_C is the peak irradiance and w_0 is the beam radius, equal to $d/2$. Irradiance at the beam perimeter is non-zero, equal to (I_C. e^{-2}) or (0.14 I_C). The Gaussian distribution is used in laser heating models, seen in Section 2.3.4.

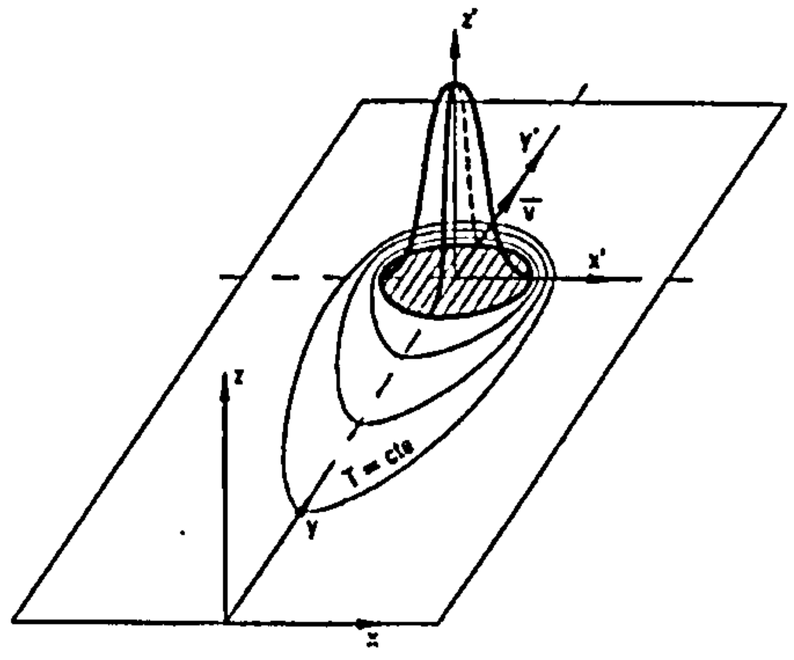

Figure 2.25
Scanning laser profile [Bugeda 1999]

The beam is reported to be absorbed into the powder bed over a finite depth. [Sun 1991], [Deckard 1995] and other authors assumed Beer-Lambert's Law to describe laser absorption against depth in SLS:

$$I_Z = (1-R).I_0.e^{-bZ} \qquad (2.11)$$

Where I is irradiance, R is the powder reflectance, b is the extinction coefficient of the powder and Z is depth into the bed. Subscripts Z and 0 mean at Z depth and at the surface respectively.

The expression $(1-R).I_0$ represents the irradiance which remains after surface reflection. The exponential term represents decay of the laser beam intensity with depth into the bed, due to absorption. The extinction coefficient is dependent on laser and powder type. The Beer Lambert equation was developed for semi-transparent continuous materials; the geometry of a powder bed is significantly different. The equation assumes that the beam travels in a straight line downwards, but the spherical opaque nature of the powder particles means that rays could be reflected in any direction. The beam is likely to spread downwards and sideways, suggests [Laoui 1999] in his work reviewed below.

It has been mentioned in 2.2.6.3 that α increases as porosity φ increases. In general, voids in a surface cause waves to be reflected multiple times, yielding more of their energy [Touloukian 1970, Steen 1998]. [Sih 1995b] proposed an equation which relates α to φ; discussed below.

Sih and Barlow considered the relationship between the emissivity ε_r (equivalent to α) of solid materials and of powder beds made of those same materials. They reported a probabilistic equation used to calculate ε_r for radiation travelling through a hole into a cavity bounded by solid material:

$$\varepsilon_{rH} = \frac{\varepsilon_{rS}}{\varepsilon_{rS} + f(1-\varepsilon_{rS})} \qquad (2.12a)$$

Where ε_r is emissivity and f is the cavity to hole area fraction. Subscripts are H referring to the cavity and hole, and S referring to the solid material. As f tends towards zero, the emissivity of the cavity tends towards that of a black body (=1). This hole emissivity was applied to the surface of a powder bed:

$$\varepsilon_{rP} = A_H.\varepsilon_{rH} + (1-A_H).\varepsilon_{rS} \qquad (2.12b)$$

With parameters as defined above. A_H is the surface area fraction of holes, subscript P refers to the powder bed. Further geometrical analysis and substitution by Sih and Barlow provides a formula for ε_r of a powder bed as a function of ε_r for solid material and bed porosity φ. Exchanging ε_r for α, a powder bed with φ equal to 55 percent would have:

$$\alpha = (4.1\alpha_s)/(3.1\alpha_s + 1) \qquad (2.13)$$

The bed absorptance α would be larger than the solid absorptance α_s in all real cases. An accuracy of ±10 percent is suggested by Sih, but the equation greatly misjudges the ratio $\alpha:\alpha_s$ in reported cases. For iron powder reported by [Tolochko 2000], $\alpha:\alpha_s$ was 1.4 :1 whereas the equation predicts 3:1. [Eyerer 1994] reports a $\alpha:\alpha_s$ of 60 :1 for copper, much higher than predicted. Sih's analysis and experiments involve no geometrical change, whereas other authors report α where material is melted. Sih's method is applicable to 3D Systems type SLS but not direct metal type SLS. In the latter case, the value of α would depend on the melting time relative to laser application time. The equation (2.13) suggests that particle diameter d_p does not affect α, which the findings of Section 2.2.5 say is only true within a certain range of d_p.

Tolochko uses the graph Figure 2.26 to demonstrate how absorptance changes with laser application time during Nd:YAG processing of nickel alloy powder in an argon atmosphere. Two stages are shown. In stage I, absorptance increases due to the temperature increase. When stage III is reached, absorptance decreases due to the melting of particles and reduction of porosity. This result is said to be typical for CO_2 and Nd:YAG laser processing of metallic powders. Three seconds of laser exposure are required to initiate melting in Tolochko's experiment, compared to less than one second in cases of direct metal SLS. The energy density used by Tolochko is relatively low.

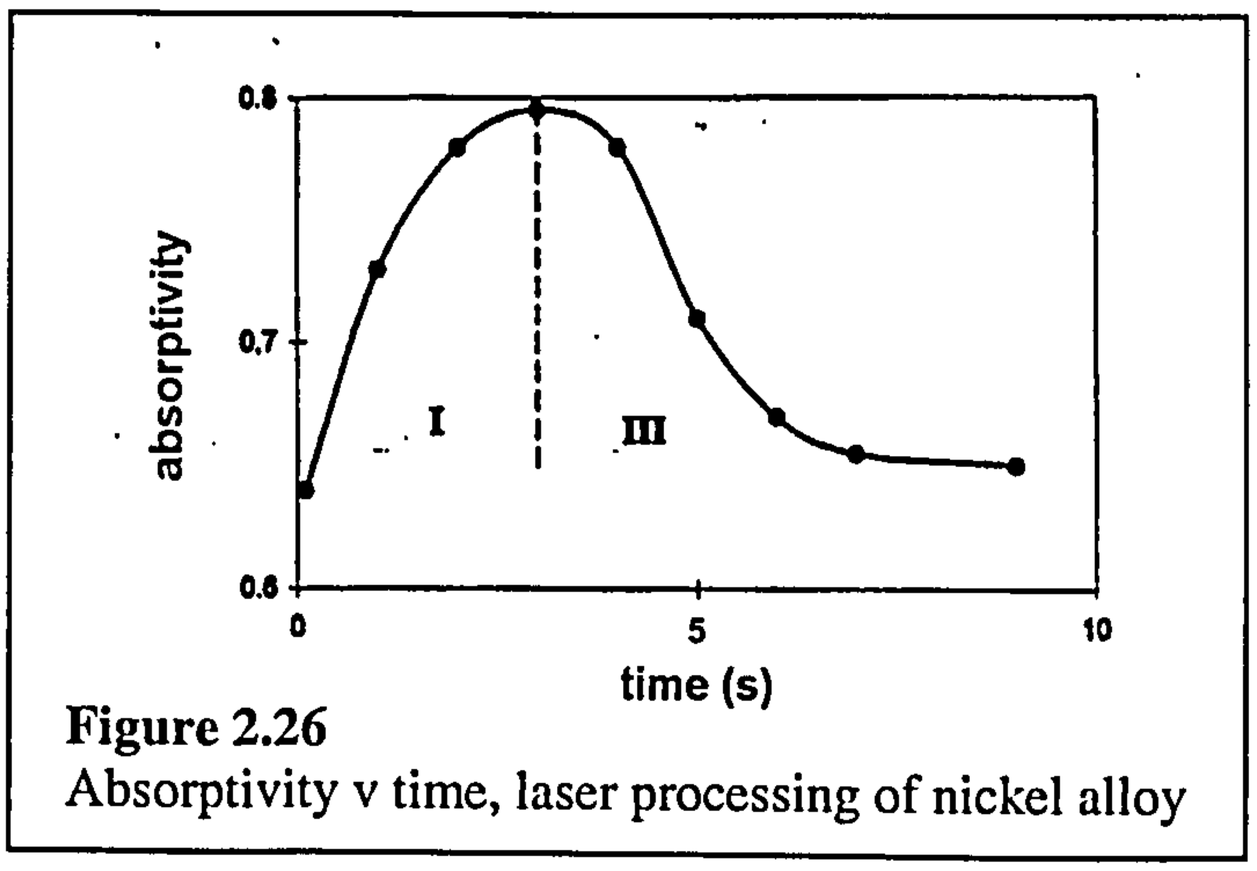

Figure 2.26
Absorptivity v time, laser processing of nickel alloy

[Laoui 1999] and [Wang 2000] carried out research into the energy absorbed by iron-copper powder beds by Nd:YAG and CO_2 lasers. It was assumed that other

heat transfer modes were negligible compared to radiation in their effect on the shape of processed material. The authors generated a ray-tracing model assuming a bed made of spheres which reflect the laser beam. Rays originate travelling downwards, and on collision with a particle they lose energy. The modelled bed porosity was much higher than reality, at 75 percent. Results were presented as cumulative absorbed energy against bed depth Z, and α against α_s (see the graph Figure 2.27). This figure agrees qualitatively with Sih's formula, (2.13) above. All laser radiation was absorbed for Z <0.9mm, and most was absorbed at Z <0.3mm. At a nominal d_p of 40μm, these positions corresponded to $22d_p$ and $8d_p$ respectively. Contrary to Laoui and Wang's modelled conclusion, [Sun 1991] assumed that radiation was absorbed at $Z < d_p$. [Childs 2001] assumed $Z < 4d_p$. This difference may relate to the assumptions made, the modelled bed porosity or the material type.

Because α_s is higher for the YAG laser, this lead to a higher modelled α (66 percent) and a lower penetration depth than for the CO_2 laser. α for the CO_2 laser was found to be 26 percent. The model is interesting as a qualitative guide to behaviour. As with Sih and Barlow's model, it does not incorporate any porosity change over time.

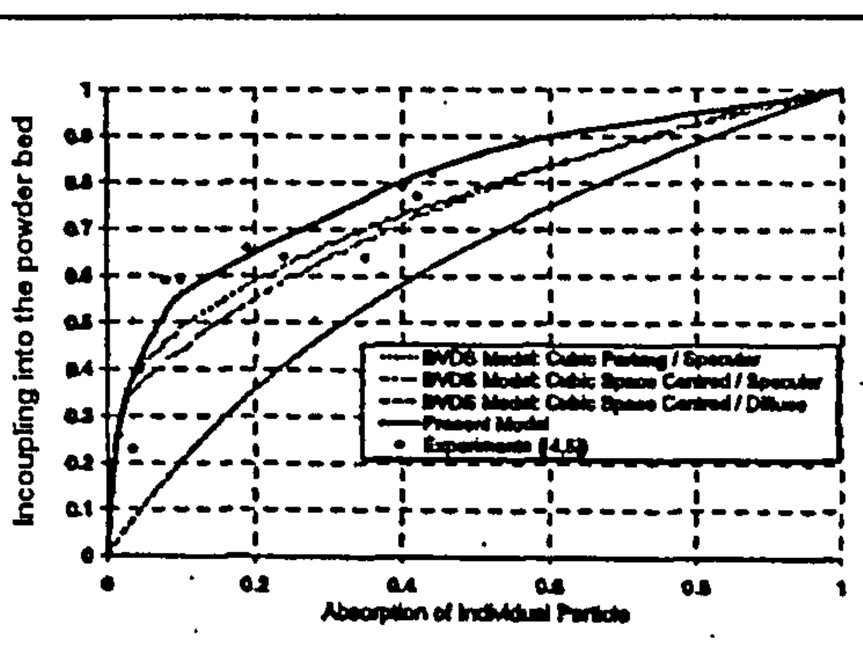

Figure 2.27
Absorptance of powder bed vs material

2.3.2 Heat Transfer within Powder Bed

Within the body of a solid material, heat transfer occurs by conduction alone. In a material powder, there are two constituent phases: powder particles and the gaseous voids between them. Adjacent particles only make solid contact over small areas, so between one particle and another, convection and radiation heat transfer are considerable in relation to conduction modes [Yagi 1957]. Heat transfer modes can be summed to form an effective conductivity k for powders. [Nelson 1995] notes that k values for powder materials are relatively closer than their solid equivalents. For instance, k for solid copper is 2000 times that of solid

polycarbonate, whereas k for copper powder is only 4 times that of polycarbonate powder. Inter-particle heat transfer clearly has a large effect on k for powders.

Researchers have constructed semi-empirical equations which relate the thermal properties of the solid and gas phases to the effective conductivity for a powder bed. It is assumed that the bed is still governed by a conduction law (described by equation (2.16) below).

The most popular equation for effective conductivity was proposed by Yagi and Kunii [Yagi 1957], for fine particles and a motionless gas:

$$k = \frac{\rho_r . k_s}{1 + \Phi \frac{k_s}{k_g}} \qquad (2.14)$$

Where k is thermal conductivity, Φ is an empirical coefficient, $0.02 \times 10^{2(0.7-\rho r)}$, ρ_r is the bed's relative density and subscripts are s for solid material, g for gas phase. "Fine" particles are those which have d_p <0.4mm. Accorded to [Sih 1995a], Yagi and Kunii's equation consistently underestimates k when applied to ceramic powders. [Churchill 1986] created a similar equation, relating k values through ρ_r.

[Damkohler 1937] suggested an equation which accounts for only the component of heat transferred due to radiation:

$$k_R \approx 4.\xi.j.d_p.\varepsilon_r.\sigma_{SB}.T_b^3 \qquad (2.15)$$

Where k_R is conductivity due to radiation, ξ is area fraction occupied by voidage canals, j is a constant approximately equal to 1, T_b is the temperature of the powder bed in K and d_p, ε_r and σ_{SB} are as previously defined.

Zehner and Schlunder put forward an equation for powder k, which was modified by [Sih 1995a] to include Damkohler's radiation effects and a particle deformation parameter. The pursuit of a higher accuracy equation applicable over a wider range of cases leads to many more terms compared to Yagi and Kunii. If the equation is used to model a dynamic situation, values must be recalculated over time. For manual working this represents a problem, but does not if computers are employed. Sih and Barlow's equation is proven to be flexible; when compared with hundreds of data sets for solid-state powders, accuracy was found to be ± 30 percent. Heat transfer inside the melt pool zone in direct metal SLS is

not expected to conform to the conductivity equations of Yagi and Kunni or Sih and Barlow: the change of state and stirring of material are not accounted for in estimating *k*.

If a powder bed can be assumed to follow solid conduction laws, Fourier's equation describes the variation of temperature against position and time:

$$\frac{\partial^2 T}{\partial x^2}+\frac{\partial^2 T}{\partial y^2}+\frac{\partial^2 T}{\partial z^2}-(\frac{\rho.C}{k}).(\frac{\partial T}{\partial t})=0 \qquad (2.16)$$

Where x, y and z are perpendicular directions in space, t is time and T, ρ, C and k are as previously defined. Fourier's equation is used in experiments and thermal process models below.

Measurement of the conductivity of powders is carried out in much the same ways as for solids. A rig described by [Tontowi 2000] and [Childs 2001] uses a steady- rather than transient-state method to measure *k*. A cylindrical stack comprising disc-shaped layers of different materials is insulated around its curved surface. Two material types are used: one is a solid material of known *k*, and the other is a powder sample. A heater at the top of the stack is used to set a uniform heat flux, which travels axially down the stack. Temperature gradients form through the material layers, reducing to ambient T at the bottom of the stack. Once a steady state is reached, T is measured at specific axial positions using thermocouple probes. Using several sets of simultaneous temperature readings and the properties of the known material, the powder *k* can be found from the relationship (derived from equation (2.16)):

$$P_H = k.A.\frac{T_a - T_b}{dZ} \qquad (2.17)$$

Where P_H is heater power, k is powder conductivity, A is the stack cross-sectional area, T is temperature and dZ is the distance between points a and b. Subscripts a and b represent the top and bottom points of a disc of material respectively.

Compared to Sih and Barlow's method, the temperature differences measured are larger, thus they are more likely to be precise. The temperature difference

causes a slight difference in the value of k between the top and bottom of the stack.

The effect of porosity on specific heat C is now considered. To calculate C for a two-material mixture, a commonly-used equation is [Yevko 1998]:

$$C_m = \frac{\rho_1.C_1.\gamma_1 + \rho_2.C_2.\gamma_2}{\rho_1.\gamma_1 + \rho_2.\gamma_2} \qquad (2.18)$$

Where C is the specific heat, ρ is the material density, γ is the volume fraction and subscript m means mixture, and *1* and *2* represent the two material phases.

For metal powders, the density of gas is relatively small, so the equation can be simplified as: $C_m = \frac{\rho_1.C_1.\gamma_1}{\rho_1.\gamma_1}$. In other words the powder specific heat is equal to the specific heat of the solid, C_1. This has been confirmed experimentally [Sih 1992]. Yagi and Kunii's equation (2.14) and equation (2.18) above contain no terms in T, so k and C of powder are assumed to vary with T as they would in the solid material.

2.3.3 Time-Dependent Heat Loss from Powder Bed Surface

Time-dependent mechanisms for heat loss from the powder bed's surface are convection, thermal radiation and material vaporisation [Sun 1991, Yevko 1998]. Whilst laser absorption and heat conduction in the powder bed discussed above have been the subject of numerous papers, less attention has been paid to surface heat loss in the SLS process. In direct SLS of room temperature steel powder, the peak difference between the melt pool and atmospheric temperature is significant, necessarily above 1000°C. Temperature differences drive convection and radiation losses, as will be seen below. The material temperature may become high enough for vaporisation. In Section 2.2.6.2 it was reported that laser application, melting and solidification of material often take less than 500ms to occur in direct metal SLS. Time-dependent heat fluxes would be largest in this 500ms interval, diminishing thereafter.

Thermal radiation has been described in Section 2.3.1.1, causing a heat flux very sensitive to temperature difference, evaluated via equation (2.7).

In convection heat transfer, a coefficient h is commonly used to evaluate heat loss from a body's surface to a surrounding medium, given flow conditions and the temperature of the body and medium. For the general case of free convection (the effect of gravity on a fluid as it is heated and its density changes), an equation has been developed [Holman 1997]:

$$Nu_f = D.(Gr_f.Pr_f)^p, \qquad (2.19)$$

Where D and p are values reported for different body geometry and fluid thermophysical properties, Nu is the Nusselt number, $= \frac{h.x_{HT}}{k}$,

Gr is the Grashof no., $= \frac{g.\beta.(T_w - T_\infty).\rho^2.x_{HT}^{\ 3}}{\mu^2}$, and Pr is Prandtl no., $= \frac{C.\mu}{k}$.

x_{HT} is the length of heat transfer area, g is acceleration due to gravity, 9.81 m/s^2, β is the volume coefficient of expansion. T and h are the temperature and heat transfer coefficient. k, μ, ρ and C have their usual meanings and refer to the fluid. Subscript f means evaluated at the film temperature, $= \frac{T_\infty + T_w}{2}$: w and ∞ refer to points on the body surface and in the bulk fluid, respectively.

Parameters must be evaluated for a set situation to calculate h. For instance, for heat lost by a horizontal cylinder (similar to the case of a single sintered line) at 80°C to air, a calculation of the product $Gr.Pr$ tells us that D=0.675 and p=0.058, therefore h=493W/(m^2.K). Thermodynamic tables provide Pr for air at a specific temperature: the quantity β is equal to $1/T(K)$, assuming an ideal gas.

The equation is designed for use in steady-temperature situations. A transient T calculation would require an accurate temperature-time profile of the melt pool surface for regular recalculation of the 6 variables.

Evaporation of material at high values of A_N has been discussed in Section 2.2.6.2. As well as reducing laser beam absorptance, it is possible that removal of heat by mass transfer would be significant at high A_N.

Authors express a variety of attitudes towards the heat transfer modes described above. [Kaplan 2001] and [Vasinonta 2000] say that convection and thermal radiation have a negligible effect on part geometrical properties in metals processing. [Williams 1996] and [Miller 1997] say that convection and thermal radiation over the course of a part build affect processed part mechanical properties. [Kahlen 2001] says that of the laser energy absorbed by the powder bed, 12 to 35 percent does not contribute to melted mass due to being lost by conduction or other time-dependent modes. [Dai 2003b] incorporates only natural convection from the powder bed surface into his model of laser processing, in which temperatures over 1000°C occur. In a comparable process, [Chung 2003] incorporates surface heat loss by radiation only. [Kandis 1999] and [Norrell 1996] disagree over which is the dominant mode at 200°C part temperature.

2.3.4 Thermal Fields in SLS-Type Applications

2.3.4.1 Measuring Temperature versus Position and Time

Various temperature measuring devices have been used by reviewed authors. Selection was based on issues such as accuracy, spatial and time definition of measurements, cost and ease of use. [Griffith 1998] inserted a thermocouple into a wall being built up by direct metal SLS. She recorded the variation of temperature against time, showing successive T spikes of reducing amplitude as the laser passed overhead to scan each new layer. Griffith also used infra-red and high-speed cameras to measure temperature in a laser-induced metal melt pool. For both cameras, the wavelength of thermal radiation emitted by the pool was recorded and converted to temperature. Values of T up to 1700°C were measured.

The benefit of using thermocouples is that they can measure temperatures within a solid body. They have a thermal inertia which must be considered when measuring transient temperatures. Imaging systems (cameras) are limited to surface readings, but have the advantage that they can measure T without removing heat, so they do not interact with the measurement zone [Magison 1990].

2.3.4.2 Thermal Field Models

Analytical models have been created to predict the temperature rise occurring in a body when a laser-like heat source is applied. [Bechtel 1974], [Cline 1977], [Lax 1977], [Carslaw 1959], [Chen 1983], [Sanders 1984] and [Festa 1987] were studied. These authors assumed the heated body to be semi-infinite and isotropic, with constant material properties. None of the models incorporated surface heat loss. Heat propagation occurred by conduction in the solid, described by Fourier's equation (2.16). The laser intensity surface distribution was assumed to be Gaussian (equation (2.10)), or constant within a zone of a certain shape. Most models assumed exponential attenuation with depth (equation (2.11)).

Temperature profiles for moving and stationary laser heat sources were compared. For moving sources, the relationship between beam speed and heat diffusion speed is key: if the ratio $U/(d.\kappa)$ is low enough, the temperature profile for a moving source resembles that for a stationary source. If U is high enough, the depth profile of temperature becomes similar to that of irradiance. The effect of the beam diameter d and attenuation depth Z_p are considered.

[Carslaw 1959] contains example equations for heat sources applied to solid bodies. One example is described here, the variation of temperature with position and time in an infinite body due to a line heat source. In order for the line assumption to be applied to SLS, the ratio $U/(d.\kappa)$ must be above a certain value.

The body is infinite in size with constant properties, at an initial temperature of zero throughout. The heat source of strength Q is applied instantaneously at t=0. Its form is an infinitely long thin line, parallel to the z axis, passing through points $x^{|}$ and $y^{|}$. Temperature is described by:

$$T = \frac{Q}{4.\pi.\kappa.t} e^{-\left(\frac{(x-x^{|})^2+(y-y^{|})^2}{4.\kappa.t}\right)} \qquad (2.20)$$

Where T is change in temperature at the point (x, y). Q is the heat flux per unit length of the line, divided by $(\rho.C)$. κ is bed diffusivity equal to $k/(\rho.C)$. t, x, y, k, ρ and C are as stated earlier.

2.3.5 Summary of Heat Transfer Investigation

A non-linear heat transfer situation exists near the powder bed surface in SLS. Laser energy is absorbed over a finite depth. Heat spreads through stirring of melted material, then spreads further due to heat conduction.

Laser radiation was discussed with reference to absorption and reflection. Convection, thermal radiation and evaporation were considered as time-dependent modes of heat loss from the bed's surface. These modes depend on temperature as well as time. Peak temperatures upwards of 1000°C must necessarily occur in direct steel SLS. Infra-red cameras and thermocouples have been noted for their ability to record high temperatures.

Analytical models of heat transfer which are applicable to SLS were compared. Models of laser irradiance against position and surface absorptance against porosity were reported. Values entered into these models are dependent on the type of laser and material. It was shown that porosity has a significant effect on absorptance. The absorptance of a surface was reported to change over time, as the surface material changed from powder to solid form. Models of conduction within the powder bed and convection from the powder bed surface were discussed.

Methods of measuring powder bed absorptance and conductivity were reviewed. Absorptance was measured using either radiation methods, calorimetric methods or the weighing of processed tracks. Conductivity was evaluated via temperature measurements within the powder bed. It was commented that experimental conditions should recreate SLS processing conditions as closely as possible.

2.4 Material Densification Process

When parts are formed by traditional solid phase sintering, a body of powder is heated throughout to a temperature just below the material melting point for minutes or hours [Jenkins 1991, Davis 1994]. In the SLS process however, powder particles are heated beyond the softening or melting point for a duration in the order of seconds (see Section 2.2.6.2). The powder bed structure is altered only in the locality of the laser application. In direct metal SLS, some particles

lose their shape completely by joining a melt pool. Traditional sintering, SLS sintering and laser cladding are compared below.

2.4.1 Densification in Traditional Sintering

Sintering is the temperature-activated process whereby adjacent powder particles bond to one another to form a solid structure [Kaysser 1991]. Pressure may or may not be applied. Porosity in the bed is reduced, and the overall surface energy of the body is reduced.

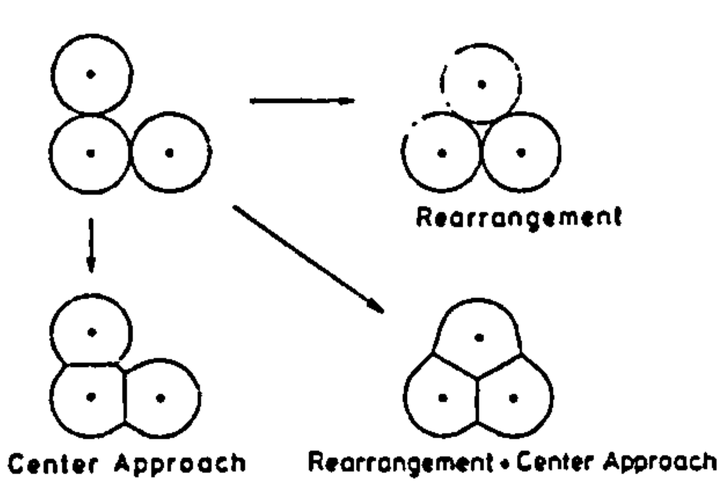

Figure 2.28 Densification in sintering

Traditional methods of sintering are known as solid phase sintering (SPS) and liquid phase sintering (LPS). SPS occurs at a temperature below the melting point of the material, and takes in the order of hours to complete. There are two mechanisms in SPS by which porosity decreases: particle rearrangement and bonding (Figure 2.28). Rearrangement causes the particles to pack more optimally. However, its effect is not as pronounced as that of bonding. Bonding in SPS is split into three characteristic stages with their own features and mechanisms [Jenkins 1991]. The stages are:

1) Solid material bridges form in the necks between individual particles. Diffusion takes place.
2) Stage 2 begins at a relative density ρ_r of 75 percent. Individual particles can no longer be distinguished. Channels of open (interconnected) porosity run along boundaries. Rapid shrinkage occurs during this phase.
3) Between ρ_r of 91 and 95 percent, stage 3 begins. Pores become isolated (closed) at grain boundaries or inside grains. Densification is slow, but pore size and grain features grow rapidly. Closed porosity is hard to eliminate, but parts may reach ρ_r of 98 percent [German 1996].

For each stage, equations can be derived from the geometry of particles/ pores and the rules of material flow. These are used to calculate the rate of reduction of porosity in SPS. [Frenkel 1945] developed an energy balance based on the viscous

coalescence of crystalline powder particles driven by a reduction of surface energy. [MacKenzie 1949] developed alternative material deformation laws. [Scherer 1976] developed a method for calculating strain rate in sintering material of $\rho_r < 94$ percent. A flexible model was developed by [Johnson 1992].

[Nelson 1993b] developed a relationship to evaluate the sintering rate of amorphous materials using the Arrhenius equation for activated reactions. Combined with MacKenzie's relationship between sintering rate and change of void fraction, the following is derived:

$$\frac{d\rho}{dt} = (\rho_{MAX} - \rho)B.e^{-\left(\frac{F}{R.T}\right)} \qquad (2.21)$$

Where ρ is bed density, t is time, ρ_{MAX} is maximum (solid) density, B is a pre-exponential factor, F is activation energy, R is the gas constant 8.31×10^3 J/(K.mol), and T is temperature in K. B and F are found experimentally for a specific material.

Liquid-phase sintering involves a mixture of two or more material phases, including a low melting-point (binding) and high melting-point (structural) material. LPS occurs faster than SPS, because the binding material melts and flows into open pores through capillary attraction. If the right temperature is achieved, the binding phase will have low viscosity leading to good wetting of the structural phase [Agarwala 1995a]. Surface tension properties of the phases can be altered by pre-alloying or addition of fluxing agents.

In a subsequent temperature cycle, the structural material diffuses through the liquid phase leading to homogenisation. Application of LPS to an SLS-type process is mentioned in Section 2.1.4.6: green parts are rapidly made by LPS then are solid-state sintered to enhance their structure.

2.4.2 Densification in SLS Processing

The bonding of powder particles in SLS occurs in the order of seconds, laser beam exposure time being in the order of milliseconds [Kruth 1996]. Solid phase rules such as that developed by Nelson, equation (2.21) above, have been used to

model 3D Systems SLS of polymers. However, the appearance of parts processed by direct metal SLS reveals that melting and flowing of material occurs as well as inter-particle necking. Microscope images Figure 2.29 illustrate a metal powder's change of structure during laser processing, as observed by [Kizaki 1992a]. Image (a) shows unprocessed metal powder, (b) shows powder after 0.2s low-power laser exposure, and the following images were taken at 0.1s intervals after this point. Bonding is still partly driven by the reduction of surface energy, but the reaction is faster than in SPS.

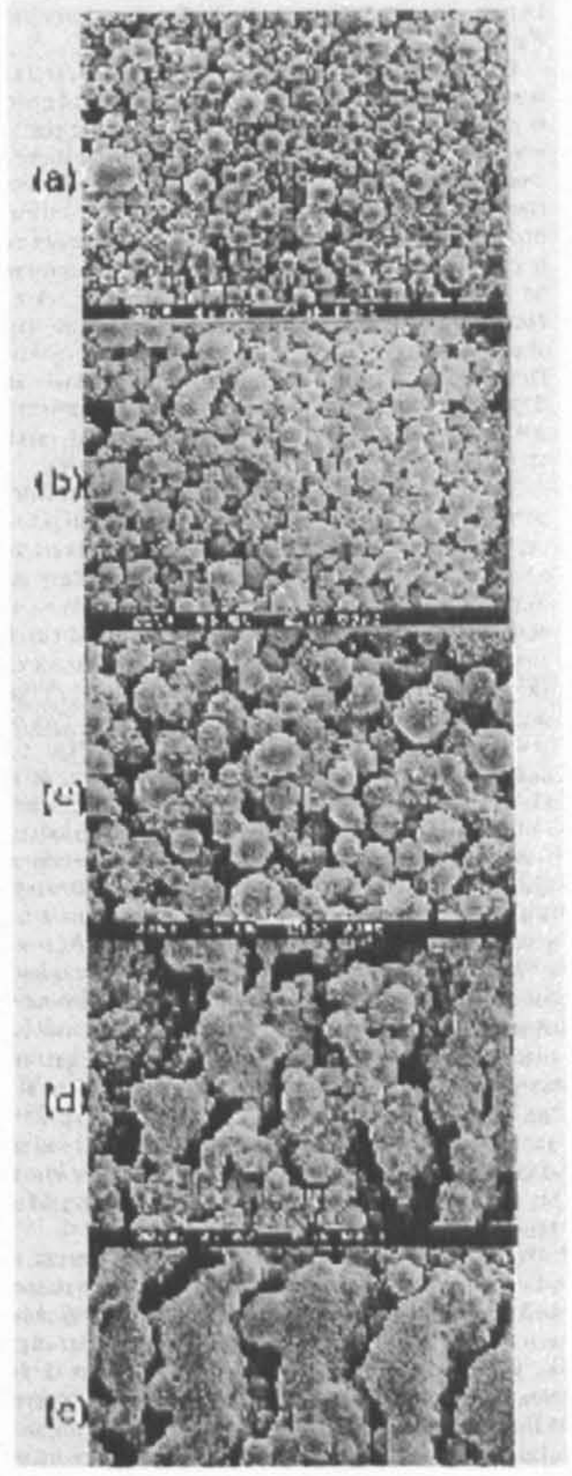

Figure 2.29 Densification in direct metal processing

The densification process in single-phase metal SLS has been further analysed in Section 2.2.6.2. A discussion of SLS process models follows in Section 2.5. In certain models of single material laser processing, the heating of material to melting point has been deemed so rapid that the influence of time on densification can be disregarded. Examples cited in Section 2.5 are the work of [Yevko 1998] and [Kaplan 2001] which simulate laser cladding. [Childs 2001] and [Dai 2003b] assumed that the material density increase at a point in the powder bed is instantaneous, and is dictated by the maximum temperature experienced.

Full melting of single-phase metals in direct SLS processing allows them to flow freely: surface tension forces drive the melted zone into a rounded shape [Tolochko 2003b]. [Agarwala 1995a] states that material shaping occurs under better control if temperatures between the material solidus and liquidus are achieved. Between these states a mixture of solid and liquid material exist, as in LPS. Controlling the solid fraction present would require good thermal control [Tolochko 2003a], or the use of a metal with widely-spaced liquidus and solidus temperatures.

The difference in cooling rates between SPS and single-phase metal SLS mean that processed microstructures are different. The grain growth over time in SPS leads to soft parts. The rapid time-temperature transition in SLS causes materials to form more hard, brittle structures with residual stress as described in 2.2.6.4.

2.5 Numerical Modelling of the SLS Process

Examples of numerical methods for simulating laser processing of material in powder form are given here. Such methods are designed for computer-integrated formulation and solution. They go a step beyond analytical methods as found in 2.3.4.2 by incorporating more detail, specifically non-linear effects [Childs 1998]. Laser radiation, heat conduction, densification and property change sub-models are integrated with procedures designed to solve the equations generated.

Some of the reasons for modelling are stated in Sections 2.5.1 and 2.5.2. In general, models are seen as a way in which to improve SFF process performance. Section 2.5.1 discusses the generalities of numerical modelling. Sections 2.5.2 and 2.5.3 discuss specific models.

2.5.1 Finite Element and Finite Difference Models

The purpose of finite element (FE) and finite difference (FD) methods is to model physical systems, to see the way they behave in response to different situations [Livesley 1983]. Design and process optimisation work can require many physical iterations, as discovered in Section 2.1.1: an FE or FD model allows initial iterations to take place before expensive facilities are required for actual testing.

As part of the modelling procedure, a physical system is broken down into discrete units. Time is divided into intervals. Space is divided into nodal points, joined by elements in FE. Nodes store values describing the state of the system, whilst elements respond to specified conditions accorded to their properties, through numerical functions. In an example of forces in a structure, nodes store forces and displacements, whilst elements respond to the forces through their

stiffness to create the displacements. A system of nodes and elements will be seen in 2.5.2.

Nodes may have multiple degrees of freedom: freedom to move, freedom for elements to bend and so on. Elements may be 1, 2 or 3 dimensional and may interpolate the transition between nodal values in a linear or more complex manner. In general, the more nodes and elements used in a model, the closer will be the model's representation of the "real world" situation.

In order to solve an FE or FD problem, systems of equations are set up. Matrices used to describe single elements are assembled into a global matrix describing the whole system. To solve a problem involving n unknown quantities, there must be n equations. Application of constraints helps to make problems determinate, so boundary conditions are used. These are data which describe conditions imposed on a system. An example in the case of forces in a structure would be that the displacement of a certain node must remain zero, because it has been fixed to the ground.

So what are the differences between the FE and FD approaches? Both make use of governing equations, which describe the behaviour of systems given certain inputs. Fourier's Law for conduction in solids has been seen earlier:

$$\frac{\partial^2 T}{\partial x^2}+\frac{\partial^2 T}{\partial y^2}+\frac{\partial^2 T}{\partial z^2}-(\frac{\rho.C}{k}).(\frac{\partial T}{\partial t})=0 \qquad (2.15)$$

The FD approach uses means to discretise an equation such as the one above. A Taylor's series expansion may be used, or the conditions at the boundaries of a control volume considered. Either way, each differential is approximated by a polynomial function at each node. For instance, a truncated Taylor's expansion of a first order differential in the x direction would look like:

$$\left(\frac{dT}{dx}\right)_{m+1,n,o} \approx \frac{T_{m+2,n,o}-T_{m,n,o}}{\Delta x} \qquad (2.22)$$

Where Δx is the distance between nodes in the x direction. T is temperature. Subscripts are m, n and o representing nodal positions in the x, y and z directions.

The Taylor's expansion is truncated. The right hand side of equation (2.22) is an interpolated estimate of the left. The same principal is adopted for *y*, *z* and *t* terms, so that a system of equations can be built.

In FE, the governing differential equation is constructed using a set of linear algebraic equations. For each node connected to a specific element, polynomial shape functions are constructed which describe the spatial variation in a quantity such as temperature using coefficients. When the shape functions for each node in an element are combined, they describe the variation of the quantity with position throughout the element using the nodal values. The equation can be differentiated with respect to direction to build up the governing equation. The coefficients and the value distribution are found by solving the governing equation at each node. Examples of FE equation building are found in [Tay 1973] and [Childs 1988].

In FD values only exist at the nodes, whereas using FE methods the value is defined continuously throughout an element using nodal values and shape factors. In terms of their performance, FE and FD have various qualities. FE performs well in cases of irregular geometry, whereas FD is easily extended into 2 or 3 dimensions, and its use of interpolation makes it more simple.

2.5.2 Childs' Model

Childs' model of the SLS process is a program in Fortran, based around a transient FE heat calculation with material properties which vary with state. The model was first developed in two dimensional (2D) form to simulate SLS of amorphous polymers and is well described by [Childs 1997a, Tontowi 2000]. The most recent 3D metal version is known as *stmet3d* [Childs 2000, Volpato 2001]. 3D analysis was developed for metals processing because of the lower scanning speed involved. The analogy between the model and the SLS process is illustrated in Figure 2.30.

stmet3d is essentially a thermal model. Shrinkage is taken into account; issues of stress and fluid dynamics are not considered. The co-ordinate system used in the model is not the standard one used in SLS: *y* represents depth in the powder bed, rather than *z*.

Two meshes are involved, with geometry and boundary conditions described in Section 2.5.2.1. The program run-time procedure is described in 2.5.2.2. Equations involved in the simulation will be described in Section 2.5.2.3. Means of handling model output and model verification work are documented in Section 2.5.2.4.

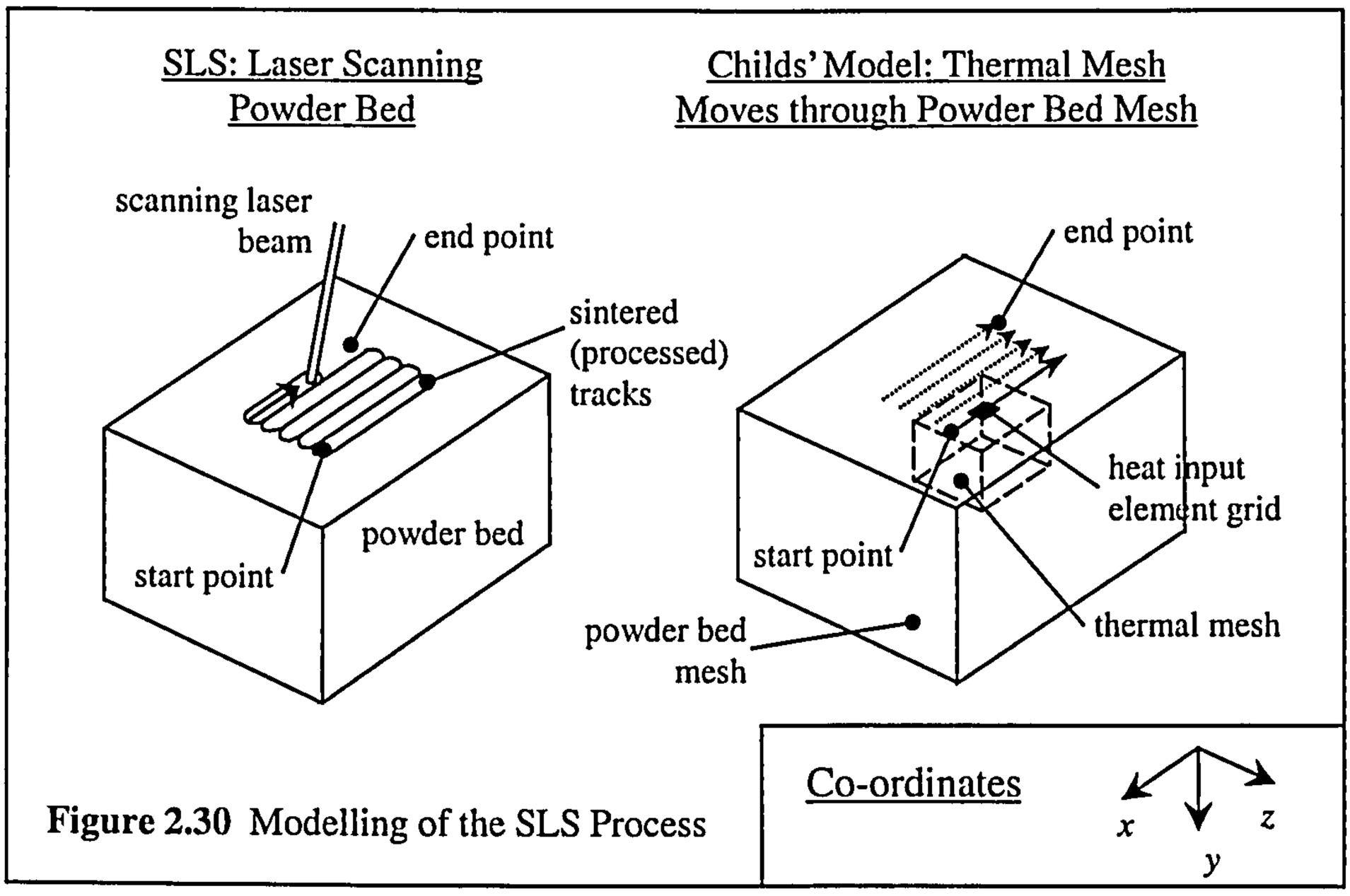

Figure 2.30 Modelling of the SLS Process

2.5.2.1 Meshes

The two meshes involved in *stmet3d* are a thermal mesh (TM) and a powder bed mesh (PBM). The geometrical details of these two meshes, and the boundary conditions for the thermal mesh, are shown in Figure 2.31 and discussed below.

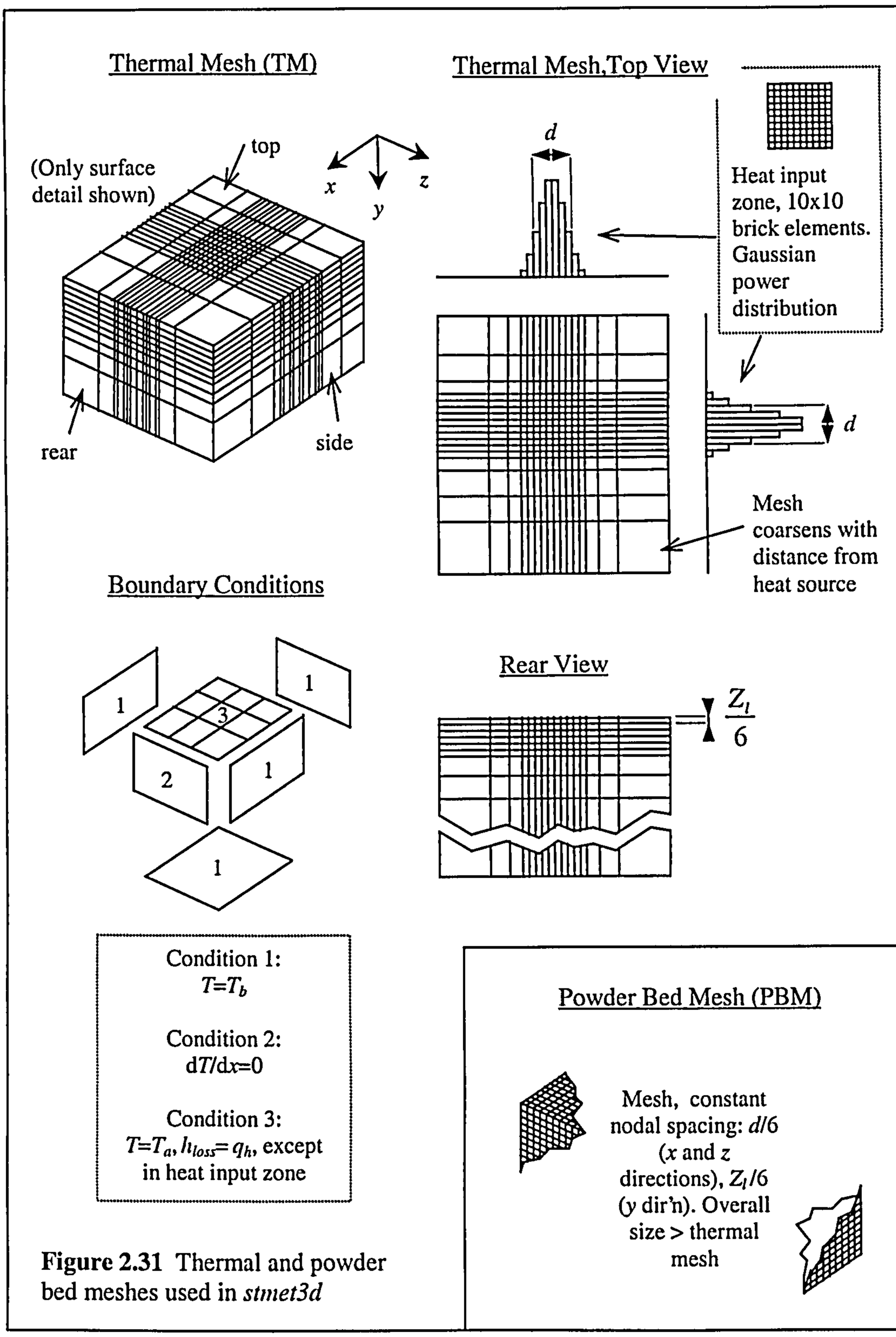

Figure 2.31 Thermal and powder bed meshes used in *stmet3d*

The thermal mesh marches through the powder bed mesh along consecutive parallel lines, in the same way that a laser scans the powder bed in SLS (Figure 2.30). On the top surface of the TM is a 10×10 element heat input zone (top right, Figure 2.31). This zone represents the presence of an incident laser beam.

Heat flux is distributed amongst elements to represent a discretised Gaussian irradiance profile. The majority of elements in the TM are purely for heat conduction. The TM's six surfaces have nodes with specific boundary conditions associated (see the bottom left of Figure 2.31 for details).

The PBM acts as a data storage matrix, holding temperature, density and thermal property data for each node. When PBM nodes and TM nodes coincide in a heat time step, the TM copies, processes and replaces PBM nodal values. PBM nodes outside the TM are considered inert for that time step.

Both meshes consist of many cuboids ("bricks") with nodes at their corners. The PBM brick size is constant at $d/6$ in the x and z directions, $Z_l/6$ in the y direction. For a beam diameter d of 1.1mm, each element in the x and z directions is (1.1)/6, or 0.18 mm long. Each TM brick size is a specified multiple of the PBM brick size, permitting coarseness of the TM away from the heat source position to reduce data and save memory. See Figure 2.31 again for a graphical representation of this. In the TM, the volume of each brick subdivides 6 times into tetrahedral-shaped quadrilateral volume elements (Figure 2.32 shows how this is accomplished geometrically).

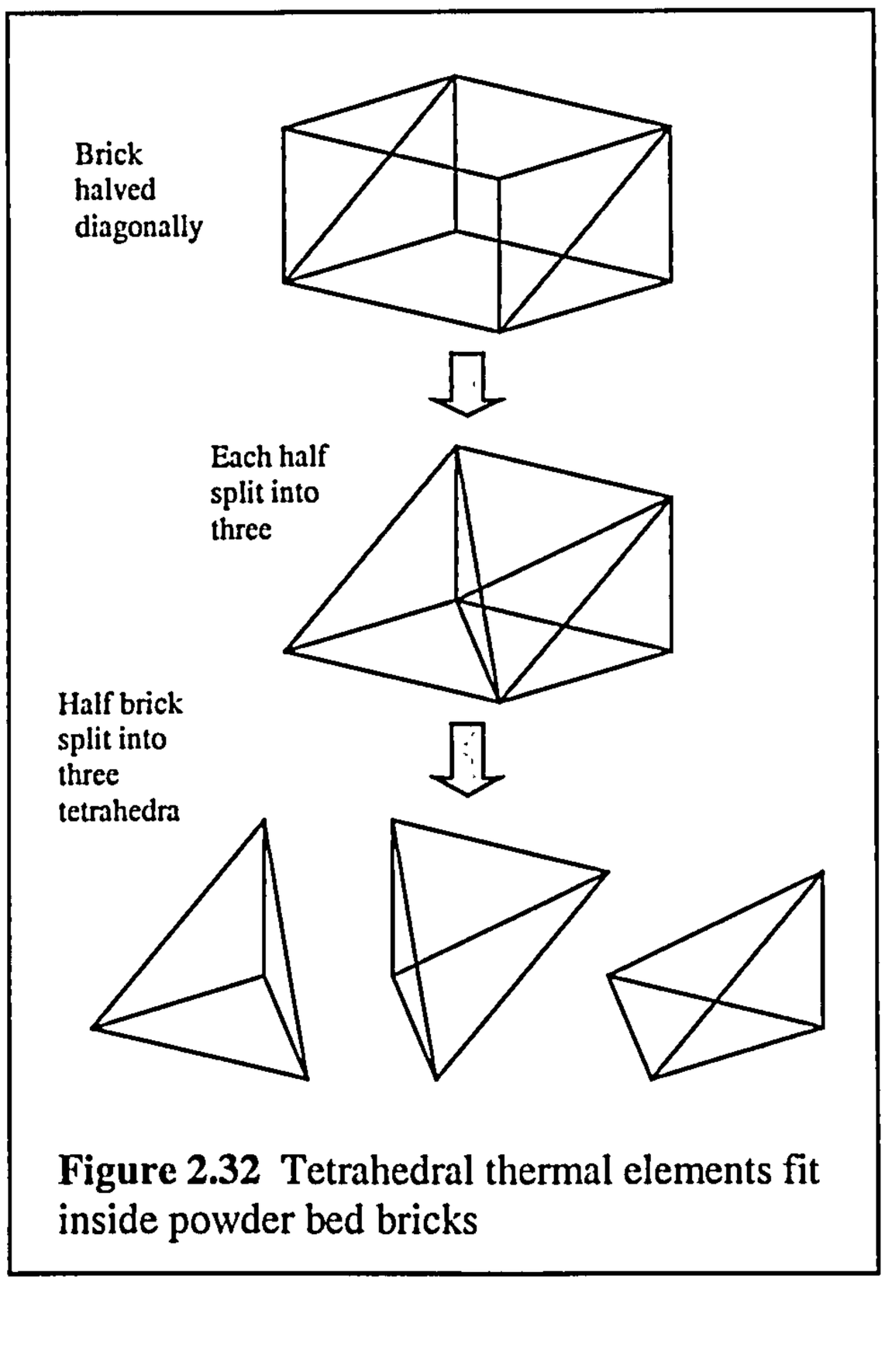

Figure 2.32 Tetrahedral thermal elements fit inside powder bed bricks

2.5.2.2 Procedure

An overview of the procedure in program *stmet3d* is provided in the flow diagram Figure 2.33. This figure is adapted from Childs' flow diagram for 2D modelling of polymer SLS [Childs 1998, Tontowi 2000].

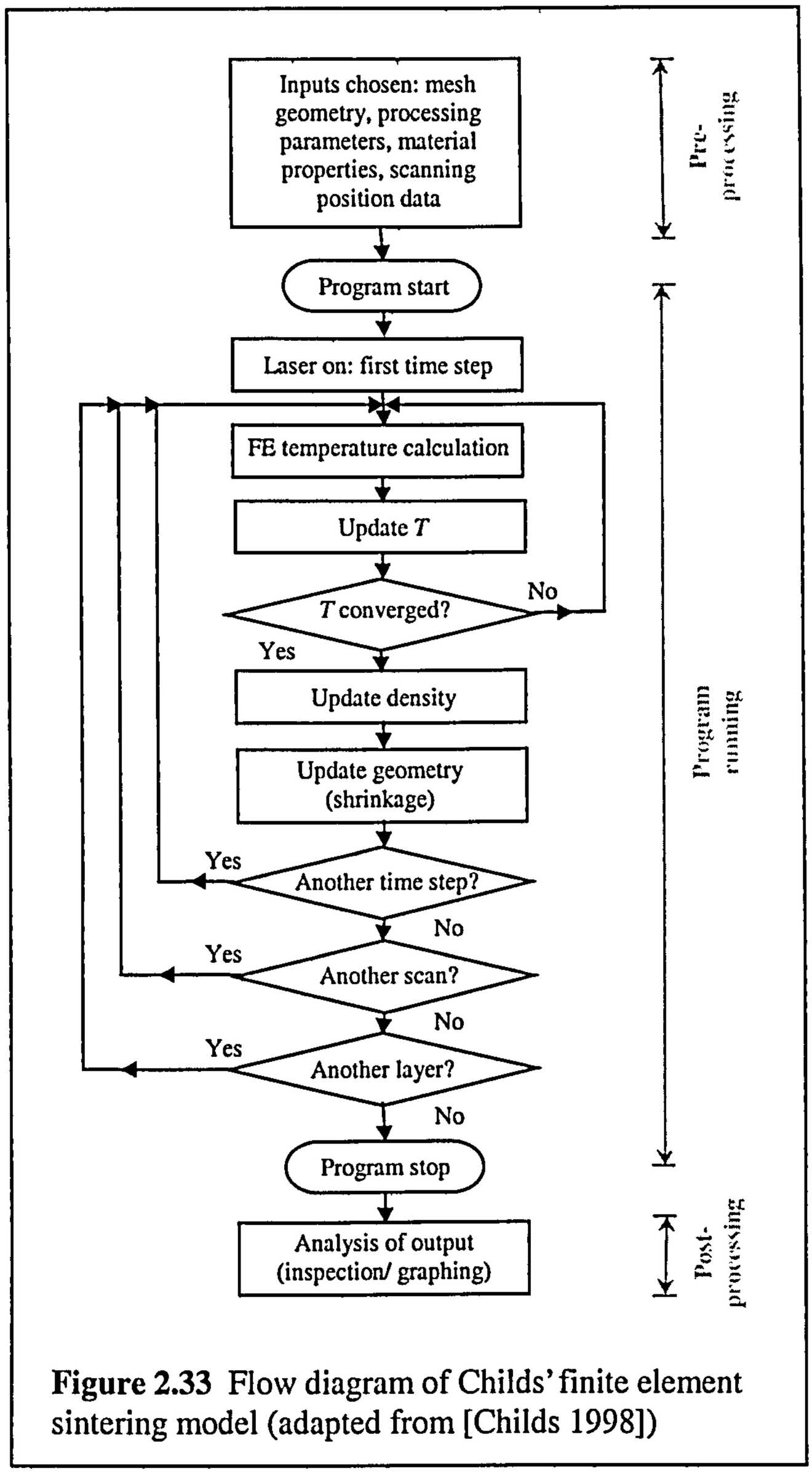

Figure 2.33 Flow diagram of Childs' finite element sintering model (adapted from [Childs 1998])

Pre-processing involves customisation of an input data file (defining the two meshes, material properties, scanning parameters and start/ stop positions). If mesh definitions are to be changed, new parameter values must be calculated to replace current ones in the program listing. Also, changes in the size of the TM and PBM meshes affect the size of parts which can be modelled.

Once the program is executed, it reads the input file. Meshes are then initialised: their nodal positions, the relationship between TM nodes and elements and the relationship between the TM and PBM nodes are specified. TM boundary

conditions and initial nodal values are set: for instance density throughout the PBM is set to that of fresh powder. For the 100 heat input elements, heat transfer coefficient and energy input profile against position are set.

The TM begins to move through the PBM, at a rate of one PBM mesh spacing per heat step. The time per heat step *DTIME* is chosen to meet this criterion. In each heat step, the TM copies, operates on then returns selected PBM values. A heat calculation produces a new temperature distribution in the TM. Material density is then calculated based on temperature: see 2.5.2.3 for the related equations. Nodal values from the TM are returned to the corresponding zone in the PBM.

In multiple heat steps, a complete line is scanned. Once a line has been scanned, the TM dwells without moving until all material has cooled to solidification point, i.e. the processed line has reached its final shape. After each scan and static dwell, the TM is translated to the starting position for the next scan and the process is repeated. TM movement through the PBM follows a unidirectional rastering pattern, with a constant spacing between scans (see Figure 2.15). The intensity of the heat input distribution remains constant during marching, representing a beam of constant power perpendicular to the bed surface.

Overlapping line scans combine to create densified layers. Once a layer has been completed, a new unprocessed layer is added on top. Layers accumulate into complete parts.

To carry out the heat calculation in the TM, a heat transfer stiffness matrix with cofactors is set up. Thermal properties C and k are recalculated at each heat step based on nodal temperature (for C and k) and density (for k). Matrices containing many simultaneous temperature equations are solved by a lower upper decomposition method [Ralston 1978]. A recent development in the program *stmet3d* is reduction to sparse format of the matrices to be solved. Values deemed insignificant are dropped by a preconditioner, then the matrix is solved by an algorithm known as GMRES. A reduction of memory usage and increase in processing speed is expected. More can be found on GMRES in [Saad 1985].

y direction (vertical) shrinkage is assumed to occur by conservation of mass as powder material turns to solid. Nodes are free to move in the *y* direction only. Shrinkage is calculated at every heat step. No mechanical analysis takes place: surface tension and residual stress effects are not considered.

Data is output to text files (known as "*Rhoplot*" files), consisting *x*, *y* and *z* coordinates, density and temperature data for each node in the processed volume of the PBM. Only the PBM nodes processed by the TM have their values output. Post-processing of output data either involves manual inspection of values, or execution of scripts on the visualisation package GSharp: described in Section 2.5.2.4.

The model has mostly been applied (by Childs and Tontowi) to polymer SLS in 2D until recently. Modelling of direct metal SLS is reported in 2.5.2.3 and 2.5.2.4.

2.5.2.3 Governing Equations

Within the program *stmet3d* there are sub-models which describe phenomena in the thermal mesh. They are described by the equations below.

In the majority of the powder bed conduction heat transfer dominates, described by Fourier's Law equation (2.16). Laser beam irradiance across the bed surface follows a discretised Gaussian distribution, described by equation (2.10).

Beam irradiance reduces with depth into the bed, as dictated by the equation:

$$DFRAC = DPA.DYAV.\left(\frac{\rho_r}{1-\rho_r}\right)^{DPN} \qquad (2.23)$$

Where *DFRAC* is the fraction of laser energy received, *DYAV* is depth in the bed, ρ_r is relative density and *DPA*/ *DPN* are experimental constants.

Powder *k* is calculated as a function of temperature *T* in K and porosity φ,

$$k_{S,T} = T.CONDV + CONDO \qquad (2.24),$$

$$k = k_{S,T}.\left(\frac{1-\varphi}{1+SIGV1.\varphi^{SIGV2}}\right) \qquad (2.25)$$

Where subscript *S* denotes solid material, and *T* means on account of temperature. *CONDV*, *CONDO*, *SIGV1* and *SIGV2* are experimentally-determined constants (taken from literature) for solid material.

Powder C is calculated as a function of T in K,

$$C = CAPO + CAPV.T \qquad (2.26)$$

Where *CAPV and CAPO* are experimentally-determined material constants.

Values of C and k as linear functions of T agree well with values found in literature [Auburn 2001].

For metal alloys, the solid fraction χ is assumed to vary linearly between 1 and 0 as temperature increases from the solidus to the liquidus value for the alloy.

$$\chi = \frac{T_m - T}{T_m - T_s} \qquad (2.27)$$

Where T_m and T_s are the liquidus and solidus temperatures respectively. A temperature recovery method [Childs 2000] reduces material temperature in exchange for latent heat of melting.

The densification law used in the program is tailored to the direct processing of single-phase metals. Density is assumed to change instantaneously and irreversibly, dependent on solid fraction χ:

$$\rho = \rho_{MAX}.(RT1 + RT2.[\tanh(5(1-\chi))]^4) \qquad (2.28)$$

Where ρ_{MAX} is solid density, *RT1* is the bed porosity and *RT2* equals (1-*RT1*). The tanh function and parameters 5 and 4 are chosen such that for χ above 0.7, almost no densification occurs. The variation of density as a function of χ is based on the way in which the viscosity of metals varies with χ [Childs 2000].

2.5.2.4 Post Processing and Verification of Model Output

Model output data are density and temperature values calculated at x, y and z positions in the powder bed. [Tontowi 2000] used the software Unimap to generate 2D contour plots of temperature T and density ρ data. Then [Volpato 2001] used the later software package GSharp Version 3.1, by Advanced Visual Systems, to achieve the same end. 3D arrays of T and ρ could be viewed in cross-sectional planes. Contour plots of ρ were used to examine the modelled part, once

a decision was taken about what value of ρ represented the transition from loose powder to solid material. Examples of modelled part cross-sections are found in Tontowi and Volpato's work. One is shown in Figure 2.17, Section 2.2.6.2.

[Childs 2001] compared modelled and experimental output for the direct room temperature SLS of stainless steel powder with a CO_2 laser. Processed track size was examined. Track widths in the model and experiments were similar if absorptance α in the model was set between 0.26 and 0.41.

[Laoui 2000] tested the model for tungsten carbide powder processed with an Nd:YAG laser. α was set at 0.8, based on experiments. He found that the model performed relatively poorly at low P and U >5mm/s, under-predicting the material melted. Predictions would have been better if the assumed conductivity could be lowered.

2.5.3 Other Numerical Models

Models which perform thermal and stress analyses have been studied, as they are applied to processes like SLS, laser cladding and laser welding. Some of these models have been described in previous sections, and so are referred back to.

In general, models of 3D Systems type SLS incorporate time-dependent viscous sintering laws as described in Section 2.4.1. Material density increases in the order of 20 percent during the 3D Systems process [Beaman 1997]. By contrast, in direct laser processing of single-phase metals, authors have chosen to relate material density to temperature or energy absorbed without the influence of time. Density can increase by large amounts, doubling in the case of [Morgan 2001b].

[Yevko 1998] and [Kaplan 2001] model laser cladding. Yevko uses 3D FD to evaluate the powder temperature distribution caused by a scanning surface power source. The volume of powder at $T > T_m$ is considered to have melted, solidifying to form an assumed clad shape. This shape is then shrunk to represent densification. Kaplan assumes an analytical T field as proposed in 2.3.4.2, providing an estimate of melt pool width and height. As Yevko, Kaplan assumes a shape for the melted material: in this case a parabolic function gives layer height with respect to position. Integration of the function provides clad cross-sectional area. Kaplan incorporated latent heat, Yevko disregarded it.

The model of [Laoui 2000] has been covered in 2.3.1.2. Ray-tracing leads to a profile of laser irradiance against position. An area solidifies if exposed to irradiance above a certain threshold. Conduction heat transfer is not considered.

[Ho 1995], [Weissman 1991] and [Williams 1996] used 1-dimensional FD thermal models to simulate laser processing. These models could only describe simple situations. Temperature profiles against time were examined. [Boddu 2003] and [Landers 2003] created analytical, dynamic models of laser processing of metal. These models were designed to provide rapid results, for real-time feedback control. They relate melt pool temperature and morphology to inputs such as laser power.

[Vasinonta 2000] used a 2D thermal FE model to construct process maps for better temperature gradient control. [Bontha 2003] continued this work by using modelled cooling rates and temperature gradients at the onset of molten metal solidification to predict the microstructure of laser-processed titanium alloy. [Tolochko 2003b] created a 2D model concerning heat transfer and densification in SLS. Laser penetration into the powder bed was considered negligible, so all heat was delivered to the bed's surface.

[Bugeda 1999], [Flach 1997], [Sun 1991], [Steinberger 2000], [Papadatos 1997] and [Dai 2003a and b] constructed 3D models of SFF processes. 3D models are better able to deal with edge effects than 1D or 2D [Tontowi 2001]. Sun and Steinberger report optical, thermal and rheological sub-models. Thermal and rheological models are similar to those already reported, but optical (laser radiation) models are unique, even compared to those of Laoui and Childs. Flach verified his model by comparing calculated temperatures with those measured by thermocouple. Steinberger and Dai compared surface temperatures using a pyrometer. [Tolochko 2003b] compared the dimensions of real and modelled parts.

Modelling workers may or may not include the change of thermophysical properties with temperature and porosity: where change is not implemented, an average value is used. Similarly, conduction and radiation heat loss to the surroundings may or may not be considered: authors' views are recorded in 2.3.3.

[Dalgarno 1996], [Jiang 2002] and [Matsumoto 2001] used FE to perform stress analyses on simple modelled parts. Dalgarno studied curl in polycarbonate parts. He added layers, then applied compressive strains to them to represent thermal contraction. Jiang extracted temperatures and sintered geometry from Childs' thermal SLS model at different points in time, to study the evolution of residual stress and deformation. Elastic deformation occurred on cooling. Thermal stresses found were six times higher in the scanning direction than in other directions. Matsumoto used a coupled heat conduction and stress model. The pattern of tensile and compressive residual stresses was studied. 3 sets of thermophysical properties were used, to represent powder, liquid and solid states.

2.5.4 Summary of Modelling Investigation

Finite element and finite difference methods are commonly used to model physical systems, by breaking them down into discrete units. Childs' finite element model simulates direct SLS of metal powders, in three dimensions. Laser energy follows a Gaussian surface profile, and an exponential depth profile. Material temperature, density, thermal conductivity and specific heat all change with position and time. Multiple layer parts can be scanned in discrete spatial steps. Processing parameters, material properties and part geometry are input to the model; density and temperature data versus position are output.

A new system has been implemented to simplify thermal matrices for solution. Changes in the capability and validity of the model under the new system should be tested. Post-processing of model output consists of manual inspection, or 2D visualisation. Limited morphological comparisons have been made between model output and the physical output from the SLS machine.

Other models of laser processing have been examined to see their scope and assumptions. Different methods of deciding the cross-sectional shape of processed tracks have been observed.

2.6 The Future of SFF- Means of Achieving Aims

Some of the goals currently driving SFF are identified, then the means by which to achieve these goals are discussed.

Ever-present in solid freeform fabrication is the need to increase process speed [Wohlers 1999, Kruth 1998]. Increased speed must not detract from the quality of processed parts however. Wohlers believes that in rapid tooling, geometrical properties are in need of improvement: namely dimensional accuracy, flatness, surface finish and mould size. [Hunt 2001] has identified accuracy and finish as key qualities to improve in SFF. A common cause of accuracy issues is the heterogeneity of process conditions, discussed at length in Section 2.2.6.3. Effects include thermal distortion whilst cooling [Deckard 1995].

[Nelson 1992] and [Dai 2003a] identify the need for powder material characterisation: a knowledge of thermophysical properties, guiding machine parameter changes to accommodate new materials. New processes and materials can increase the applications for SFF technology [Calder 2001].

Means by which SFF processes have been improved in the past include hardware redesign, such as the use of polygonal laser scanning mirrors to reduce necessary rotation angles (Figure 2.34 derived from [Steen 1998]), or the dual beam heating method from [Benda 1994]. Powders have been redesigned too, optimising particle diameter [Karapatis 1998b, Boivie 2003] or alloying to improve processing properties [Agarwala 1995a]. SFF process speed can be increased by introducing multiple, parallel processing tools. Multi-material SFF is now meeting new requirements in medical and electronic fields of work [Calder 2001].

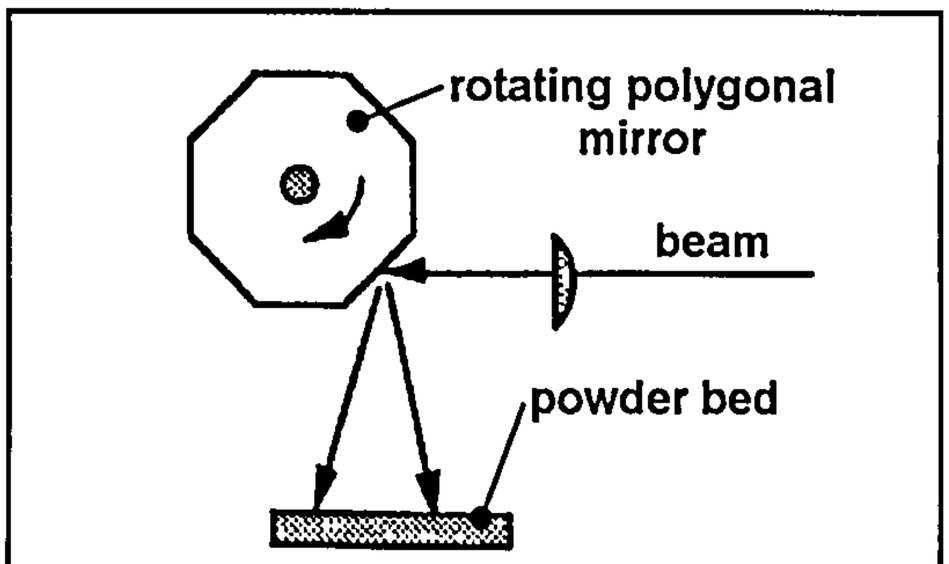

Figure 2.34 Polygonal scanning mirror

Many authors suggest that to optimise both geometrical and mechanical part properties, better process control is required [Dai 2003b, Griffith 1998, Williams

1998]: in particular, better thermal control [Eyerer 1994, Vasinonta 1999, Bontha 2003]. Heterogeneous processing conditions mentioned can be countered through feed-forward or feedback control systems.

A feed-forward system uses a process model such as those reviewed in 2.5 to predict part properties for a given set of machine input parameters. Optimum input values can be iterated towards as the model runs repeatedly with the machine off-line, before any parts are made. [Papadatos 1998] proposes using this system to vary laser power settings during a build.

A feedback system uses closed loop (CL) feedback to adapt machine parameters in real time during processing. Sensors report values such as temperature or melt pool height to a controller, which acts to moderate build conditions [Landers 2003]. Benda and Eyerer successfully implemented CL temperature control through laser power adaptation. A plant model can be incorporated in CL control to explain how measured and controlled quantities relate to each other. This model should be simple and analytical, argue [Tsai 2000] and [Boddu 2003], because a numerical calculation would be too time-consuming to apply to on-line control of laser processing. More information on current control technology can be found in [Steen 1998].

[Prakash 2003] conducted a Taguchi study on an SFF process. The build rate, hardness and porosity of parts was compared against six machine input parameters. Such a study can identify optimum parameter values, and reveal the relative importance of each.

2.7 Summary of Literature Survey

SFF processes provide a modern solution to rapid product development and rapid tooling needs. Freeform geometrical shapes are created in a layer-by-layer fashion. SLS is a type of SFF process, which uses a scanning laser to selectively fuse material powder. A three-dimensional structure is formed. Metal parts may be infiltrated during a post process, or may be made directly. The latter option is faster. A machine has been built at Leeds University for direct SLS of room-temperature stainless steel powder. This machine has been used to research the effect of atmosphere and certain other machine parameters.

Generic research into SLS process parameters has been reviewed. One means of relating part qualities to input parameters is process mapping, covered in Section 2.2.6.1. It is discovered that direct SLS of room temperature steel involves material being melted, and a temperature rise of over 1000°C in under 1 second. Direct SLS parts display characteristic features, such as a reduction in scan depth from the first to the second and following scans in a layer. Features such as this can compromise part accuracy. The cross-sectional shape of scans can change, depending on laser power and speed.

The scanning laser beam delivers energy to the powder bed as electromagnetic radiation. A certain percentage is absorbed into the bed, the remainder is reflected away. The absorbed heat melts the powder, or may be lost to the surroundings by conduction, convection and thermal radiation modes. Models of heat transfer applicable to SLS were considered. Powder absorptance was reported to change with porosity. Knowledge of powder material thermal properties can aid understanding of heat transfer in the process.

Methods of measuring powder bed absorptance and conductivity are reviewed. It was observed that there was a lack of data derived in the conditions specific to a laser beam scanning metal powder of changing porosity in an argon atmosphere. The density of SLS materials increases as they are processed. In solid phase sintering, densification occurs below the melting temperature over hours' duration. For this reason, densification models which assume instantaneous density changes are considered more appropriate than models of time-dependent viscous sintering. Surface tension acts in the molten state to drive material into a balled shape.

A 3D finite element Fortran model has been written by Childs, to simulate direct SLS of metals. Heat transfer and densification sub-models are included. Machine and material parameters are input into the model, density and temperature values against position are output. A change made to the model (the use of sparse matrices) remains to be tested. Morphological comparisons between real and modelled parts are limited to date.

Authors suggest that the SLS process may be developed further by increasing the process speed, improving dimensional accuracy and surface finish, and by characterisation of powder materials used. Methods of improving the process include hardware redesign and better process control. Process control involves adaptation of machine parameters for optimal performance.

2.8 Aims of Work Reported in This Thesis

Given the information which is presented in this chapter, opportunities to develop the direct metal SLS process have been identified. It is intended to study the thermal situation occurring during direct SLS of single-phase metals, to increase understanding. The Leeds experimental SLS station described in Section 2.2.4 will be used for this purpose.

As a part of this study, the thermal properties conductivity k and absorptance α of metal powder will be measured under conditions typically encountered in direct SLS. The effect (if any) of the main machine parameters on material k and α values will be checked. It is known that layers made from several parallel, overlapping scans are affected by the change in k and α of processed material as opposed to fresh powder, mentioned in 2.2.6. It is intended to investigate this property change and its effect. A study of the mass and shape of tracks processed at different powers and speeds will be undertaken, following on from Hauser's work reported in 2.2.6.3 and 2.3.1.1.

Development and further verification work will be done on the Fortran numerical model of the SLS process, *stmet3d*. Opportunities have been identified to ease the preparation of model input data. Communication of the model's progress during run time will be improved, as will the communication of output data. The nature and capability of the model in its sparse matrix-using form will be recording and tested, via process mapping and a morphological comparison of modelled and manufactured parts.

Verification of the model *stmet3d* is seen as a step towards use of the model for feed-forward process control (FFPC), to help refine the direct SLS process.

CHAPTER THREE

3 HEAT TRANSFER EXPERIMENTS

The findings of Chapter 2 have suggested some opportunities to develop understanding of heat transfer in direct single-phase metal SLS. The theory and intentions behind experiments are explained, then experimental equipment and procedure are detailed.

3.1 Introduction

Thermal experiments will focus on the manufacture of single lines and layers of material. In Section 3.2, an opportunity is recognised to find the conductivity k and absorptance α of a powder via an equation first introduced in Section 2.3.4.2. Both properties are found through measurement of temperature in the powder bed. An investigation of transient state effects in SLS has been undertaken, reported in Section 2.2.6.3. The thermal aspects of transient behaviour in direct single-phase metal SLS are studied in this chapter.

The Leeds experimental SLS rig is described in more detail in Section 3.3. The materials to be tested are specified in 3.4.

Two quite different systems were used to measure temperature against position and time in the material powder bed whilst a laser beam scanned the bed's surface. These two methods required apparatus constructed from existing and custom-designed components. A specification and description of components for each of the two measurement systems appears in Sections 3.5 and 3.6.

An evaporation study explained in Sections 3.7 and 3.13 looks at what happens to the mass and shape of processed tracks created at different powers and speeds. The study is based on Hauser's track cross-sectional profiles of Section 2.2.6.2.

Section 3.8 provides information on the setting up of experiments. In Section 3.9, powder bed density measurement is described. 3.10, 3.11 and 3.12 describe a series of thermal experiments. Each experiment required the collection of up to 45 individual results, therefore multiple runs were involved. A run is one measurement cycle. A full listing of the experimental runs undertaken in 3.10, 3.11 and 3.12 is found in Appendix A.

Simple but fundamental observations about the laser-induced thermal field in the powder bed are made in Sections 3.10 and 3.11, the results of which were used to refine the design of experimental equipment and to refine the procedure for Section 3.12. Experiments were carried out over a range of scanning parameters (power P, scan speed U and scan spacing s) and powder sizes, in an ambient and inert atmosphere. During contact temperature measurement experiments, data was collected at a high sample rate on multiple channels. To increase the speed of selecting out relevant values from data files storing hundreds of numbers, a computer program was written to automate the task.

Sections 3.14 and 3.15 explain the manufacture and sectioning of single layer parts for comparison with numerical model output. Parts were made then sectioned in order to compare them dimensionally with output from the numerical model of the process, *stmet3d*. In 3.15, two preliminary studies are discussed. A method was developed for dimensional analysis of part cross-sections, and the SLS machine's flexibility was tested with a view to varying the laser power setting for each individual scan. The work of 3.14 and 3.15 support the notion reported in Section 2.8, of testing the validity of the model and working towards feed forward SLS process control.

In most experiments, only one powder was used: stainless steel 314S HC with particle size interval 75-150μm. In Section 3.12 however, the thermal properties of 314S HC and two further materials are calculated.

Treatment of data gathered from the work described in this chapter can be found in Section 5.1. Results are presented and discussed in Chapter 6.

3.2 Theory- Use of Carslaw and Jaeger's Equation to Calculate Thermal Properties

Following on from the research of Chapter 2, some means is required to find material thermal properties in a situation representative of SLS. It is desired to see how material absorptance changes in different processing situations.

Carslaw and Jaeger's equation (2.20) of Section 2.3.4.2 describes the temperature rise occurring in an infinitely large body due to the application of an

instantaneous, infinitely long line heat source, analogous to SLS. This equation has been chosen in preference over the other analytical models studied in 2.3.4.2. Carslaw and Jaeger's equation can express temperature as a function of P, U, α, k, t and y after manipulation (see below). It approximates the form of a moving heat source, without the use of integrals or error functions.

In SLS the heat source is applied at the powder bed surface, so the equation has been manipulated. Figure 3.1 depicts the situation represented. The co-ordinate system of equation (2.20) has been altered to be consistent with the modelling work described in the next chapter. The infinite body is split in half, to exist only where $y \geq 0$. No heat may leave the body, so the source strength Q represents that laser energy which is absorbed into the bed. If the uniform initial temperature in the body is non-zero, then it is best to replace the temperature term T with dT, or temperature rise. If the infinite line heat source is imagined to run along the x-axis (y and z equal to zero) on the surface of what is now a semi-infinite body, twice the amount of heat will be supplied to the remaining half of the body, i.e.

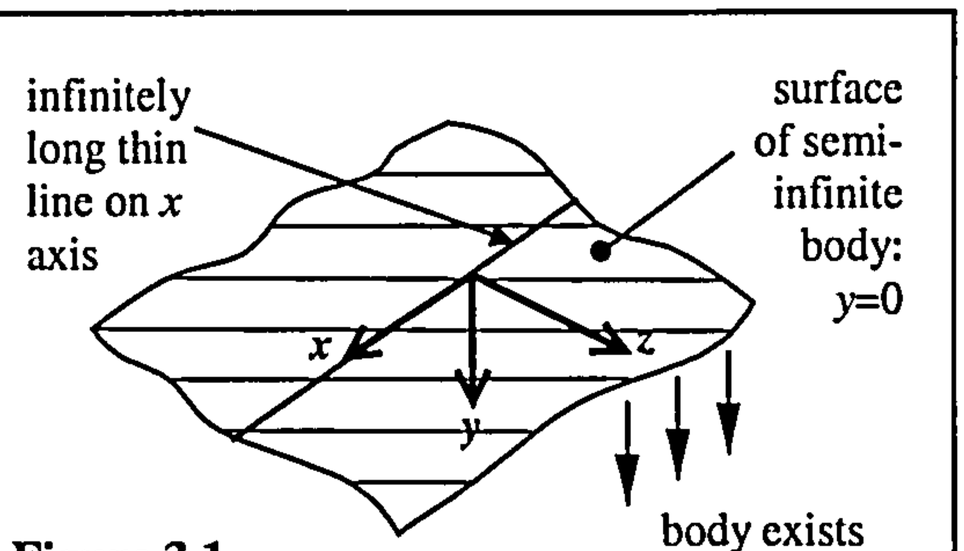

Figure 3.1
Visualisation of line heat source system [Carslaw 1959]

$$dT = \frac{Q}{2.\pi.\kappa.t} e^{-\left(\frac{y^2+z^2}{4.\kappa.t}\right)} \qquad (3.1)$$

Where dT is the temperature rise in the body at a specified position and time, t is time elapsed since the instantaneous application of heat, y and z are distances from the line in the y and z directions and κ is the diffusivity of the powder bed.

For positions vertically below this line source (i.e. z=0):

$$dT = \frac{Q}{2.\pi.\kappa.t} e^{-\left(\frac{y^2}{4.\kappa.t}\right)} \qquad (3.2)$$

Differentiating with respect to t at constant y,

$$\left.\frac{d(dT)}{dt}\right|_{y=const.} = \frac{-Q}{2\pi.\kappa.t^2}.e^{\left(\frac{-y^2}{4\kappa.t}\right)} + \frac{Q}{2\pi.\kappa.t}.e^{\left(\frac{-y^2}{4\kappa.t}\right)}.\frac{y^2}{4\kappa.t^2} \qquad (3.3)$$

Equating equation (3.3) to zero, the time to reach maximum temperature at a specific point, t_{Tmax}, is introduced:

$$t_{T\max} = \frac{y^2}{4\kappa} \tag{3.4}$$

Where diffusivity κ is related to conductivity k, powder density ρ and specific heat C as shown:

$$\kappa = \frac{k}{\rho.C} \tag{3.5}$$

Absorbed power P_A is the product of input laser power P and material absorptance α:

$$P_A = P.\alpha \tag{3.6}$$

Source strength Q is related to energy absorbed into the powder bed as follows:

$$\text{Energy input per unit length} = Q.\rho.C \tag{3.7}$$

So for a laser source, moving with speed U:

$$\frac{P_A}{U} = Q.\rho.C \tag{3.8}$$

Substituting t for t_{Tmax}, equation (3.4), Q, equation (3.2) and P_A, equation (3.6) into (3.8), an expression for the maximum temperature rise dT_{max} is derived:

$$dT_{\max} = \frac{0.234\alpha.P}{U.\rho.C.y^2} \tag{3.9}$$

Equations (3.4) and (3.9) provide a means by which both the conductivity k and absorptance α of the powder being tested may be evaluated. All other quantities appearing in these equations can be set or measured. Temperature readings taken at points of different depth in the bed and at different values of laser power and scan speed are to be analysed. The method is tested first, then used to learn more about property changes in the direct single-phase metal SLS process.

Equations (3.4) and (3.9) assume a line heat source which is infinitely thin; in the SLS process a laser beam with a finite diameter d is used. It is anticipated that at depths into the powder bed which are less than the beam radius ($d/2$), temperature profiles would come to resemble those found for a plane heat source. For this reason, temperature measurements will be made at depths which are at

least several times d. At such depths, temperature profiles will approach those of an infinitely thin source.

[Chen 1983] studied a situation similar to that of Carslaw and Jaeger. He looked at the shape of temperature fields in relation to the speed of movement of a Gaussian surface heat source. The approximation to a line heat source is believed to be acceptable, given that the condition set by Chen is observed: if $U > 2.\kappa / d$, the temperature field appears like that occurring due to a line heat source rather than a point heat source. d is the laser beam diameter. For stainless steel 314S powder properties (which are reported in Chapter 7), diffusivity κ equals 7.4×10^{-8} m^2/s. The beam diameter d is 1.1mm, so $2.\kappa / d = 0.13$mm/s. Provided that a laser scanning speed U well above 0.13mm/s is maintained in experiments, the condition is met.

Carslaw and Jaeger provide an equation similar to (2.20) to describe the situation of an instantaneous, infinitely large plane heat source. This equation can be manipulated in the same way as was demonstrated in the derivation of equations (3.4) and (3.9). The infinite plane equations below are useful in representing the scanning of single layers:

$$dT = \frac{Q'}{2\sqrt{\pi.\kappa.t}} e^{-\left(\frac{y^2}{4.\kappa.t}\right)} \tag{3.10}$$

Source strength Q' is the heat flux per unit area of the plane, divided by $\rho.C$. Ways of expressing energy input per unit area are equated below, incorporating scan spacing s:

$$\frac{\alpha.P}{U.s} = Q'.\rho.C \tag{3.11}$$

Leading to two equations from which k and α can be found:

$$t_{T\max} = \frac{y^2}{2\kappa} \tag{3.12}$$

$$dT_{\max} = \frac{0.484\alpha.P}{U.\rho.C.s.y} \tag{3.13}$$

3.3 Existing Experimental Equipment- SLS Rig

This section further describes the equipment introduced in Section 2.2.4. The figure 3.2 shows a schematic layout of the system.

Laser power is provided by two Synrad 120W continuous-wave CO_2 lasers, with beams combined to create 240W power capacity. The combined beam passes through a beam expander (type V+S Scientific BEZ-10) which increases the beam diameter from 4.4mm to 18mm. The beam is then focussed, and begins to converge (decrease in diameter). The beam is reflected by two galvanometer-controlled mirrors rotating about perpendicular axes, directing it through a window into the SLS processing chamber. The rotation of the mirrors directs the beam across the surface of the material powder bed. The beam diameter at the bed's surface is 1.1mm. A refrigerator cools water which is circulated through the laser housings to cool them.

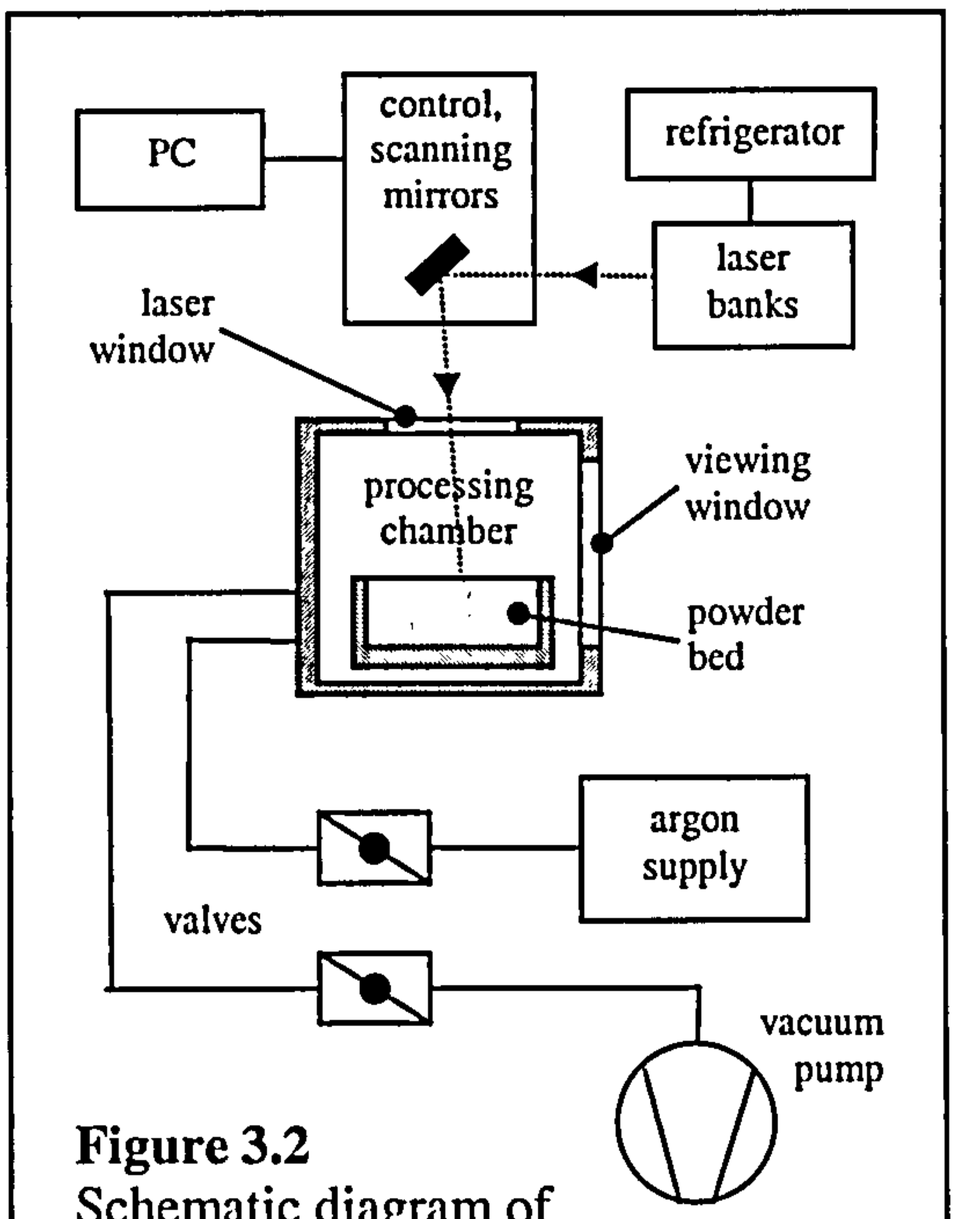

Figure 3.2
Schematic diagram of sintering rig system

Laser on or off switching and mirror rotation are controlled by a General Scanning 2-axis digital scanning controller. The galvanometers on which each mirror is mounted are position controlled in a closed loop. The controller receives instruction from a PC, running *PC-Mark* software by General Scanning. The SLS machine user defines the geometry to be scanned with HPGL-type plotter code input into the PC. Scan speed U and power P can be assigned to sub-sections of the scanned geometry using *PC-Mark*. In all work reported here, U is assigned on the PC whilst P is set manually using a dial. Scan speed up to 1000mm/s is available.

Figure 3.3 shows the processing chamber in more detail. A window in the top of the chamber allows the laser beam to enter. The beam terminates at the powder bed, which is contained by a tray. Tray design is detailed in Section 3.5.2. The

tray is slotted into a holder assembly inside the chamber, allowing NC-controlled lateral movement during experiments. The holder is driven by a stepper motor through a lead screw. Vertical powder bed NC motion is available for manufacture of multiple layer parts, but is not used here. A removable, sealable viewing window allows the process to be observed, as well as providing access to the chamber between experiments.

A pump and argon bottle are attached to the chamber so that the air inside can be removed and replaced with an inert processing atmosphere. A meter displays the chamber pressure during the process. No powder preheating is provided, so the temperature throughout the powder bed is ambient when processing begins.

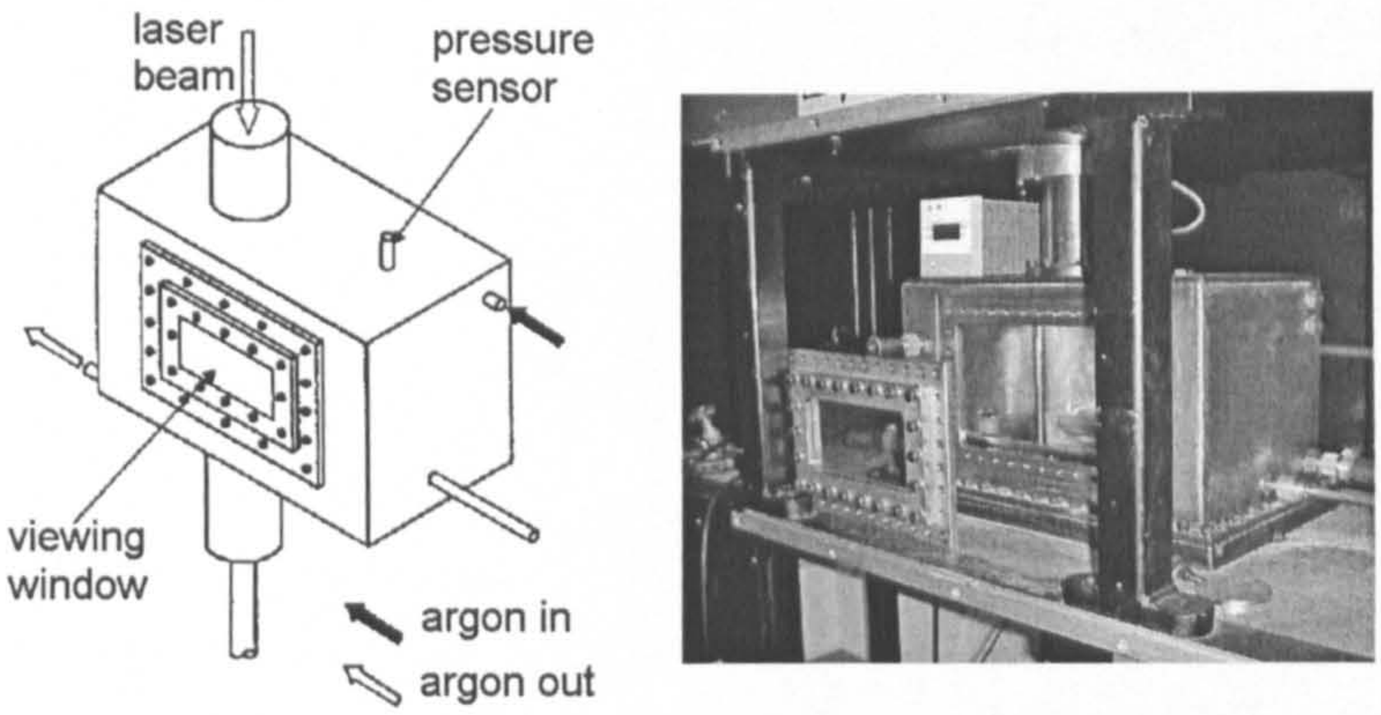

Figure 3.3 SLS processing chamber: diagram and photograph

3.4 Materials Tested

The powder used in most cases is Osprey Metals stainless steel 314S HC powder, with size distribution d_p between 75 and 150μm and constituents stated in Table 3.1. "Bal." means "balance", i.e. the remaining percentage.

Element	Fe	Ni	Cr	C	Si	P	Mn	S
Percent	Bal.	19.85	24.36	0.443	1.43	0.017	0.94	0.006

Table 3.1 Constituents of 314S HC stainless steel powder used

Element	Fe	Mo	Cr	C	Si	S	Mn	V	W	O
Percent	Bal.	5.15	4.1	0.92	0.5	0.01	0.05	6.5	6.5	0.09

Table 3.2 Constituents of M2 stainless steel powder used

Thermal property measurement (reported in 3.12) takes place for 314S of size distributions d_p 10-20μm, 75-150μm and 150-300μm, to see the effect of particle size on k and α. A cumulative frequency plot of d_p shows an approximately normal size distribution [Osprey 1997] for these samples. The polymer-coated steel powder developed for 3D Systems SLS, known as Rapid Steel 2, was tested in the same way. Rapid Steel 2 is stainless steel 316 with 3 percent polymer binder. The average particle diameter of Rapid Steel 2 is 30μm. Gas-atomised M2 stainless steel powder of size 75-150μm was also tested. The feasibility of testing the properties of water-atomised M2 steel powder of size 75-150μm was investigated. M2 steel has constituents as stated in Table 3.2.

3.5 Contact Temperature Measurement

The first temperature measurement method used was one in which a device is inserted in the measurement position. The merits of such a method are discussed below.

In the implementation of a contact temperature recording system, four functions had to be integrated. These were measurement and recording of temperature, containment of the powder bed, a measurement positioning system and a vacuum feed-through. A specification and solution for the temperature measurement and recording system follows in Section 3.5.1. The powder bed container, positioning system and vacuum feed-through are specified then realised in 3.5.2.

3.5.1 Specified Existing Equipment

A specification was drawn up for the temperature measurement and recording function:

- A sample time and response time below 1 second was considered necessary, due to the expected speed of temperature rise reported in Section 2.2.6.2;

- Also seen in Section 2.2.6.2, bed temperatures increase from ambient to steel melting point (around 1300°C). Ability to cover this temperature range is required;
- It is wished to observe the thermal field without disturbing it, so devices inserted into the bed must be of low mass. This also relates to device response time;
- Temperature reading accuracy should be within ±2 percent;
- Multiple readings should be taken simultaneously to save experimental time;
- The recording system should be portable;
- Output should be compatible with spreadsheet software for manipulation.

To measure temperatures occurring within the body of the powder bed, a device would have to be found which could be positioned at points within the bed. Resistance thermometers were considered, but type K thermocouples were chosen for their small junction size (low thermal inertia/ heat removal), high temperature ceiling (1250°C), and accuracy (quoted as ±1% if calibrated correctly). Thermocouples purchased came in the form of two conductors of diameter 0.3mm, sheathed in dual mineral insulation. They were sourced from RS, code 151-209. Junctions were spot-welded manually using an RS J60M instrument welder.

The recording system solution was a trolley-mounted PC. A National Instruments terminal block of type TBX-68T was connected to the PC via a NI4351 input card. The terminal block could accommodate 14 thermocouples simultaneously, with a resulting minimum sample time of 0.6 seconds. The PC ran National Instruments VirtualBench-Logger version 2.5 data logging software. Thermocouple readings could either be taken in degrees Celsius or volts DC. Temperature-time curves for each channel were displayed on screen during experiments. Data was output as a text file consisting a column for each channel and a row for each interval in time.

3.5.2 Custom-Designed Equipment

A new powder bed holding tray was deemed necessary for the purpose of temperature experiments. A tray specification was created:

- Large enough to be effectively infinite in size, i.e. no significant temperature rises at the walls;
- Should have flat upper faces to support manual spreading and flattening of the powder bed surface;
- Should fit into the holder assembly built into the chamber, and be of such dimensions that the powder bed surface is at the laser beam waist position vertically.

And for the measurement positioning system:

- Allow temperature measurement to take place at many (or any) positions;
- Facilitate the entry of temperature measurement devices into the bed;
- Support positioning of these devices with an accuracy of ±0.2mm.

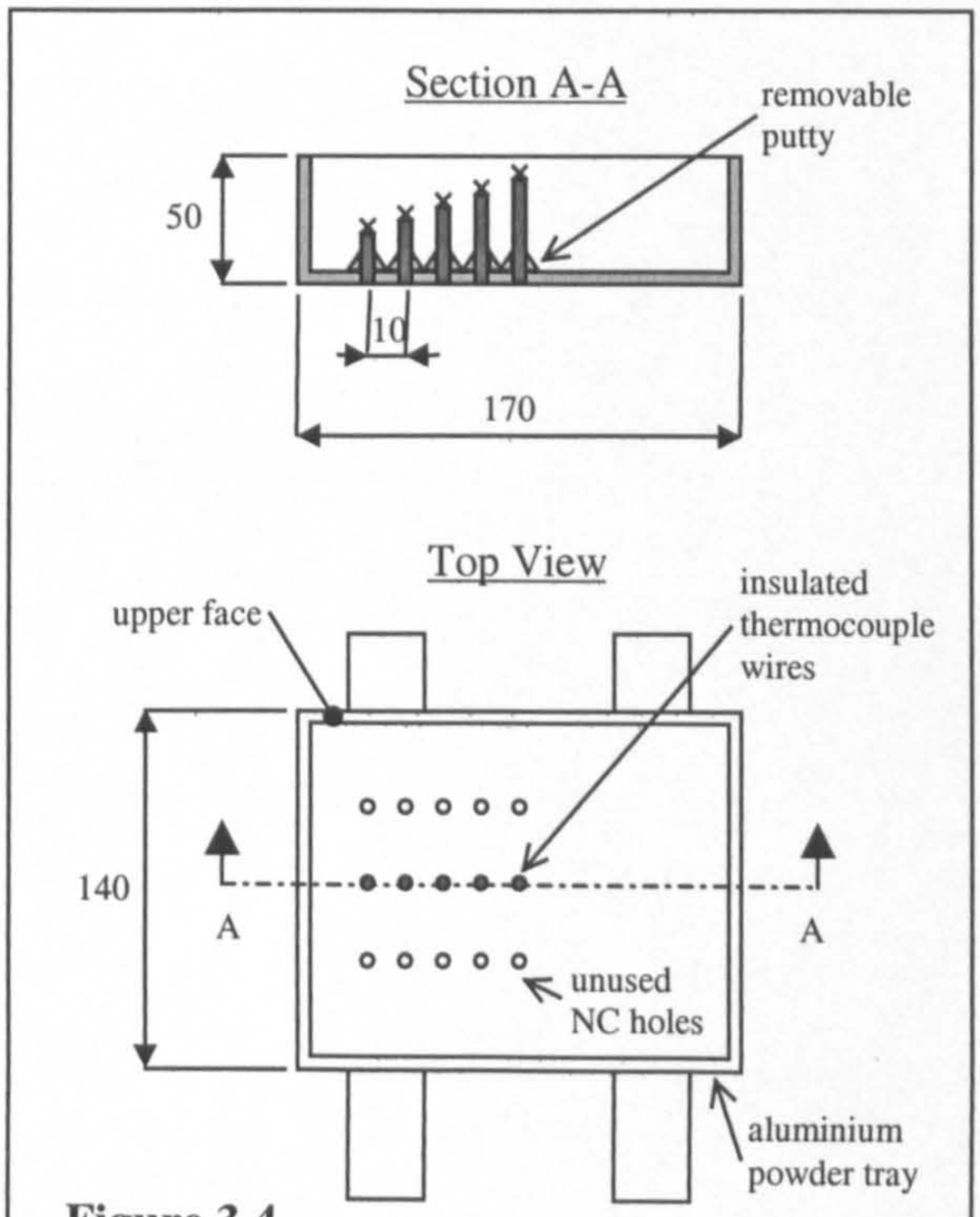

Figure 3.4
Temperature measurement tray **1**
All dimensions in mm

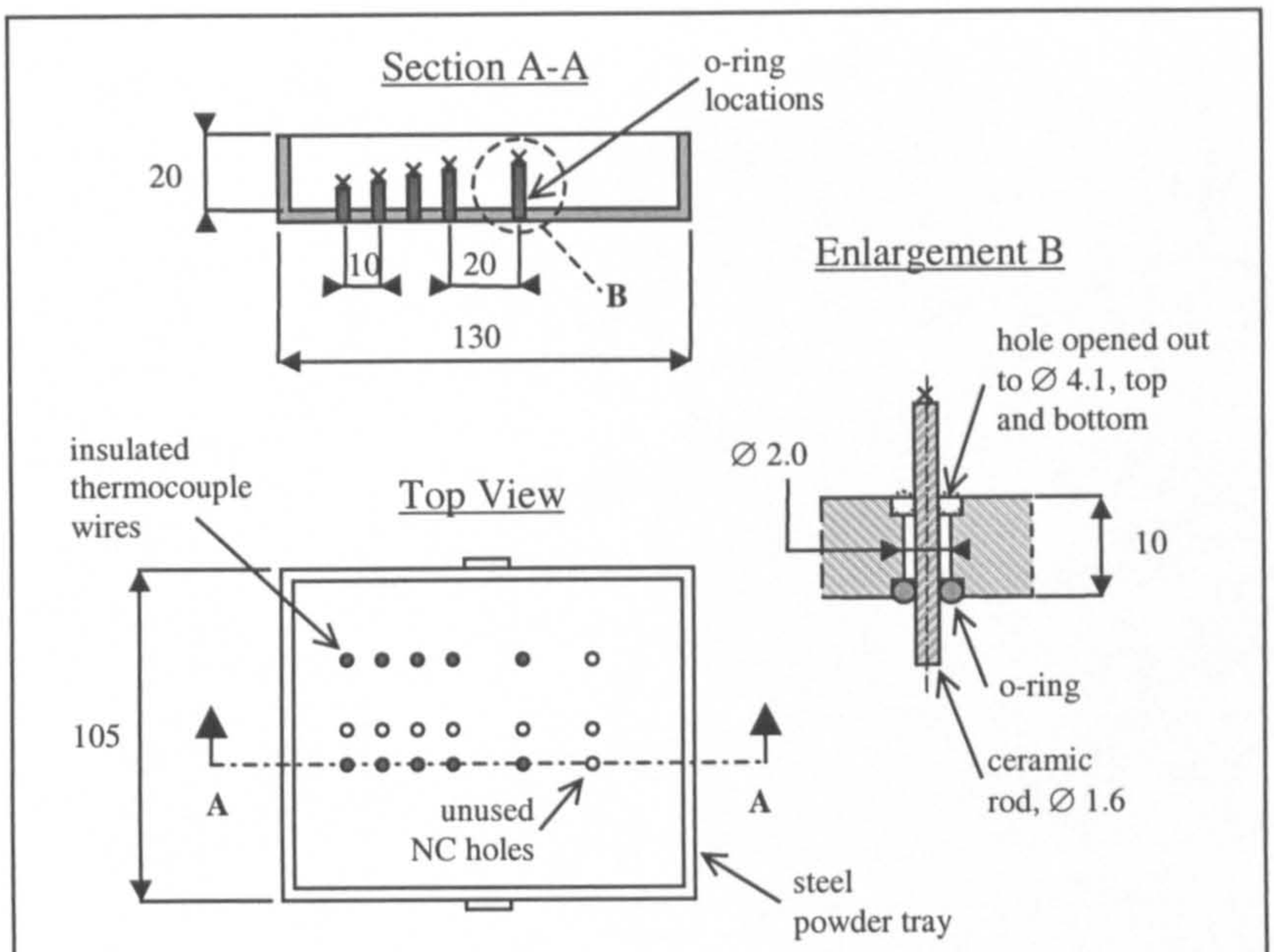

Figure 3.5 Temperature measurement tray **2**
All dimensions in mm

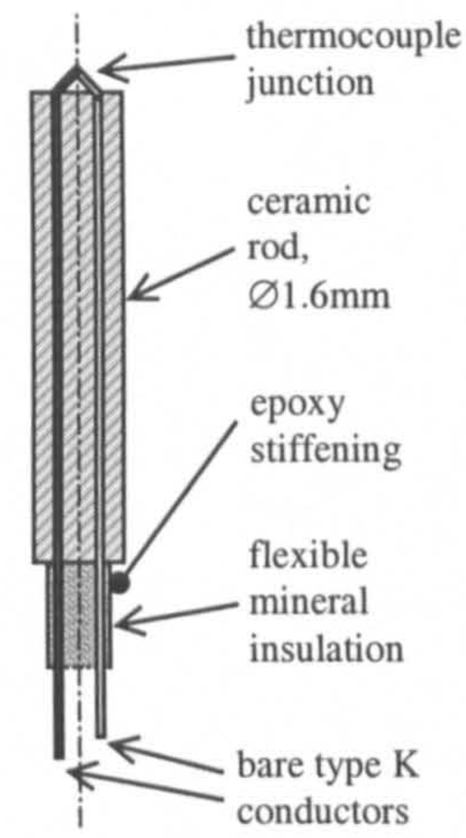

Figure 3.6
Ceramic rod with conductor wires

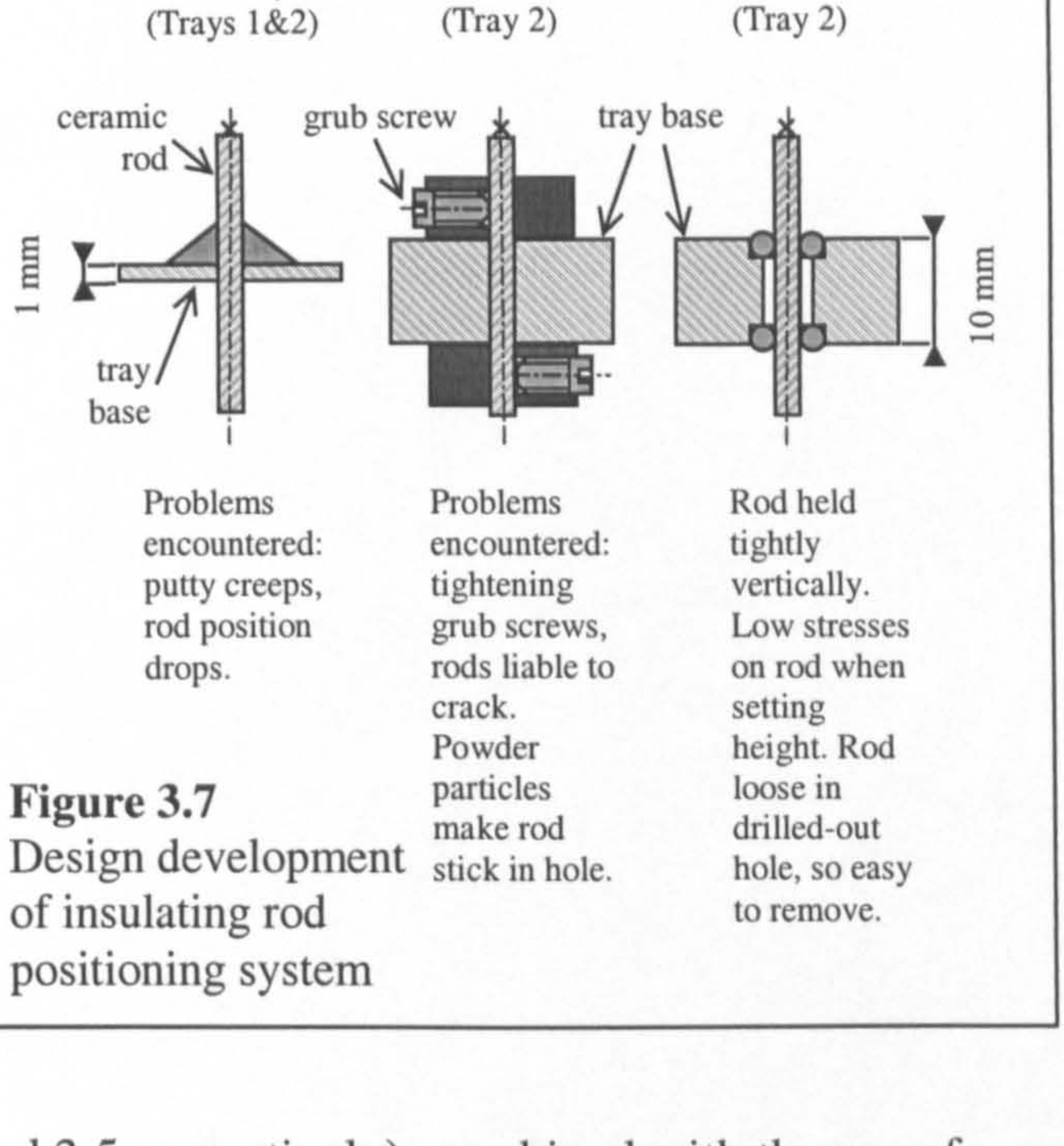

Figure 3.7
Design development of insulating rod positioning system

Trays 1 and 2 (Figures 3.4 and 3.5 respectively), combined with the use of ceramic rods were designed to meet the needs of powder bed containment and measurement positioning. Tray 2 is an improved design, based on feedback from tray 1. Ceramic rods of 1.6mm diameter were chosen to carry the thermocouple wires inside the powder bed tray, for a combination of reasons. These were

thermal and electrical insulation, temperature resistance and rigidity for accuracy of junction positioning. Each rod has two internal axial holes for the nickel-chromium and nickel-aluminium type K conductors. See Figure 3.6 to see how the thermocouple wires fit inside ceramic rods. Epoxy resin was used to stiffen the conductors at the transition between the insulation and ceramic rod because this was found to be a stress concentration point, at which the conductor snapped most often.

For tray 1, the resulting powder bed was 50mm deep. Tray 1 was constructed from bent and welded 3mm aluminium plate, with holes NC drilled into the base. Tray 1 was used for the thermal field and edge effects experiments of Sections 3.10 and 3.11. Three methods were used at different times to locate the ceramic rods into the NC holes of trays 1 and 2: see the diagram Figure 3.7 for a description. In tray 1, putty was used to vertically locate the thermocouple junctions (design A in Figure 3.7 and image (ii.) in Figure 3.8). This design gave rise to three issues relating to the accuracy of the measurement position: vertical movement of the ceramic rod due to creep of the putty over time, horizontal movement of the rod relative to the NC hole ("wobble") and poor perpendicularity of the tray bottom relative to the side walls as manufactured. Positional accuracy of the measurement position was estimated to be ±0.5mm.

Tray 2 had a powder bed depth of 20mm, which is less than half that of tray 1. The choice of depth was influenced by the results of a thermal field study, which will be described later in Section 3.10. The new tray is made from 9mm thick aluminium plates, milled then bolted together. This means that the new NC holes in the tray's base are 9mm deep. The shallower bed and deeper NC holes lead to higher horizontal precision of the measurement position. The tray is also shorter and narrower than the original, meaning less powder to recycle after experiments, which increases the experimental speed. Corners of the tray are much closer to 90° than had been the case using bent aluminium plate. Tray 2 has been designed with a specific width and a vertical slot, to fit into the processing chamber's holder assembly, for variable but repeatable lateral positioning.

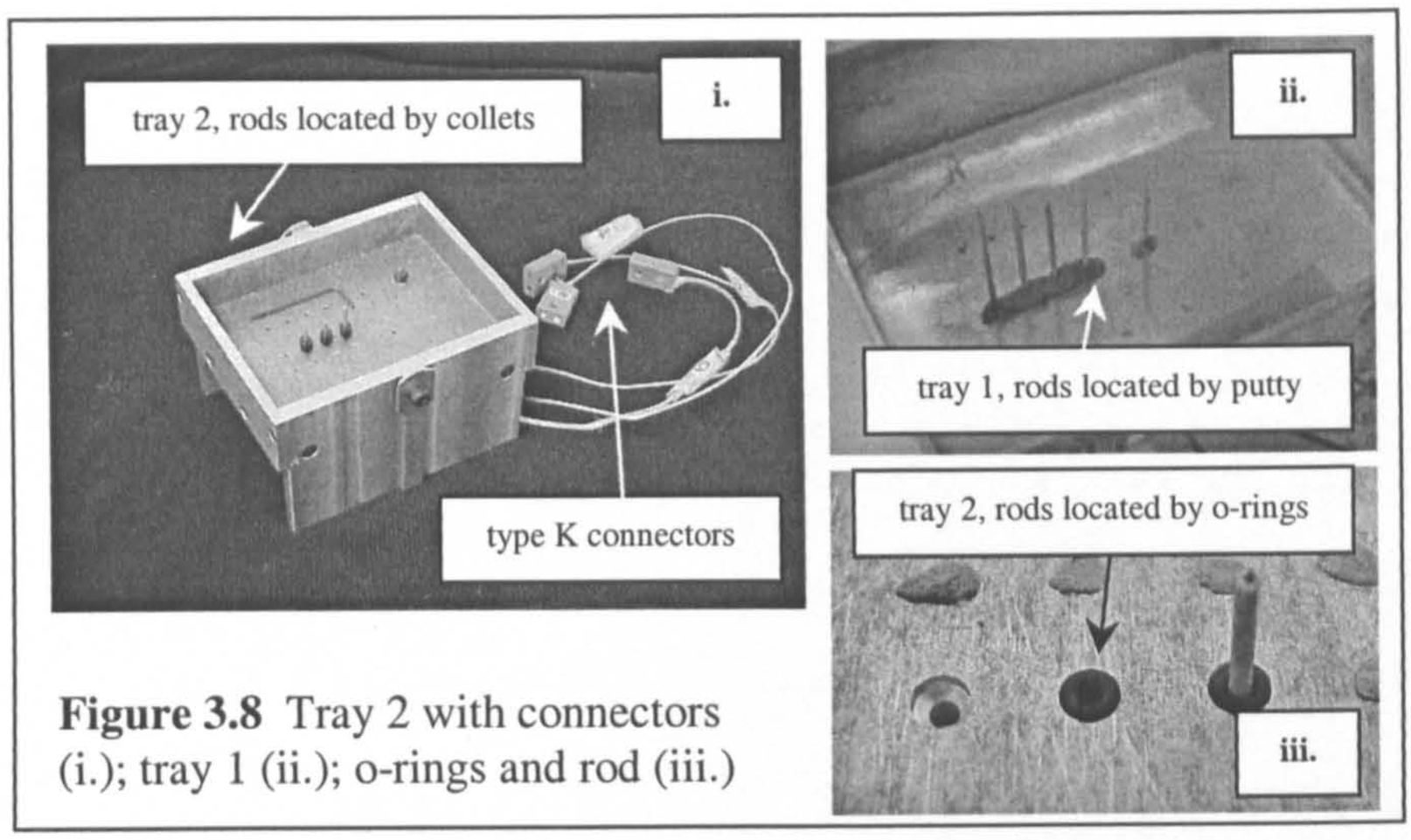

Figure 3.8 Tray 2 with connectors (i.); tray 1 (ii.); o-rings and rod (iii.)

Ceramic rods were initially located in tray 2 using design A. Although there was no horizontal movement of the ceramic rods any more due to an interference fit into the NC holes, it was found that once powder got into the holes, the rods became stuck. They were very difficult to move, and rod breakages resulted. The NC holes were then widened by 100μm and collets were used to vertically locate the ceramic rods (design B in Figure 3.7, image (i.) in Figure 3.8). The rods were held fast, but because the end of each collet's grub screw was quite sharp, it could fracture rods as it was tightened. The NC holes were then modified to incorporate o-rings (design C in Figure 3.7 and enlargement B of Figure 3.5), the final design. Each NC hole was widened by 100μm then widened further at the top and bottom, to the recommended o-ring cylinder diameter. The o-rings succeeded in holding the rod solidly in place, without causing stress concentrations on the rod surface whilst being fitted and removed. The rod was held on the axis of the hole, and did not get stuck any more. To see a photograph of this arrangement, refer to image (iii.) in Figure 3.8.

It was considered important to be able to carry out experiments in an inert atmosphere, representative of conditions typically found in direct metal SLS. The main challenge of measuring temperatures during argon atmosphere processing was establishing a means of entry to the chamber for thermocouple wires whilst maintaining vacuum conditions. The following was required of a solution:

- Facilitate entry to the processing chamber for multiple thermocouple wires;

- Withstand a pressure change of 1 bar across it when the chamber is being evacuated and backfilled;
- Should use blanked, threaded holes currently existing in the chamber wall;
- Allow the powder bed tray to be transported in and out of the chamber between experiments, for the emptying and refilling of powder.

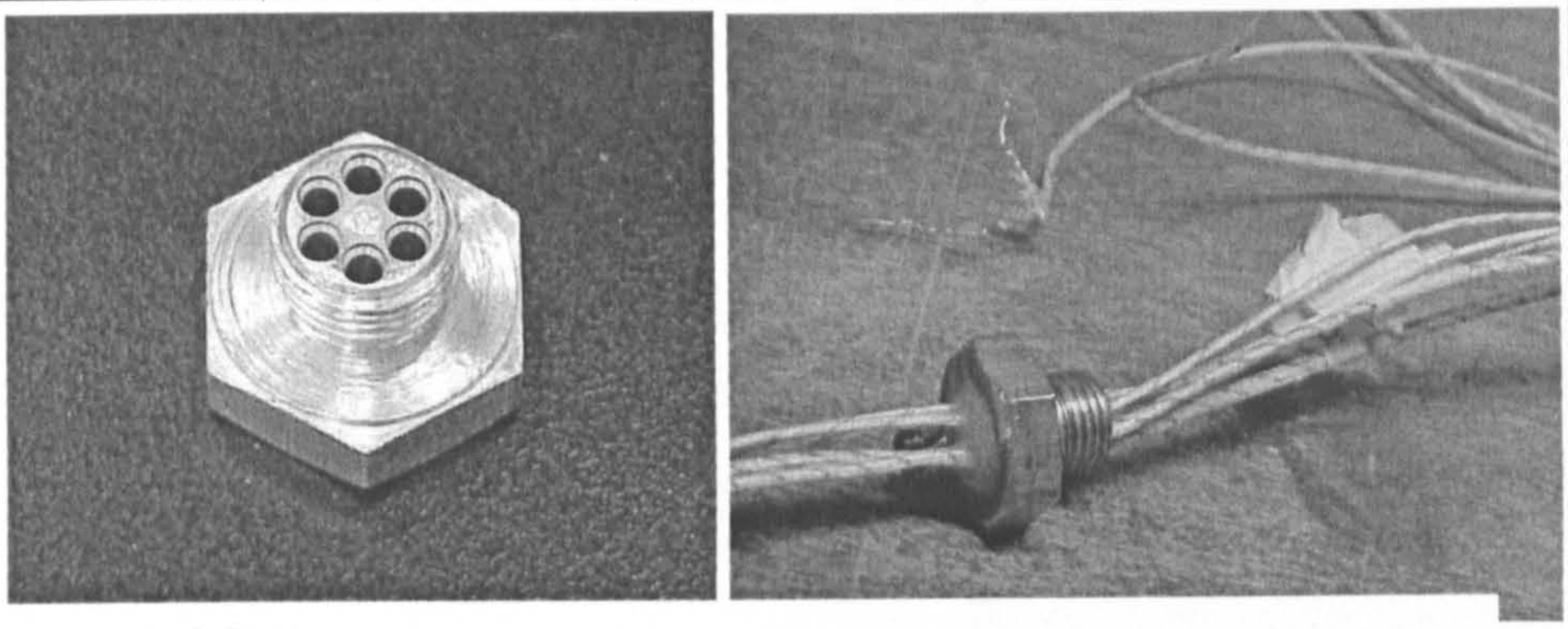

Figure 3.9
Threaded thermocouple vacuum feed-through, without and with wires

Commercial solutions were investigated, but the final design was a custom one. A ¼' BSP bolt was NC drilled with 6 holes of 2.5mm diameter. The thermocouple wires were stripped of their insulation over a 5mm section, then threaded through the bolt up to the stripped section. Epoxy resin was applied between the bare wires and the inner surface of the drill holes to form a seal. See the pictures of this arrangement in Figure 3.9.

To transport the powder bed tray in and out of the chamber, it was necessary to break each thermocouple wire between the feed-through and tray positions. Regular removal and replacement of the bolt was not acceptable because it involved 20 rotations, which would have severely twisted the wires. Circuit breaking was performed by cutting then twisting the wires in early tests using tray 1. Type K plug and socket connectors were then purchased (image (i.) in Figure 3.8).

3.6 Non-Contact Temperature Measurement

In non-contact temperature measurement, the device is positioned remotely. Powder bed tray 2, as described in Section 3.5.2, was used for this purpose. New

temperature measurement (3.6.1) and vacuum (3.6.2) systems were specified and realised.

3.6.1 Specified Existing Equipment

Requirements of the non-contact temperature measurement system are identical to those set out in Section 3.5.1. In relation to bullet point three of that section, non-contact measurements do not disturb the thermal field whatsoever. Only temperatures on the surface of the powder bed can be measured, however.

To learn more about the material phase change and shape change reviewed in 2.2.6.2, it was desired to record temperatures in the melt pool zone during laser application. A melt pool temperature-time profile would allow an estimate to be made of time-dependent heat loss from the powder bed's surface (see Section 2.3.3).

Temperatures in the melt pool would be liable to melt a contact device such as a thermocouple. For this reason, non-contact measurement devices were investigated, namely pyrometers and a thermal imaging camera. A pyrometer can only take a point temperature reading, and there were no such devices freely available to practise with. Therefore an infra-red thermal imaging camera was loaned, an Agema 880. It was used to repeat contact measurement experiments and for extra studies. A schematic diagram has been constructed for the infra-red camera system, Figure 3.10.

The temperature ceiling of the camera was 1500°C, with accuracy ±2°C once calibrated. The camera produced 280×175 pixel video images of temperature, represented by colour contours, within the field of view. Video was viewed on the scanner display and data acquisition PC. A scene could be viewed in black and white (easier

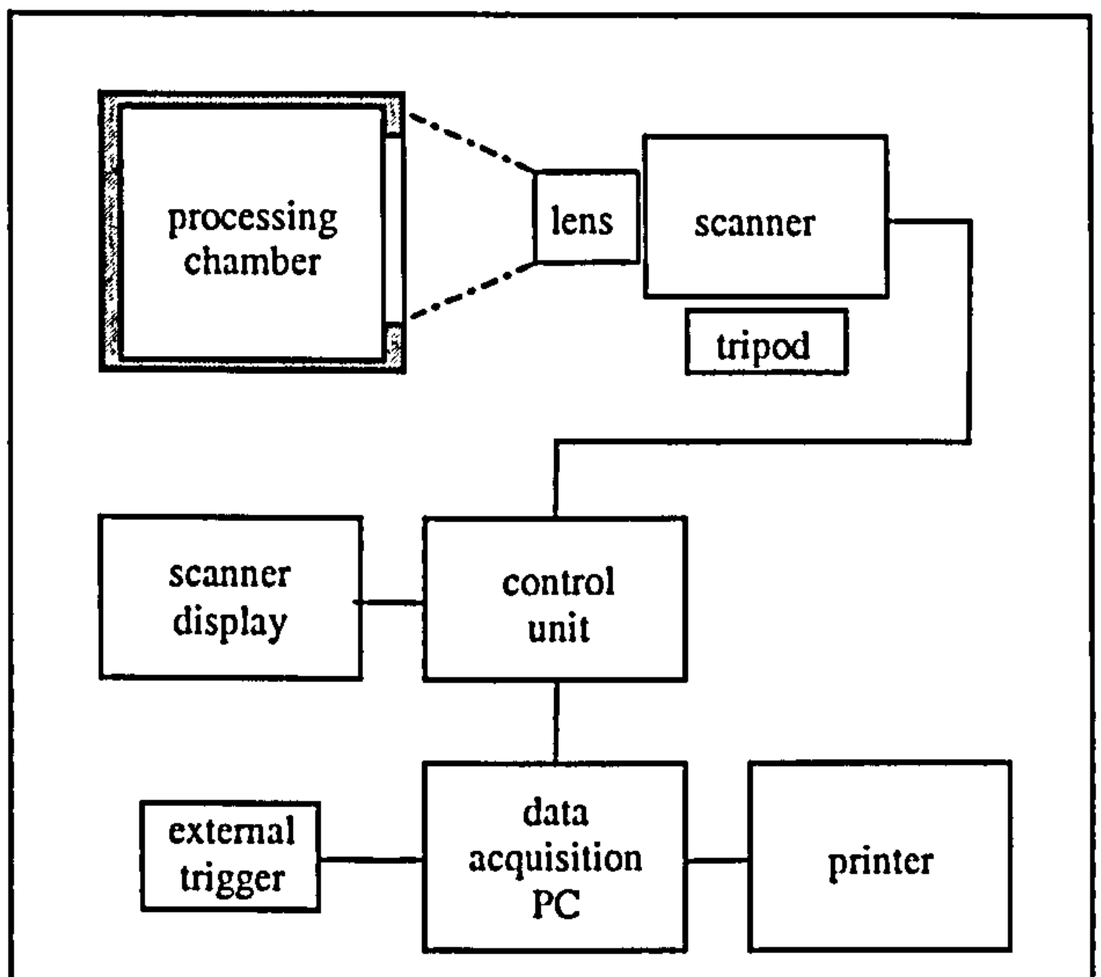

Figure 3.10
Schematic diagram of thermal camera system

to understand), or colour (good for definition of information). Display and output options were selected on the data acquisition PC. Thermal images provide a record of temperature versus position at a set time, these could be output as bitmaps.

It was also possible to measure temperature versus time at a set position by using spotmeters. These were positioned on screen to record temperature at up to 5 locations in the camera's view, with a sample time of 0.46 seconds. Unfortunately, due to the age of the camera system, spotmeter temperature versus time data was not directly compatible with any analysis software. The only output option was to print the data onto paper as a graph.

Three camera apertures could be selected, to change the potential temperature range and sensitivity. For each aperture, the temperature level and range could be adjusted on the control unit. The specification for the system stated that a CO_2 laser filter was fitted to the camera, but unfortunately this was not the case. Such a filter would have eliminated any effect of the laser beam radiation on temperature readings. The camera was cooled using liquid nitrogen.

3.6.2 Custom-Designed Equipment

It was intended to use the thermal camera to record temperature versus position during SLS processing in an inert atmosphere (which will be discussed further in Section 3.12). The process chamber's current polycarbonate viewing window absorbs and scatters infra-red, so the camera could not make good readings. The first solution to this problem to be considered was an infra-red transmissive window, capable of withstanding 1 bar pressure difference during air evacuation and backfill with argon. But transmissive material is costly, and it would be time-consuming to manufacture a surround for the window which was compatible with the chamber. The window would need to be thin enough not to interfere with infra-red emissions from the bed, but thick enough to withstand the pressure change. So, an alternative was considered, a way to create a sealed volume between the camera lens and the chamber entrance (see Figure 3.10). The solution chosen was a strong plastic bag, glued to a rigid cardboard frame at one end (to

seal around the processing chamber entrance), and with a hole at the other (to seal around the camera lens using elastic bands).

Black card was used to line the chamber, to prevent laser radiation being reflected from the steel walls.

3.7 Evaporation Study- Introduction and Equipment

At the end of Section 2.2.6.3, a previous study by Hauser, of parts made using the experimental SLS rig of Section 3.3, is described. The cross-sectional morphology of single line scans is examined, and the mass of material melted is observed for different values of scanning P and U. In certain cases at U below 7mm/s, a decrease in energy supplied leads to more material being melted, which is the opposite of what normally occurs. This change is accompanied by a change in the cross-sectional shape of scanned tracks, from having a concave to a convex upper surface. Considering the energy balance equation (2.9) of Section 2.3.1.1, the mass of tracks is proportional to the energy absorbed and retained until the point of solidification. The proportion of energy being used to generate solid mass is somehow changing in these cases. A cause for this change has not been ascertained, so it is studied in Section 3.13.

Potential causes for a reduction in laser energy efficiency are discussed in Sections 2.2.6.1 and 2.2.6.2. They are energy loss by mass transfer if material is evaporating, a reduction in heat reaching the powder bed due to evaporation causing a vapour cloud which blocks the laser beam, or possibly some unknown phenomenon. In terms of molten metal fluid mechanics, a reduction of surface tension with temperature could cause the upper surface of tracks to form a concave shape, but this could not contribute in any known way to a reduction of melted mass. An important untested clue in identifying the cause of reduced efficiency is the mass of processed material and the mass of the zone immediately surrounding the processed material. If metal vapour is being lost from the processing zone, removing heat, some mass will be lost from the processing zone during laser application.

Any mass lost from the processing zone would have heated from melting to vaporisation temperature then undergone a latent phase, which would be accompanied by a minimum energy loss of:

$$E_{LOSS} = m_V (C.dT_{M-V} + L_V) \qquad (3.14)$$

Where C is specific heat, m_V is the evaporated mass, dT_{M-V} is the temperature change from melting to vaporisation point and L_V is the latent heat of vaporisation.

The melting points of iron, nickel and chromium lie close to 2750°C. The 3 elements have an L_V of around 6000 kJ/kg [Kaye 1995]. This compares to L_M of around 250 kJ/kg for melting. dT_{M-V} is about the same as dT_{A-M} (from ambient to melting temperature). When averaged over the temperature intervals, C for dT_{M-V} is around 1.5 times C for dT_{A-M}. Compiling this information, the energy required to melt 1kg of steel from room temperature is only one seventh of the further energy required to vaporise the same mass. However, the importance of this information depends on how much (if any) mass is lost from the processed zone by evaporation.

To test this, some powder will be placed in a small container. The processing zone will be weighed before and after laser processing. Mass will be measured using a set of Mettler AJ100 electronic weighing scales, with a range 0-110g and a digital readout in grams to 4 decimal places. To be suitable, the container must therefore weigh less than 110g when full of powder, have a surface area not much greater than the processed area, and must resist high temperatures with no degradation.

A plastic bottle cap was the first container tested: it began to degrade at experimental temperatures, losing mass. A small china cup (pictured later) was considered next. Whilst exposed to 1200°C for 4 hours, no evaporation of the cup or its enamel coating occurred. The cup was therefore chosen for the experiment. It was cut down from 50 to 20mm in height, which reduced its weight.

3.8 Experimental Preparations

Before using the SLS rig for each experiment, a preparation procedure was followed. Refer to Figure 3.2 once again for the hardware arrangement.

The processing chamber and powder bed tray were vacuum cleaned to remove any remaining powder particles. If an argon atmosphere was required, a valve on the argon bottle was opened and the delivery pressure was set. All electrical supplies were switched on. The focal length setting of the laser beam expander was checked. Laser goggles were worn when operating the CO_2 laser, a respirator and gloves were worn whilst handling the powders.

With the tray sitting outside the chamber, powder was poured into the tray. The tray corners were tapped to settle the powder, a little more powder was added then the powder bed surface was levelled with the tray's surface using a steel ruler.

The tray holder assembly was centralised in the chamber. The tray was slotted into the holder. The viewing window was bolted into place.

Scan geometry was specified (number of scans, length and position) on the PC using a simple program. Scan speed was assigned to scan geometry using the *PC-Mark* software.

Laser power was set via a dial. Power at the powder bed position was calibrated against dial position regularly, using a Machen Instruments 200W laser power probe.

If processing in argon, the atmosphere in the chamber was evacuated using the pump then replaced from the argon bottle. This occurred twice, before a 15-minute continuous flow of argon to purge any remaining oxygen.

Various safety interlocks and switches were actuated. Laser scanning was initiated by entering a command in *PC-Mark.*

3.8.1 Use of Thermocouples

Before experiments began, the type K thermocouples were calibrated in water cooled from 100 to 0°C, against an externally-calibrated probe. A comparison was made between the 0.3mm diameter thermocouple wires used and some similar 0.2mm diameter wires, to see if the change in junction mass caused any change in the response time and peak temperature measured.

Before filling the tray with powder, the thermocouples (inside their ceramic rods) were inserted and adjusted for height. Adjacent NC holes were used, meaning the measurement positions were spaced at 10 or 20mm intervals in the scanning direction (refer to Figure 3.5). O-rings were slid onto the ceramic rods

above and below the powder bed tray's base and were pushed into their locations (see Figure 3.5 again). The rods' vertical positions were set then the o-rings were pushed into position once more. The depth of thermocouple junctions in the powder bed was set using a digital Vernier caliper, measuring in hundredths of a millimetre.

The vacuum feed-through was fitted to the chamber. With the tray inside the chamber, the thermocouple circuit was completed by connecting the type K connectors. The logging software on the PC was set up. The output file name, sample time (0.6 seconds), number of significant figures in output and number of channels read from (6) were set. Before beginning each run, a check was made that all wires were reading reasonable values.

After the first few uses of the experimental equipment, priorities for improvement of the process were established. Time spent using the SLS laser rig was restricted due to the needs of other users, so a reduction of the time taken and increase in readings taken per experimental run was required. More readings could be made by improving reliability (the number of useful readings as a percentage of all readings taken). Poor reliability was largely caused by thermocouple circuit failure. Rod location designs A and B (Figure 3.7) caused the rods to snap often, leading to snapping of the thermocouple wires. The wires also snapped often at the bottom of the rod, hence the epoxy reinforcement implemented in 3.5.2. The positive and negative conductors had identical appearance outside of their sheathes, which allowed them to be connected backwards occasionally: this problem was remedied by coloured marking of the wires.

Experiments undertaken using the thermocouples are tabulated in Appendix A, pages 2 to 4. Included are preparatory tests, thermal property measurement (described 3.12 below), a thermal field study (3.10 below) and an end effects study (3.11). The link between Appendix A and specific results is explained in Chapter 5.

3.8.2 Use of Infra-Red Camera

The infra-red camera system was set up as shown in Figure 3.10. Before experiments, the aperture, level and range dials had to be set on the camera to achieve the desired temperature interval. A printer was set up to output colour temperature versus time curves for the spotmeters. The black card mentioned in 3.6.2 was stuck around the chamber walls.

Calibration of the camera involved calculation of the emissivity ε_r of the object viewed, in this case the powder bed. A function built into the camera allows ε_r to be calculated. A furnace was used to heat the powder bed to 200°C, then the camera was trained on the bed. The temperature of the area viewed was input into the camera, allowing it to calculate ε_r. The effect of viewing angle on the ε_r value calculated was checked: ε_r was 0.65 at 34° from perpendicular to the bed surface, and 0.67 at 52° from perpendicular. All camera work to be done involved viewing at within this interval of angle, so consistency was good.

When an argon SLS processing atmosphere was required, the sealing bag of 3.6.2 was utilised. The chamber was evacuated and refilled twice with the viewing window fitted as previously described. The window was then removed, and the sealing bag fitted to the chamber entrance using adhesive sealing tape round the cardboard frame. Some leakage was observed around the edges of the frame in the following 20-minute purge of argon, but the flow of gas was from the chamber to the lab atmosphere, meaning that the argon purity inside was maintained.

The camera needed liquid nitrogen in order to operate- a risk assessment was carried out in relation to handling, storage, accidental spillage and disposal protocol for this substance.

Because there was no appropriate filter, the CO_2 laser could be seen to interfere with the camera picture. This will be seen in results (Chapter 6). A larger uncertainty in temperature measurements was assumed whilst the laser was operating: otherwise accuracy is as stated in 3.6.1.

Experiments undertaken using the infra-red camera are tabulated on page 1 of Appendix A. Included are preparatory tests, thermal property measurement (described 3.12 below) and a thermal field study (3.10 below). The link between Appendix A and specific results is explained in Chapter 5.

3.9 Measurement of Powder Density

In the equations (3.4), (3.9), (3.12) and (3.13) of Section 3.2, one of the quantities which must be evaluated in order to calculate the k and α values of a powder is density ρ. This was measured with a method using the weighing scales specified in Section 3.7. Two powder types and different size ranges were tested. Powder was held in the cup used in the evaporation study of Section 3.7. This cup is 20mm deep, the same depth as powder bed tray 2, in case the gravitational head of powder has an effect on its packing density.

The mass of the cup, the mass of the cup full of powder and the mass of the cup full of water (both substances made flat to the rim of the cup) were measured. Using these three masses, density could be calculated.

Density was measured three times for each powder, and the average taken. Stainless steel 314S HC powder, of size fractions 10-20μm, 75-150μm and 150-300μm, was tested. Also gas-atomised M2 stainless steel, size fraction 75-150μm, and Rapid Steel 2 powder were tested.

3.10 Thermal Field Study

This study was carried out using powder bed tray 1. There were three aims: to develop the design of the tray, to develop the experimental procedure and to learn more generally about the change in temperature against position and time in the powder bed during and after laser application. Temperature was recorded whilst single lines were scanned over a broad range of machine parameters. Readings were taken at positions within the bed using the thermocouple system, and at positions across the bed's surface using the infra-red camera system. The size and magnitude of the thermal field against time could be observed.

The range of parameters tested were: measurement depth y from 1 to 11mm, laser power P from 20 to 160W, scan speed U from 4 to 32mm/s and air and argon atmospheres.

3.11 End Effects Study

This study was carried out using tray 1. The aims of the study were as the second and third aims stated in the last section. The express task was to determine the limits of the steady behaviour sector of the thermal field generated by the scanning of single tracks. The unsteady nature of temperature distribution with depth at scanned line ends has been discussed in Section 2.2.6.3. It is also predicted by the analytical models of Section 2.3.4.2. The diagram Figure 3.11 shows the location of the steady behaviour zone. The temperature contours shown are those occurring directly below the scanned line. The steady zone is defined by the condition $dT/dx = 0$, where x is the scanning direction. The steady behaviour zone identifies the limits of where thermocouples can be positioned in experiments, as $dT/dx = 0$ is a condition essential for making the infinite line assumption of Section 3.2.

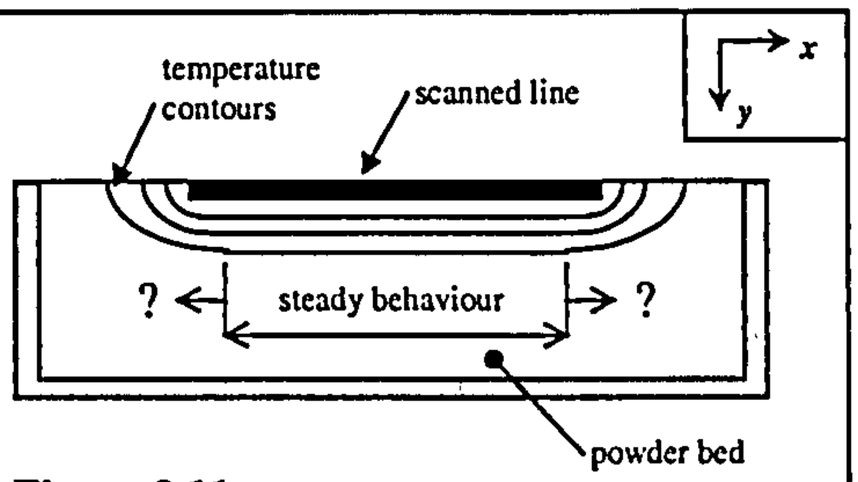

Figure 3.11
Sectional view of powder bed: processed scan and temperature distribution

Power, speed and depth were constant during the study: $P = 120$W, $U = 6$mm/s and $y = 5$mm. There were 8 experimental runs. For each run, a 60mm line was scanned with the thermocouples located at three 10-millimetre spaced x positions. This meant that readings were taken at 24 unique x positions relative to the end of the 60mm scan, to discover where the steady condition would be met.

3.12 Thermal Property Measurement

The background to this activity is stated in Section 3.2. The effective conductivity k and absorptance α of powders were calculated based on experimental results. The effect of the geometry scanned, the powder size and type, atmosphere and scanning strategy were tested. Also the effect of parameters P, U and s on properties was investigated. k and α were measured using the

thermocouple temperature measurement system, but k was also measured using the thermal camera. Scanning of single lines and layers was considered analogous to the heat source cases set out by Carslaw and Jaeger, reported in 3.2. The validity and scope of the analogies were tested before they were used to calculate material thermal properties. Equations (3.4), (3.9), (3.12) and (3.13) were used for this purpose, explained in Chapter 5. Laser power and scan speed were varied following a set program in most cases. Scan spacing was varied in the case of scanning single layers. In all sub-sections of 3.12 except 3.12.3, only 314S HC powder was used. In 3.12.3, the other powder types are tested. Powder bed tray 2 was used throughout.

Minimum values of power and scan speed were observed so that the laser-induced temperature profile was effectively the same as that of a line heat source, but there was enough heat to create a temperature rise easily distinguishable from device noise.

Each experimental run involved 40 minutes of preparation as described in 3.8, then temperature data collection which took 5 minutes. A full list of experimental runs is tabulated in Appendix A.

3.12.1 Procedure- Thermocouple (Contact) Measurement

Laser scanning and temperature logging were begun in synchronisation. Scanning was always completed in under 60 seconds. Logging was continued long enough to get a temperature peak (temperature traces could be seen on-screen), and a decent amount of data afterwards. Data was recorded in Volts DC, to be converted to temperature afterwards.

3.12.2 Procedure- Infra-Red Camera (Non-Contact) Measurement

The infra-red camera was used to verify thermocouple-based measurement of k in the situation of single line scanning. Spotmeters were trained on the powder bed inside the processing chamber, each at measured distances in the z direction (across the bed's surface, perpendicular to scanning: see Figure 3.11) from the centre position of the line to be scanned. An option was selected on the data acquisition PC to trigger temperature logging manually. Laser scanning and

temperature logging were begun in synchronisation. Scanning was always completed in under 60 seconds. The printer connected to the data acquisition PC printed a temperature versus time graph, for multiple spotmeters.

3.12.3 Single Line Experiments

Material	Powder d_p Interval (μm)	Atmo-sphere	P Range (W)	U Range (mm/s)	Contact or non-contact method
314S	75-150	Air	40-160	1-15	Contact
314S	10-20	Argon	40-160	1-15	Contact
314S	75-150	Argon	40-160	1-15	Contact
314S	150-300	Argon	40-160	1-15	Contact
314S	75-150	Argon	160	0.5	Contact
314S	75-150	Argon	160	1.0	Contact
314S	75-150	Argon	160	10.0	Contact
M2	75-150	Argon	40-160	1-15	Contact
RS2	Avg. 30	Argon	40-160	1-15	Contact
314S	75-150	Air	40-160	1-15	Non-cont.

Table 3.3 Program of experiments carried out for single line scans

Experiments were carried out, following the program in Table 3.3. The first 9 experiments involved the use of thermocouples. The final experiment was carried out using the thermal camera. Temperature versus time data was gathered, from which the values t_{Tmax} and dT_{max} could be extracted. Each experiment was based on single lines 60mm long, scanned on the powder bed surface.

In the experiments where thermocouples were used, the laser scanned directly over the thermocouples' positions. Based on the findings of Section 3.11, thermocouples were positioned 20mm or more from the edge of the scanned line in the x direction. This ensures that temperatures read are independent of x. A standard program of power and speed values for experiments was devised, ranging from 40 to 160W and 1 to 15mm respectively. This only changed where α was measured at single values of U. As a result of experiments in Section 3.10,

the upper and lower limits of thermocouple measurement depth y had been discovered: 2 and 6.5mm respectively. At less than 2 millimetres below the bed surface, the thermocouple junction had melted into the processed tracks. At y= 6.5mm, P of 40W and U of 15mm/s (the lowest E_L combination in the experimental program) brought about a temperature rise of 1.2°C. 1°C had been chosen to be the lowest acceptable temperature rise.

When using the infra red camera, measurements were taken at different positions in the z direction, as opposed to the y direction when using thermocouples. In Carslaw and Jaeger's situation of an infinite line heat source where no heat is lost from the surface of the semi-infinite body, the measured temperature profiles should be the same whether in the y or z directions.

Once the method was established, one experiment could be done in 6 runs, taking just under a day to complete.

3.12.4 Single Line Relasing Experiments

This section and the following section investigate the effect of scanning strategies on the thermal situation in SLS. It has been observed in Section 2.2.6.3 that in the raster scanning strategy, the first track scanned is the largest and that tracks become successively smaller, down to a steady state size. It was suggested that this is due to the reduced α and increased k of previously processed material which is partially rescanned by the laser. The effect of rescanning on α was tested here and in the next section.

The experimental method used was similar to 3.12.3, except that the same 60mm line geometry was scanned multiple times in the same position. 6 runs yielded 30 results. The bed was allowed to cool to a uniform temperature between runs. The effect on α of material changing from powder to solid form (with reduction of porosity) was tested in argon.

3.12.5 Single Layer Experiments

Single layers are raster scanned with a degree of overlap in SLS. To calculate thermal properties k and α, layers were approximated to an instantaneous plane

heat source covering the surface of a semi-infinite body, as discussed at the end of Section 3.2.

It was to be seen whether α would change compared to values calculated for single lines, due to the partial rescanning of previously-processed material. The effect on α of a change in scan spacing s was tested.

Layer dimensions and values of U were tested initially, to see the limits of the infinite instantaneous plane heat source assumption. If a layer is too large, it can not be scanned in a time assumed instantaneous; too small a layer can not be assumed to be infinite in size. A layer size of 20×40mm was chosen for these reasons. Higher scanning speeds were necessary than were used for single lines, to maintain the instantaneous heat application assumption. 10 experiments were carried out in argon, at constant P but with s changing in inverse proportion to U such that the energy density A_N and the scanning time remained constant. s ranged from 0.2 to 1.1mm, U ranged from 27.5 to 300mm/s.

The selected range of s was based on likely minimum and maximum values. 1.1mm is equal to the beam diameter d, and is the maximum track width likely to occur for the range of U [Hauser 2001].

3.12.6 Semi-Automated Treatment of Thermocouple Measurements

The VirtualBench logging software used outputs a text file with temperature versus time data for up to 6 thermocouple channels. A program was developed in Fortran to read through this file, picking out the initial temperature and time, and the maximum temperature (dT_{max}) with corresponding time (t_{Tmax}) for each channel. The maximum temperature was found through comparison and conditional replacement of values. A listing for the program can be found in Appendix B. An account of how the program was operated is included in Section 5.4.1.

3.13 Evaporation Study

An introduction to this study appeared in Section 3.7. The study was intended to determine whether energy was lost from the powder bed by evaporation at certain values of P and U, and if so how much.

Electronic scales were used to measure the mass of the cup and powder. "Control" weigh-ins occurred first. The cup full of powder was entered into and removed from the processing chamber with no laser sintering. It was weighed before and afterwards, to check that the weight remained the same.

Then two experiments were done. Experiment 1 took place at P equal to 160W and U equal to 0.5mm/s, number 2 took place at P of 160W and U of 1.0mm/s. The two sets of P and U values were chosen because the first was found by Hauser to result in scan cross-sections with a concave upper surface, and the second was found to lead to cross-sections with a convex upper surface (referring to Figure 2.20). Each experiment consisted of the following:

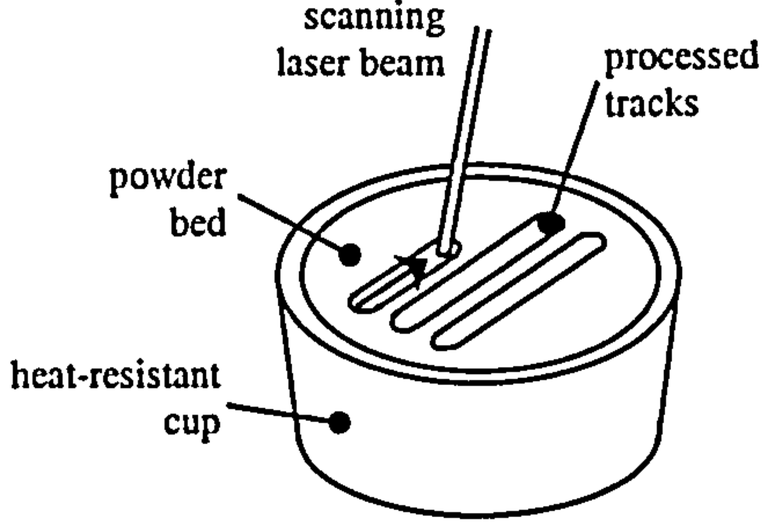

Figure 3.12 Evaporation study

- The cup was filled with powder, then the powder was spread flat to the cup's surface with a metal ruler;
- The mass of the cup and powder was weighed, before processing;
- 5 parallel tracks were scanned on the powder surface in the cup (see Figure 3.12);
- The mass of the cup and powder was weighed, after processing;
- The processed tracks were removed from the cup and weighed;
- This took place 3 times in each experiment, and the average mass was taken.

The mass of the cup will not change from before to after SLS processing. Any change in the mass of the cup and powder would indicate a change in the mass of the processing zone. It is suggested that if a change occurs, this would be due to material evaporation. The mass change due to evaporation between experiments 1 and 2 can be compared to the change in mass of the processed tracks. There are two theories which may explain an increase of melted mass corresponding to a reduction of energy supplied: evaporation heat loss or a blocking vapour. The results of experiments 1 and 2 will determine which theory is the most likely.

Evaporation heat loss is assumed to begin with. Equation (2.9) from Section 2.3.1.1 is used to see how much energy is diverted from the melting of material between the two experimental cases, assuming a constant α. The mass of the processing zone before and after processing tells whether the energy lost by evaporation decreases between experiments 1 and 2, and if so equation (3.14) from Section 3.7 is used to decide if the amount is sufficient to explain the lower melted mass at the lower U. If the amount is not sufficient, then a reduced absorptance due to a blocking vapour is the favoured explanation.

In 3.12.3, the α value corresponding to the same two sets of P and U values has been measured using the thermocouple system. The results will be compared to those of this section.

3.14 Manufacture and Sectioning of Single Layers

The validity of the SLS finite element modelling program *stmet3d* described in Section 2.5 needs to be tested. For this purpose, a comparison was made between cross-sections of manufactured parts and cross-sections of parts generated by numerical modelling. Chapter 4 contains more information on the aims of this exercise. Manufactured and modelled parts were morphologically analysed and compared, as described in Chapters 6 and 7.

	P=60W, U=1mm/s	P=120W, U=6mm/s	P=155W, U=12mm/s
$s = 3\,d/6$	3 parts	3 parts	3 parts
$s = 5\,d/6$	3 parts	3 parts	3 parts
$s = 9\,d/6$	3 parts	3 parts	3 parts

Table 3.4 Single layer manufacturing, machine parameters (d= 1.1mm)

s was chosen at 3/6, 5/6 and 9/6 times the beam diameter d. s must be set as a multiple of $d/6$ in the model. $3d/6$ and $5d/6$ are values seen to produce strong, flat layers using the experimental SLS rig. $9d/6$ was thought to be the maximum likely scan spacing, given the P and U values chosen. P and U were selected after inspection of a process map by [Hauser 2001]. 60W, 1mm/s and 120W, 6mm/s were selected because these combinations are said to produce high quality, uniform tracks. Continuous tracks of a slightly lower quality are formed at 155W,

12mm/s. Energy density A_N takes 9 unique values for the parameter combinations selected. Track cross-sectional shape is expected to differ for the P and U combinations selected.

The y-z plane was chosen for sectioning layers, as shown in Figure 3.13. This plane was selected because the largest geometrical changes are seen, making it of the most interest. In the scanning (x-y) and depth (x-z) planes, layer shape does not change greatly except at the edges.

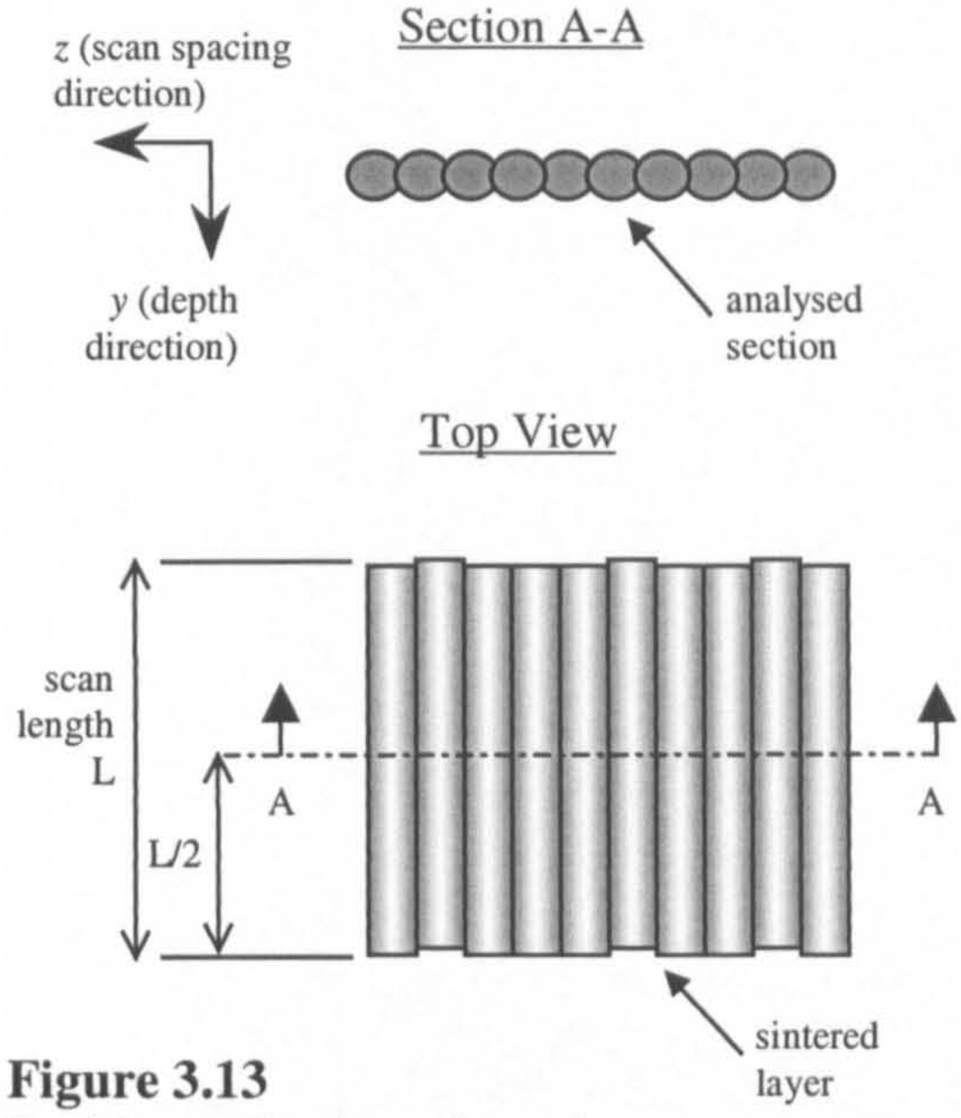

Figure 3.13
Position and orientation of cross- sections analysed

It would be easier from an experimental point of view to weigh samples and compare their mass against model output, but automated mass analysis is not currently possible for modelled parts. Area analysis has been semi-automated using a method developed as part of this work, requiring software introduced in Section 3.15.1. The method is described in Section 5.1.

A procedure was followed to prepare samples for analysis. Single layers were direct-SLS processed using the equipment of 3.3. Layers consisted of 10 parallel scans with each scan being 10mm long. Processing parameters s, P and U were as written in Table 3.4.

Unidirectional scanning was chosen, although the laser equipment and process model can be modified for bi-directional raster scanning.

Layers were removed from the bed and cleaned off. Each layer was mounted on small supports, and immersed in epoxy resin (allowing the layer to be clamped and sectioned without any deformation). The epoxy-coated layer was sectioned with a Struers Accutom-5 cutting wheel. It was sectioned through the centre in the scanning direction (as denoted in Figure 3.13). One half of the layer was reset in epoxy, to create a disc which could be evenly polished. The surface of the cross-

section was ground and polished using Metaserv 2000 and Metalo machines, down to 1μm polishing particle size.

An enlarged view of the polished section was created on a profile projector, a Nikon V-16D by Nippon Kogaku K.K. A grid was fitted over the projection screen to provide a millimetre scale on the image for working out its dimensions later. A digital camera was used to take pictures of the projector screen, the image being a steel layer cross-section with an overlaid grid. A typical image will be seen in Section 5.1.

The amount of labour involved in this operation was quite large: the effort required in creation of manufactured part cross-sections for analysis will be compared with that required to create numerically-modelled part cross-sections in Chapter 7.

3.15 Experimental Support Development

3.15.1 Dimensional Analysis of Single Layers: Use of Image-Pro Software

Images as prepared in Section 3.14 had to be analysed to evaluate their dimensions. The general shape of layer cross-sections was analysed manually. Calculation of area and relative density could be automated using Image-Pro Plus Version 3 (by Media Cybernetics L.P.). Areas in an image having a particular colour can be analysed almost instantaneously for area, with graphical feedback to confirm the perimeter of the area analysed. The software works faster and more accurately than manual square counting, which took a few minutes per cross-section when attempted. The method of using Image-Pro will be described in Chapter 5.

3.15.2 Feed-Forward Process Control Feasibility Study

As a basic requirement for feed-forward process control (discussed in Section 2.6), the possibility of varying laser power on a scan-by-scan basis on the SLS rig was investigated: this is possible. It would then be possible to vary laser power to counter the natural reduction in size from the first to the second and third scans in

layer processing. Variation of power is preferable to variation of scanning speed between adjacent scans, which is also possible. It would be harder to adapt the numerical model to reflect changing U. The ability to model the process is vital for FFPC.

There was not enough time available to try refining the cross-sectional geometry of manufactured parts via power modulation, so this has not been undertaken. The work of 3.14 was considered more fundamental.

CHAPTER FOUR

4 NUMERICAL MODEL DEVELOPMENT

4.1 Introduction

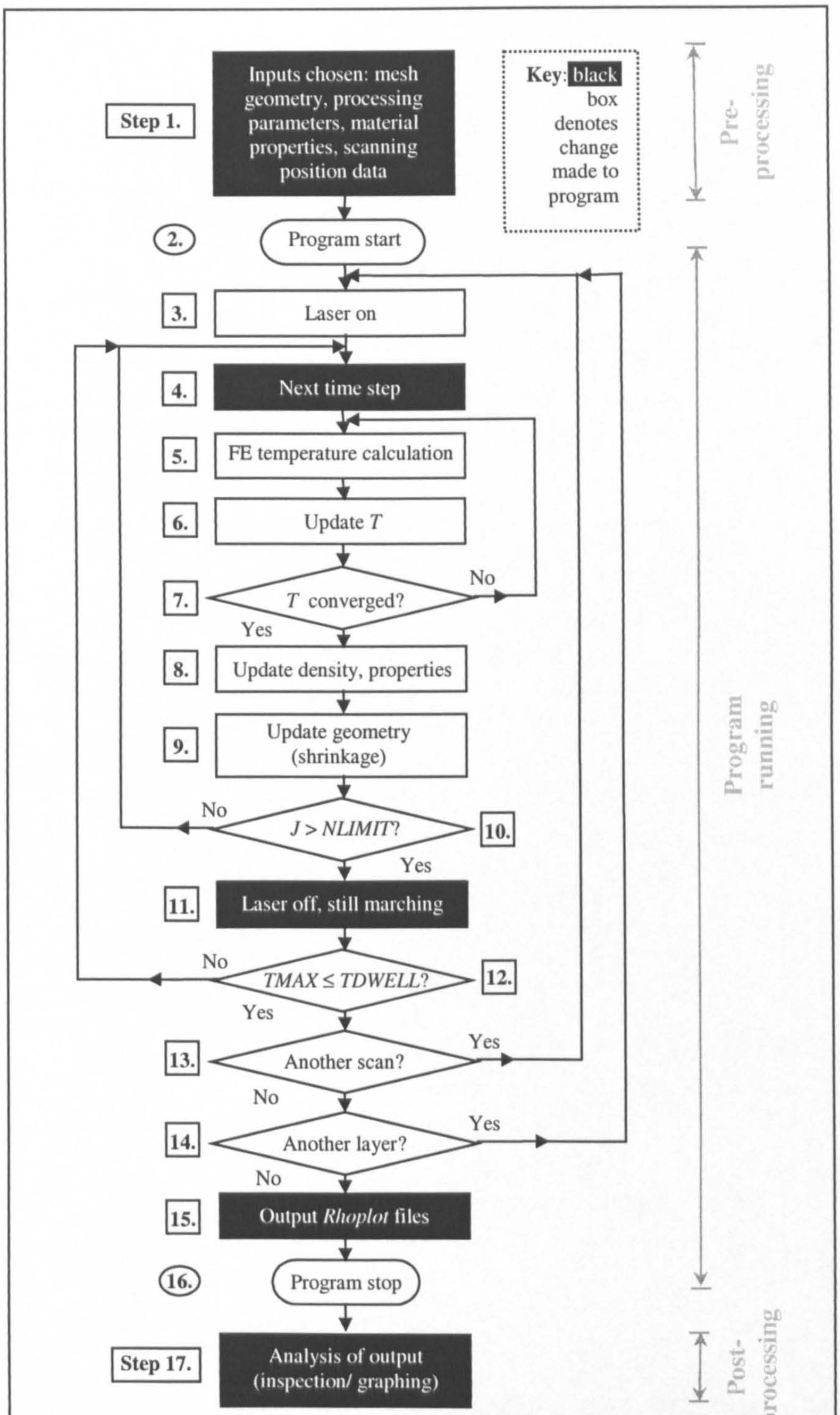

Figure 4.1
Refined flow diagram of Childs' finite element sintering model

In Section 2.5.2, the Fortran SLS process model *stmet3d* was described. *stmet3d* is to be developed and tested as part of this work.

The model *stmet3d* is based on the direct SLS of stainless steel from room temperature. Changes have been made at various stages of Childs' program *stmet3d* in this work. To explain where these changes occur in the program's execution, Figure 4.1 has been constructed. The figure is a more detailed version of the flow diagram Figure 2.33 presented in Section 2.5.2.2. Where changes have been made to a step in the process as part of this work, boxes in the flow diagram appear black. Sections of the *stmet3d* program code which were modified are included in Appendix C.

Changes have been made to the model code and to inputs at process step 1 in Figure 4.1. These relate to harnessing the increased capability of the model due to addition of sparse matrix solution methods (ILUT and GMRES decomposition) in process step 5 by another worker (described Section 2.5.2.2), and to supporting the concept of feed-forward process control (FFPC), discussed in Section 2.6. Pre-processing (also step 1) has been sped up through automation of the repetitive calculations required to prepare the input file and parameters in the code if conditions change. More information is printed to screen during run time (step 4) for program performance analysis, and new formatting of output files (step 15) reduces their size. Post-processing (step 17) has been enhanced through development of more visualisation and analysis options for model output. A change has been made to the laser scanning procedure in the model (steps 4 and 11), in an attempt to remove an unexpected phenomenon.

The form of modelled parts and the status of the temperature calculation related to scan spacing s, power P and scan speed U is investigated and classified.

Step 1 in Figure 4.1 involves reading process parameters and material properties. 17 such values were set, and remained constant throughout modelling work. The values are as reported in Table 4.1. *TDEG0* is the temperature of the powder bed before SLS begins. *TDWELL* is the temperature condition at which the TM is allowed to move from the end of one scan to the start of the next, see Section 4.3. *TSOL* and *TMELT* are the temperature limits of the material latent

phase, *TLAT* is the latent heat of melting. *HLOSS* is a powder bed surface heat transfer coefficient. *RHOPOW* is the fresh powder density, *RHOSOL* and *RMAX* are the density of solid material. *DPA* and *DPN* are laser penetration constants used as shown in equation (2.23), Section 2.5.2.3. *CONDO* and *CONDV*, *CAPO* and *CAPV*, *SIGV1* and *SIGV2* are used to calculate changes in thermal properties with temperature and porosity, explained by equations (2.24), (2.25) and (2.26) in Section 2.5.2.3.

TDEG0	*TDWELL*	*TMELT*	*TSOL*	*TLAT*	*HLOSS*
20 °C	1260 °C	1380 °C	1280 °C	308000J/kg	0 W/(m^2.K)
RHOPOW	*RHOSOL*	*RMAX*		*DPA*	*DPN*
4356 kg/m^3	7850 kg/m^3	7850 kg/m^3		1.33	1.0
CONDO	*CONDV*	*CAPO*	*CAPV*	*SIGV1*	*SIGV2*
7.83 W/(m.K)	0.0183 W/(m.K^2)	437 J/kg	0.275 J/(kg.K)	6.05	0.78

Table 4.1 Process parameters and material properties set in file *stme3dat*

4.2 Mesh Refinement and Increase in Modelled Part Size

The original meshes were sized as follows: thermal mesh (TM), 17×17×17=4,913 nodes. Powder bed mesh (PBM), 85×20×50=85,000 nodes.

The ILUT and GMRES subroutines discussed in Section 2.5.2.2 make more efficient use of PC memory, providing new opportunities for usage of the model. Two key variables in ILUT, namely *DROPTOL* and *LFIL*, determine the amount by which the matrices to be solved in modelling step 5 are simplified. *DROPTOL* and *LFIL* were set to 0.005 and 10 respectively, throughout this work.

To make use of the program's extended capability, mesh data in the program input file *stme3dat* were changed. The TM was equipped with a greater number of smaller nodes. Originally, a TM *y* element had a minimum height of 0.083mm. This was considered quite large, given that modelled layers are in the order of

1mm deep. The number of *y* elements in the TM was doubled, and the height of each element was halved, to see if this would change the shape of modelled parts. The element length in the *y* direction is proportional to the specified layer depth (see Section 2.5.2.1), so to halve the element length, the layer depth was reduced from 0.5 to 0.25mm. The depth of the TM was increased also, by adding 11 further *y* nodes. These extra nodes doubled the TM depth, from 2.5mm to 5mm. A comparison was made of output geometry in 3 pairs of cases: before and after GMRES implementation, for a coarse and a fine TM, and for the original and increased TM depth.

In all, the TM had 5 *x* nodes, 28 *y* nodes and 2 *z* nodes added. In the *x* and *z* directions, nodes were added to improve the definition of the TM around the edges of the heat application zone. In the *x* direction, two further nodes were added to move the laser beam profile backwards in the TM. This was done to equalise the distance from the edge of the heat application zone to the front and side surfaces of the TM.

65 *x*, 10 *y* and 80 *z* nodes were added to the PBM, permitting parts to be made from a greater number of longer scans.

Trial and error were required in the beginning to discover the new maximum size of the TM and PBM for which the program had sufficient memory to run. Extra stack and paging memory were allocated to assist. Changes made to the TM and PBM were expedited by use of a spreadsheet, details of which are found in Section 4.4.

4.3 Modification of Bed Scanning Procedure

Values of material absorptance are entered into *stme3dat* in pre-processing, step 1 in Figure 4.1. *stmet3d* was modified to accept a value of absorptance for each scan, whereas previously one value had been used for the whole part. The aim was to recreate the effect which partial rescanning has on powder absorptance for metals in layer rastering. This followed on from the work of Song in Section 2.2.6.3, and was intended to draw on findings made in the work of Sections 3.14 and 4.7 to follow.

A change was made to the TM's behaviour at the end of each scanned line in the model. This was implemented at steps 4 and 11 in Figure 4.1. In the original procedure, the TM stopped moving once a scan was complete, waiting ("dwelling") until all nodal temperatures were below the steel solidification point. When this condition was met, the processed geometry would not change further, so the next scan was begun. The reason for the change was a vertical "hook" feature seen on the end of many modelled scans (examples in Figure 4.2). It was thought this might be due to the TM dwelling static over the end section of a scan, as opposed to marching along the rest. If material in the rest of the scan was not solidifying before it left the TM, the scan end zone could have been getting more heat dissipation time compared to the body of the scan. The solid volume at the scan end would have experienced a biased level of growth.

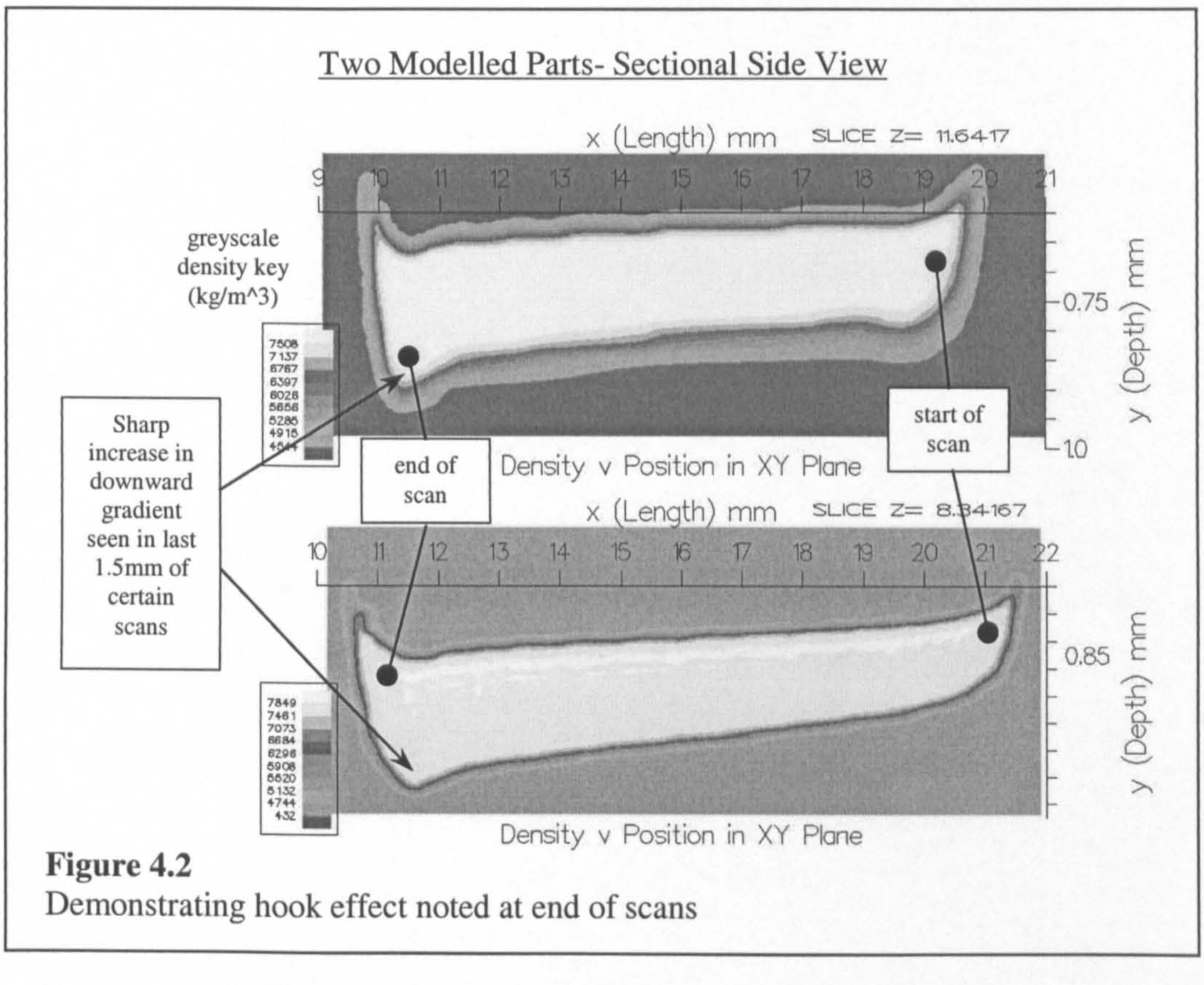

Figure 4.2
Demonstrating hook effect noted at end of scans

A new marching cool down scheme tested in this work provided consistent treatment of all nodes processed by the TM, and was efficient with run-time. In the new scheme, the TM continued to march once the laser heat input had been switched off. Nodal temperatures were checked at each heat step after switching off. If all temperatures were below the solidification point of the material (i.e. the output geometry would not change any further), the next scan was begun. If the

temperature condition was not met, the TM continued to check temperatures and march on until an entire TM length after the heat input was switched off. If this point was ever reached, a warning would appear and the next scan would be begun.

Modification of the scanning direction was considered, in order to have back and forth rather than unidirectional raster scanning. This would not be difficult to implement, but it was found easier to modify the experimental rig to a unidirectional scanning style so no change was made.

4.4 Ease of Use, Feedback and Output File Size Reduction

Whenever changing the size of the PBM or TM, parameters relating to the meshes had to be recalculated and changed at several points in the program listing. Selection of values in the *stme3dat* input file (step 1 in flow diagram Figure 4.1) also depended on the PBM and TM size. The dimensions of parts to be modelled had to be chosen carefully. If the scan start and end points or the number of scans or layers specified was too great, the TM left the interior of the PBM during run time, causing the program to crash. For this reason, a spreadsheet *stmet3d.xls* was created on Microsoft Excel 97. Refer to Table 4.2 to see its inputs and outputs. The spreadsheet used size information about the PBM and TM to perform two useful functions. The x, y and z size of the TM and PBM were entered as a multiple of the PBM element size. The millimetre length of a PBM element was known, reported earlier in Section 2.5.2.1. Values were automatically calculated for the parameters which had to be changed in the program listing, and the number of layers and extreme part dimensions which were permissible were provided. The spreadsheet generated maximum scan start and end positions in millimetres. This provided a guide to the part dimensions entered manually into the file *stme3dat*. For the situation where both meshes were to be changed in size, *stmet3d.xls* automated 20 essential and 5 advisable calculations.

Powder Bed/ Thermal Mesh Parameter Calculator **stmet3dgmres**

Powder bed mesh param.s		
n10	n11	n12
150	30	130
mnelg	mnodg	mling1
3459780	3529500	181
mling2	mling3	
150	130	
mnglay		
30		

Thermal mesh parameters		
n1	n4	n6
22	45	19
mnmq	mnelw3	mnodt3
10	99792	18810
mnline1	mnline2	mnline3
45	22	19
mielm		maja
769		264388

Nodes in beam diameter
7

Largest therm. mesh spacing		
x	*y*	*z*
8	12	8

Key: underlined values are inputs, other values are calculated outputs.

Powder Bed/ Thermal Mesh Node to Maximum Dimension Calculator

X	Total no. of "*x*" PBM elements in thermal mesh	Elements in front of heat source
	42	13
Y	Total no. of "*y*" PBM elements in thermal mesh	
	120	
Z	Total no. of "*z*" PBM elements in thermal mesh	Elements right/ left of heat source
	36	13

No. of layers	*z* start	No. of scans × spacing		*x* start	*x* end
9	20.4	16.5	_am		
			_am2/3	11	22.9

Table 4.2 Layout of *stmet3d.xls*, with inputs and outputs for model *stmet3d.f*

To improve feedback from the program during run time, the main program was modified to write it's current scanning position (current layer, scan and heat step) to screen. This occurred at step 4 in the flow diagram, Figure 4.1. The modification was made because in trials, certain input parameters were found to slow or freeze the model's progress during running. In case of the program

crashing or temperature fields failing to converge in the FE heat calculation, the position of the problem's occurrence would now be known. This became important due to the possibility of modelling larger parts, because running the program once could involve hundreds of heat steps.

Two other feedback features were added. At the end of program execution (step 16 in Figure 4.1), total run time was reported for performance records. The maximum number of cool steps required, with corresponding scan, were now reported. This indicated how quickly scans cool to solidification once the laser heat input had ended.

New formatting was applied when writing nodal density and temperature output to *Rhoplot* text files (step 15 in the flow diagram). Density and temperature data files were typically of 50-90 MB size, which soon filled up a PC hard drive and took time to burn to CDs. Attention was therefore turned to reduction of output file size. Redundant space characters were found to be present, and the number of significant figures for output values was greater than could be represented graphically (the Fortran 95 default being 6). The new formatting reduced file sizes by a typical 40 percent.

4.5 Handling of Model Output- Visualisation

It was more important than ever to have good visualisation of the model's output- the changes described in Section 4.2 meant that larger and more complex parts were being modelled. A 3D view of the modelled part was desired. This would be more useful than sectional views for communicating the general form of the part, and would help in diagnosing problems with the model or the process. This role of communication and verification is similar to that of rapid prototyping, described in Chapter 2. Scripts were developed to better visualise the model output, using two pieces of software. This work relates to the post processing step, number 17 in the flow diagram Figure 4.1.

4.5.1 Use of GSharp Software

GSharp 2D contour plots have been useful to see how density varies with position in cross-sections of parts. Referring back to Section 2.5.2.4, Tontowi and

Volpato first developed scripts to analyse the output of *stmet3d* in this way. Volpato added the writing of *Rhoplotx* and *Rhoplotz* output files to *stmet3d*. These two files contain the same co-ordinate and property data as *Rhoplot* mentioned before, but re-ordered to describe the powder bed as slices in planes of constant x and constant z respectively.

As part of this work, Volpato's GSharp script was changed to add the name of the file being analysed to output graphs, then from there was modified in 2 directions. The first version was modified to display first 3 then 1 x-y slices rather than y-z slices for the process mapping work of Section 4.6 below. The growth of parts in the scan direction could then be analysed. A second version was developed for single layer cross-section dimensional analysis work: refer to Appendix D for a copy of the script. A demonstration graph is displayed in Figure 4.3. Here, a single y-z plane cross-section is viewed. A 0.2mm grid is superimposed onto the section for manual examination of the image. Area colour mapping of density was made more suitable for the application, by reducing the number of colours from 10 to 3. Each colour (dark grey, light grey and white) represented a material state through the chosen density interval: unprocessed powder, partially densified powder and solid material.

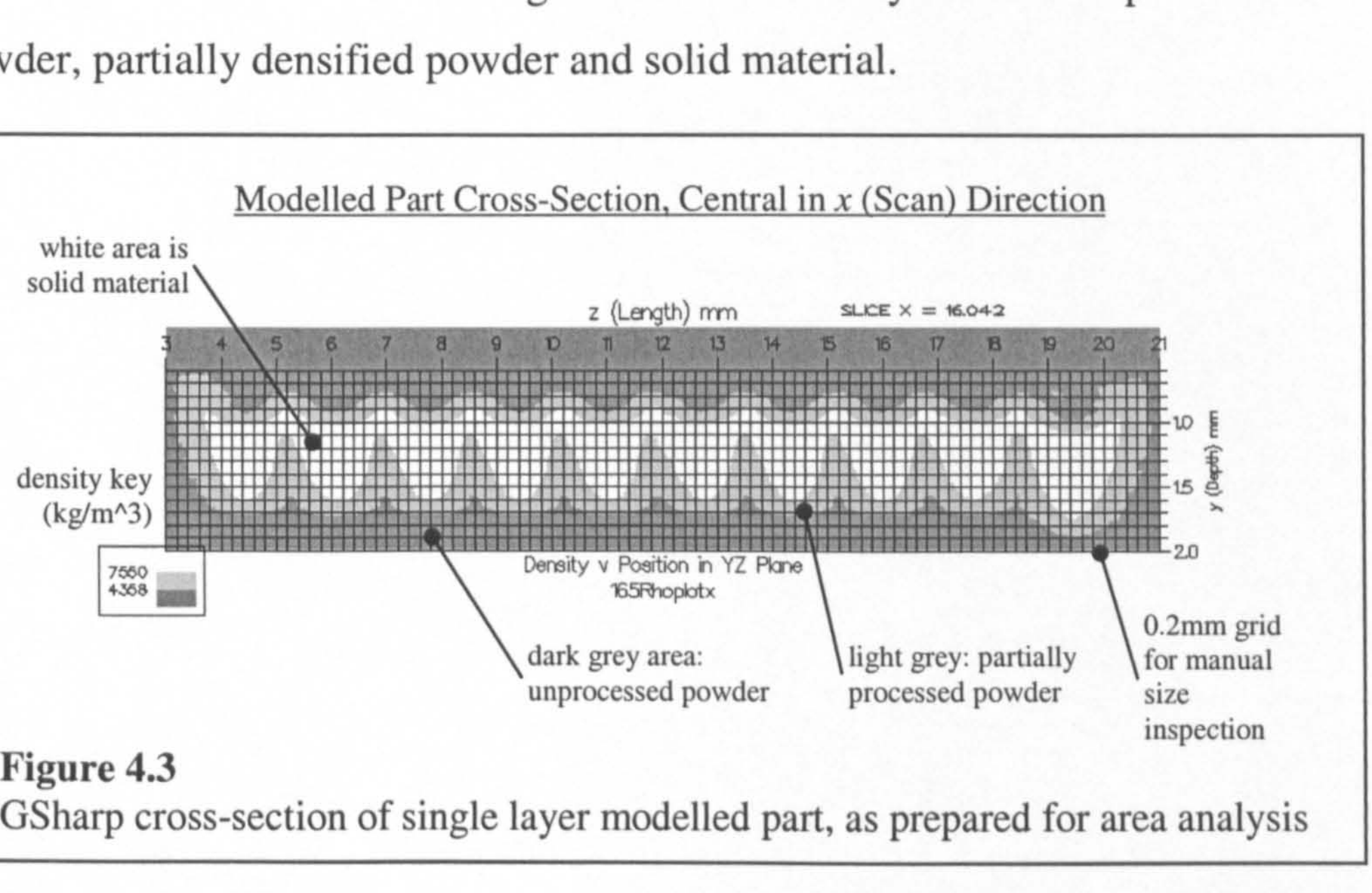

Figure 4.3
GSharp cross-section of single layer modelled part, as prepared for area analysis

A slight modification was made to prepare modelled parts for automated cross-sectional area evaluation. The grid of Figure 4.3 was removed. Solid material appeared as white, which allowed Image-Pro software to distinguish it from the surrounding area. Area evaluation by Image Pro is described later, in Section

5.2.3. The aspect of the graph was adjusted in the GSharp script, so that when saved as a jpeg image, it had the same number of pixels per modelled millimetre in both the *x* and *y* directions. A further version had solid material appearing as black on a white background, for reporting purposes. Such black-on-white sectional images will be seen in Chapter 7.

4.5.2 Use of Matlab Software

Matlab 6 by The MathWorks, Inc. was investigated because it has many 3D visualisation functions. A method of generating perspective views of modelled parts was sought. A script was developed for this software, refer to Appendix E for a copy. Matlab read all values from a *Rhoplot* text file into a 2D array, then rearranged values into four 3D arrays, a form compatible with Matlab's 3D graphing functions. Three arrays were for *x*, *y* and *z* co-ordinates in the powder bed, the fourth was the plotting quantity (which could be either density or temperature). The script then ran a command "Isosurface" to generate a surface linking all points at a specified value of the plotting quantity: connecting all points at which density was equal to 7500kg/m^3 provided the surface of the solid part. Isosurfaces could be set to be semi-transparent as well as opaque, to create 3D contour maps. To accentuate particular features of the visualised geometry, the viewing and lighting angle were specified. A grid and title/ axis labels were added.

Perspective and Bottom View of Modelled Single Line Temperature Field

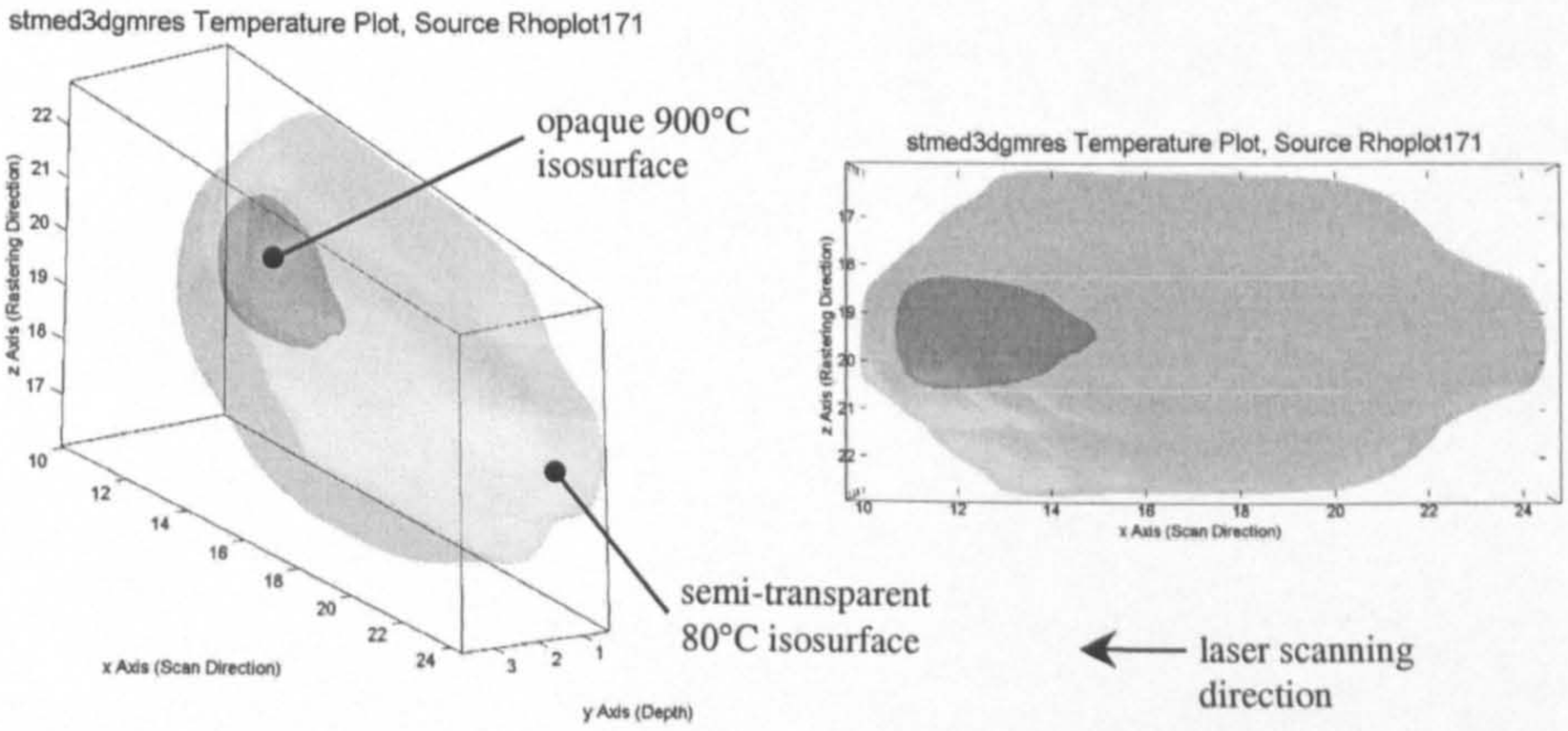

Figure 4.4 Matlab-generated temperature isosurface plots

In Figure 4.4, a perspective and bottom view of a modelled (scanning laser-induced) temperature profile is provided as an example of what is now possible. The temperature in the thermal mesh can be seen to reduce with distance from the laser heat application zone. Matlab was initially applied to examine single and twin scans in 3D for the first time. It was then used on temperature data as in Figure 4.4, to investigate freezing of the program during running. Its main use however was for process mapping, see Section 4.6.

4.6 Process Mapping for Model

The ability to see modelled parts in 3D has provided a good opportunity to benchmark the model. Single layer parts were made for the study, consisting of 10 parallel scans, each of 10mm length. The model was run with parameters (*s*, *P* and *U*) spanning the feasible range. The resulting part was examined then classified against parameters, similar to the process mapping studies based on real parts in Section 2.2.6.1 (see Figure 2.16). In 4.4, it has been mentioned that certain input parameters caused *stmet3d* to freeze in execution. If this occurred, it was also marked onto the process map to see if a pattern would emerge. If the temperature field failed to converge to the pattern dictated by the heat equation to within a set tolerance, a notification was printed to screen and steps 5, 6, and 7 of Figure 4.1 were repeated until convergence criteria were met. If the criteria were never met, an infinite loop occurred.

Input material properties were those of stainless steel powder, as stated in Section 4.1. A range of power *P* from 0 to 200 Watts was used, the power available in the experimental rig. *U* was taken from 0 to 70 mm/s, at which point the energy density A_N was too small to create coherent parts even at maximum *P*. Scan spacing of 3/6, 5/6 and 9/6 times the laser beam diameter *d* was the same set chosen for single layer analysis of manufactured and modelled parts in Section 3.14. *s* ranged from the minimum to the maximum likely to occur.

In each modelled part, two values of absorptance were used, each one applied over five scans. This was done to generate results more quickly and save time. It had been found that the scan depth tends to a steady value after three rastered scans.

The objective of process mapping was to check that the model ran appropriately over the parameter ranges of interest, and to see the pattern of part characteristics against parameters.

4.7 Verification of Model against Experiment- Use of Image-Pro Software

Papers reviewed in Section 2.6 demonstrated a keen interest in the use of numerical SFF process models to direct machine parameters in a feed-forward process control (FFPC) system. However, before this is possible the model to be used has to be verified to prove that it can accurately anticipate the process outcome in all possible situations. As a result, the fitness of Childs' *stmet3d* program was tested in a feedback mode. Sectioned 10-scan single layer manufactured parts created in Section 3.14 were compared against modelled part cross sections. A morphology (shape) study of manufactured and modelled parts helped to assess the model's accuracy and realism.

The same input parameters were used, the same single layer shape was scanned and the same measurements were made on cross-sections of modelled parts as for manufactured parts. Cross-sectional views were created in the *y*-*z* plane at the part's centre in the scanning direction as for manufactured parts (illustrated in Figure 3.13). The GSharp script described in 4.5.1 was used to generate 3-colour sections with no grid. Selection and use of Image-Pro software for the analysis of cross-sections is discussed in Section 3.15.1 and Section 5.2.3. Comparison of morphology occurs in Chapter 7.

CHAPTER FIVE

5 PROCESSING OF RESULTS

This chapter explains how raw experimental data and model output from activity in Chapters 3 and 4 are converted into the desired form. Examples of processing procedures are provided for clarity. Results and discussion of results can be found in Chapters 6 and 7.

5.1 Thermal Experiments

A record was kept of all thermal experiment parameters, found in Appendix A as indicated earlier. Examining page 1 of Appendix A (infra-red camera experiments), graphs 1 to 18 were plotted to test the camera system and to contribute data towards the thermal field study. Certain graphs between numbers 19 and 45 were used to calculate k for stainless steel 314S HC, d_p of 75-150μm, processed in air. Graphs 46 onwards contributed towards the thermal field study, and were used in an attempt to measure α directly by recording peak temperatures in the melt pool. Peak temperatures could not be identified from graphs due to laser interference: readings demonstrated a large degree of noise within the critical time interval.

On pages 2 to 4 of Appendix A, date-coded thermocouple experiments are listed with the corresponding conditions. For experiments which contribute towards thermal property calculations a series number is quoted, linking experiments with results as tabulated in Chapter 6. Other than for thermal property measurement, thermocouple experiments were carried out to test the measurement method (040200), study end effects (170500, 120700 and 130700 up to n3) and to contribute towards the thermal field study (full range of results).

5.1.1 Powder Density

One of the values required to determine the thermal properties of a powder was its density. This was measured using a cup, scales and water. Section 3.9 describes the method by which readings are obtained.

New subscripts for use in this section are provided:

P= powder, *W*= water,

CE= empty cup, *CF*= cup full (of powder/ water).

The empty cup was weighed (m_{CE}). The cup was filled flat to the top with water and weighed ($m_{WCF} + m_{CE}$).

The cup was then filled with loose-packed powder and the surface of the powder was wiped flat to the top of the cup with a ruler. The cup was weighed to find the total mass ($m_{PCF} + m_{CE}$).

Calculations were made using the results:

[1.] $(m_{WCF} + m_{CE}) - m_{CE} = m_{WCF}$ (mass of water needed to fill cup).

[2.] $\rho_W = 1000 \text{kg/m}^3$, therefore $V_{CF} = m_{WCF} / 1000$.

[3.] $(m_{PCF} + m_{CE}) - m_{CE} = m_{PCF}$ (mass of powder needed to fill cup).

[4.] $m_{PCF} / V_{PCF} = \rho_P$.

Example for stainless steel powder- 314S HC, d_p of 75-150 μm

Measurements: $m_{CE} = 30.2$ g,

$m_{WCF} + m_{CE} = 42.92$ g, $m_{PCF} + m_{CE} = 89.67$ g

So:

[1.] $m_{WCF} = 12.72$ g

[2.] $V_{CF} = 12.72 \times 10^{-6}$ m^3

[3.] $m_{PCF} = 59.47$ g

[4.] $\rho_P = 4680$ kg/m^3.

5.1.2 Thermal Field Study

The objectives of this study were described in Section 3.10. The thermocouple and infra red camera systems were used to record temperature versus time and position during direct SLS. It was hoped to discover some useful observations and rules concerning change in temperature related to the parameters *P*, *U*, *x*, *y*, *z* and *t*.

Output files from the National Instruments thermocouple logging software used are of a specific format. A few initial lines are provided to state the date and other relevant information, then tab delimited data follow. Each row of data corresponds to a moment in time. Column 1 contains the time at which readings were taken, then the following 6 columns provide temperature readings for each thermocouple channel in degrees Celsius. Output files were imported into Microsoft Excel 97, then viewed as line graphs. An example of graphed logger output looks as shown in the temperature versus time graph, Figure 5.1. The three curves shown in the figure are for different values of P at a constant U and measurement depth y.

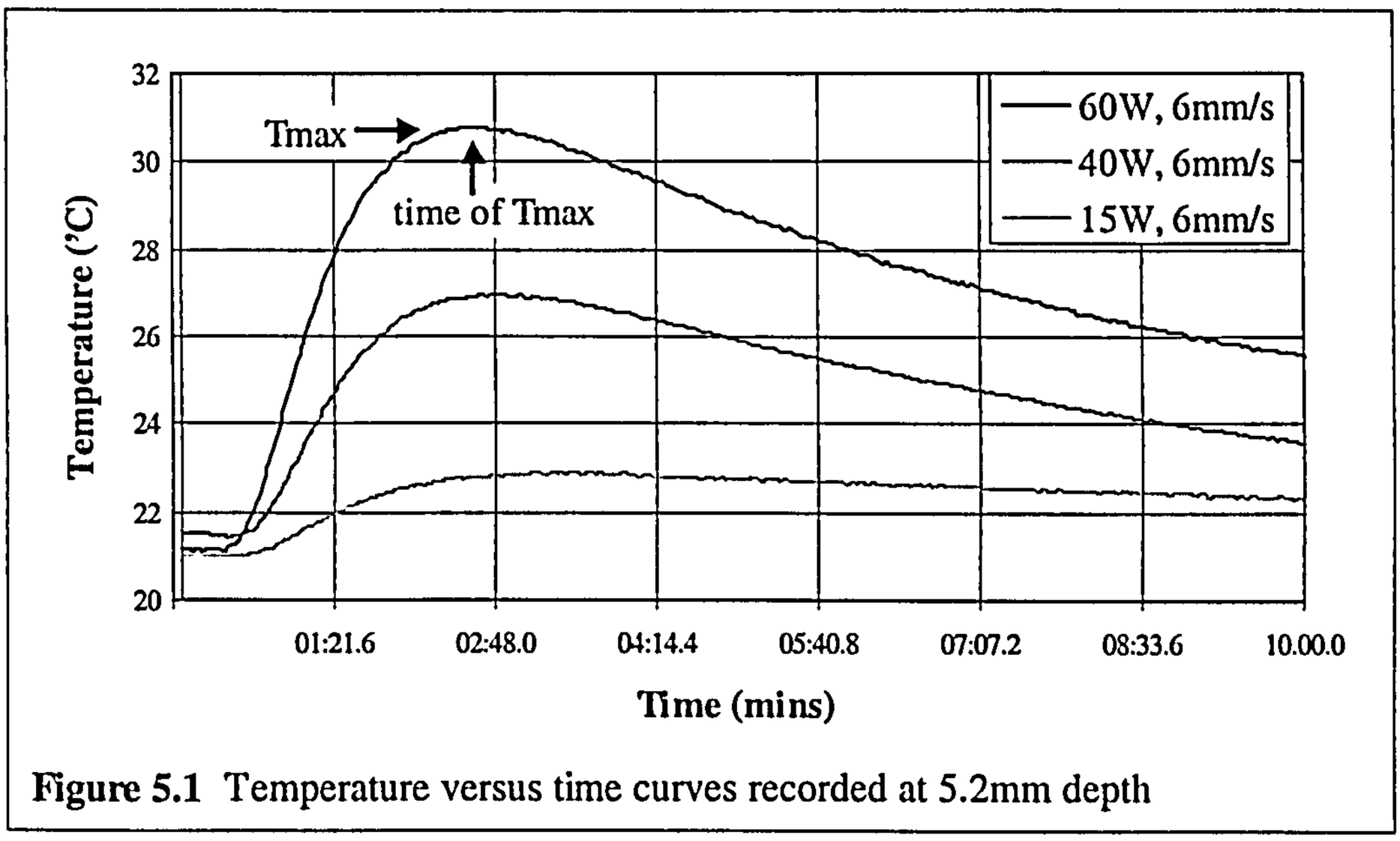

Figure 5.1 Temperature versus time curves recorded at 5.2mm depth

5.1.3 End Effects Study

First introduced in 3.11, this study made use of temperature versus time curves similar to those shown in Figure 5.1. From each curve (representing a different junction position), T was selected out at 5 moments in time. A single graph was created, of temperature versus x at the 5 points in time, which can be seen in Section 6.4.1.

5.1.4 Thermal Property Measurement

A procedure was developed to calculate the powder bed thermal properties k and α using experimental data. Spreadsheets were created on Microsoft Excel 97 for this purpose. All Excel spreadsheets are made available on a CD attached to the back cover of this document, so that the source data and methodology can be examined. See Section 6.5 for more details of spreadsheets. The same calculation procedure was used for single lines and relased single lines. For single layers, the equations used were slightly different. An example of the procedure followed for single lines is provided in 5.1.4.1, then the elements which differ for single layers are described in 5.1.4.3.

5.1.4.1 Single Lines

Following the experiments of Section 3.12.3, output files of temperature against time were generated, as described in Section 5.1.2. Output from each channel took the form of a curve, rising then falling with time as shown in the graph, Figure 5.1.

Around 30 curves of temperature versus time were collected in each experiment, in groups of 6 per output file. dT_{max} and t_{Tmax} were extracted then graphed in groups to reduce random error in calculating k and α. The method of transforming results into dT_{max} and t_{Tmax} then into k and α is provided below.

[1.] Text files, containing 6 columns of temperature-time data, were read by the Fortran program described in 3.12.6. The program selected out the initial and maximum values of temperature in each column, with corresponding times. These were written to the PC screen by the program.

[2.] Initial and maximum temperatures with corresponding times were tabulated in rows on Excel. The conditions corresponding to each measurement were added to the relevant rows: P, U and y.

[3.] Excel calculated the difference between the initial T, t values and those corresponding to the maximum temperature. The difference values are dT_{max} and t_{Tmax}.

[4.] Excel also calculated the quantities y^2 and $P/(U.y^2)$.

[5.] Graphs were created of t_{Tmax} versus y^2, and dT_{max} versus $P/(U.y^2)$. See Figures 5.2 and 5.3 for examples.

[6.] A straight line was plotted on each of these graphs. The gradient of the line was used to calculate the thermal properties looked for. Considering equations (3.4) and (3.9) from Section 3.2:

- Gradient of t_{Tmax} versus y^2 is equal to $1/(4\kappa)$ or $\rho.C/(4k)$.
- Gradient of dT_{max} versus $P/(U.y^2)$ is equal to $0.234\alpha/(\rho.C)$

[7.] For these two cases the known values are entered, to leave one unknown quantity in each case: k and α respectively.

The linearity of points and the intercept of the line of best fit in the graphs helps to validate the infinite line heat source assumption made.

Examples are now provided for different situations, with reference to the graphs Figures 5.2 and 5.3.

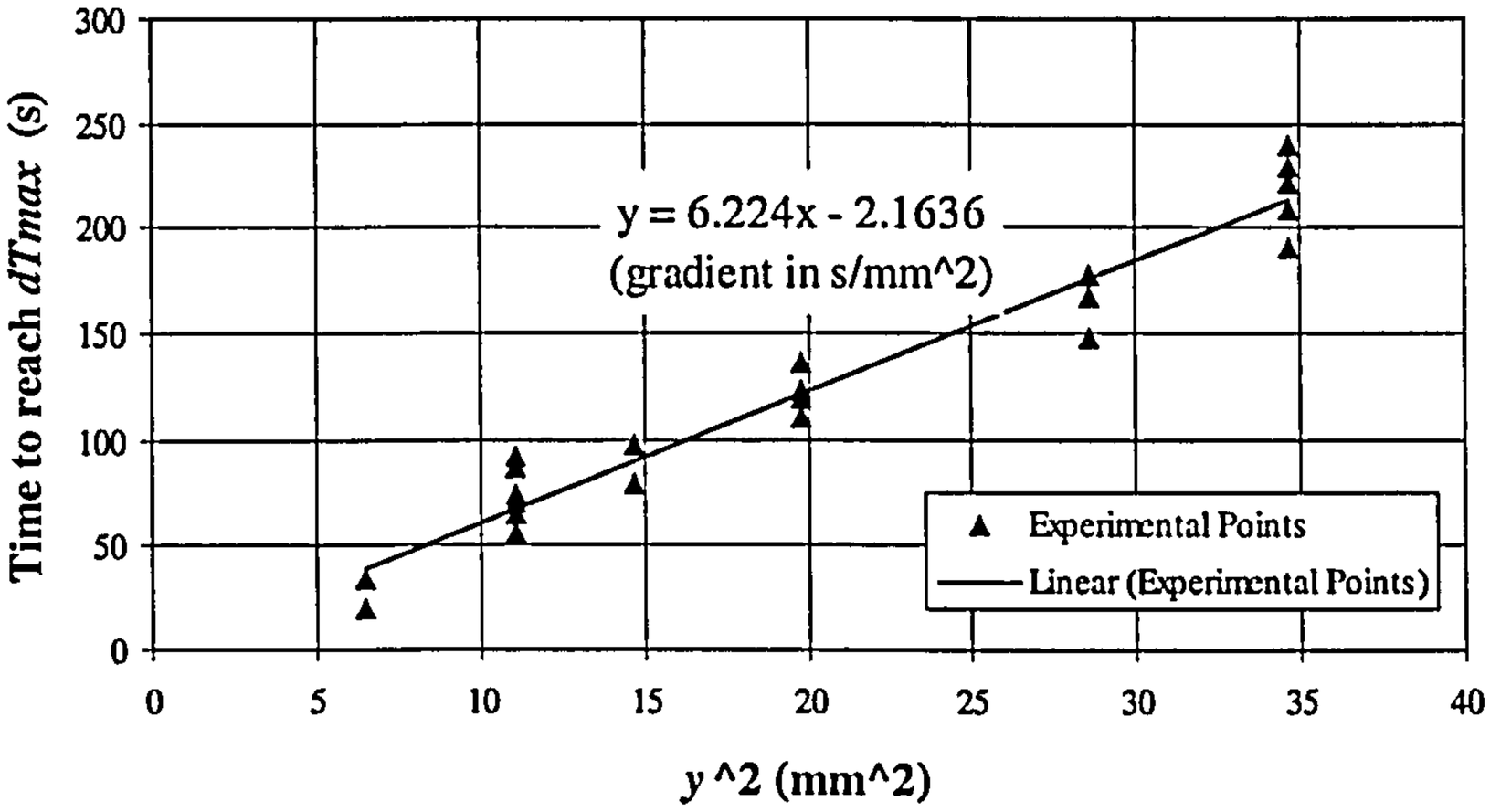

Figure 5.2 Time to *dTmax* versus y ^2 for 314S HC single line in argon

1. Conductivity of 314S HC, d_p of 10-20μm in argon (full conditions are as Series 1.2, Table 6.2 in Chapter 6 later):

- From Figure 5.2: $t_{Tmax} = 6.22\times10^6 y^2$
- $\rho.C/(4k) = 6.22\times10^6$ s/m^2

- For 314S HC 10-20μm, ρ measured as 3914kg/m^3
- For stainless steel 314, value of C at 20°C assumed, 460 J/(kg.K) [Holman 1997]
- 1 remaining unknown: for 314S HC 10-20μm in argon, k=0.15W/(m.K)

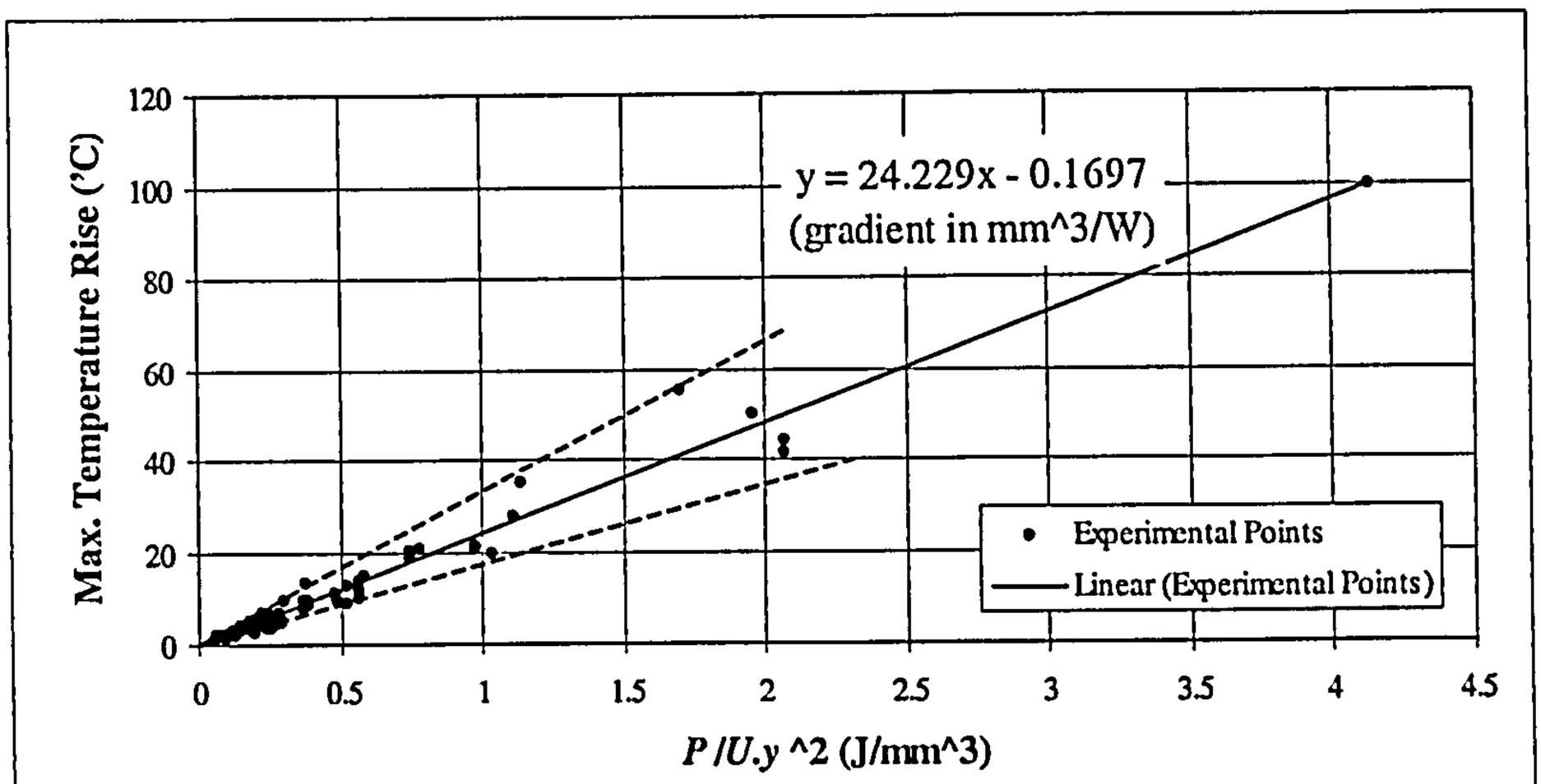

Figure 5.3 *dTmax* versus $P/(U.y\text{^}2)$ for 314S HC single line in air

2. Absorptance of 314S HC, d_p of 75-150μm in air (full conditions are as Series 1.1, Table 6.2 in Chapter 6):

- From Figure 5.3: dT_{max} =24.23×10^{-9} $P/(U.y^2)$
- $0.234\alpha/\rho.C$ =24.23×10^{-9} m^3/W
- For 314S HC 75-150μm, ρ measured as 4675kg/m^3
- For stainless steel 314, value of C at 20°C assumed, 460 J/(kg.K) as above
- 1 remaining unknown: for 314S HC 75-150μm in air, α=0.21

Values of C for Rapid Steel 2 and M2 materials were taken as 479 (measured by [Volpato 2001]) and 460 (assumed the same as 314S) J/(kg.K) respectively.

Conductivity in the case of stainless steel 314S single line scans processed in air was confirmed with the infra red camera. The camera took 31 temperature-time curves. These were processed in a similar way to that described in the numbered points above. Curves were collected at positions in the z rather than y direction. Printed graphs of T against t had to be examined individually to find

dT_{max} and t_{Tmax}. Graph 43 (as described in Appendix A) is featured in Figure 5.4 as an example. The figure has been marked with the positions of dT_{max} and t_{Tmax}.

Graphs were scanned, then the co-ordinates of the relevant positions were found on Paint Shop Pro version 7.02, JASC Software. Co-ordinates were converted to seconds and degrees Celsius to get dT_{max} and t_{Tmax}. k was calculated using MS Excel 97 as described, but substituting y for z.

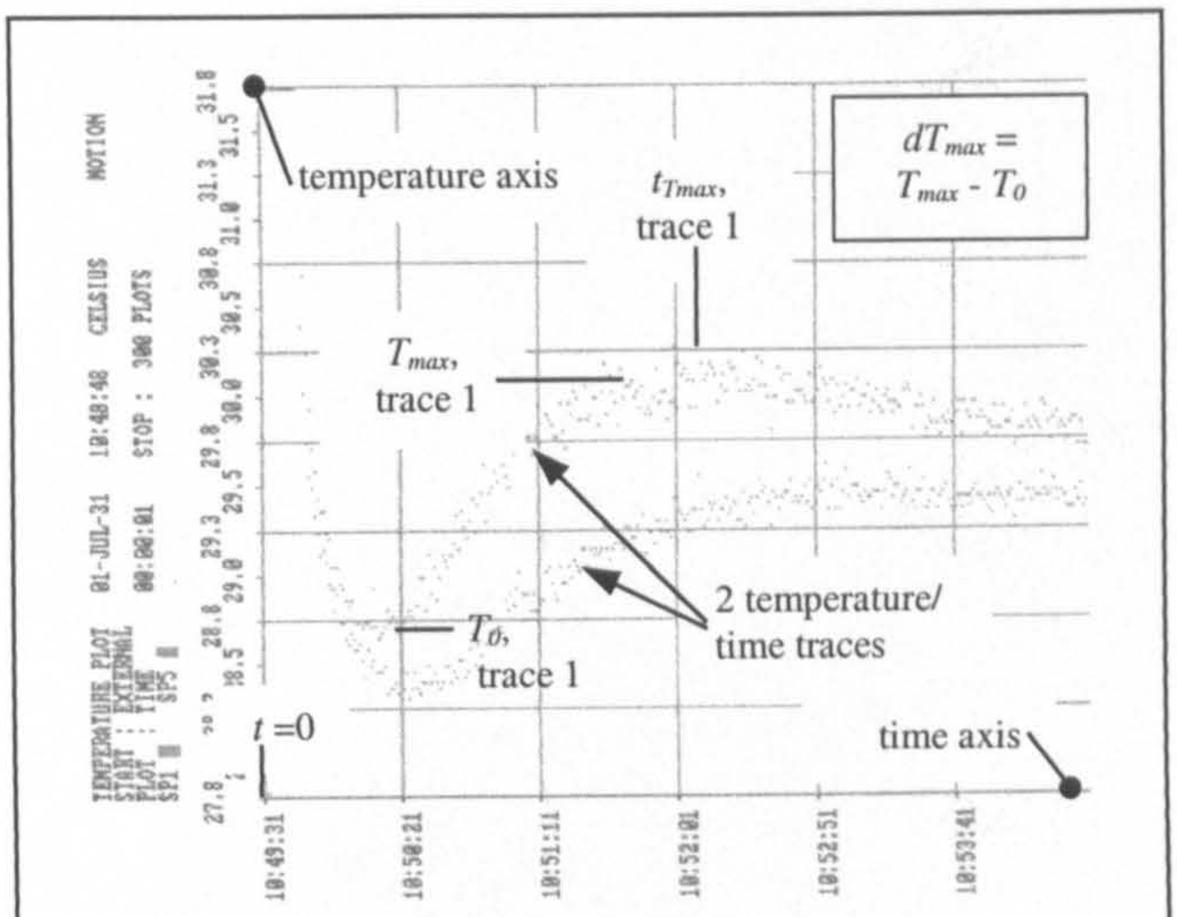

Figure 5.4 Sample infra red camera output

5.1.4.2 Single Line Relasing

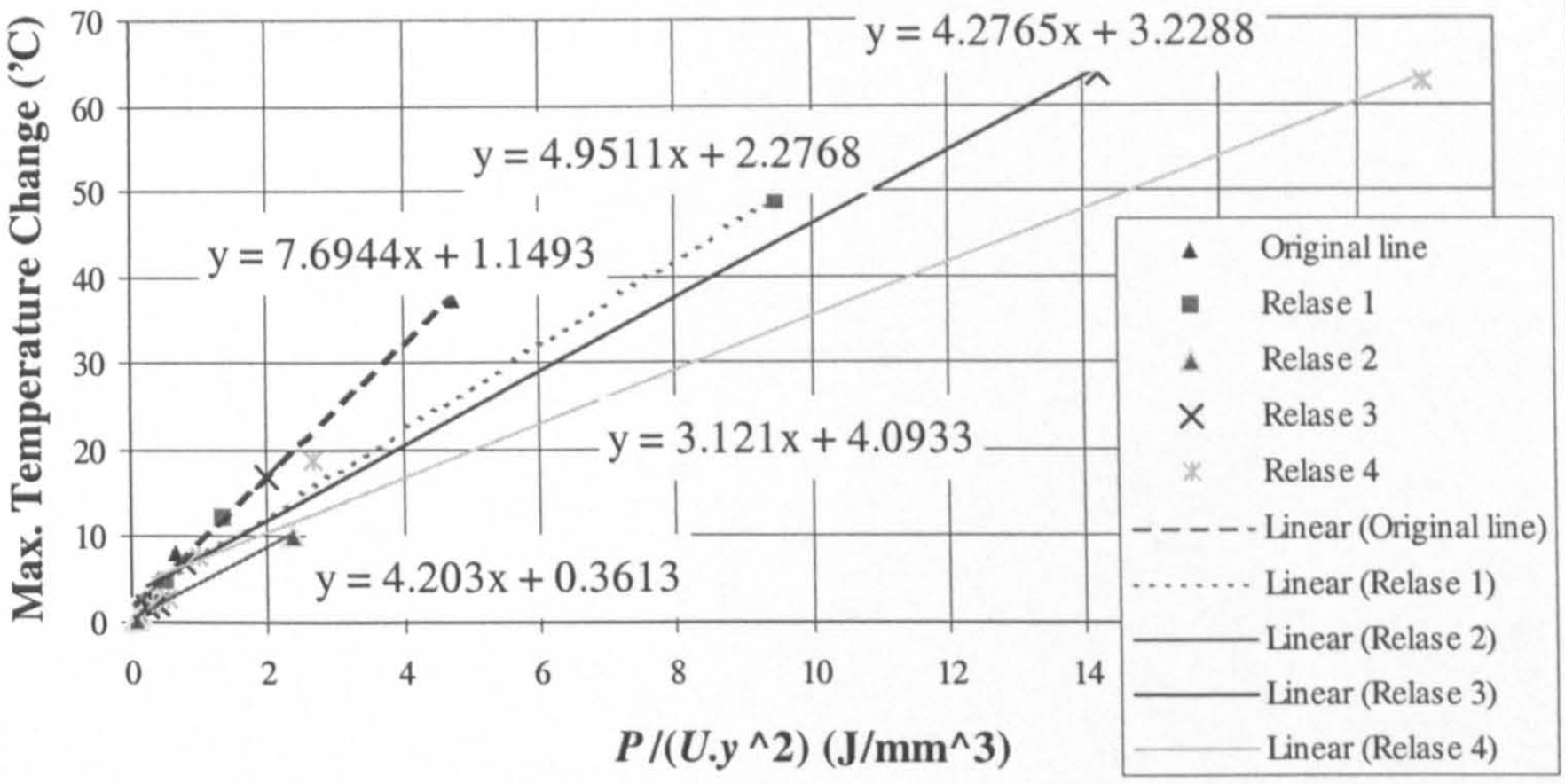

Figure 5.5 Finding absorptance, steel in argon, relased lines

Taking the results generated in the manner described in Section 3.12.4, a procedure identical to that of 5.1.4.1 has been followed to find the change in absorptance of the powder bed as it is processed multiple times with the laser. See Figure 5.5, a graph with a curve displayed for each scan of the laser. The gradient

of the curves diminishes with the number of successive scans. Full experimental conditions are as Series 2.1, Section 6.5.2.

5.1.4.3 Single Layers

Results were gathered as stated in Section 3.12.5. Carslaw and Jaeger's equation for an instantaneous plane heat source was applied. Full experimental conditions are as Series 3.1, Section 6.5.3.

The procedure from 5.1.4.1 for finding k and α can be used for layers if the points numbered 4 to 6 are replaced in the following way:

[4.] Excel calculated the quantities y^2 and $P/(U.s.y)$.

[5.] Graphs were created of t_{Tmax} versus y^2, and dT_{max} versus $P/(U.s.y)$. See Figure 5.6.

[6.] Straight lines were plotted on these graphs. Gradients of lines were used to calculate the thermal properties looked for. Considering equations (3.12) and (3.13) from Section 3.2:

- Gradient of t_{Tmax} versus y^2 is equal to $1/(2\kappa)$ or $\rho.C/(2k)$.
- Gradient of dT_{max} versus $P/(U.s.y)$ is equal to $0.484\alpha/(\rho.C)$.

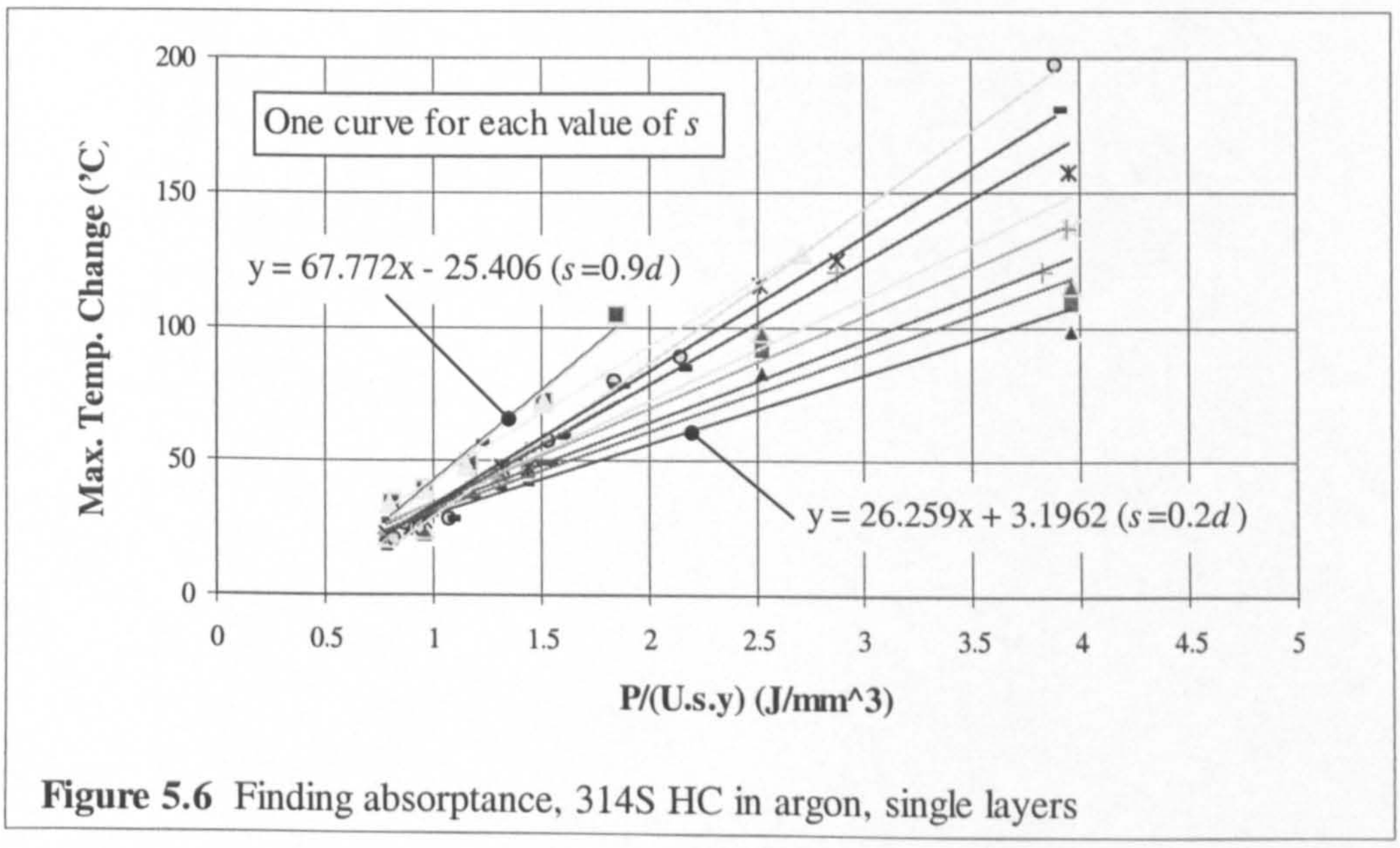

Figure 5.6 Finding absorptance, 314S HC in argon, single layers

5.1.5 Evaporation Study

The results of weighing undertaken in Section 3.13 were processed. There were two experiments: number one at P=160W, U=0.5mm/s, and number two at P=160W, U=1.0mm/s. Knowing the mass measured at various points, changes in mass between the two experimental cases are converted into changes of energy usage to help provide an explanation for the shape change and mass change of scans communicated in Section 3.7.

The mass of processed tracks can be related to the energy absorbed. The equation reported in Section 2.3.1.1 is used:

$$E_M = \frac{m}{L}(C.dT + L_M) \qquad (2.9)$$

m is used to find the energy which contributes to material melting, $E_M.L$, for the two cases studied. L, C, dT and L_M are as reported in 3.7, the same in both cases. The change in E_M is compared to the total laser energy supplied for the two cases.

Also compared between the two cases is the mass lost from the processing zone during processing. If energy is being absorbed by the bed but is not evident in the mass of processed tracks, perhaps it has been lost due to vaporisation. The equation related in Section 3.7 is applied to mass measurements made before and after processing, assuming that the change in mass is caused by vaporisation:

$$E_{LOSS} = m_V(C.dT_{M-V} + L_V) \qquad (3.14)$$

5.1.6 Dimensional Analysis of Manufactured Single Layer Cross-Sections

Area and relative density were evaluated for 27 manufactured and cross-sectioned single layer parts. Evaluation was carried out via digital camera images, of parts manufactured and sectioned as described in Section 3.14. The top image in Figure 5.7 is an example. The solid area and area-based relative density of each section was evaluated using a semi-automated process.

Image-Pro software described in Section 3.15.1 was used to find the area of cross-sections. Firstly a white-on-black mask was generated for area analysis, where white represents solid material. This was done automatically by Image-Pro, exploiting the difference between the colour of the solid steel section and

surrounding epoxy. The boundary between black and white areas was fuzzy in places once the mask had been applied, so some manual touching-up was carried out using Paint Shop Pro version 7.02, by JASC Software. The result can be seen in the bottom image of Figure 5.7. Image-Pro can then evaluate the white area in square millimetres, given a dimensional calibration factor. This factor was provided via the grid overlaid onto profile-projected parts, as in the top image of Figure 5.7.

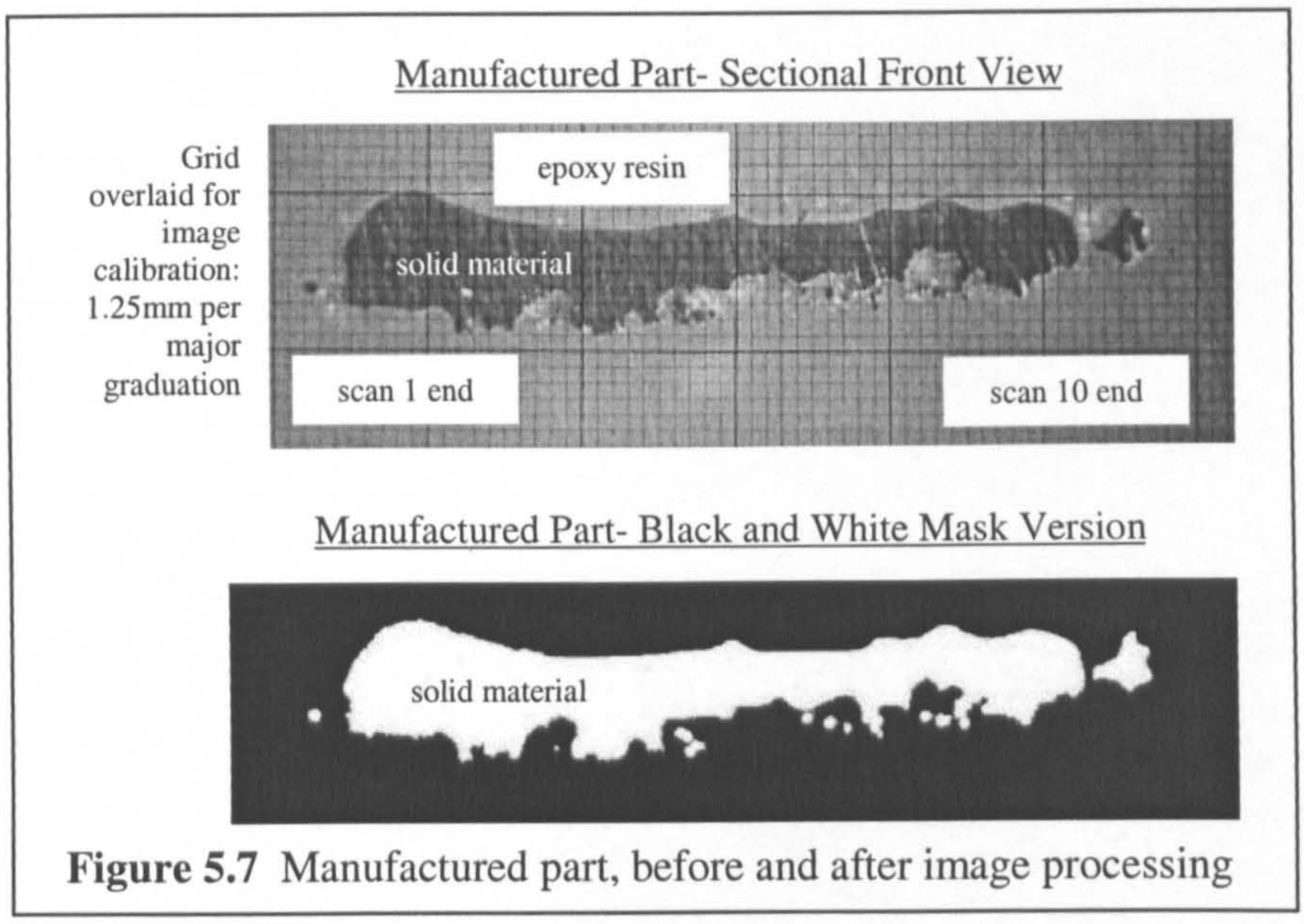

Figure 5.7 Manufactured part, before and after image processing

A line was overlaid onto the image, then the length of the line in the image was input in mm. A command was used to get a report of the sectional area in square millimetres. Where a section had several areas separated by pores, a statistics option was used to see the sum value of constituent areas. Image Pro can automatically generate a convex hull around a section, then evaluate the area within this hull. The convex hull feature was used to calculate the area-based relative density of parts.

The thickness and roughness of layers, changes in thickness and roughness and the shape of the constituent scans (if these are discernible) have been inspected manually. Results are presented in Chapter 6 (general comments on single layers) and Chapter 7 (dimensional analysis of single layers).

An estimate has been made of how much worker time per part was required to generate white-on-black layer cross sections. The stages are: making parts, setting

them in epoxy, sectioning, resetting in epoxy, grinding and polishing, profile projection and photographing, mask creation and touch-up. 50 minutes per part is estimated.

5.2 Numerical Modelling

A record was kept of all parameters input to the model (*stme3dat* files), an abbreviated version of which can be found in Appendix F. Each running of the program was allocated a number: input and output files were named accordingly. 190 runs were executed, for the purposes stated in Chapter 4. Below is an account of how the output of *stmet3d* was processed in various ways.

The results and discussion from this work can be found in Chapter 7.

5.2.1 Visualisation of Model Output

5.2.1.1 Use of Matlab Software

The Matlab script was run on *Rhoplot* files one by one. Two versions of the script were used: the most popular of these automatically generated 3D views of parts from density versus position data. The second version was used to make 3D temperature plots, reading data from the fifth (temperature) rather than the fourth (density) column of *Rhoplot* files. Two views of each part were created as standard: one diagonal perspective view and one end view (in the *y*-*z* plane). These were saved as jpeg format images. Occasionally, if the two standard views did not provide enough detail of the part, other views were examined.

For process mapping use, the *x* to *y* to *z* aspect was set to automatic, which allowed the part's shape in the *y* (depth) direction to be accentuated, the *y* being the shortest dimension in single layer parts. For the comparison of modelled versus manufactured parts, the viewed aspect is set to reflect the actual size: 1 to 1 to 1.

5.2.1.2 Use of GSharp Software

Scripts written for GSharp automatically generated sectional contoured views from *Rhoplotx* and *Rhoplotz* files. As was stated in Section 4.5.1, two scripts were developed for different applications. The first was used in process mapping, see Section 5.2.2. Version 2 was used for cross-section dimensional analysis (see Section 5.2.3).

5.2.2 Process Mapping

The Matlab script as described in 4.5.2 was run on *Rhoplot* files. An archive was made of all output geometry: approximately 90 parts were made for the purpose of process mapping. Each part has two α values associated with it (explained in Section 4.6), so well over 100 results were gathered. Examples of 3D visualised single layer parts are provided in Section 7.2.1.

Five classifications were devised to express the quality of modelled parts, based on general observations. These classifications were:

(1) Successfully modelled layer;

(2) Insufficient material melted (i.e. adjacent scans did not join up);

(3) No material melted;

(4) Depth not tending to steady state (i.e. out of control part growth);

(5) Heat calculation non-convergence.

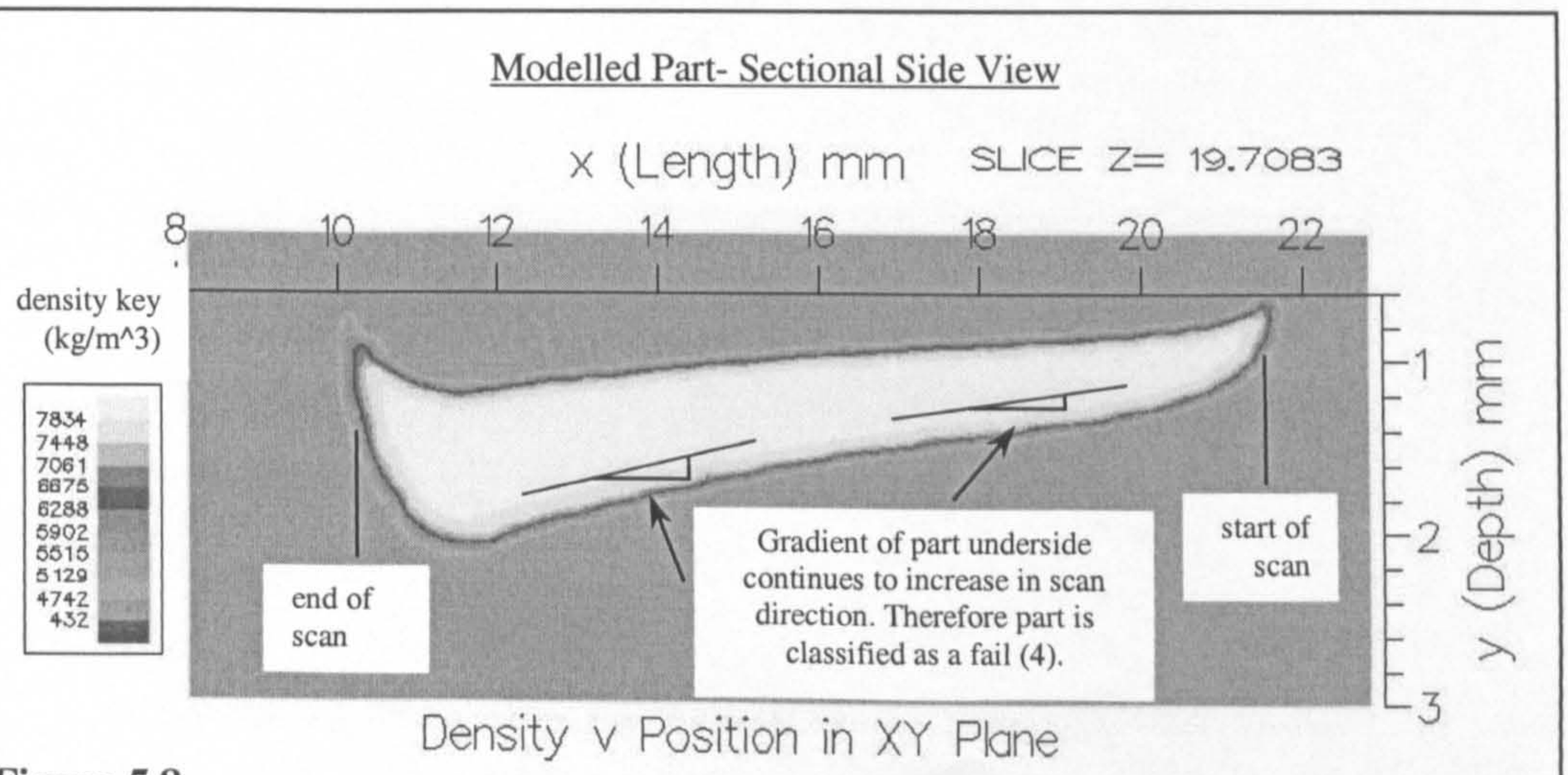

Figure 5.8
Use of GSharp images for decision making in model process mapping

Only classification (1) represents a "pass", the other 4 classifications represent parts which are not considered useful (2 and 3) or have not been modelled adequately (4 and 5).

Some parts were easy to categorise based on examination of Matlab plots: for instance, where adjacent scans did not join together. If it was not possible to categorise parts from the 3D image, GSharp was used on relevant *x*-*y* sections. This was mainly required to ascertain whether part growth was out of control. It had to be judged whether the growth gradient, dy_{SCAN} / dx, was reducing in the scan direction -*x*. An example is shown in Figure 5.8. Points were assembled on 3 graphs of *P* against *U*, one graph for each of 3 values of *s*.

5.2.3 Dimensional Analysis of Modelled Single Layer Cross Sections

Cross-sectional area and relative density in *y*-*z* slices of modelled parts were evaluated for comparison with sintered layers. The purpose of the comparison and method for generating modelled sections were described previously in Section 3.14. The procedure for analysing the area of cross-sections was the same as is described in Section 5.1.6, except that the initial stages were not required.

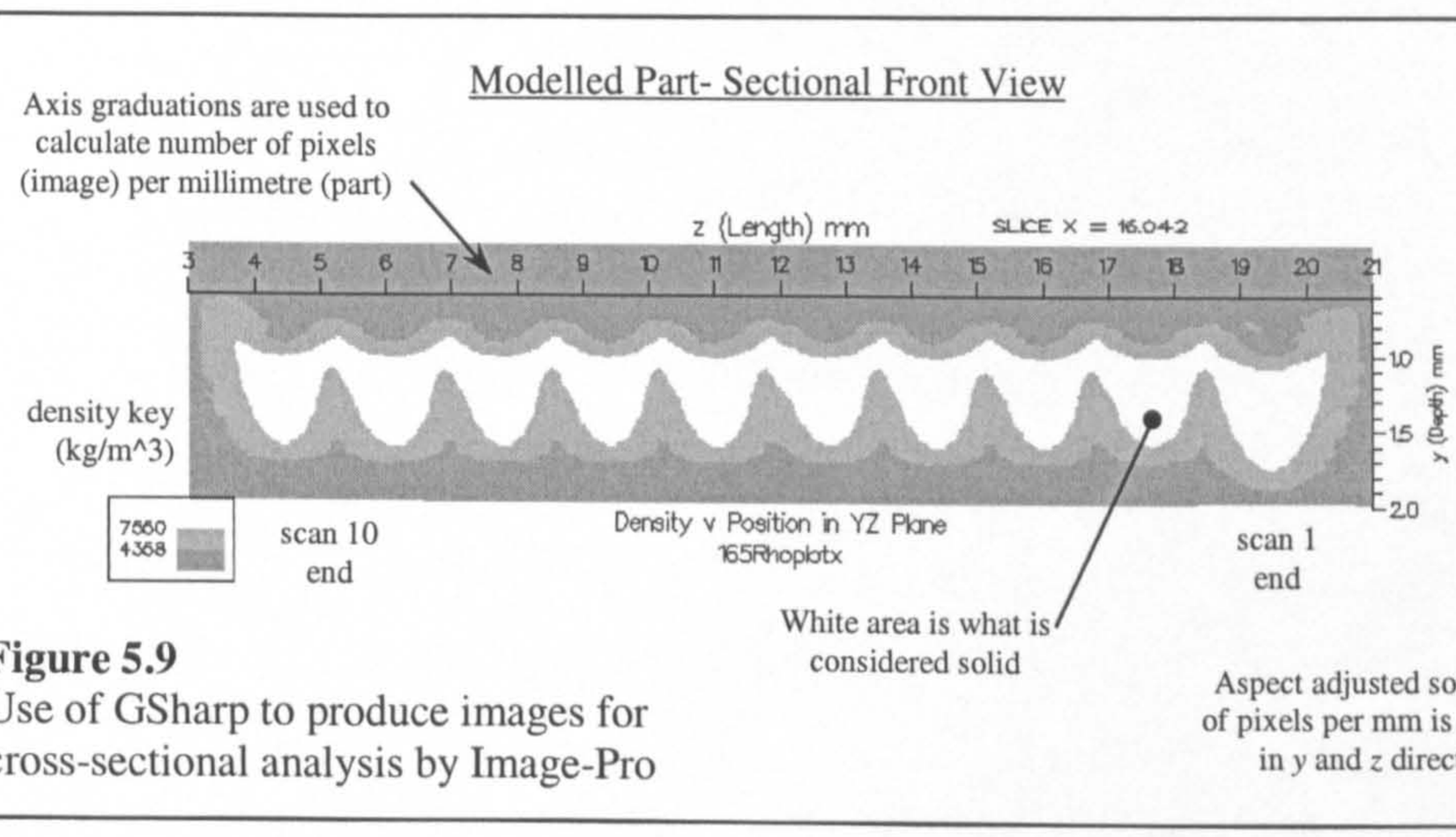

Figure 5.9
Use of GSharp to produce images for cross-sectional analysis by Image-Pro

In 4.5.1, a GSharp script is described which was developed specifically for single layer sectional area analysis. See Figure 5.9 for sample program output. The solid part is already denoted by a sharp colour change from grey to white. This means creation of a colour mask as required in 5.1.6 is not necessary. The

axis graduations applied by GSharp were used for image calibration purposes, much as the overlaid grid was used in 5.1.6. The calibration factor was the same in both the y and z directions.

The thickness and roughness of layers, changes in thickness and roughness and the shape of the constituent scans (if these are discernible) have been inspected manually. Results are presented in Chapter 7.

In worker time, the generation of modelled black and white cross sections (inputting model data, running the model, transferring the *Rhoplot* files to GSharp, finding the centre slice and saving it as an image) was estimated to take 15 minutes per part.

CHAPTER SIX

6 RESULTS AND DISCUSSION: THERMAL EXPERIMENTS

Results and discussion sections are presented together here, for each set of experiments from Chapter 3. Results take the form of tables, graphs and images. Chapter 6 ends with a summary, and recommendations for future experimental work.

6.1 Powder Density

Results here are as calculated in Section 5.1.1.

6.1.1 Results

The table 6.1 shows the measured density for 5 powder types. Values for 314HS and M2 stainless steel were found experimentally as part of this work. The density of 3D Systems' Rapid Steel 2 is as reported in literature [Volpato 2001, McAlea 2000].

Material Type, Particle Size Interval	314S, 10-20μm	314S, 75-150μm	314S, 150-300μm	M2, 75-150μm	Rapid Steel 2, 22-53μm
Density (kg/m^3)	3914	4675	4609	4435	4210

Table 6.1 Density of powders used in thermal property study

6.1.2 Discussion

Values found here compare well with previously-measured values [Eane 2002]. The powders measured above pack at approximately 56 percent of full density. This value lies at the low

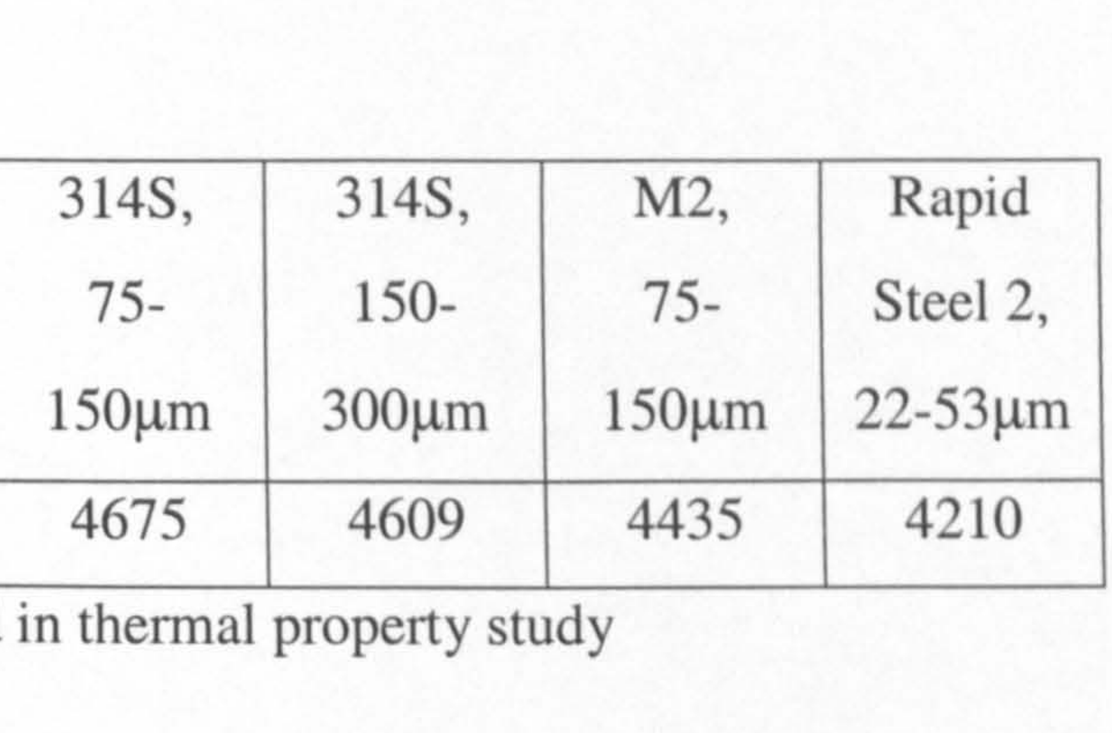

Figure 6.1
Magnified view of steel powder

end of the 52 to 68 percent range determined for perfect spheres in Section 2.2.5. Looking at Figure 6.1, a magnified image of the 314HS 75-150μm steel powder, the particles seen are roughly spherical but have lumps on their surfaces. These are often the result of smaller "satellite" particles which become stuck to them in the atomisation process. Surface lumps would contribute to friction between particles and hence to the low bed density.

The 10 to 20 micron 314S powder had the highest surface area to volume ratio, so inter-particle friction would be the highest; density was the lowest. The 75-150μm 314S had a higher density than the 150-300μm 314S, possibly because the 75-150μm fraction had been sieved and reused a few times, becoming more smooth in the process.

6.2 Thermocouple Calibration and Wire Diameter Comparison

This work was carried out before thermal experiments began, and was described in Section 3.8.1. Figure 6.2 shows the thermocouple readings logged from 5 channels simultaneously against temperature. The gradient of the best fit line is within 4 percent of the value obtained using the manufacturer's chart data.

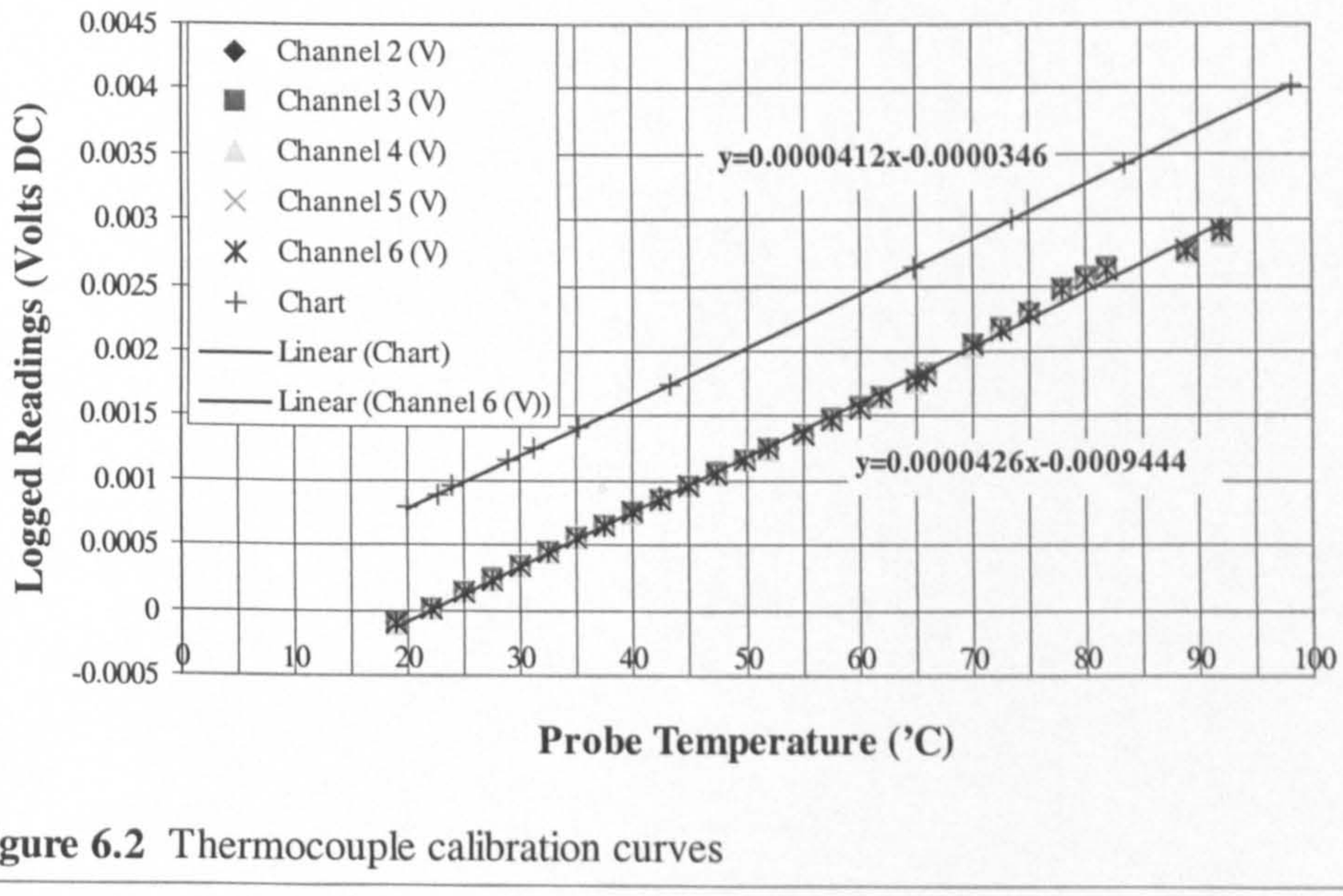

Figure 6.2 Thermocouple calibration curves

A linear relationship is assumed between the thermocouple voltage and the measured temperature. The calibration results are used to find the variables *a* and *b* in equation (6.1).

$$T = a.V_R + b \qquad (6.1)$$

Where T is the temperature in Celsius measured by the thermocouple probe, and V_R is the thermocouple reading in Volts DC. The gradient from the graph was inverted to find that a was 23600. b can be ignored because in all cases, the value of interest is the temperature rise dT, so b cancels out.

A comparison was made between thermocouples with conductor wires of 0.2 and 0.3mm diameter. A step temperature rise of 200°C was applied to the wires to see if their response time was noticeably different. No difference was seen in the two sets of traces on heating, but the traces diverged at low temperature when cooling. The response when heating is most important because once T_{max} has been measured, the remaining data is of little relevance.

6.3 Thermal Field Study

The data examined in Section 5.1.2 is summarised here. Infra red camera then thermocouple results are presented.

6.3.1 Results

Figure 6.3 shows thermal images of the steel powder bed surface during and after SLS laser application. Temperature is represented by tone. White represents high temperature, black represents low temperature. Interference is seen in the top two images, appearing as angled lines. This is caused by infra-red electromagnetic emissions from the laser as it fires.

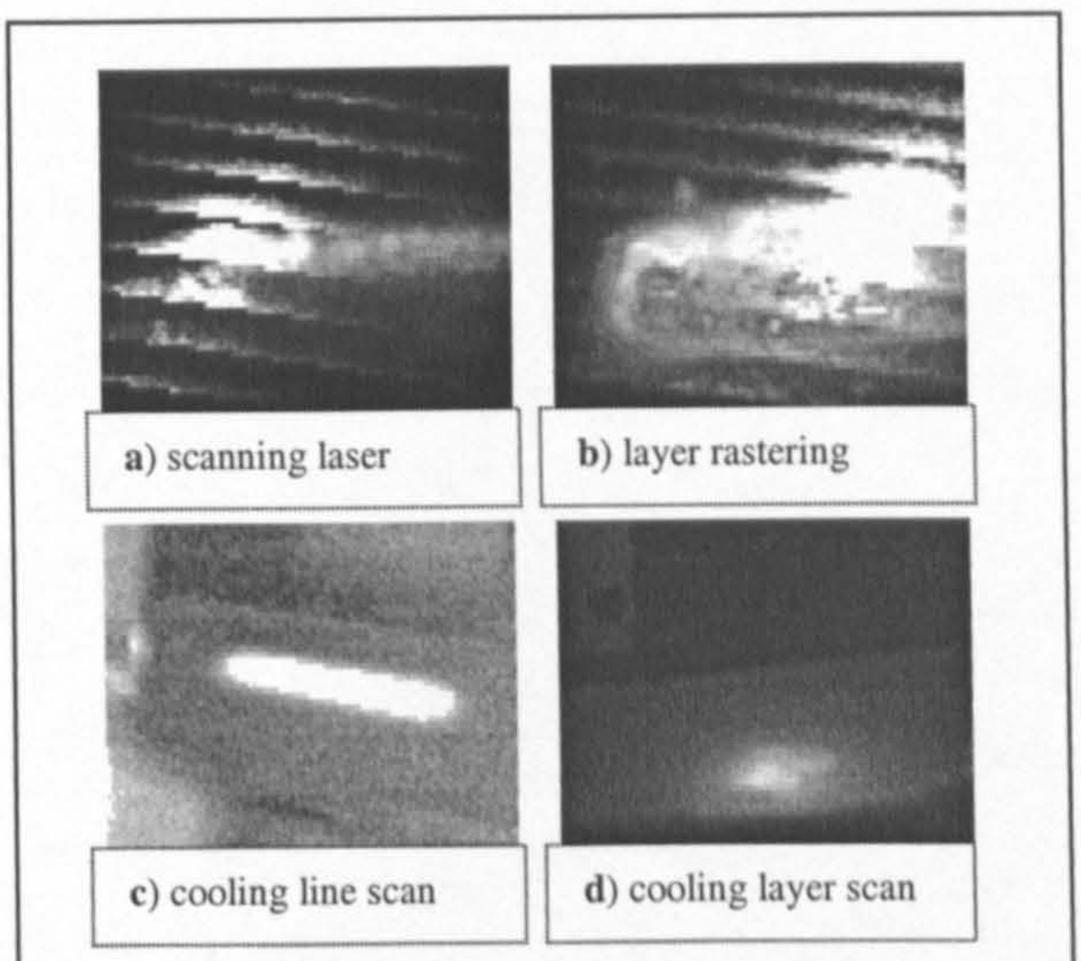

Figure 6.3 Thermal images of metal SLS

Image **a** shows the laser scanning from right to left. The temperature at the centre of the laser application spot was always above the maximum value which could be read by the camera, 1500°C. In the cases studied (power P from 20 to

150W, at scan speed U of 6mm/s), the temperature at a scanned point on the powder bed surface fell below 1200°C in under or around 1 second, once the laser had passed overhead. Material below 1200°C will be in a solid state. Image **b** shows a reversal of the scan direction in bi-directional raster scanning. The scanned path can be seen. The zone around the position of direction change experienced a relatively large exposure time. Temperature remained above 1200°C for up to 3 seconds under the same P and U range as in image **a**.

Image **c** shows a single scanned line, cooling once the laser had been switched off. The processing conditions were P=150W, U=6mm/s. The size of the heated zone surrounding the line was observed: the area where the temperature rise was greater than 10°C did not extend further than 10mm from the perimeter of the line. Image **d** shows a cooling layer. A measurable change in temperature (1 or 2°C) could be observed at up to 20mm from the perimeter of the layer.

In all cases, the scanning laser heated material from room temperature to melting point in an immeasurably small time, well below half a second.

Figure 6.4 shows temperature-time curves recorded by thermocouples placed in a bed of stainless steel 314S HC 75-150μm powder. The laser beam scanned single line tracks directly over the thermocouple positions in an air atmosphere. P, U and y were varied.

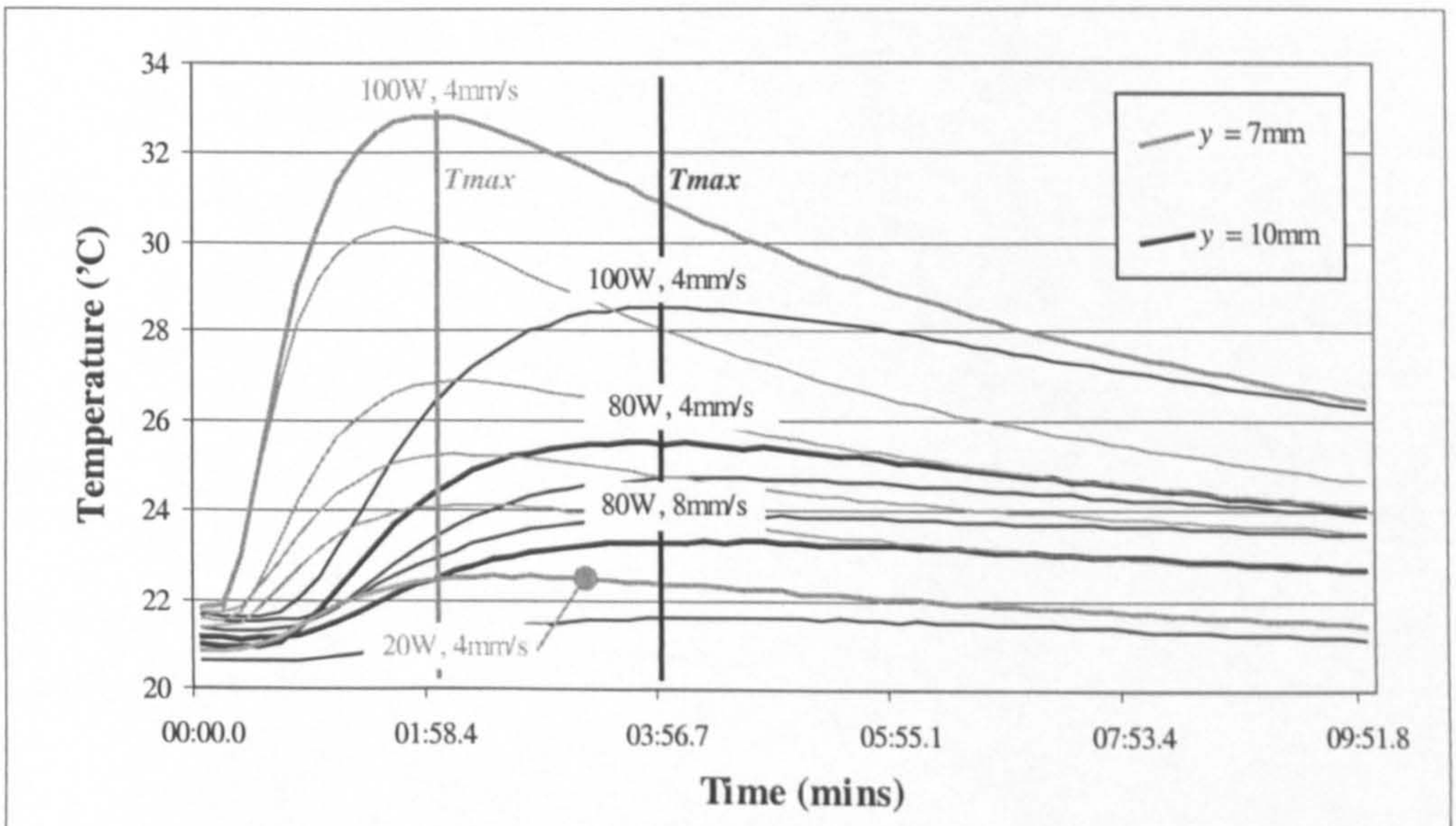

Figure 6.4 Temperature versus time graph. Varying P and U at two values of y

6.3.2 Discussion

Discussing the results obtained by the non-contact method, the infra red camera shows that at the bed's surface, temperatures reached are beyond the material melting point, but only endure in the order of seconds. In the situation for traditional sintering of metals, temperatures are held at a level close to, but below, the melting point for minutes or hours. The non-contact results support the notion of melting as opposed to sintering in the direct single phase metal SLS process. They also support the choice of a time-independent, temperature-based density calculation in Childs' model of the process, as opposed to a calculation based on necking of adjacent particles over time as in viscous sintering.

It has not been possible to obtain an exact temperature profile for the melt pool surface during laser scanning, for the following three reasons:

- Laser electromagnetic emissions interfered with the infra red camera readings;
- Peak temperatures were above the camera's maximum level;
- The laser-induced temperature rise occurred at over 1000°C per second, too fast to be observed in the camera's sample time of 0.46s.

A more modern thermal camera, with a CO_2 laser filter fitted, would provide a more accurate surface temperature profile, which could allow estimates of heat loss by convection and thermal radiation to be made.

Results obtained using the contact method provide an opportunity to comment on the thermal field in the powder bed, with respect to P, U, x, y and z parameters.

Figure 6.4 contains some typical temperature versus time curves, obtained using the thermocouple system. 12 curves are displayed at y equal to 7mm (light-coloured curves) and 10mm (dark-coloured curves) below the position of scanned lines. U was set at 4 or 8mm/s, P was varied from 20 to 100W. Certain curves have been annotated, for comparison.

Some elementary observations can be made based on Figure 6.4 (where parameters not mentioned in the following points are held constant):

- When P is increased, the measured temperature rise increases. This is logical, because the energy supplied to the bed increases.
- When U is increased, the measured temperature rise decreases. Increased U leads to a reduced laser exposure time and therefore less energy input.

- When y is increased, the measured temperature rise decreases and curves elongate on the time axis. These are illustrated by the two curves at 100W, 4mm/s and the vertical lines denoting time to T_{max} respectively. The laser-induced temperature front spreads radially into the powder bed from the laser application zone, reducing in magnitude with depth and taking more time to reach greater depths.
- The time to reach T_{max} is constant at a particular value of y, independent of P and U. See the vertical lines, denoting time to T_{max}.

These four observations were found to hold true in all results gathered. They are predicted by Carslaw and Jaeger's equation (2.20), lending support to the instantaneous infinite line heat source assumption which was made in measuring thermal properties, Section 6.5.

A few key facts have been compiled concerning temperatures measured in the powder bed, using the contact method whilst scanning single lines:

- The highest temperature change read was 320°C, under conditions P=160W, U=0.5mm/s, y=2.1mm. At the same power and speed but with y=6.8mm, the highest temperature change read was 50°C.
- Under the full range of P and U tested, up to 160W and as low as 0.5mm/s respectively, the maximum temperature rise at y=13mm was always below 10°C. The thermocouple voltage rise was not significantly larger than circuit noise at 15mm depth. This equates to a temperature rise of less than 1°C.
- At low P and high U, the measurable temperature field was small. At P=20W and U=4mm/s, the maximum temperature rise at y=3mm was always below 10°C.

The discoveries about temperatures at y=13 and 15mm were made using powder bed tray 1 (see Section 3.5.2), and were the basis for the shallower powder bed tray 2.

6.4 End Effects Study

Temperature data recorded 5.2mm beneath the end of a 60mm processed line scan were organised as described in Section 5.1.3. They are displayed and discussed here.

6.4.1 Results

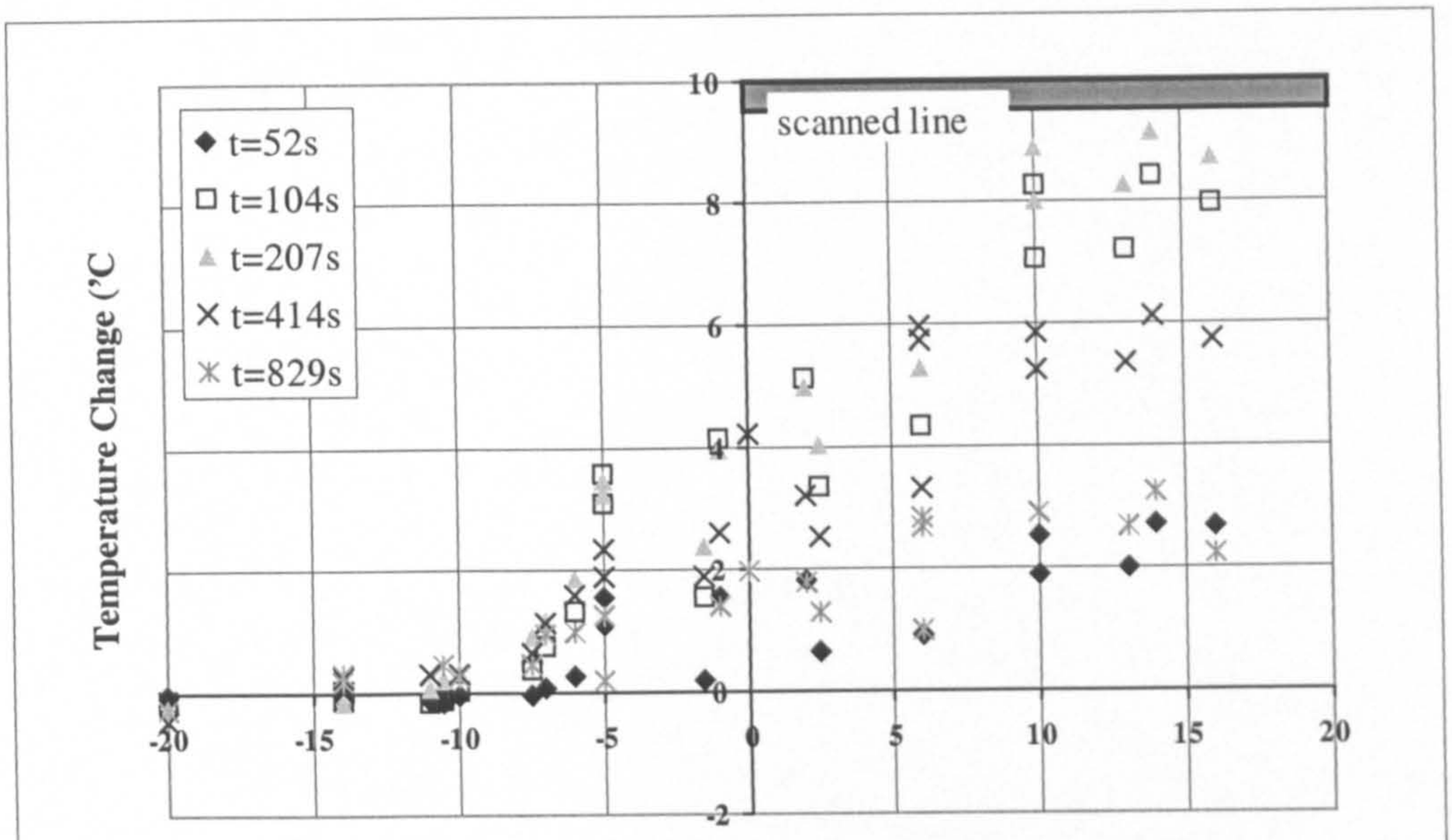

Figure 6.5 Temperature versus x at points in time, 5.2mm beneath scanned line

The graph Figure 6.5 shows how temperature varies with position at five time intervals, approaching the end of a 60mm-long processed line. The position of the scanned line has been superimposed at the top of the graph for guidance.

6.4.2 Discussion

Refer to Figure 6.5. The measured temperatures continue to increase directly underneath the end of the scanned line. Temperature begins to level out with position, until $dT/dx = 0$ underneath a position approximately 12mm along the line. The path of any curve fit to points at a particular time interval is a matter of some interpretation. At the most conservative interpretation, the steady state temperature zone ($dT/dx = 0$) was reached after moving 15mm from the line end.

This is true at all time intervals. This information was fed back into the positioning of thermocouples in the powder bed for single line thermal property measurement.

6.5 Thermal Property Measurement

The results presented in the sub-sections of 6.5 were processed in the corresponding sub-sections of Section 5.1.4. Excel spreadsheets were created to calculate k and α from temperature data. Spreadsheets include the original thermocouple readings against time. For the thermal camera, raw temperature data are recorded on scanned, numbered graphs. The spreadsheets and graphs can be found on a CD attached to the rear of this document. Each pair of thermal property results reported in this section have been allocated an experimental series number, to tie them in with the contents of the CD and the tables of Appendix A. Column 1 of Appendix A page 1 denotes graphs which were used in thermal property measurement. Column 2 performs this function for thermocouple data on pages 2 to 4 of Appendix A.

The values of k and α reported for single lines scanned in air and argon, and single layers and relased lines scanned in argon have been presented previously in a paper [Taylor 2001].

6.5.1 Single Lines

Materials tested were stainless steel 314S HC and M2 (both gas atomised), and 3D Systems Rapid Steel 2. When a feasibility study was conducted on M2 water atomised steel powder, it was discovered that due to the low bed density, melted material penetrated as much as 4.5mm into the powder bed. Under these conditions, the measurement depth y would become too difficult to evaluate.

6.5.1.1 Results

Below are Tables 6.2 and 6.3, results for the contact (thermocouple) and non-contact (infra red camera) measurement methods. These are followed by a graph used to calculate α at single values of U, under conditions as series 1.5, 1.6 and

1.7, Table 6.2 and Appendix A. Table 6.4 compares calometrically-measured (by the contact method) values of α to values estimated based on the mass of material melted by the laser. Thermal properties for steel are as assumed in sections 3.7 and 5.1.4.1.

Exp. Series No.	Mat-erial	Powder d_p Range (μm)	Atmo-sphere	P Range (W)	U Range (mm/s)	k (W/ (m.K))	α (0-1)
1.1	314S	75-150	Air	40-160	1-15	0.25	0.21
1.2	314S	10-20	Argon	40-160	1-15	0.07	0.08
1.3	314S	75-150	Argon	40-160	1-15	0.15	0.09
1.4	314S	150-300	Argon	40-160	1-15	0.13	0.13
1.5	314S	75-150	Argon	160	0.5	0.15	0.04
1.6	314S	75-150	Argon	160	1.0	0.18	0.15
1.7	314S	75-150	Argon	160	10.0	0.14	0.18
1.8	M2	75-150	Argon	40-160	1-15	0.12	0.13
1.9	RS2	Avg. 30	Argon	40-160	1-15	0.19	0.10

Table 6.2 Powder conductivity and absorptance as found by contact method

Exp. Series No.	Mat-erial	Powder d_p Range (μm)	Atmo-sphere	P Range (W)	U Range (mm/s)	k (W/ (m.K))	α (0-1)
1.10	314S	75-150	Air	40-160	1-15	0.19	-

Table 6.3 Powder conductivity as found by non-contact method

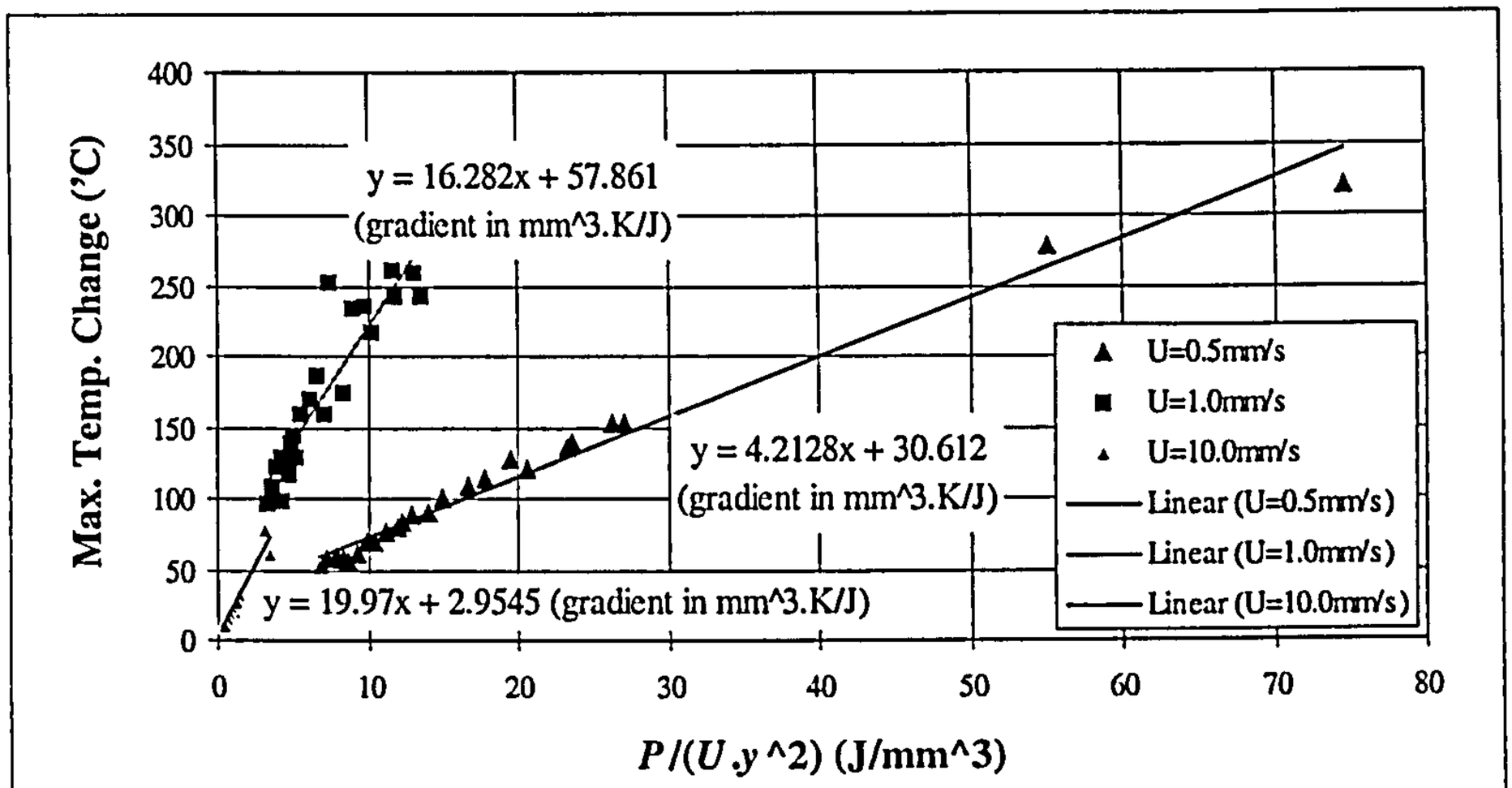

Figure 6.6 *dTmax* versus $P/(U.y^2)$, 314S HC in argon at single values of *U*

Experiment: *P*=160W, *U*=0.5mm/s Laser energy supplied: 19.2kJ Mass of 60mm-long scan: 1.7g Energy required to melt scan: 1.8kJ Mass-related α: 0.094 Calometrically-measured α: 0.04	Experiment: *P*=160W, *U*=1.0mm/s Laser energy supplied: 9.6kJ Mass of 60mm-long scan: 4.5g Energy required to melt scan: 4.7kJ Mass-related α: 0.49 Calometrically-measured α: 0.15

Table 6.4 Results and calculations based on α versus *U* experiments

6.5.1.2 Discussion

This section has been split into independent discussions of conductivity results, absorptance results and the accuracy of measurement methods.

6.5.1.2.1 Conductivity Results

The effective conductivity of a powder bed depends on the properties not only of the powder particles, but also of the surrounding gas phase. Experimental series 1.1 and 1.3 in Table 6.2 display the difference in measured conductivity for steel powder in an air and argon atmosphere. Yagi and Kunii (Section 2.3.2) proposed an equation which predicts that the conductivity of steel in air will be 1.5 times that of steel in argon. This agrees reasonably with a comparison of *k* between

series 1.1 and 1.3, which suggest a ratio of 1.7. Based on series 1.2 and 1.4, the effect of particle size on k is slightly greater than the effect of atmosphere, over the interval of d_p tested.

6.5.1.2.2 Absorptance Results

Figure 5.3 shows experimental points, compiled on a graph for the calculation of α. Points on the graph are scattered radially from the origin, which suggests a range of possible α values are being measured in different experimental runs. For instance, in Figure 5.3 the best fit gradient is 24, but might extend as high or low as 17 or 32 (denoted by the dashed lines). It was thought that perhaps α changes with laser beam power P and speed U. A new experiment was undertaken to measure α at constant values of U, the results are seen in Table 6.2 series 1.5, 1.6 and 1.7 and Figure 6.6. At a single value of U there is a lower radial spread of experimental points. The implications of this are considered. If a single value of α is required for an untested material, a process map as made by Hauser should be created to decide what operating range of P and U is required. One can then be more focussed in experimentally evaluating α for this specific range. A large change in absorptance is related to the issues discussed in Section 6.6, occurring at speeds under 7mm/s.

Series 1.1 and 1.3 of Table 6.2 show how absorptance decreases from an air to an inert processing atmosphere. This agrees qualitatively with the observations of [Hauser 1999a], that larger volumes of material were melted in air processing than in argon processing. He theorised that this was due to oxides forming on the processed material surface in air. Based on series 1.3, 1.8 and 1.9, the material type also appears to have a significant effect on α.

It might be expected that the absorptance values reported in Table 6.2 would correlate well to the corresponding mass of material melted. For instance, increasing U from 0.5 to 1mm/s creates a 275 percent increase in α (series 1.5 and 1.6, Table 6.2). The mass of tracks processed as part of these experiments were

expected to exhibit a similar change. The relationship between measured α and track mass is considered now.

A comparison was made between calometric (thermocouple) and mass-related α, for the two instances series 1.5 and 1.6 in Table 6.2 discussed. Results can be found in Table 6.4. At P of 160W for U equal to 0.5 then 1.0mm/s, the energy supplied by the laser to 60mm long tracks was 19.2 and 9.6kJ respectively. Five 60mm tracks were weighed for U equal to 0.5 and 1.0mm/s. Putting values for steel into equation (2.9) (see sections 3.7 and 5.1.4.1), the energy required to melt a certain mass of material can be calculated. For the masses measured, a minimum of 1.8 and 4.7 kJ were required to form the 0.5 and 1.0mm/s tracks respectively. This indicates mass-related α of 0.094 and 0.49 respectively. Mass-related absorptance can be compared to the α values of 0.04 and 0.15 which were calometrically measured (Table 6.4). The mass-related α increases 5.2 times between U of 0.5 and 1.0mm/s. The calometric α increases 3.8 times between U of 0.5 and 1.0mm/s. α increases several times over in both cases as would be expected, but the calometric and mass-related measurements do not agree on exact values.

It has been established that when the laser is applied, the powder bed melts rather than sintering. It is worth checking though, that the surface energy converted to heat during reduction of surface area when powder turns to solid does not contribute significantly to the amount of material melted. This is particularly relevant when powder size d_p changes. It can be seen in Table 6.2, series 1.2, 1.3 and 1.4, that as the average powder size increases, the absorptance measured increases. It is questioned whether this could be a result of the powder's surface area to volume ratio. An order-of-magnitude calculation, using 1 J/m^2 as the surface energy of steel [Wojciechowski 1999] for a typical single line sintered from 75-150 μm steel powder, gives the result that surface area reduction contributes less than 0.0001 times the energy provided by the laser beam to the melt pool. Thus surface energy is not thought to be the cause of α changing with d_p. The cause of α changing with d_p is as yet unknown, perhaps related to the surface roughness of particles.

As a final comment on absorptance, data reference books demonstrate how sensitive α (often quoted as emissivity) can be to such factors as material constituents, surface geometry and finish. These factors are worth considering when comparing data gathered here and elsewhere.

6.5.1.2.3 Accuracy of Measurement Methods

Values of k obtained in equivalent cases should be comparable. A set of four such cases are series 1.3, 1.5, 1.6 and 1.7 of Table 6.2. For the four cases, k is 0.16 on average, with a maximum variation of 16 percent. Referring to Figure 5.2, the intercept of the line fitted is worth considering. Carslaw and Jaeger's theory dictates that this intercept should be equal to zero. Here the intercept is -2.2; other graphs plotted demonstrate intercepts which are similarly small. This is a good indication for the method used to calculate k.

k has been measured using both the thermal camera and thermocouple systems (series 1.1 and 1.10, tables 6.2 and 6.3). Temperatures were measured perpendicular to the scanned line in each case, but across the bed's surface using the thermal camera, and vertically down using thermocouples. The resulting k would be the same if both measurement systems were perfectly accurate and if Carslaw and Jaeger's assumptions were perfectly true (that is, if zero heat loss took place across the powder bed surface). k measured using the thermocouples was 32 percent higher than was measured using the thermal camera.

The Carslaw and Jaeger-derived infinite line approximation was tested in a new way: temperatures measured in the powder bed at a set time after laser application were integrated over 5 radial areas in the powder bed, orthogonal to the laser scanning direction. Summing the deduced heat in these areas:

$$\text{Energy per unit area in powder bed} = P.\alpha / U, \approx \sum_{1}^{k=5} (A_k.C_k.dT_k) \qquad (6.2)$$

Where A is the area of each radial area in the bed. Thermocouple data files 250902n2 and 250902n5 were analysed at 62 and 75 seconds elapsed respectively, using a C of 460J/(kg.K). This method yielded 2 values of α within 30 percent of those calculated using the infinite line procedure of Section 5.1.4.1 on

thermocouple temperature measurements. The checking method above is crude, but it demonstrates that values found are of the correct order.

Figure 5.3 is considered, a graph of experimental results from which α is calculated. As for k above, the intercept of the fitted line on this graph should be close to zero; at -0.17 it is very close. Intercepts are not always so small in magnitude, but are always less than 5 percent of the plotted temperature range.

Examining the absorptance results presented in Table 6.2, it can be seen that all values lie below 0.25. In the closest comparable situation found in literature, Tolochko reported α of 0.45 for iron powder processed with a CO_2 laser in an inert atmosphere. The first reason why Tolochko's measurements might be higher than found in this work is the geometry of the material surface. Whereas Tolochko maintained the powder state of tested materials, all experiments from this work involve processing to solid. Processing changes the absorptance of the material surface, as discussed in Section 6.5.2. As an indication of the powder bed α before melting took place, the infra red camera calculated the emissivity of a stainless steel bed in air as 0.66 at a constant 200°C. A second influence on α readings is that in the calometric experiments presented here, absorptance measurements are based on the heat which diffuses into the powder bed, whereas Tolochko's experiments were radiation-based, considering energy reflected. It is possible that the effects of conduction and convection-based surface heat loss in the seconds following laser application act to significantly reduce the energy measured by the thermocouples. From the point of view of fully understanding heat transfer in SLS, both measurement methods are considered useful. For the practical application of creating scans of consistent size in an SLS-processed layer, it is thought that measuring the heat retained by the bed (as has been performed in this work) is more important.

6.5.2 Single Line Relasing

Absorptance was measured during multiple passes of the laser over the same area. The powder used was stainless steel 314S HC, 150-300μm in size. The

atmosphere was argon. Other experimental conditions were those of series 2.1 in Appendix A.

6.5.2.1 Results

Table 6.5 has been derived from Figure 5.5 and demonstrates how α varies with the number of rescans. Figure 6.7 shows photographs taken of relased lines.

Scan No.	1	2	3	4	5
α (0-1)	0.13	0.084	0.074	0.072	0.054

Table 6.5 Absorptance against number of scans, 314S HC single line in argon

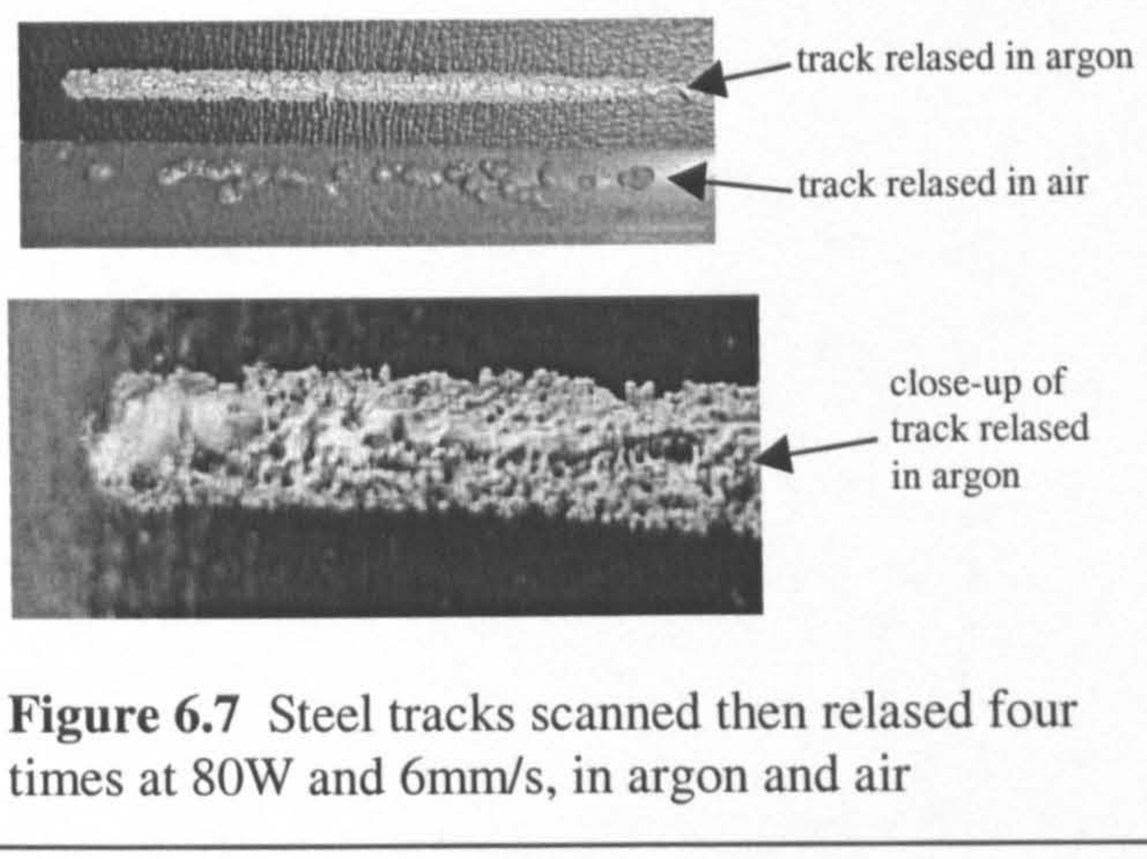

Figure 6.7 Steel tracks scanned then relased four times at 80W and 6mm/s, in argon and air

6.5.2.2 Discussion

Table 6.5 shows α reducing with the number of relases. With each successive scan the surface material becomes more smooth and has less porosity. This geometrical change has an effect on absorptance. The value of α on the first pass is 0.13, which is the same as was measured for another experiment involving the same powder and similar conditions, series 1.4 of Table 6.2. After the fifth pass of the laser, α had reduced to less than 50 percent of its initial value. Absorptance reducing with each rescan is supported by the findings of Section 2.3.1.2. Equations (2.12a) and (2.12b) predict that α will reduce as φ reduces.

The images in Figure 6.7 show how atmosphere makes a difference to the surface condition of processed tracks. The track processed in argon becomes

smooth and shiny (low absorptance of visible light) after several scans. Shiny silver parts were produced consistently, indicating that the inert atmosphere was created successfully. Tracks processed in air became blackened, presumably because of surface oxidation. They also exhibited high surface tension behaviour, sometimes forming a line of unconnected ball shapes as shown in the figure.

6.5.3 Single Layers

6.5.3.1 Results

The gradients of curves from the graph Figure 5.6 were used to generate the graph Figure 6.8, of α versus s. A range of absorptance values from 0.11 to 0.28 can be seen as s varies. The peak α occurs at s of approximately 0.9mm. The powder used was stainless steel 314S HC, 150-300μm in size. The atmosphere was argon. Conditions are those of series 3.1 in Appendix A.

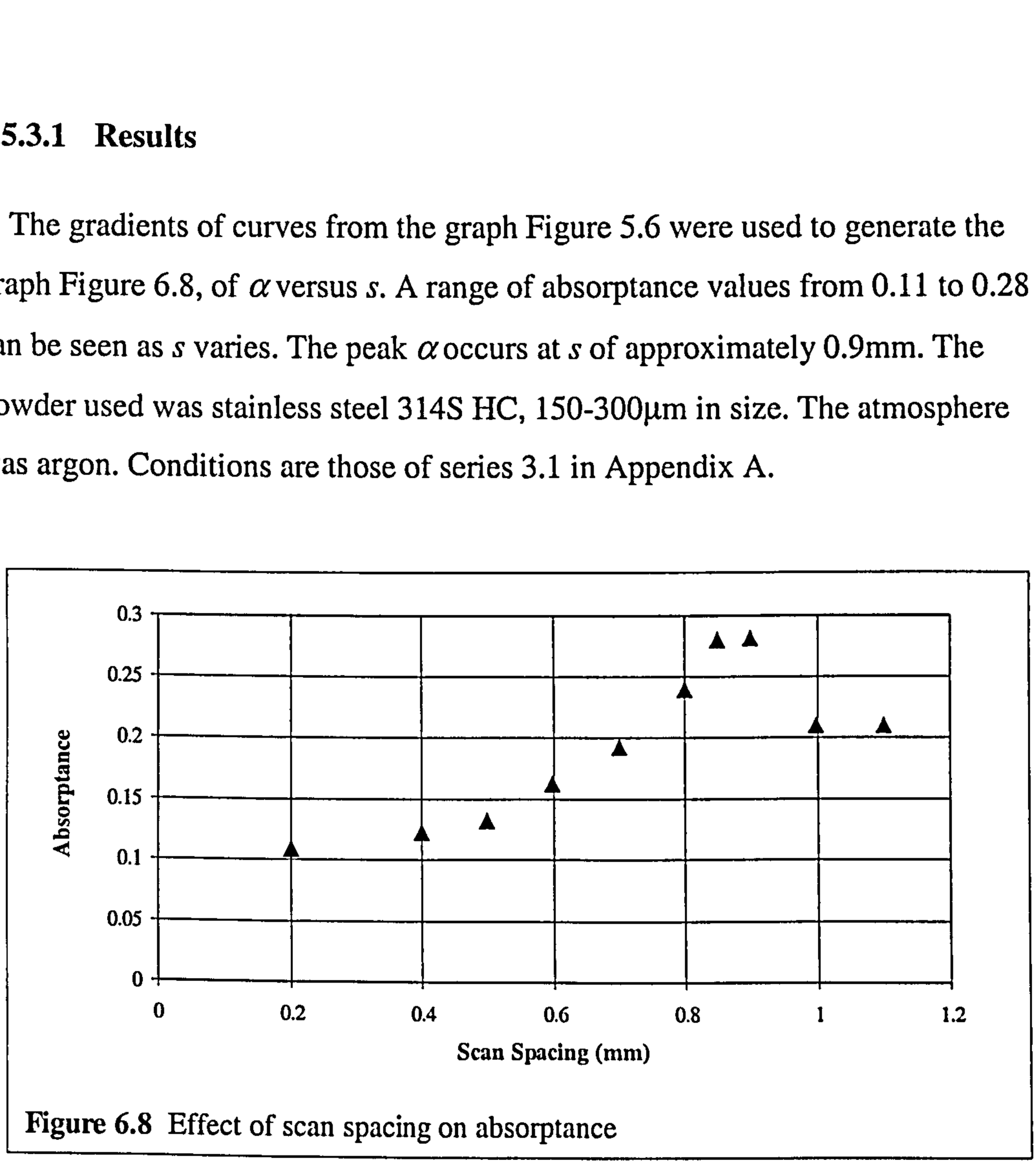

Figure 6.8 Effect of scan spacing on absorptance

6.5.3.2 Discussion

The change in α with s shows a pattern of α rising from s= 0.1 to a peak at around s= 0.9, then falling until s=1.1mm (equal to the beam diameter d). The

graph will be considered in two sections, for s below 0.9mm then for s above 0.9mm.

Section 6.5.2 shows that previously-scanned (partially or fully melted) material exhibits a lower absorptance than fresh powder. In the case of layer scanning considered here, the area scanned after the first line is a combination of previously-scanned material and unscanned material. As the scan spacing s increases, the ratio of unscanned to previously-scanned material increases. Therefore α would be expected to increase, which is true in the region where s is below 0.9mm.

The rule just described appears to break down at s above 0.9mm. It must be remembered that the scanning speed U was varied in inverse proportion to the scan spacing s, to keep the layer scanning time constant. As s increased, U decreased. The duration over which an area of material is exposed to the laser beam increases as U decreases. The decrease in α may relate to the increase in laser exposure time, as was observed by Tolochko (stage 3 in Figure 2.26, a graph of α versus exposure time).

The absorptance value found for single lines with the same material and atmosphere was 0.13, which lies within the range of α found here. The combinations of P and U used in the two sets of experiments are very different, so values of α should not be expected to be directly comparable considering what is said in Section 6.5.1.2.2 about α versus P and U.

6.5.4 General Comments- Thermal Property Measurement

In calculating k and α, it is assumed that properties k and C are constant. k and C change with temperature in reality. The value of C used in calculating k and α from Section 5.1.4 is a room temperature value, chosen because temperatures measured in the vast majority of relevant cases (considering particularly position and time) were below 100°C. Between room temperature and 120°C, k and C change by less than 25 percent. It is believed that the assumed temperature-independence of calculations will place an uncertainty of no more than 25 percent on the absolute values of k and α reported here.

6.6 Evaporation Study

The outcome of processing data as described in Section 5.1.5 follows.

6.6.1 Results

Figure 6.9 is a photo of 2 scans, 10mm in length. The concave, depressed surface of the scan processed at 0.5mm/s and the convex surface of the scan processed at 1.0mm/s can be seen.

Results of the study are presented in Table 6.6. Energy values have been calculated from measured masses as detailed in Section 5.1.5.

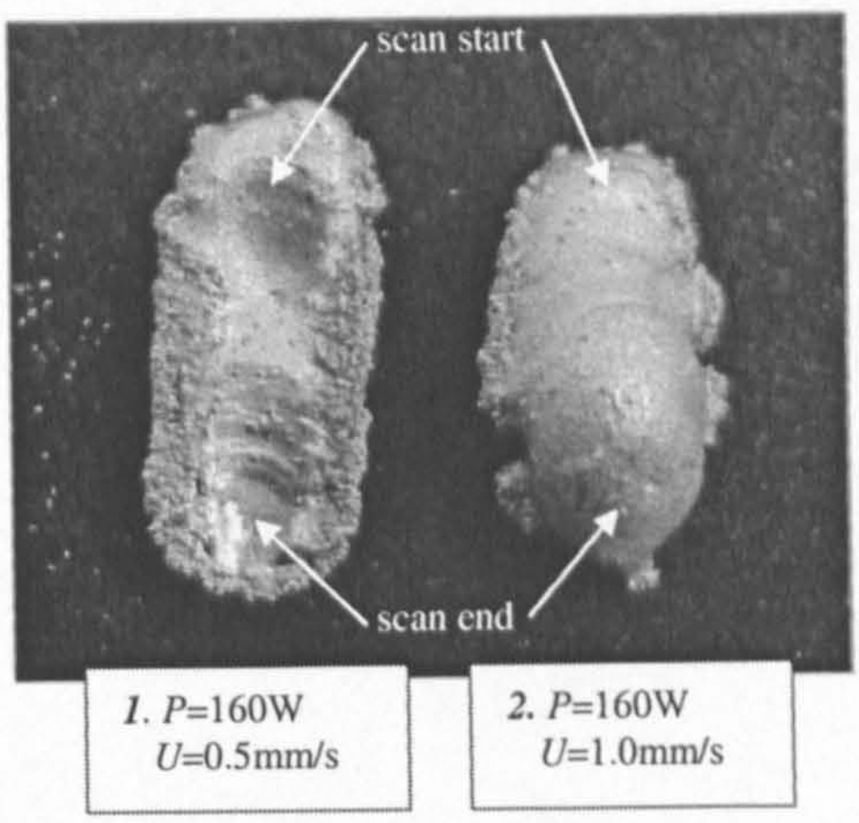

Figure 6.9 Two steel scanned tracks

Experiment 1: P=160W, U=0.5mm/s	Experiment 2: P=160W, U=1.0mm/s
Laser energy supplied: 16kJ Mass of scans: 2.61g Surface shape: concave Processed zone mass reduction: 9.8mg	Laser energy supplied: 8kJ Mass of scans: 3.65g Surface shape: convex Processed zone mass reduction: 15mg
Energy Values	Energy Values
Energy required to melt scans: 2.7kJ	Energy required to melt scans: 3.8kJ
Maximum energy lost by evaporation: 71J	Maximum energy lost by evaporation: 110J

Table 6.6 Results and calculations based on evaporation study

6.6.2 Discussion

The change in the mass melted per unit of energy supplied, and the change of scan cross-sectional shape as reported by Hauser in Section 2.2.6.3 has been observed.

The scan created at U=1.0mm/s is convex over its surface, see Figure 6.9. The convex surface is caused by surface tension in the steel's liquid state, which dominates gravitational force to drive the melt pool into a rounded shape. The liquid steel is easily shaped because its viscosity is low. The shape of scans at U=0.5mm/s follows the description of plasma recoil pressure depressing the melted surface in Section 2.2.6.2. Energy supplied to scans decreases from experiment 1 to 2, yet melted mass increases. This is believed to indicate vaporisation of the steel, either removing heat from the processing zone or blocking the laser beam.

It was calculated in Section 3.7 that the energy required to melt 1kg of steel starting at room temperature is only one seventh of the further energy required to vaporise the same mass. Based on the mass measurements made before and after SLS processing, any energy removed by vaporisation is insignificant compared to the amount of energy required to melt the processed tracks. In fact, it is seen that as the melted mass decreases (from experiment 2 to experiment 1), the mass lost from the processing zone decreases also. This counters any notion of an energy balance explained by vaporisation heat loss.

Combining the facts, a depressed scan shape and reduction in material melted with negligible reduction in the mass of the processing zone support the notion of a blocking vapour forming at certain P values for low U (below 7mm/s). This is worth bearing in mind if such low U is to be used. There is a limited value to processing at very low U, from the point of view of the lead time to make parts.

6.7 Sectional Analysis of Single Layers

Discussed here are general observations about the morphology of the single layers made, analysed in Section 5.1.6. Area analysis of layers is reported in Chapter 7, because it relates to verification of the numerical model.

6.7.1 Results

Figure 6.10 provides perspective and top views of a typical 10-scan layer, manufactured at s=5d /6, P=60W and U=1.0mm/s. In Figure 6.11 some characteristic features of layer cross-sections are illustrated. Table 6.7 presents all 27 layers, cross-sectioned for analysis.

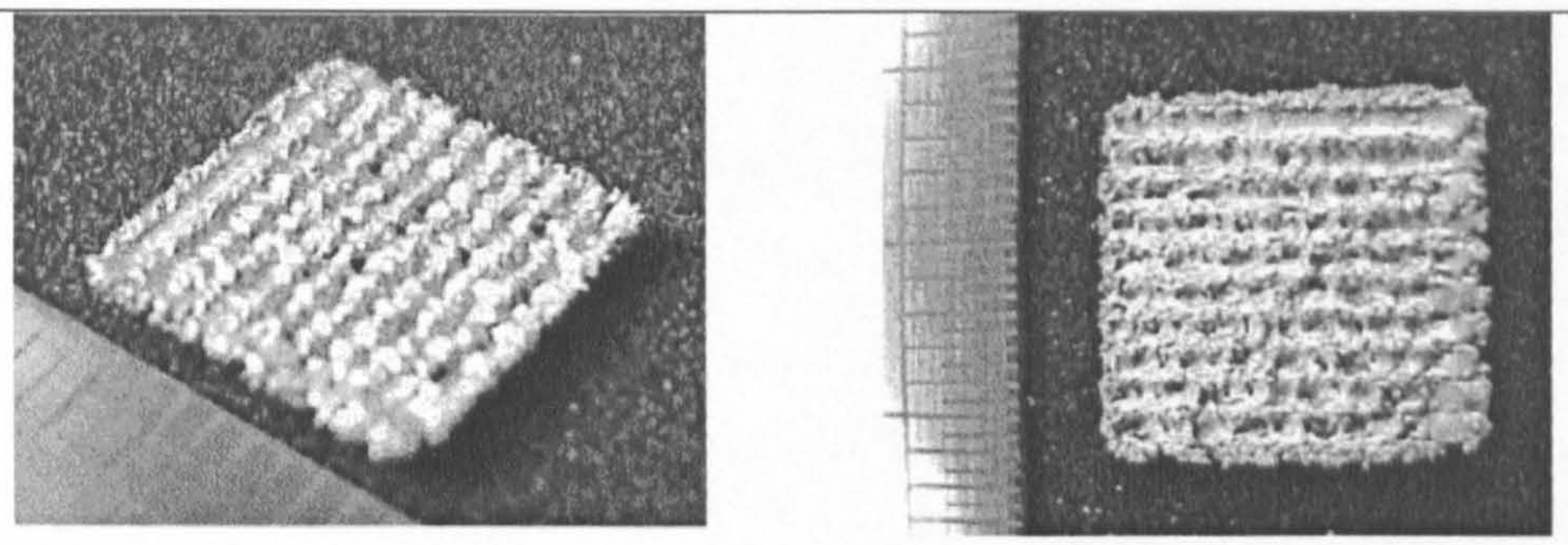

Figure 6.10 Perspective (left) and top view (right) of manufactured layer

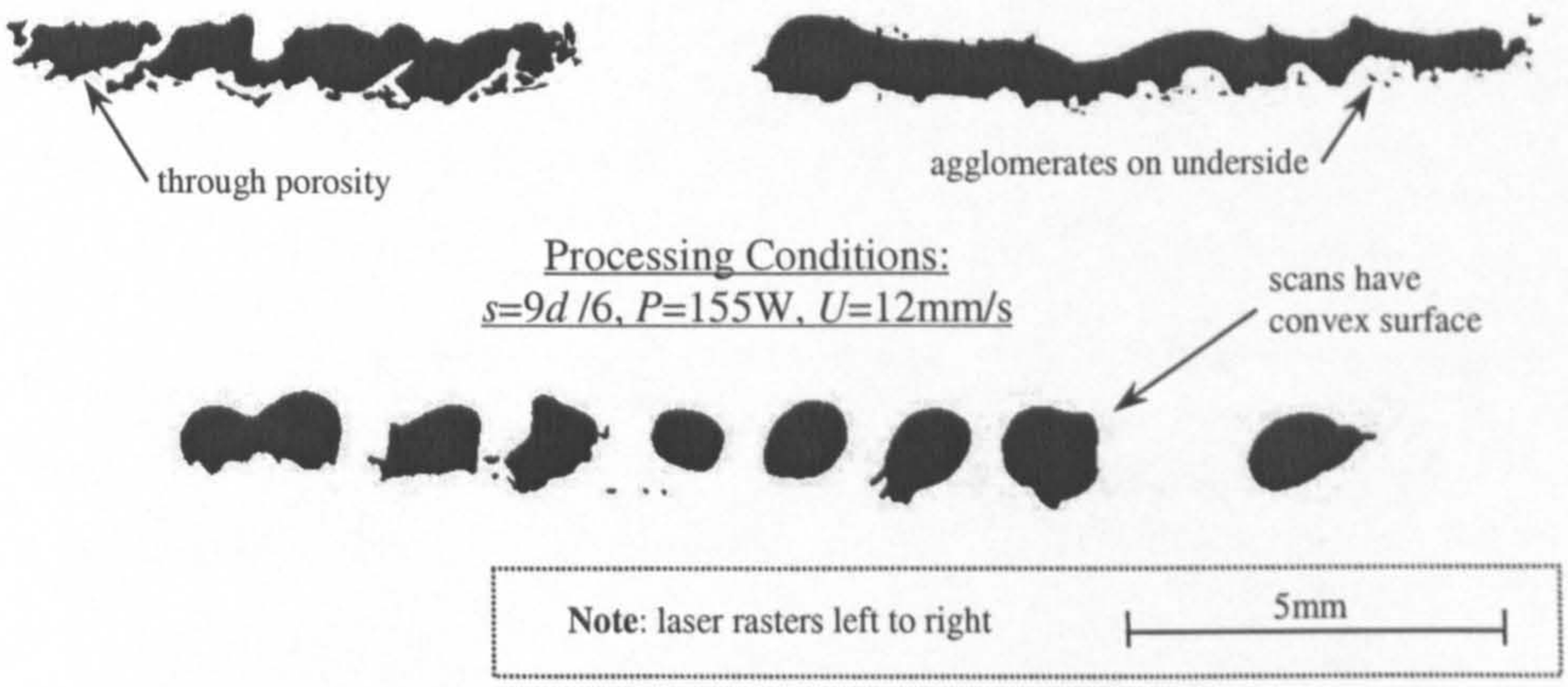

Figure 6.11 Enlarged views of a sample of manufactured single layer sections

	P=60W, U=1mm/s	P=120W, U=6mm/s	P=155W, U=12mm/s
s = 3 d /6			
s = 5 d /6			
s = 9 d /6			

Table 6.7 Manufactured single layers, against machine parameters (d= 1.1mm)

6.7.2 Discussion

For brevity, the layers from Table 6.7 are referred to by their parameters, in the form "*s*-*P*-*U*", where *s*, *P* and *U* have their usual meanings.

5 of the 9 sets of parts display through-porosity, i.e. pores which isolate one area from another. This makes some parts appear as though they are split into pieces, but in three dimensions all parts are continuous. At $s=9d/6$, there is through-porosity between each scan, and the shape of scans can be seen distinctly. Porosity is believed to be caused by a lack of available powder in the locality of previously processed material (explained in Section 2.2.6.3), and insufficient energy density for molten material to flow into the pores.

The majority of each layer's area is fully dense, which means that full melting of material is taking place. Around the edges of sections (particularly the underside), small fragments of material can be seen. These are clumps of particles which reached a temperature high enough to bond together, but not high enough to flow into the main melt pool.

At small *s* and low P/U, the first line scanned (FLS) is noticeably bigger than the others in each layer. This occurs in the 3*d*/6-120-6, 3*d*/6-155-12, 5*d*/6-120-6 and 5*d*/6-155-12 layers. These same layers are less flat than the other samples, due to the FLS on the left hand side and curling in the body of the layer. Curling of parts at high values of A_N was reported by various authors in Section 2.2.6.3. Parts made at 5*d*/6-155-12 have the lowest upper surface roughness.

At *P*=60W, *U*=1mm/s, layer depth continues to grow in the rastering direction (left to right): a steady depth has not definitely been reached. Depth seems steady throughout for 9*d*/6-120-6 and 9*d*/6-155-12 layers.

A change can be seen in the shape of scans, related to *P* and *U* values. At most *P* and *U* settings, the surface of scans is convex. At *P*=60W and *U*=1mm/s, the surface of scans is slightly concave. This is particularly noticeable at $s=9d/6$ and in the FLS of layers. Reasons for this shape change at low speed are as discussed in Section 6.6.

In general, a trade-off would be required in choosing which of the parameter combinations from Table 6.7 make the "best" layers. For example, the parts with the highest relative density were those identified as having a large FLS.

6.8 Summary of Thermal Experiments

It has proven possible to carry out thermal experiments in a situation representative of the direct single phase metal SLS process. In particular, an inert processing atmosphere, a scanning laser and melting rather than just heating of material have been recreated.

A method has been developed which uses analytical equations adapted from literature to predict the conductivity k and absorptance α of a powder bed whilst single lines and layers are scanned. Contact and non-contact temperature measurement systems have been constructed from existing and custom-designed equipment. Temperature data was processed with the assistance of a specially-written Fortran program, Excel and Paint Shop Pro. Manufactured layers were sectioned and analysed for area and relative density using Image Pro software.

Use of an infra-red camera has provided some idea of temperatures occurring on the powder bed surface in direct SLS of room-temperature stainless steel powder using the Leeds experimental rig. At a P of 20W and U of 6mm/s, heating of material from room temperature to the melting point occurred in less than half a second. Peak temperatures measured were above 1500°C. At P of 150W and U of 6mm/s, material fell below solidification temperature in 3 seconds or less for bi-directional raster scanning. A temperature rise of 1°C could be measured at up to 20mm from the perimeter of scanned layers.

Below the powder bed surface, temperatures were measured using thermocouples. Observations were made which support Carslaw and Jaeger's instantaneous infinite line heat source assumption. The highest temperature measured within the bed whilst scanning single lines was 320°C, at P of 160W, U of 0.5mm/s, y of 2.1mm. At 15mm depth into the bed, the measured temperature rise never exceeded 1°C.

Powder bed k and α were measured during the scanning of single lines, using a calometric method. k values ranged from 0.07 to 0.25W/m.K, α was measured at between 0.08 and 0.21. k was found to depend on the atmospheric gas used, and on powder particle size. α was found to depend on the atmosphere used, reducing from an air to inert gas atmosphere. α is affected by the powder material type. α

was seen to increase with increasing laser scanning speed U, more than four-fold over the range 0.5 to 10mm/s at P of 160W. It has been seen that when measured α values increased or decreased, the mass of material melted followed the same pattern. However, the magnitude of changes in the measured α were not the same as the magnitude of changes in processed track mass.

A line was scanned on the bed's surface, then was rescanned 4 times to see the effect on absorptance. α reduced from 0.13 on the first scan to 0.054 by the fourth rescan. A reduction of porosity and smoothening of the scanned surface due to the laser's action was observed. The result is consistent with the findings of [Sih 1995b] and [Tolochko 2000], who state that the absorptance of a powder bed decreases as the porosity decreases.

The effect of scan spacing s on α was tested for raster scanning of layers. α was found to increase from 0.11 at s=0.2mm, to a peak of 0.28 at s=0.9mm. Increasing s from 0.9mm, α fell back to a value of 0.21 at s=1.1mm. As s increased from 0.2 to 0.9mm, the amount of rescanned material reduced, so it was expected that α would increase. For s greater than 0.9mm, a reduction in α is suggested to be caused by a reducing scan speed, hence a greater laser exposure time.

A study was made of an apparent reduction in the proportion of laser energy contributing to melting of material, which occurred at low U. The physical form of scanned tracks was noted. Measured masses were related to modes of energy use. It was concluded that the most likely cause of this reduction in melted mass was the formation of a metal vapour cloud, which blocked the laser energy's path to the powder bed.

Single layer part cross-sections were morphologically analysed. Fragments of material were seen on part undersides, and through-porosity was observed. In some cases, the first line scanned was noticeably larger than the following scans.

Although a thorough statistical analysis has not been performed, an experimental uncertainty of ±35 percent on values of k and α is suggested. This figure is based on a comparison of 4 equivalent cases, and measurements made using contact and non-contact techniques.

6.9 Possibilities for Future Experimental Work

Following on from observations made in Chapters 3, 5 and 6, some ideas for continuation of this work are proposed.

Experimental methods have been developed in this project, to evaluate material thermal properties in the range of situations reported in Section 6.5. The main test subject has been a single type of metal powder. Any metal powder can be tested for conductivity and absorptance in the reported way. It would be interesting to see if observations made for stainless steel powder are generic for metals. For instance, what would be the pattern of absorptance against scan spacing for layer scanning of a different metal powder type.

A natural extension to thermal experiments (and modelling work) would be to study the situation occurring during the scanning of multiple layers. Powder respreading introduces new thermal and mechanical issues which must be addressed when trying to understand the thermal situation.

The infra red camera borrowed generated some valuable results, such as were reported in Section 6.3.1. However, a more modern version would have had Microsoft Windows-compatible output, saving hours spent processing results. A carbon dioxide laser filter for the camera would have reduced the noise which was superimposed onto readings whilst the laser was firing.

Temperatures have been measured on the surface of and inside the powder bed to calculate material absorptance. The relationship between absorptance and melted mass was investigated. A further way to improve understanding of energy usage in direct metal SLS would be to make radiation-based absorptance measurements, using an integrating sphere. Specifically, the magnitude of measured absorptance is of interest, for comparison with values presented here.

Statistical analysis could be performed on a set of conductivity results, to quantify the experimental repeatability. For instance, a t-test could be performed. This would require the repetition of a single experiment. It is estimated that the necessary data gathering would take several weeks.

In the evaporation study discussed in Section 6.6, it was suggested that at low scanning speed, the effective absorptance of the powder bed was reduced by the presence of a blocking metal vapour above the processing zone. To test this theory, a flow of shielding gas could be introduced during SLS processing. The use of shield gases was briefly mentioned in Section 2.2.6.2. The flow of gas is aimed at the point where the laser interacts with the work piece. Any metal vapour present above the work piece is blown away by the gas. The gas has a similar transmittance to that of air. If the theory of Section 6.6 was correct, the use of a shield gas would increase the energy absorbed into the powder bed. The mass of processed material would increase, compared to the situation where no shield gas was used.

The SLS apparatus described in Section 3.3 could be developed to provide preheating of the powder bed. Infra red camera results demonstrate the high increase and decrease of temperature with time during the process. Accorded to the findings of work reviewed in Chapter 2, powder preheating would lead to better bonding, less residual stress and less brittleness of manufactured parts.

Finally, a comment is made on the method used to prepare manufactured layers for area analysis. In future, opaque rather than semi-transparent epoxy resin would be used to suspend the sectioned layers. Light shining through the resin meant that the edges of the layers were poorly defined ("fuzzy") in digital photographs. This problem doubled the time required to create white-on-black masks for area analysis, as touching up was necessary.

CHAPTER SEVEN

7 RESULTS AND DISCUSSION: NUMERICAL MODELLING

Results and discussion are presented together to introduce the new 3D views of modelled parts, and to address the objectives of Chapter 4. Model output is displayed either as sectional or 3D views: it will be seen that both formats have their uses, depending on the requirement. General observations are made about the execution of the modelling program. Chapter 7 ends with a summary, and recommendations for future modelling work.

7.1 Introduction to Modelled Part Geometry

The thermal mesh (TM) size settled on for the sparse matrix-using version of the model was 22×45×19= 18,810 nodes, 3.8 times more than before modification. The final powder bed mesh (PBM) size was set at 150×30×130= 585,000 nodes, 6.9 times more than pre-modification. These mesh sizes are close to the maximum which is possible without overloading the available PC memory.

The spreadsheet *stmet3d.xls* calculated that the new meshes allowed an increase in the potential modelled part size from 4.0mm × 4.9mm × 7 layers to 11.9mm × 19.2mm × 9 layers. More part size increases would be possible by decreasing the number of nodes in the TM, to allow more nodes in the PBM. The potential effect of any change to the TM on the geometry of modelled parts would have to be tested before proceeding.

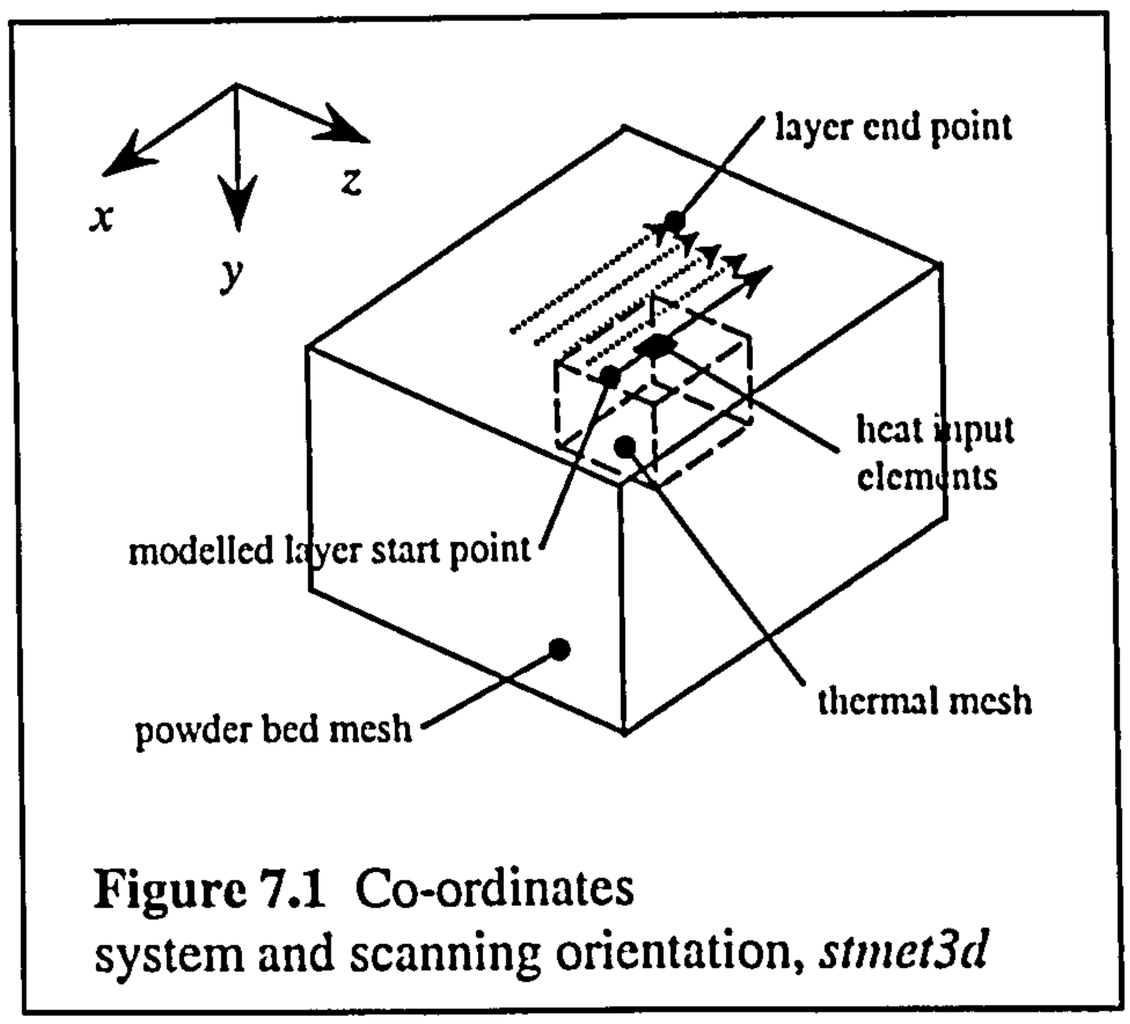

Figure 7.1 Co-ordinates system and scanning orientation, *stmet3d*

Below in Sections 7.1.1 and 7.1.2, the new larger part size and Matlab 3D visualisation are demonstrated in some views of modelled scans and layers. Figure 7.1 is useful as a reminder of how co-ordinates relate to the laser scanning and rastering directions.

7.1.1 Single Line Scan and Pair of Overlapping Scans

These simple shapes were chosen because they show the generic features of modelled geometry.

7.1.1.1 Results

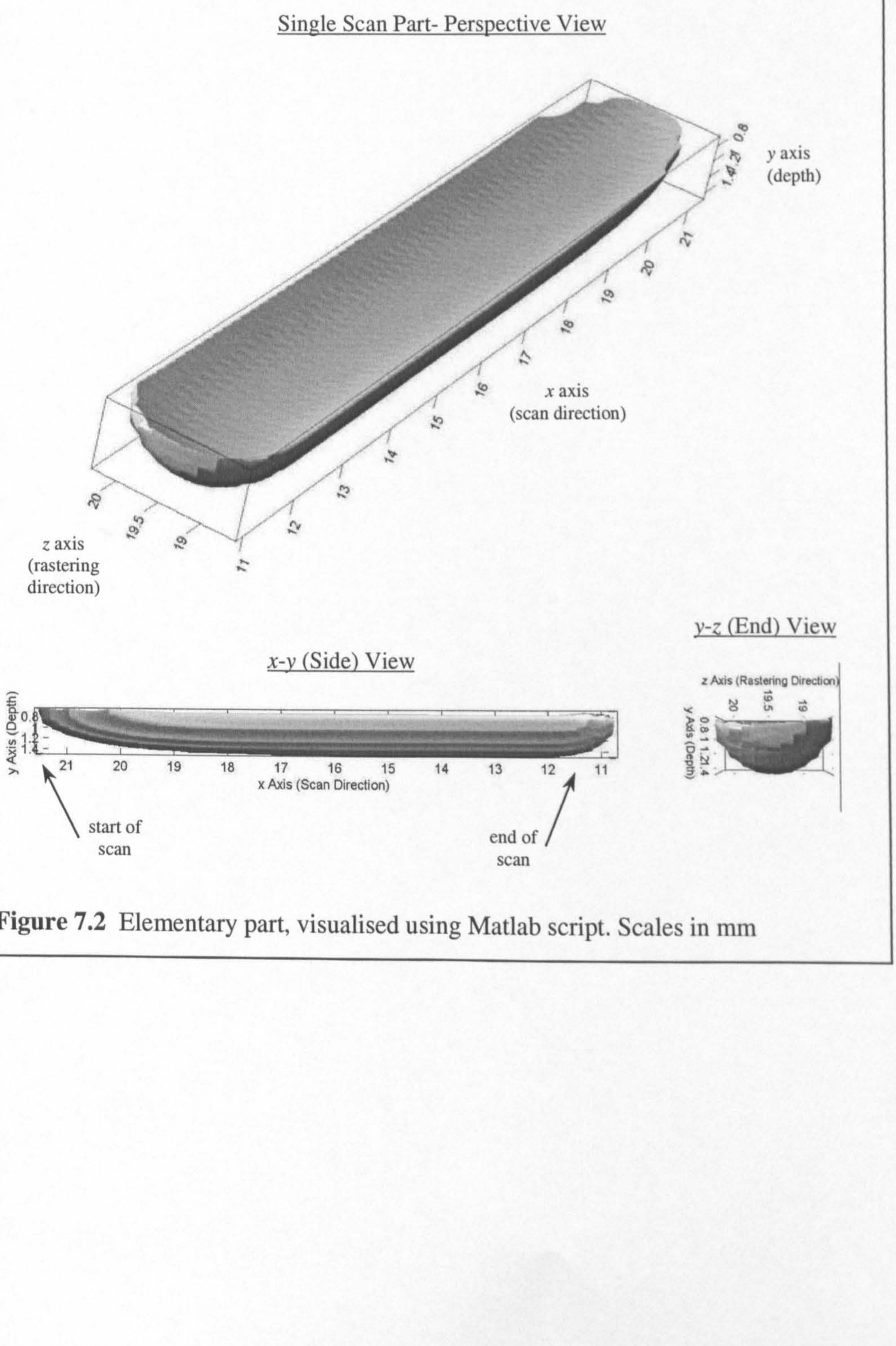

Figure 7.2 Elementary part, visualised using Matlab script. Scales in mm

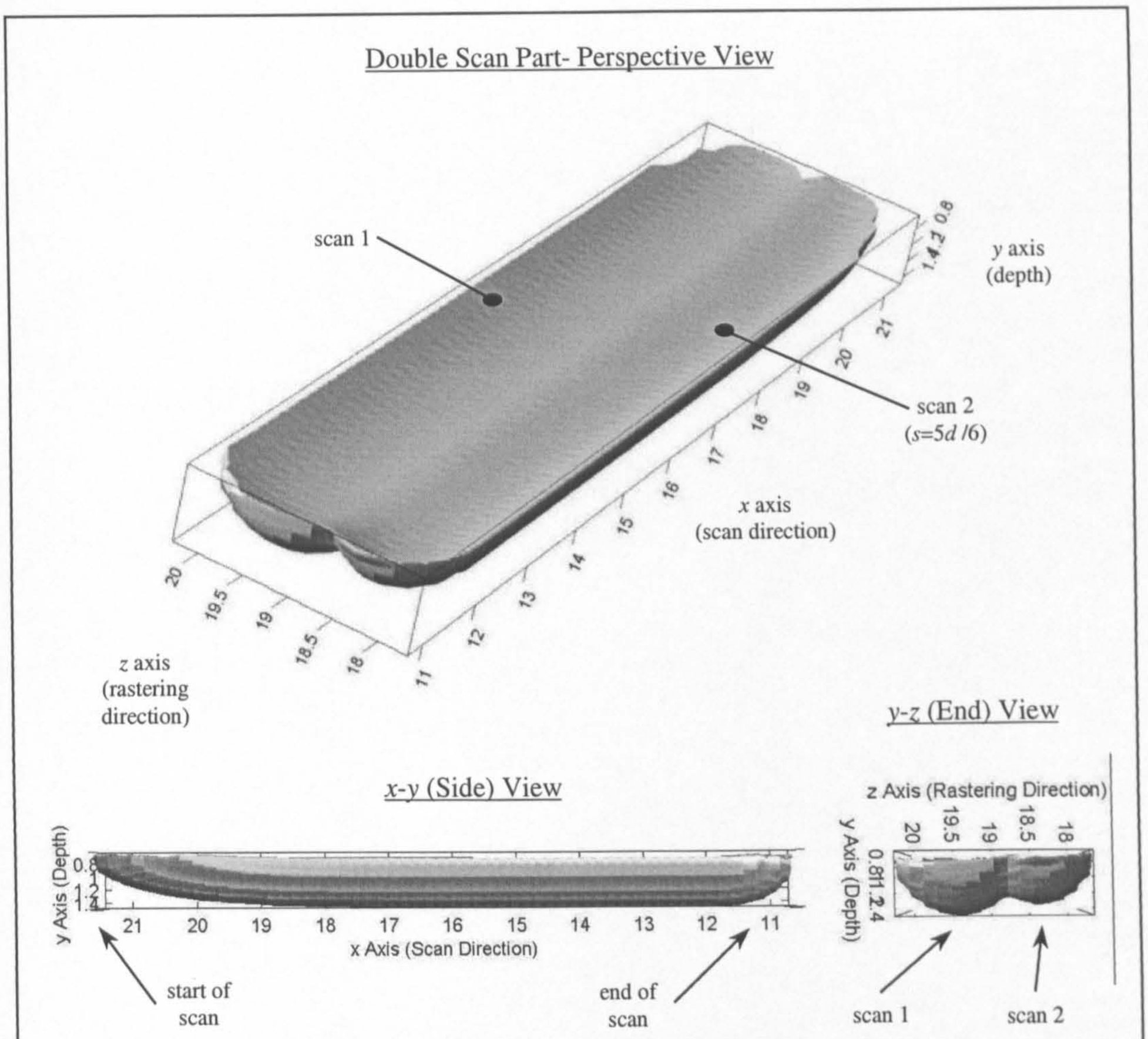

Figure 7.3 Elementary part, visualised using Matlab script. Scales in mm

Figures 7.2 and 7.3 depict a single scanned track and two parallel overlapping scans respectively. They were modelled using the program *stmet3d*, then post-processed in Matlab as discussed in Section 5.2 to generate 3D views. Power P was 100W, absorptance α was set arbitrarily to 1.0, and scan speed U was 6mm/s. For the double scan, s was $5d/6$. The aspect ratio used for the 3D images here is (1,1,1). The three sectional views in Figure 7.4 are of the temperature field for the single scan, at the point in time where laser scanning ended.

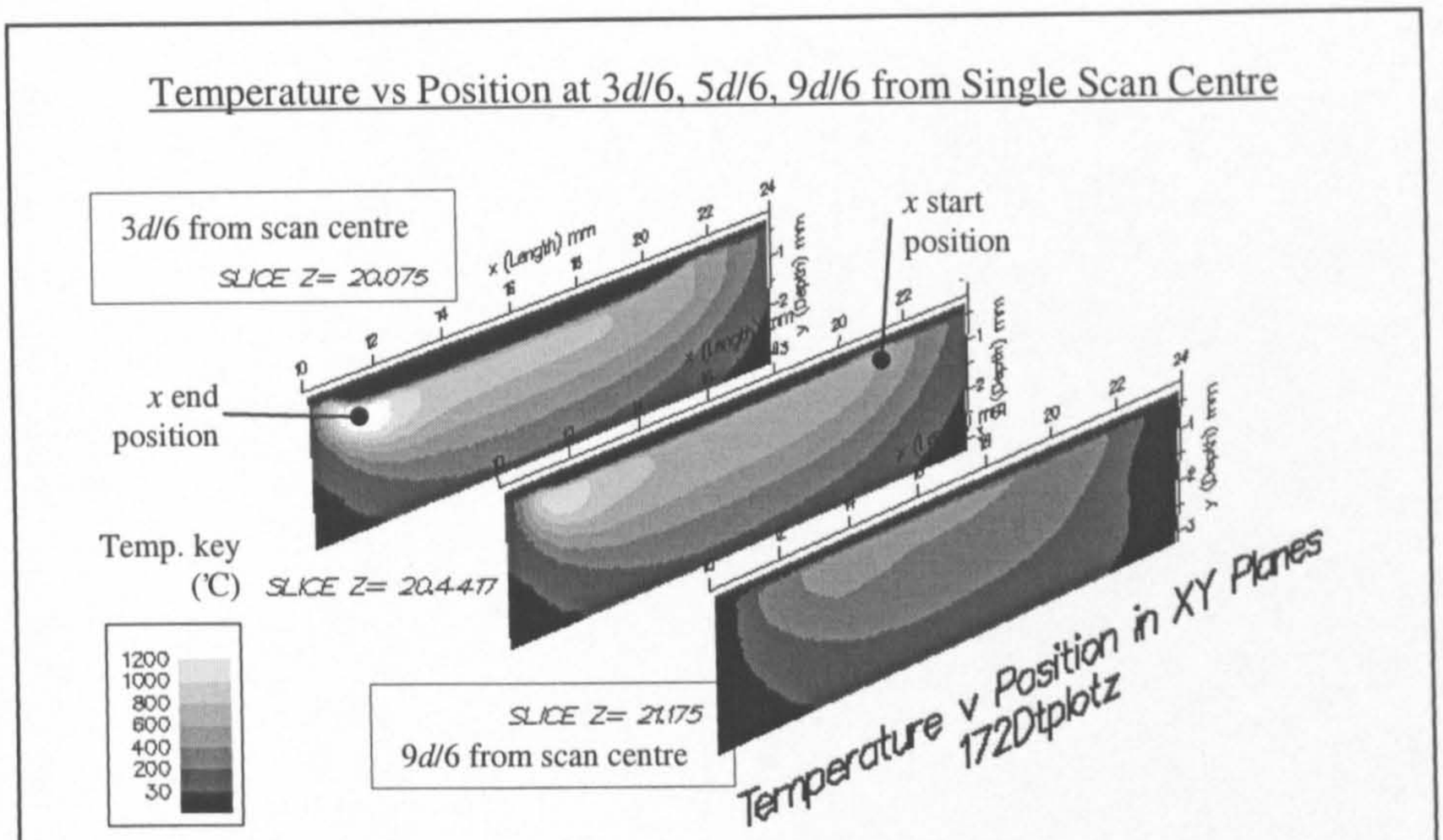

Figure 7.4 Temperature field at the time of completing a single scan

7.1.1.2 Discussion

It can be seen that in the transverse (y-z) plane, each scanned track has a half-moon shape. The upper surface is concave, the lower surface is convex. The upper surface can be seen in the perspective view, the lower surface in the end view of Figure 7.2. On the upper surface, shrinkage and densification increases towards the centre of the laser beam profile, where the irradiance is greatest. On the underside, the part is rounded due to radial diffusion of the laser's heat into the powder bed. The depth of scans increases in the scan direction. Scan width also increases with distance in the scan direction.

Concerning the two overlapping scans of Figure 7.3, the first of these to be scanned is bigger because once processed it has a higher conductivity than the rest of the bed. It acts as a heat sink when the second line is scanned.

The similarities and differences between modelled and real (manufactured) scans is to be discussed in Section 7.4.

A question exists over what density value constitutes the transition from semi-dense powder to solid material in modelled parts. To create the parts shown, a value of 7500kg/m^3 was selected. Referring to a GSharp section, Figure 4.2 in Section 4.3, density falls from 7500 to 7000kg/m^3 over approximately 0.1mm around the part perimeter. The solid volume encompassed is not sensitive to the choice of powder-to-solid density within this likely range.

7.1.2 Single Layers

7.1.2.1 Results

Figure 7.5 shows a 10 scan part with $s = 3d/6$. The aspect ratio here is (1,1,1) as in 7.1.1.

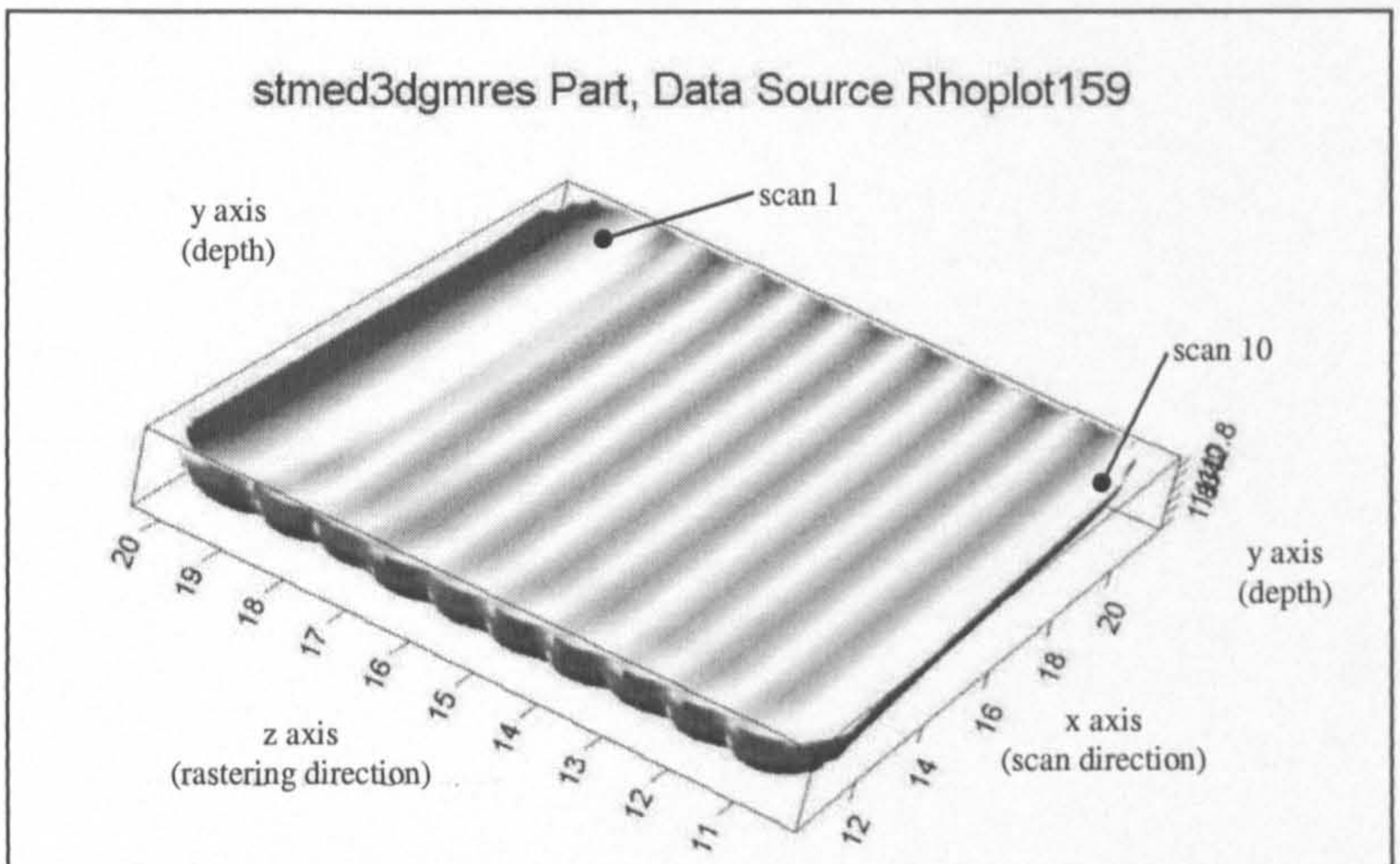

Figure 7.5
Ten scan single layer part modelled by *stmet3d*

7.1.2.2 Discussion

The features seen in the modelled layer are similar to those of one- and two-scan parts in 7.1.1. The transverse sectional shape of scans is of the same half-moon type. Scans become deeper and wider in the scanning direction. The first scan is the biggest, acting as a heat sink when the second line is scanned. Scan depth reduces from the first to the second scan, and from the second to the third scan. Scan depth reaches a steady state by the third scan, true for all values of P, U and s tested later in Section 7.3. The morphology of modelled layers resembles that of real layers in some ways, but does not in others: this will be discussed more in 7.4.

7.2 Comparison Between Original and Modified Program Output

Changes have been made to the model program code and meshes, recounted in Sections 4.2 and 4.3. Five changes have been made which may affect the model's output: use of the GMRES sparse matrix method, increase in TM *x* spacing, doubling of the TM definition, doubling of the TM depth and the marching cool down procedure. Any effect of these changes is demonstrated in 7.2.1 via parts which are identical in nature except that the changes mentioned above are made. Multiple parts had been modelled and compared in each case, but only one is shown.

7.2.1 Results

Figure 7.6 contains two images of GSharp 3-section views. The pre-GMRES version of the model has generated the output on the left, and the GMRES version has created the output on the right. The dimensions of both scans in the three sections are virtually identical. A small part is used for the comparison, comprising only 2 short scans. As has been said, the potential modelled part size has been increased with the introduction of GMRES.

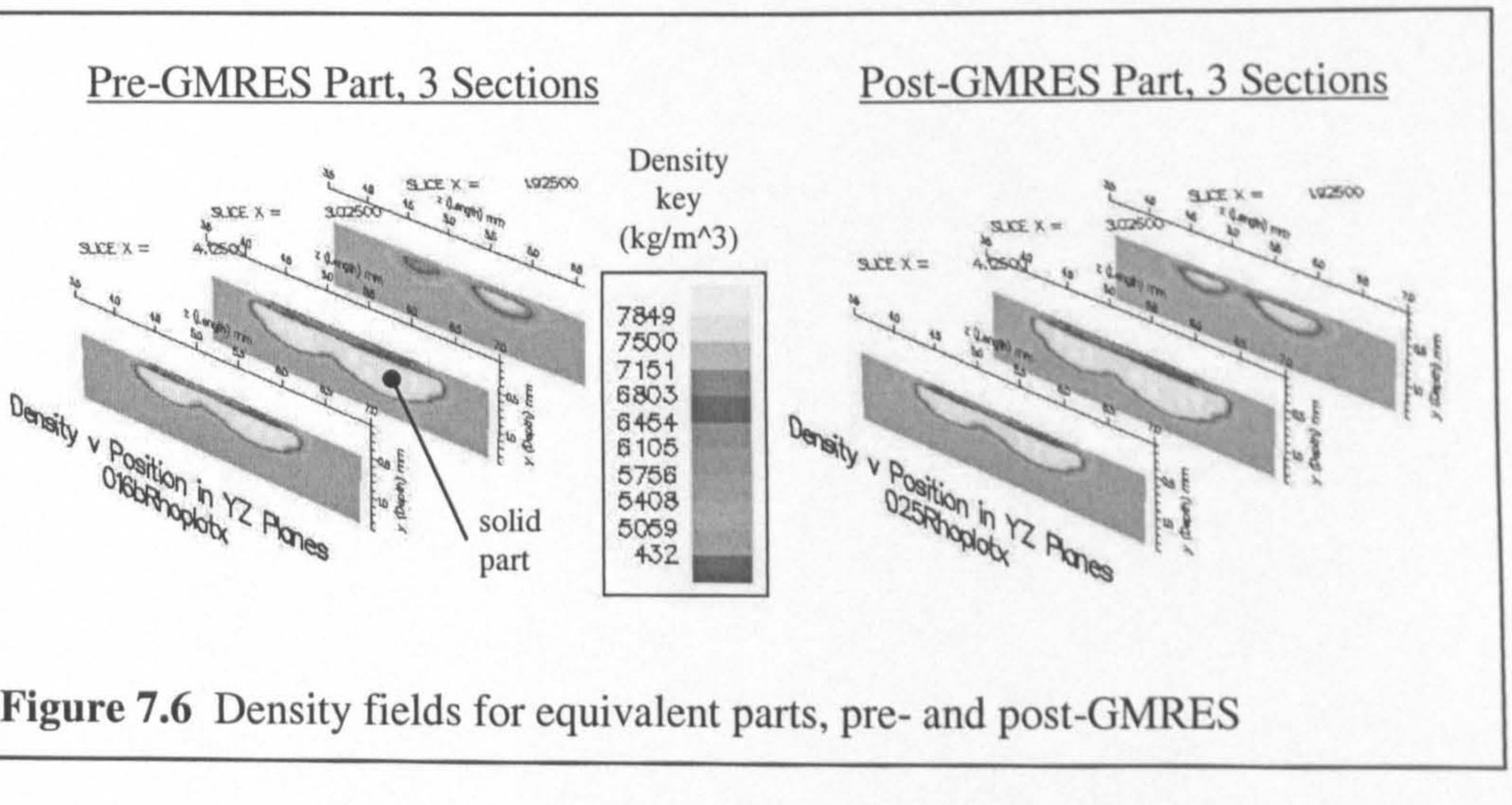

Figure 7.6 Density fields for equivalent parts, pre- and post-GMRES

Doubling of the nodal density in the TM was tested with the GSharp single section view in Figure 7.7. The part on the right, made using the denser mesh, has a slightly better defined (less angular) surface. As shown by the dimensions quoted in the figure, both parts are of the same shape and size.

To test the increase in TM depth and change of procedure from marching to static cool down, 3 Matlab views of 3 parts were created, displayed in Figure 7.8. The part made with a TM which continued to march onwards as the bed cooled down is no different from the one made with a TM which did not move at the end of each scan. The only difference seen between these two sets of parts is due to a change in the lighting angle. However, deepening the TM from 2.5 to 5mm had a big effect on geometry, removing the "hook" feature from the underside of the part.

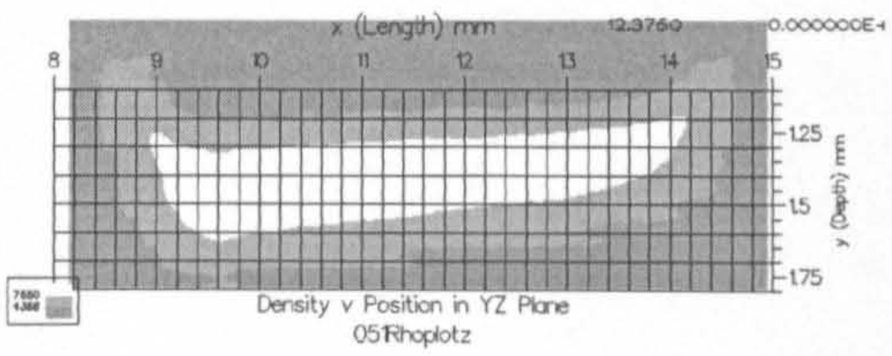

Measurements: Top left tip to bottom, 0.375mm
Top right tip to bottom, 0.44mm

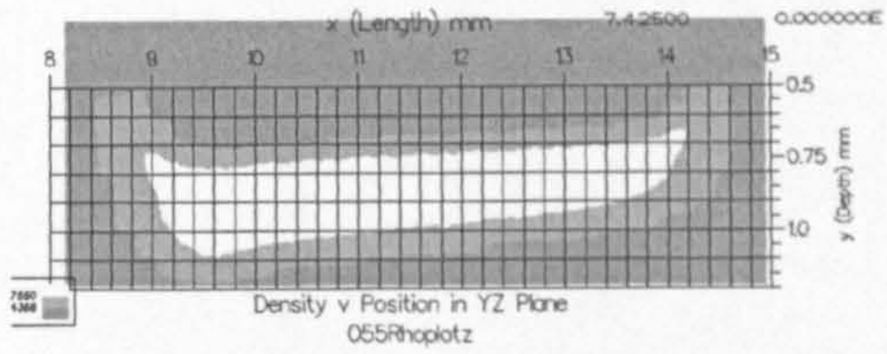

Measurements: Top left tip to bottom, 0.375mm
Top right tip to bottom, 0.44mm

Figure 7.7 Density fields for equivalent parts, pre- and post-TM refinement

Original Thermal Mesh, Static Cool Down

Side Views

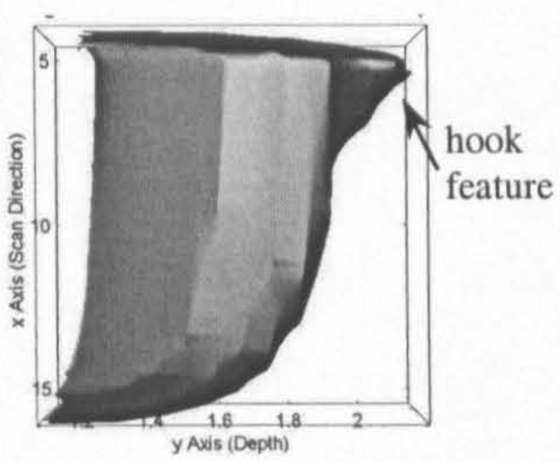

End Views

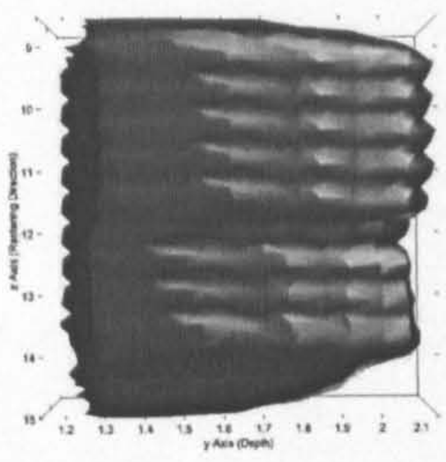

Top Views

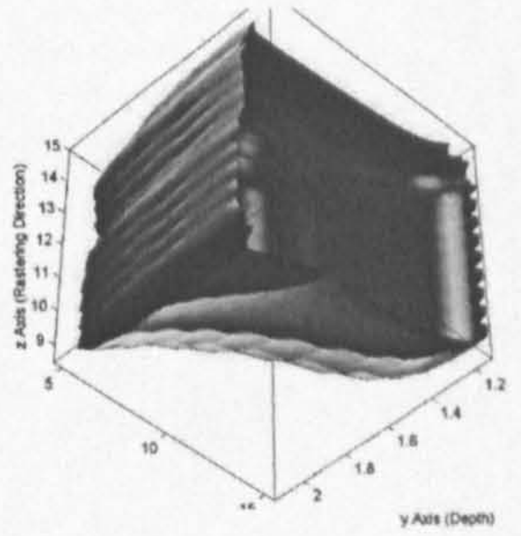

Original Thermal Mesh, Marching Cool Down

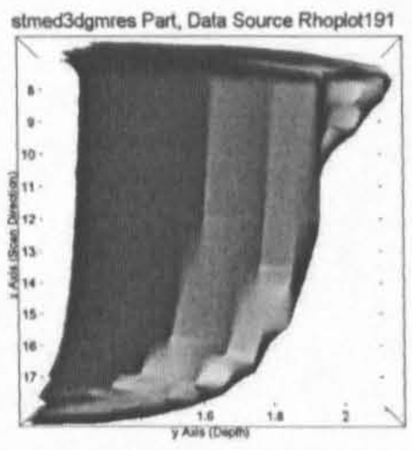

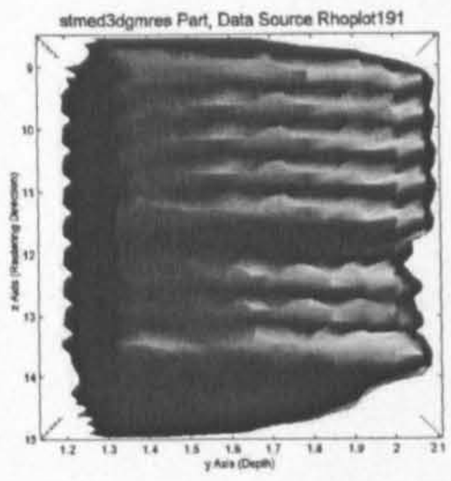

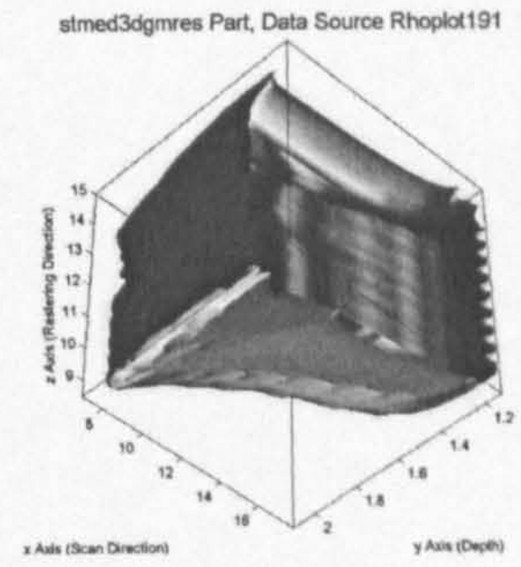

Deeper Thermal Mesh, Marching Cool Down

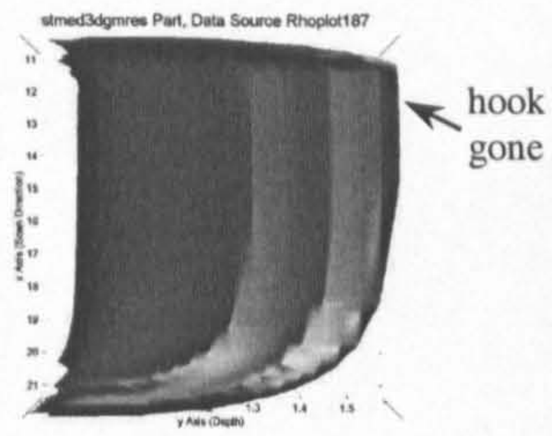

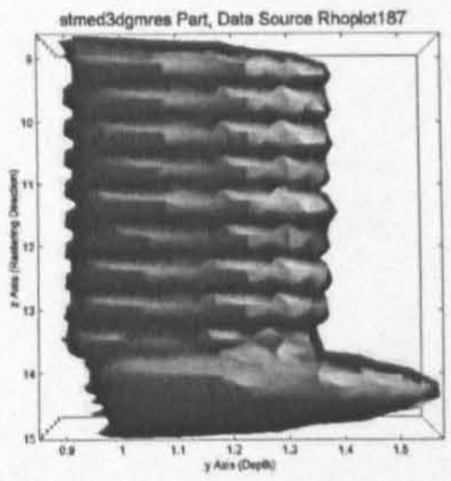

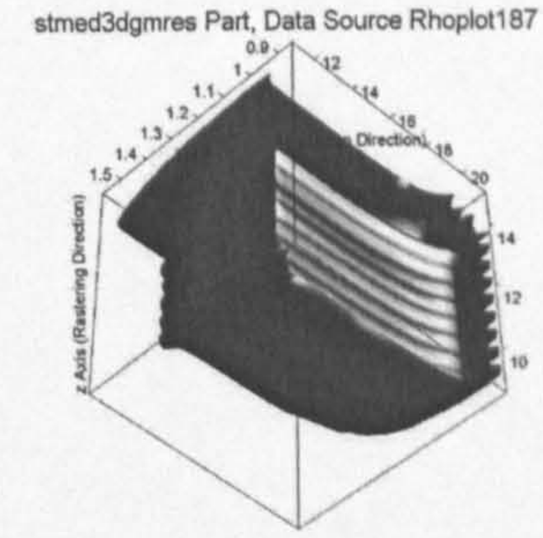

Figure 7.8 Single layer used to test thermal mesh and scanning procedure changes

7.2.2 Discussion

Figure 7.6 proves the acceptability of sparse matrix methods for rapid program execution without reducing the validity of the FE calculation. Figure 7.7 suggests that the experimental doubling of the TM *y* nodal density was unnecessary. Returning to the original TM *y* node density (requiring 17 nodes) will allow either a larger PBM or a smaller running time to be achieved.

In Figure 7.8, the effect of measures used in an attempt to reduce or stop out-of-control part growth are shown. The first measure to have been taken (the result of this has not been shown) was to increase the *x* distance between the front of the TM and the heat application zone, to make it equal to the distance from the sides of the TM to the heat application zone. This had no effect on modelled parts. For a top view of the TM showing the new position of the front and side surfaces relative to the heat application zone, see the diagram Figure 7.15. The -800°C surfaces denote the corners between the front and sides of the TM; the main 1000°C surface surrounds the heat application zone.

The next measure to be taken is displayed in Figure 7.8, namely the change from a static to a marching cool down period. This change did not remove the hook feature seen on the end of modelled scans as described in Section 4.3. It had been considered that a possible cause of this feature was a bias in exposure time between the main body and the end of a scan. The TM dwelling over the end of a scan might have allowed extra growth of the scan end to occur. However, this could only be true if some material in the main body of the scan had been left behind by the TM with a temperature still above the melting point (i.e. that area of the scan had an unrealised potential to grow further). The new marching procedure showed that material in a melted state was not leaving the TM, because there were always less than 15 (and typically less than 6) marching cool steps at the end of a scan before the temperature fell below solidification point. A minimum of 19 cool steps would be required before any processed material would begin to leave the TM.

The identical nature of parts made using both procedures means that either of them could be used in future. The marching cool down allows the program to be executed slightly faster, whereas the static cool down permits modelled parts of greater size to be processed.

In contrast to the two previous changes, the increase in TM depth had a marked effect on modelled parts (Figure 7.8). With the TM depth increased to 5mm the scan depth reaches a steady value at x=14.5mm, whereas it had continued to increase in the scan direction (to form the hook feature) at a TM depth of 2.5mm. It should be remembered that the bottom surface of the TM has a boundary condition that temperature is equal to 20°C. Deepening of the TM appears to improve the resemblance of modelling conditions to those in experiments, where the powder bed is effectively of infinite depth. Although the TM depth increase removed the hook in the case of Figure 7.8, it has not eliminated the hook phenomenon completely as will be seen in Section 7.3.1.

7.3 Numerical Model Process Mapping

Below are the results of process mapping for the model *stmet3d*, an activity which was introduced in Section 4.6. Throughout the mapping exercise the TM had 22×45×19 nodes, the TM depth was 5mm and the marching cool down procedure was used. Data was processed as stipulated in Section 5.2.2. The maps are intended for two purposes: primarily to test the ability of the model, then for comparison with the experimental process maps of [Hauser 1999a], first mentioned in Section 2.2.6.1.

For the purpose of comparison, Hauser's maps are reproduced here. Figure 7.9 shows the four experimental process maps, for stainless steel 314S powder processed in argon using the experimental equipment of Section 3.3. Each map is for a different powder fraction, with a particle size denoted above the graph. Maps are split into four areas, to indicate the outcome of processing at a particular power and speed. Areas in the key have the following meanings:

- Area 1- Melting with bonding exhibiting low surface tension phenomena;
- Area 2- Melting with breakages;

- Area 3- Partial melting and no bonding;
- Area 4- No marking.

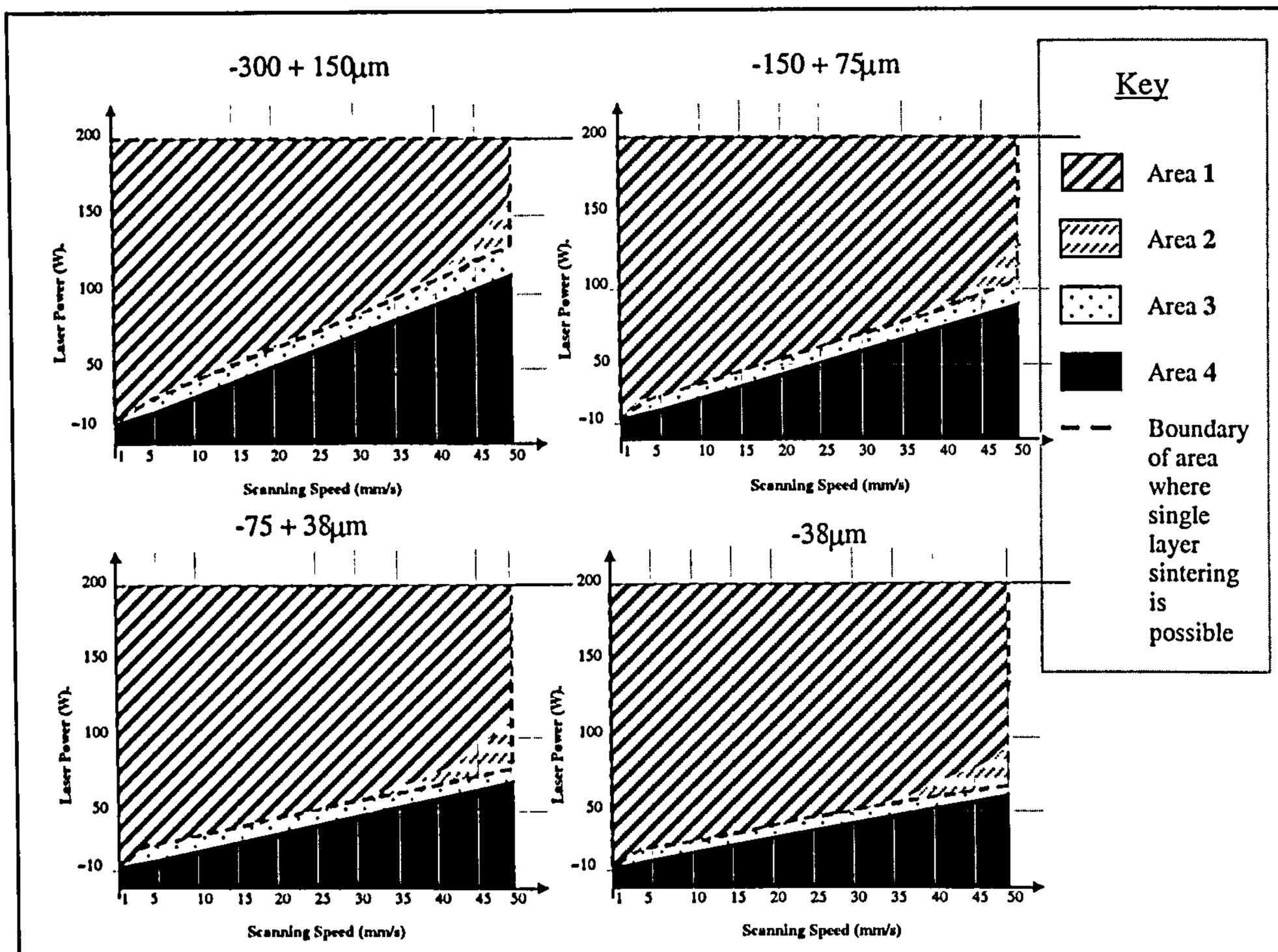

Figure 7.9 Process maps by Hauser, for stainless steel 314S layer processing

7.3.1 Results

In this section there are four process maps for the model, Figures 7.11 to 7.14. Two maps are for $s = 3d/6$, then there is one for each of $s = 5d/6$ and $s = 9d/6$. There is also a temperature surface plot, Figure 7.15, showing two views of a TM temperature field which failed to converge.

The four process maps have a common key, which is provided in Figure 7.10. Areas 1 and 2 from Figure 7.9 are equivalent to area 1 in Figures 7.11 to 7.14. Areas 3 and 4 from Figure 7.9 are equivalent to areas 2 and 3 in Figures 7.11 to 7.14. Areas 4 and 5 in Figures 7.11 to 7.14 have no experimental equivalent.

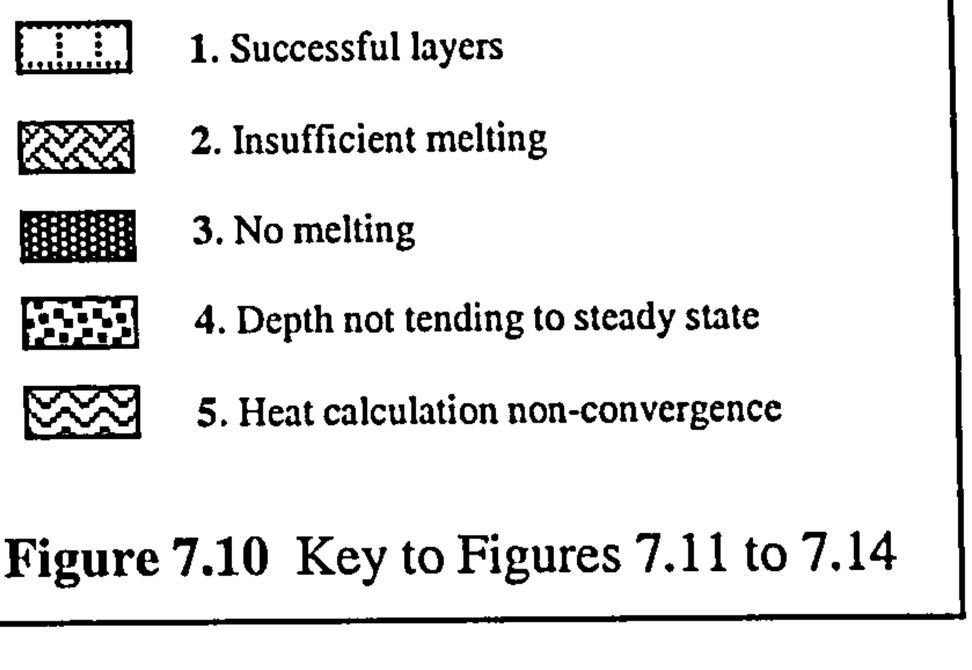

Figure 7.10 Key to Figures 7.11 to 7.14

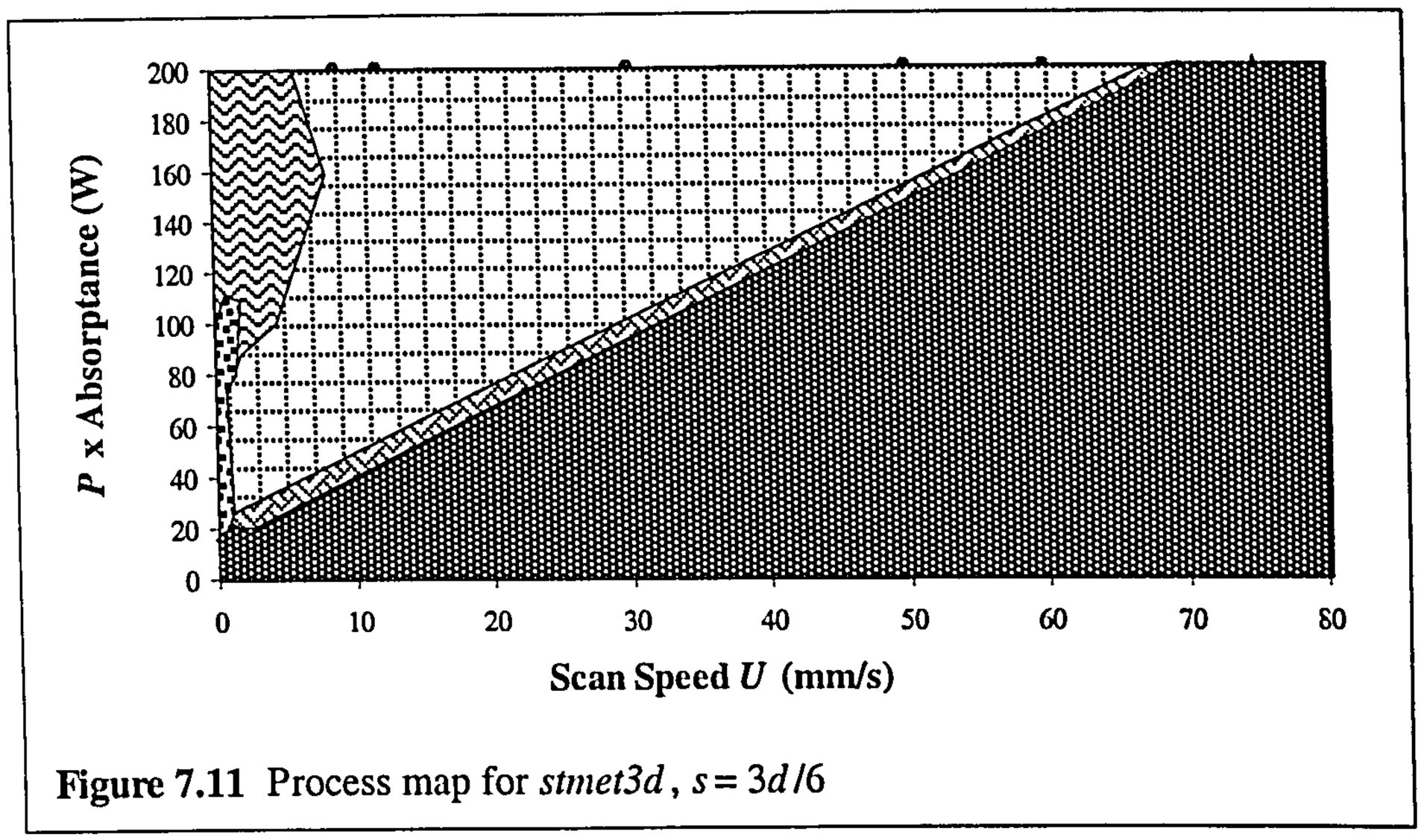

Figure 7.11 Process map for *stmet3d*, $s = 3d/6$

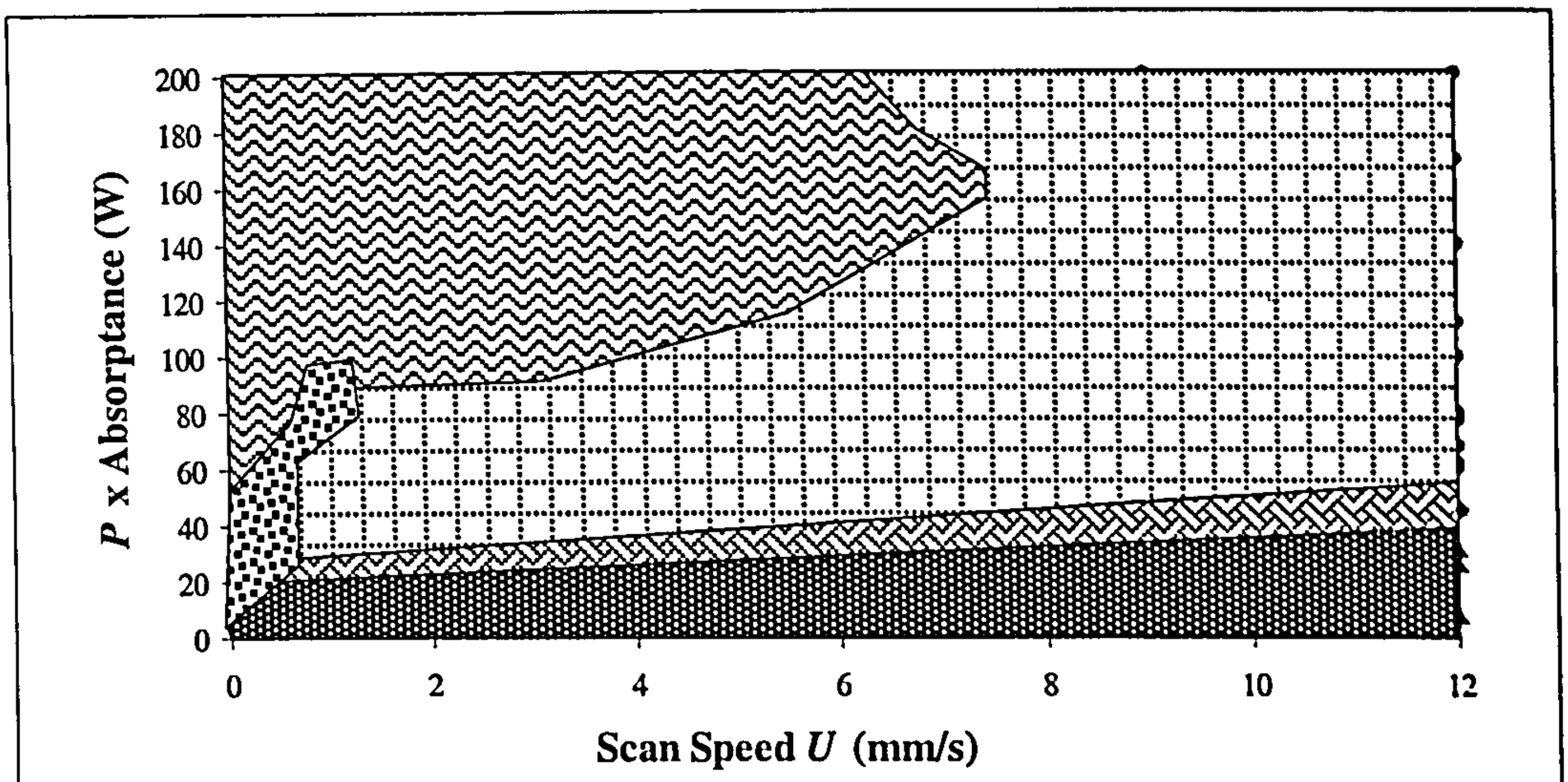

Figure 7.12 Enlargement of process map Figure 7.11 for *stmet3d*, $s = 3d/6$

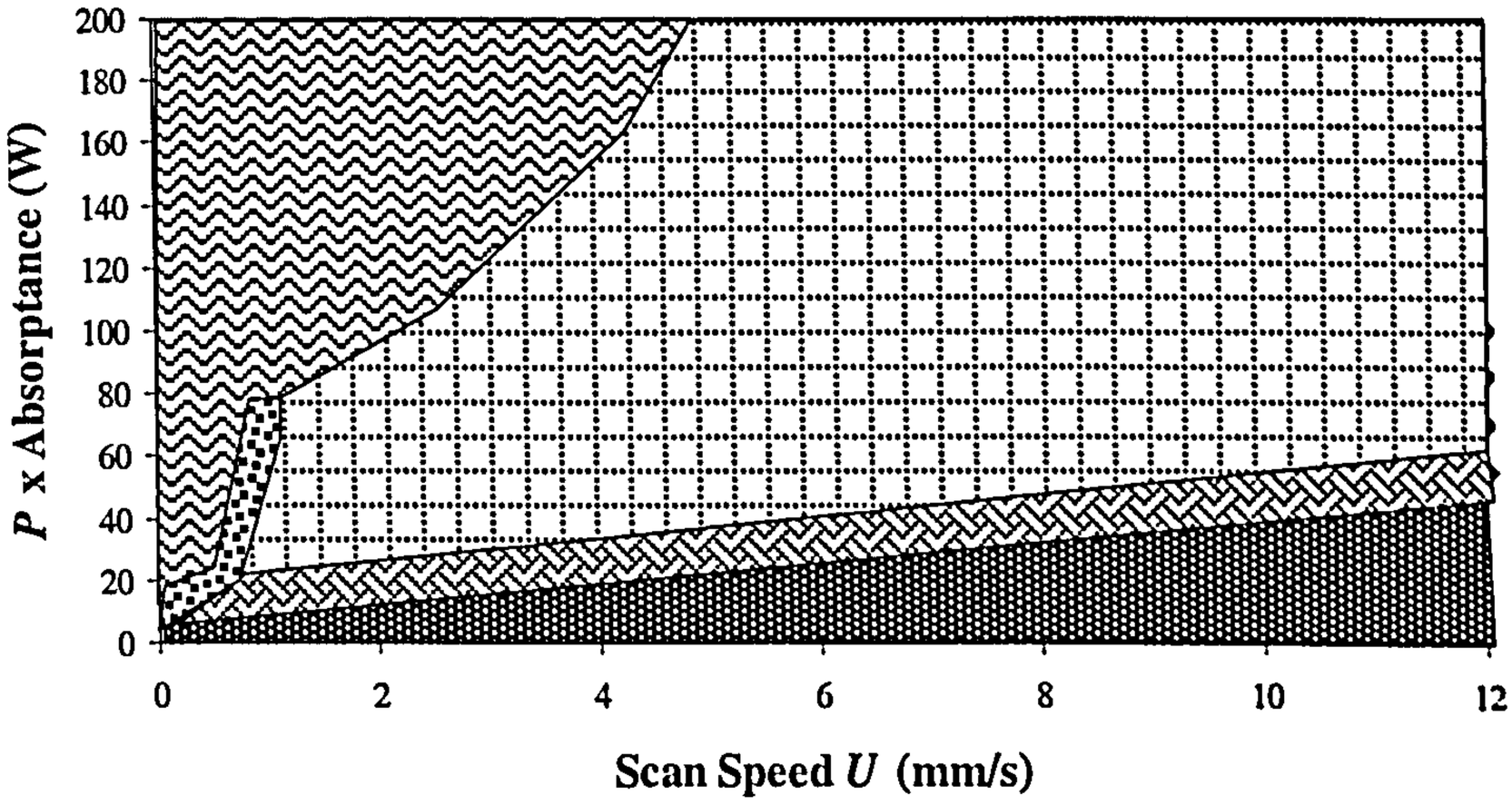

Figure 7.13 Process map for *stmet3d*, $s = 5d/6$

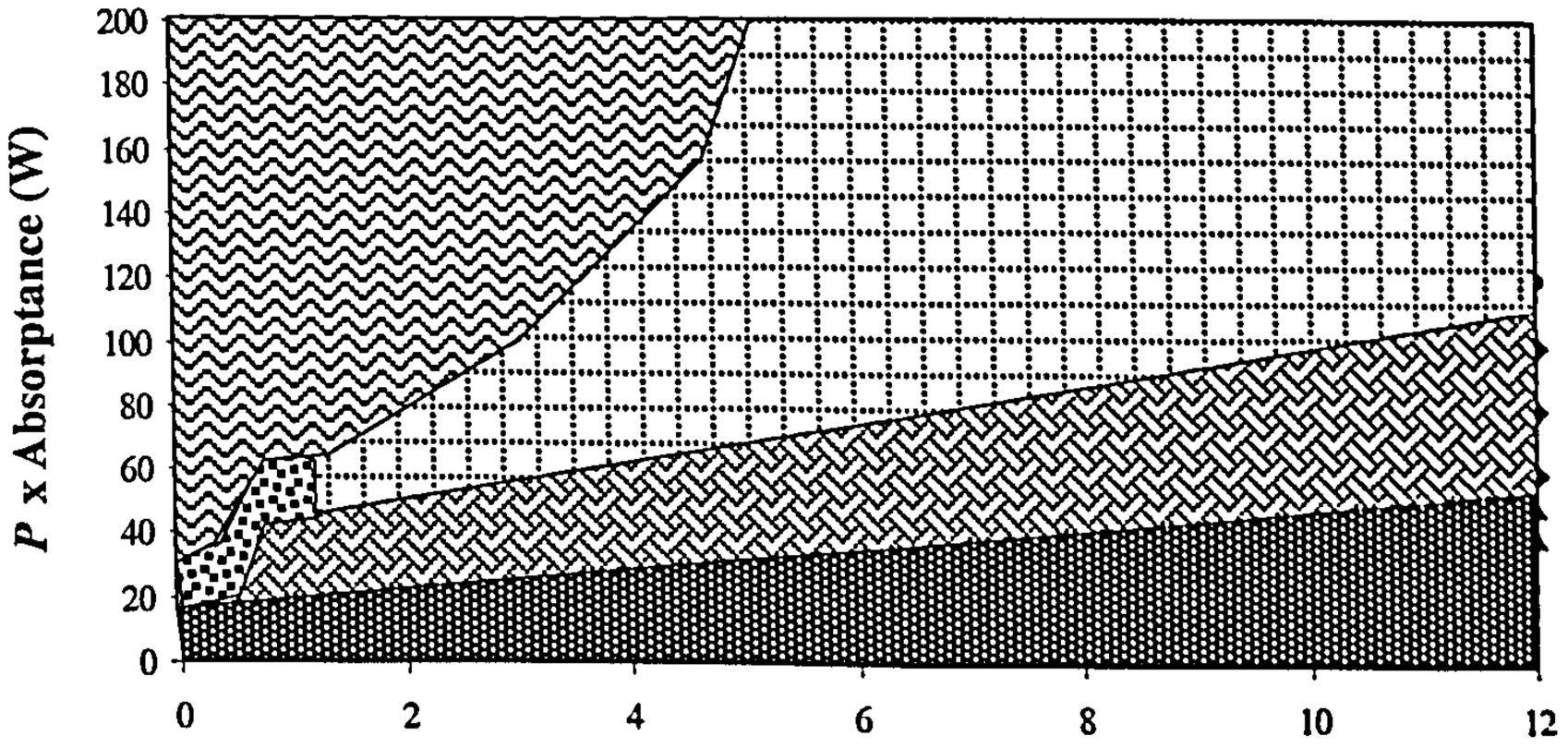

Figure 7.14 Process map for *stmet3d*, $s = 9d/6$

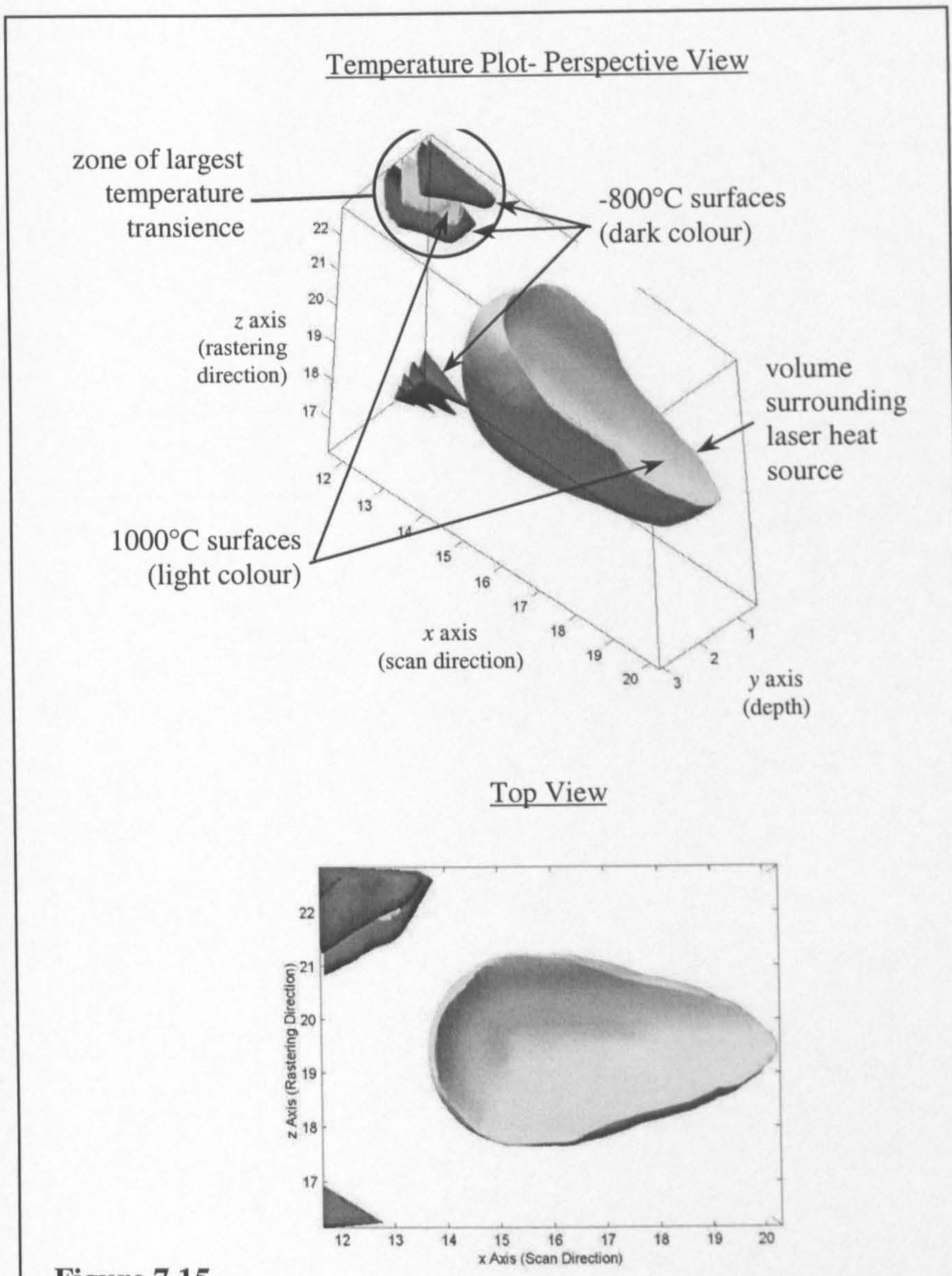

Figure 7.15
Temperature surface plot for case of non-convergence

7.3.2 Discussion

The process maps shown, Figures 7.11 to 7.14, display the degree of success with which modelled single layers are created, over a range of P and U for set values of s. The running of the model is discussed first, then a comparison is made with the maps by Hauser, which were shown in Figure 7.9.

It can be observed that for U less than 10mm/s, parts may grow out of control or the program *stmet3d* may fail to complete execution (shaded areas 4 and 5 as

shown in the key Figure 7.10) at certain power levels. These two cases are associated with the modelling process, and are not reflected in experimental process maps. At U equal to 4mm/s, areas 4 and 5 are found at $P.\alpha$ greater than 100W. At the extreme case of U equal to 0.5mm/s, there were no successful modelling runs at any value of $P.\alpha$. Put simply, the problems of constant increase in part depth and FE calculation non-convergence correspond to high values of A_N, for U below 10mm/s.

At U above 10mm/s, parts can be modelled over a wide power range. The limiting factor is a minimum power level required to make coherent parts, which increases as U increases. If A_N is too low, individual scans do not join one another (insufficient melting, area 2). If A_N drops further, temperatures do not reach a sufficient level for any solid material to form (no melting, area 3). At $P.\alpha$=200W (the top line) on each map, the range of U over which coherent parts can be made reduces as s increases. The highest speed at which adjacent scans will join for s =3d /6 is around 65mm/s. For s =5d /6 the equivalent point is 52mm/s, and for s =9d /6 it is 25mm/s. As s increases, the power required to create connected scans increases, which is to be expected.

With a TM depth of 5mm, hooking of modelled parts occurs only at U of 1mm/s or below. In extreme cases, the part was seen to encroach on the bottom surface of the TM. It has been discussed in 7.2.2 that an increase in TM depth previous to process mapping had reduced the hooking problem.

A brief consideration has been given to the boundary condition on the rear surface of the TM: see Figure 2.31. The boundary condition set means that no heat may flow through the rear surface in the x (scanning) direction. It was considered whether this might encourage heat to flow in the plane of the rear surface (y-z) to the bottom surface of the TM, to cause the hook feature on parts. However, exactly the same hooks occur using the static cool down as when using the marching cool down procedure. If the rear surface boundary condition was affecting part growth in the y direction, the size of hooks would actually be increased by using the marching cool down procedure.

In the top left corner of the modelling process maps are cases where the heat calculation failed to converge. This caused the program to repeat the heat calculation infinitely, because temperature distributions did not fit the defined pattern. A 3D temperature surface plot at a point in the program's execution where the model looped infinitely as described is shown in Figure 7.15. The conditions for the run are $P.\alpha = 140$W, $U = 2$mm/s. The value of s is not relevant, as the program began to loop before completing the first scan.

In the figure, surfaces have been created to link points which are at a temperature of 1000°C and -800°C. Extremes of temperature -7000°C to 5000°C were seen at a handful of nodes. The temperature variation with position does not resemble anything seen in experiments, and the large negative temperatures found have never been seen in any parts where the program ran successfully (i.e. with convergence of the heat calculation). The worst temperature oscillations were at the corners between the front, side and top surfaces of the TM, which were also close to the heat source elements. These were the locations most restrained by local boundary conditions. The high fluctuations in the temperature field explain why the heat equation failed to converge.

The modelling process maps are now compared with the experimental process maps.

A set value of laser absorptance is not assumed for the modelling process maps. The y-axis of these maps represents the product of P and α, whatever the particular values of P and α may be. The form of the modelling maps is therefore slightly different from the experimental ones. In particular, it is now known that experimental α values are speed-dependent at low U (Section 6.5.1). If it is assumed that α was equal to 0.2 in all cases, then in fact the maximum value of P times α available using the experimental machine would be 240 times 0.2, or 48W.

Even if the value of α is assumed to be equal to 1.0, the power at which coherent layer scanning becomes possible at a certain value of U is higher in modelling than in experiments. The model underestimates the amount of material melted, a conclusion which agrees with what is found in 7.4.3. The border lines between areas of no material melted, insufficient melting and full melting and

bonding are linear on experimental and modelling maps, which supports the validity of modelling. The shape of areas 1, 2 and 3 for modelling is the same as for the corresponding areas of the experimental maps, Figure 7.9.

Referring to area 4 of the modelling maps, depth not tending to steady state in the scanning direction (the hook phenomenon) is something which has not been seen under any circumstances (P, U, and s values) in manufactured parts.

In terms of applying the model to process control of SLS manufacturing, areas 4 and 5 on the modelling maps are not considered a large problem. They occupy positions of high P and low U. As has been discussed in Chapter 6, the experimental processing speed is hoped to be quite high, almost certainly above 0.5mm/s, in order to be competitive with other SFF processes in terms of part build time.

The areas on the modelling process maps would be expected to change in size and shape if model inputs were changed. For instance, if the specific heat of the powder material were reduced, all areas would be expected to shrink down on the y-axis. Material would require more power to melt properly. Increasing the depth of the TM has already (Section 7.2) increased the power limit at which parts begin to grow out of control, and could further increase this limit. Experimental process maps show a dependence on d_p of the power at which coherent layer manufacturing becomes successful. This might be reflected by model results if a change in the input powder density (a function of d_p) was made.

Model process mapping has not been performed before for *stmet3d*, and has, it is hoped, provided information useful for model development. The comparison of model and experimental process maps adds to the comparisons made in Section 7.4.

7.4 Dimensional Analysis of Single Layer Sections

Cross-sections of experimentally-produced single layers (discussed in Chapter 6) were compared dimensionally against numerical model output. The purpose of this work is as stated in 4.7, the results for modelled parts were obtained as detailed in 5.2.3.

The sections analysed had been made through the centre of each layer in the scan direction as in Figure 7.16. The results of this comparison between manufactured and modelled parts leads to a discussion of the model's features and accuracy.

The work displayed in Section 7.4 has been presented in a recent paper, [Taylor 2002]. The same layer identification format is sometimes used as in Chapter 6, *s-P-U*.

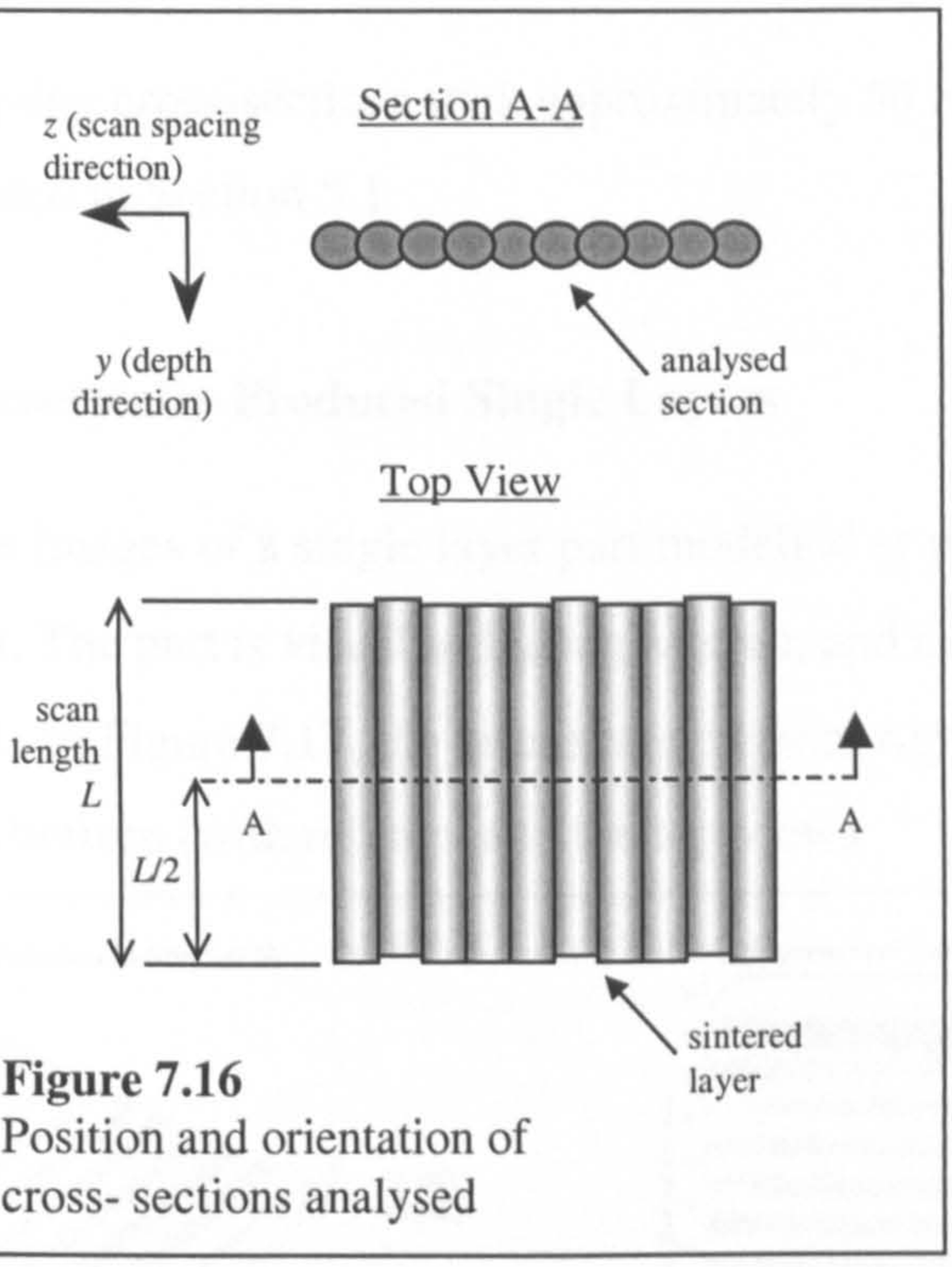

Figure 7.16
Position and orientation of cross- sections analysed

7.4.1 Results: Experimentally-Produced Single Layers

Figure 7.17 shows close-up photographs of a single layer part manufactured at $s = 5d/6$, $P = 60$W, $U = 1.0$mm/s. The figure has already been seen in Section 6.7. With reference to the top view, the laser scanned from right to left and rastered from top to bottom.

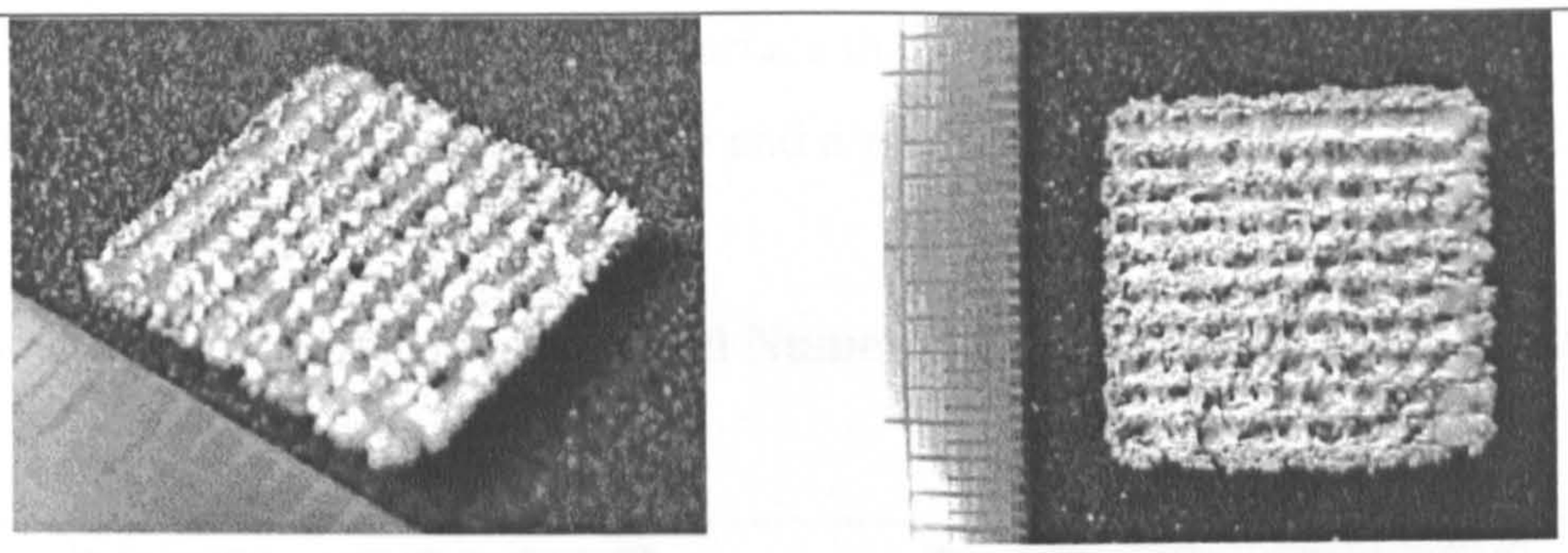

Figure 7.17 Perspective (left) and top view (right) of manufactured part

Making and analysing cross-sections took approximately 50 minutes of worker time per part, estimated in Section 5.1.

7.4.2 Results: Numerically-Produced Single Layers

Figure 7.18 shows images of a single layer part modelled at $s = 5d/6$, $P = 60$W, $\alpha = 1.0$, $U = 1.0$mm/s. The part is visualised using Matlab, and has been seen already in 7.1.2.1. As in Figure 7.17, the laser scanned from right to left and rastered from top to bottom (with reference to the top view).

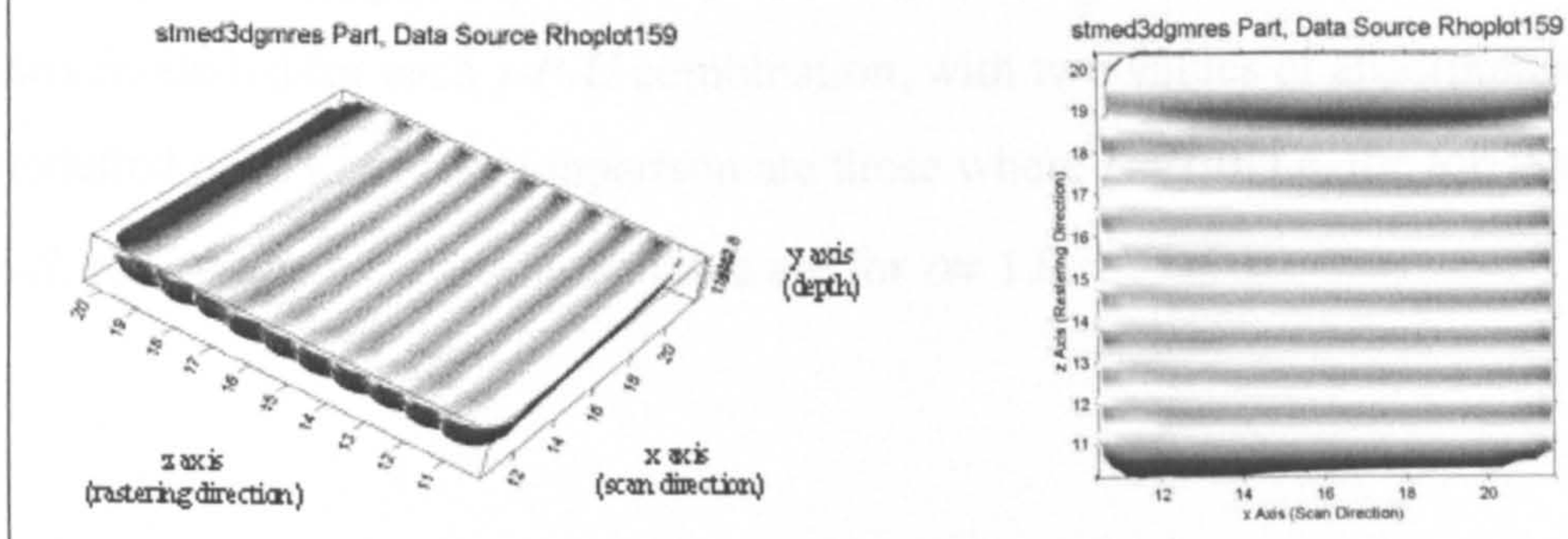

Figure 7.18 Perspective (left) and top view (right) of example modelled part

It took approximately 15 minutes of worker time per part to make and analyse cross-sections, estimated in Section 5.2.

7.4.3 Discussion- Layer Features

Certain features are noticeable in Figure 7.17 and 7.18. Individual scans of the laser can be distinguished. Common to both layers, the first line scan (FLS) has a noticeably different appearance in comparison to the following scans. The

modelled part has a much smoother surface than the manufactured part. The manufactured part has a pitted surface and a granular appearance at the edges.

7.4.4 Results: Experimentally- and Numerically-Produced Layer Sections

Figure 7.19 Mid-sections of a manufactured (left) and modelled (right) part. Laser rasters from left to right hand end of sections as shown.

A typical manufactured and modelled part are displayed in the figure, 7.19. In Figure 7.19 and in Table 7.1, the first line scanned is on the left hand side, and the last line scanned is on the right hand side.

Table 7.1 is a comparison of layer cross sections manufactured and modelled at 9 combinations of s, P and U. The area and area-based relative density of parts are compared.

For each of the nine s-P-U combinations, three manufactured parts were sectioned and analysed; quoted values are the average of three. There were two parts modelled for each s-P-U combination, with two values of absorptance. The modelled parts used for comparison are those where $\alpha = 1.0$, i.e. the top layer in each row. Values quoted in the table are for $\alpha = 1.0$.

Conditions		Manufactured Parts (Average Values are Quoted)			Modelled Parts (Values Quoted are for α=1.0)		
s (mm) [d=1.1 mm]	P (W), U (mm/s)	Profiles	Area (mm^2)	Rel'tive Density (%)	Profiles: Top, α=1.0 Bottom, α=0.5	Area (mm^2)	Rel'tive Density (%)
3d/6	60, 1	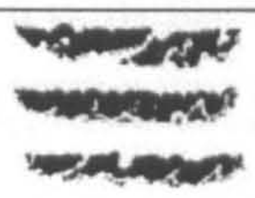	5.0	68		3.4	76
	120, 6		4.2	63		3.2	72
	155, 12	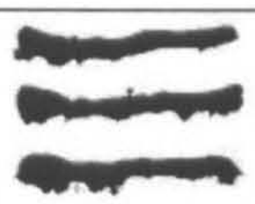	3.8	66	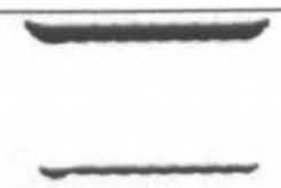	2.9	78
5d/6	60, 1	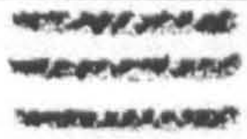	6.7	59	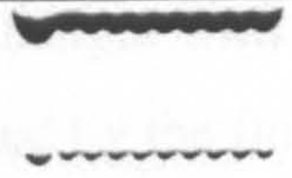	5.0	73
	120, 6		6.4	64	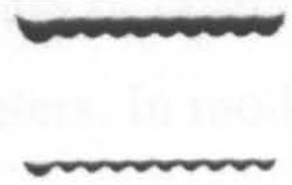	4.8	76
	155, 12	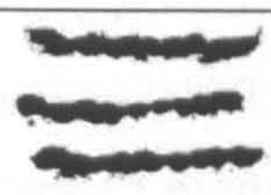	7.1	65	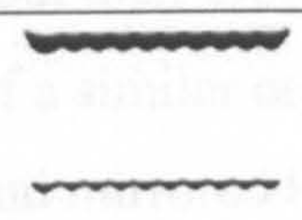	4.1	78
9d/6	60, 1	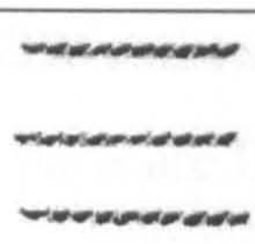	10.5	58	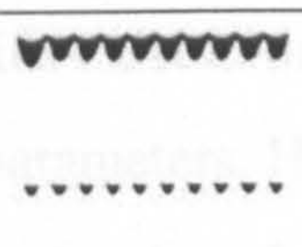	7.3	57
	120, 6	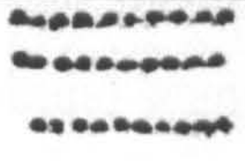	12.2	56	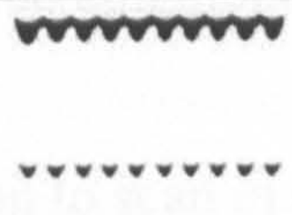	7.1	64
	155, 12	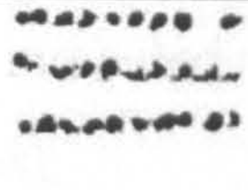	8.8	45	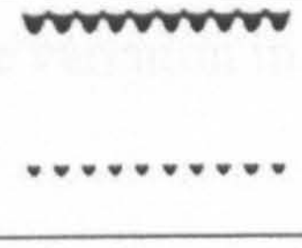	5.8	58

Table 7.1 Comparison of manufactured and modelled part cross-sections.
Note: part profiles scaled to fit table- scale varies according to s value.

7.4.5 Discussion- Comparison of Layers

This discussion will first examine general layer morphology, then will look at the sectional area and relative density results of Table 7.1. Finally, comments will be made about the scope of the model.

In manufactured parts, groups of particles are seen attached to the perimeter of layers, particularly on the part undersides. This can be seen best in Figure 6.11. Such particles are not seen surrounding modelled parts. The model assumes the powder bed to be a continuous medium of varying density, so would not predict satellite groups of particles.

Real parts have a greater change in shape than is predicted by the model. This applies to changes in processing parameters, and to random changes in parts made at the same parameters. The two issues are dealt with separately in the following two paragraphs.

Manufactured part morphology is discussed in Section 6.7.2. To summarise, the shape and size of the FLS and proceeding scans changes with parameters. Scans demonstrate two cross-sectional shapes, determined by the fluid mechanics of the steel in its liquid and gaseous phases. The roughness of layers, presence of through voids and flatness also depend on parameters. In modelled layers, individual scans change in size with parameters, but their cross-sectional shape remains the same, discussed below. The FLS is of a similar or greater size than the proceeding scans in manufactured parts, a trend mirrored by the model except in parts made at 60W and 1mm/s. No through voids exist in the modelled parts at $\alpha = 1.0$. Modelled parts are flat at all processing parameters. Higher roughness is observed at high scan spacing in both manufactured and modelled parts; the curvature of individual scans is more distinct.

Random geometrical variation is seen from scan to scan in a manufactured layer. Examining modelled sections, there is little variation in shape or size from one scan to the next.

Low s, high P and low U lead to high energy input per unit area, A_N. For this reason, parts manufactured and modelled at $s=3d/6$ are expected to have (and do have) a higher processed density than parts processed at $s=9d/6$. The relationship between A_N and relative density is not a linear one however, as demonstrated in Table 7.1.

Experiments and modelling agree that the amount of material melted decreases with decreasing s. Previously-processed material can act as a heat sink for laser

energy, and this effect increases with reduction of *s*. Furthermore, rescanned solid metal absorbs a lower proportion of incident laser energy than fresh powder as shown in Section 6.5.2. The heat sink effect is recreated in modelling, and is the reason why the FLS is of similar or greater size compared to the following scans in modelled layers. The absorption effect is not recreated in modelling, and is discussed later in this section.

Experimentally-generated parts display a lower relative density than modelled ones. This is due to the rougher, more porous and sometimes curled shape of manufactured parts. The area-based relative density values quoted for parts will be slightly higher than the actual (volumetric) relative density, because greater porosity exists at the layer ends than in the centre.

In the sets of 3 parts manufactured at identical parameters (Table 7.1), there can be a variation in cross-sectional area of up to 14 percent from the average value quoted. In contrast, there is complete repeatability every time a modelling run is repeated.

The model always underestimates the amount of material melted, even at the highest value of absorptance. With α assumed to be 1.0, manufactured layers have 30 to 75 percent more area than modelled ones. There are two possible reasons why this might be so. The first lies in the model's handling of temperature information between the end of one scan and the start of another. In the current version of *stmet3d*, temperature fields created by preceding scans are overwritten. Temperatures in the TM are reset to *TDEG0* (20°C) at the start of each new scan. This effectively removes heat from the bed. Referring to Figure 7.4, a temperature snapshot has been captured at the end of laser scanning when P=100W, α=1.0 and U=6mm/s. Temperature field x-y sections are shown at certain distances from the scan centre. Even at a spacing $9d/6$ from the beam centre, the majority of the area shown is above 200°C. If this temperature was retained, the effect on the size of the following scan would be expected to be significant.

A second possible cause of discrepancies between modelled and manufactured part size lies in material conductivity values. Equations (2.24) and (2.25) in Section 2.5.2.3 describe how the model calculates k as a function of temperature and porosity using the parameters *CONDO*, *CONDV*, *SIGV1* and *SIGV2*. Values of the four parameters as used throughout this work are reported in Table 4.1.

Applying the four values from Table 4.1 to equations (2.24) and (2.25), a room temperature k value of 1.1W/(m.K) results. This is several times larger than experimentally-measured values of k from Chapter 6. Examples of measured values are 0.15W/(m.K) for stainless steel 314S of d_p 75-150μm in argon (series 1.3) and 0.25W/(m.K) for the same powder in air (series 1.1). Assuming that *CONDO* and *CONDV* values are appropriate for stainless steel (both constant for a particular material), *SIGV1* and *SIGV2* must be changed to suit the powder particle size and atmospheric gas. Changing *SIGV1* alone, an increase from 6.05 to 56 would be required to obtain a room-temperature k value of 0.15W/(m.K). It is not known what effect a change in *SIGV1*, hence k, would have on the dimensions of modelled parts. Modelling work had been well underway once the k results of Chapter 6 were obtained so for consistency, changes were not made to the model parameters.

Some phenomena occurring in the direct single phase SLS process are not included in the model. One of these is liquid metal balling. Surface tension causes rounding of tracks on the top side and underside. Another phenomenon is material vaporisation, believed to affect a minority of cases. At low U and high P (for instance 1mm/s and 60W), it affects scan size and shape as described in Section 6.6. The model always predicts a half moon scan shape, for reasons stated in 7.1.1.2. Modelling of effects such as surface tension would be a large task.

The model does not include stress analysis, so it can not predict the mechanical interaction between adjacent scans. Asynchronous cooling causes asynchronous shrinkage, as discussed in Section 2.2.6.3. This may cause manufactured parts to curl at high A_N. In larger parts, asynchronous cooling can cause cracks to appear. Without stress analysis, all modelled parts appear flat (with no curling).

It is possible to set a coefficient of time-related heat transfer from the modelled part surface to the surroundings. In this modelling work, negligible surface convection and radiation are assumed so the coefficient is set to zero.

The "absorption effect" was discussed earlier: once material has been processed, its surface transforms from porous powder to a solid track. The absorptance of the fresh powder is higher than that of processed material. It has been mentioned that the model assumes the powder bed to be a continuous

medium, with no understanding of the arrangement of particles and pores. This was part of the reason for implementing variable absorptance per scan in the model. It had been intended to simulate the absorption effect in the partial rescanning of material, but there was not enough time to carry out such work.

Time-wise, estimates for generating cross-sectional results are 15 minutes per layer using the model, and 50 minutes per layer using the experimental method. This provides an argument for developing the model as a substitute for experimental trial and error.

7.5 General Comments on Running Program

Factors affecting the modelling program's running time are discussed, and comments on reliability are made.

Step 7 in Figure 4.1 shows a test being made on the TM temperature field. Notification is given on screen when the temperature field has not converged to a specified form in the FE heat calculation. This notification appears constantly if running at too high an energy density (see Section 7.3). During normal operation, some non-convergence occurs if P and U are approaching the values where the program froze in the maps of 7.3. This non-convergence was usually seen to occur in the marching cool down steps, or in the first few heating steps: at points when the situation was most transient. Any reported non-converge makes running time increase, as the FE calculation must be repeated many times. A heat step lasts several times as long as normal in this case.

Comparing model running time against the number of scans modelled, 1 scan took 25 minutes, 2 scans took 46 minutes, and 10 scans took 215 minutes. All scans were of the same length. Running time increases in near proportion to the number of heat steps required, which increases in proportion to the amount of geometry scanned. The size of modelled parts also increases the amount of time taken to initialise the meshes and to write output files, but these subroutines require less than 5 percent of run time.

Although it does not change the number of heat steps, choice of scan speed affects the program running time for U<20mm/s. See the graph, Figure 7.20. P and s values in the graphed cases are those at which adjacent scans first join together (i.e. a similar amount of material has been melted in each case, for consistent treatment).

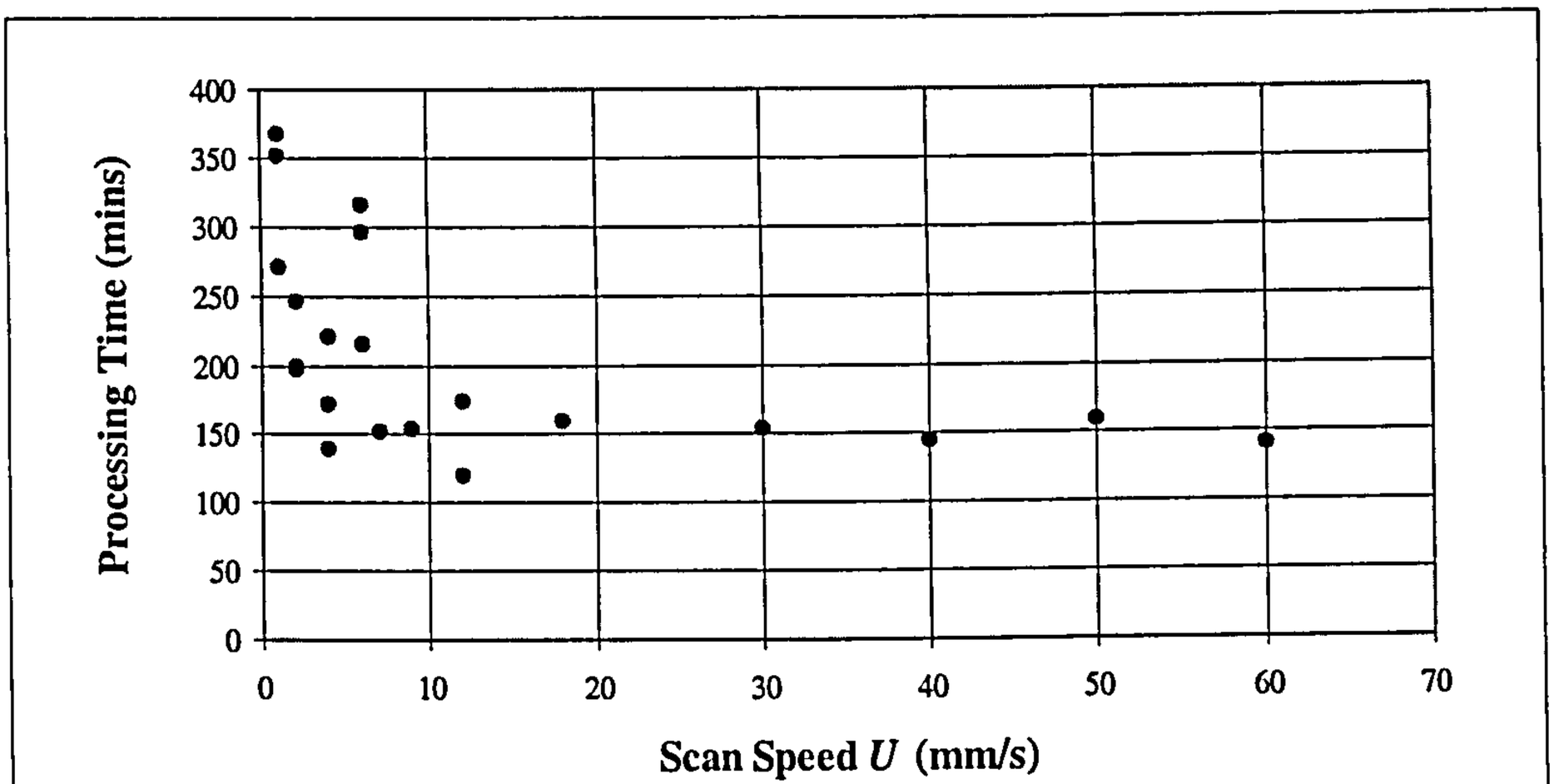

Figure 7.20 Processing time versus scan speed selected for *stmet3d*

Implementation of sparse matrix methods (ILUT and GMRES) had a profound effect on the model's running speed. Heat steps were processed at one every 4 seconds, as opposed to one every 40 minutes before GMRES. This represents a 600-fold speed increase. Running speed is dependent on mesh sizes- smaller meshes run much faster. When the TM and PBM sizes were increased 3.8 and 6.9 times respectively post-GMRES, the time taken to execute the program increased 3 times. There are typically 590 heat steps involved in modelling a layer of ten 10mm scans.

The marching conditional cool down procedure saves time over the static cool down, generally speaking. TM temperatures cool to below solidification level in 2 or 3 (cooling) heat steps on average.

The model has a high reliability rate, running to completion if the limiting process parameters are observed (Section 7.3). Freezing of the program not related to a high energy density (as mapped in Section 7.3) only occurred in 2 out of 110 runs.

7.6 Summary of Numerical Model Development

An existing Fortran-based model of the direct metal SLS process, known as *stmet3d*, has been developed and tested. Much has been achieved with model: firstly the thermal mesh (TM) and powder bed mesh (PBM) have been increased in size. In particular, the nodal density and overall size of the TM in the y direction have been increased. The number of nodes in the TM was increased 4 times, and its depth was doubled. The PBM size has been increased 7 times, so that larger parts may be modelled.

The program code was modified to allow a new value of absorptance to be set for each scan. This will eventually allow the absorptance effect, discussed below, to be taken into account. A modification was made to the modelling procedure, to have conditional marching rather than a static dwell of the TM whilst nodes cooled at the end of each scan. The change was made in an attempt to remove an unwanted "hook" feature, appearing at the end of scans.

A spreadsheet was constructed to ease the process of changing TM and PBM sizes. 20 essential and 5 advisable calculations were made automatically by the spreadsheet. *stmet3d* was made to write it's current layer, scan and heat step to screen during execution, so that if calculations froze, the last position would be known. If the model ran to completion, running time was output for performance analysis. Reformatting of output files reduced their size by 40 percent. 2D visualisation of model output using GSharp software was improved by changing colours and adding a grid, for process mapping and sectional analysis work. 3D visualisation was made possible for the first time using Matlab software, very useful for communication of model output. Density or temperature data could be viewed from any angle in 3D.

Process maps were constructed, to relate modelled part qualities to input power P, scan speed U and scan spacing s. If the model failed to run properly, this was also marked on the maps. Approximately 90 parts were modelled to compile 3 process maps.

Modelled part cross-sections were analysed for area and relative density using Image Pro software.

3D modelled scans were presented for the first time, displaying a half-moon cross-sectional shape and a first line scan which was larger than following scans in the case of layers. Each scan became deeper and wider in the scanning direction. 3D parts were compared to see the effect of sparse matrix calculations, changes in the TM and use of the conditional marching cool down. The only change to have a significant effect on output parts was the deepening of the TM from 2.5 to 5.0mm. This change removed a "hook" feature seen on the underside of parts. With the TM depth at 5mm, the scan depth reached a steady value.

3 process maps showed model output characteristics versus P and U at s equal to $3d/6$, $5d/6$ and $9d/6$ (where d is the laser beam diameter). It was observed that for U below 10mm/s and high A_N, problems of excessive part growth and model freezing could occur. A case where the model froze was investigated, and local temperature fluctuations of thousands of degrees Celsius were found. When process maps for modelling and SLS experiments were compared, the shape of areas denoting particular part characteristics were found to be similar.

The area, relative density and morphology of manufactured and modelled layer cross-sections were compared. It was noted that modelled parts had smoother surfaces than manufactured parts. Manufactured parts showed random variation in shape, modelled parts did not. Individual scans in manufactured parts had a circular or half-moon cross-sectional shape; in modelled parts the cross-sectional shape was always a half moon. Manufactured parts had a first scan larger than the following scans in 5 out of 9 cases; in modelled parts, the first scan was always the largest. The model recreated the higher k of processed (densified) material as compared to fresh powder, but not the lower α. Modelling and experiments agree that material melted decreases with decreasing s.

The model underestimates the amount of material melted, by 30 to 75 percent when α is set to 1.0. A factor contributing to this underestimate is the way the model discards temperature data at the end of each line scanned, resetting to 20°C. This practice effectively removes heat from the bed. The value of k used in the model is several times larger than values measured in Chapter 6; this may have an effect on modelled part size. Modelled layers have a higher relative density than manufactured layers, due to their smoother, less porous and flatter nature.

The model does not include stress analysis or molten metal surface tension effects, which are seen to influence manufactured part morphology.

The execution speed of the model was considered. It was discovered that run time increased in near proportion to the amount of geometry scanned. Non-convergence of the FE calculation at low U and high A_N slowed execution. The use of a sparse matrix FE solution method increased running speed 600 times.

7.7 Possibilities for Future Modelling Work

Following on from observations made in Chapters 4, 5 and 7, some ideas for continuation of this work are proposed.

In 7.4.5, it has been noted that modelled layers are smaller than layers manufactured with the same parameters. The model resets temperatures in the powder bed to 20°C once each line has been scanned, which removes heat from the bed. It is thought that if existing temperature data was maintained between one scan and the next, this would increase the volume of melted tracks. The value of model parameters *SIGV1* and *SIGV2* should be reviewed; a comparison has shown that powder conductivity in the model is several times larger than has been measured experimentally. This may affect the size of modelled parts.

Modelled and manufactured parts are dimensionally and morphologically compared as part of this work. Activity such as recommended in the paragraph above will hopefully improve the extent to which the modelling process recreates the manufacturing process. More loops of comparison and feedback are required, to iterate the behaviour of the model towards that of the direct metal SLS process. Once the output of the model and the manufacturing process are sufficiently similar for all likely input parameters, the model can be used to optimise power settings per scan. One aim in doing this would be to generate scans in a layer and layers in a part which are of a consistent size. Optimised machine parameters would be passed from the model to the machine, for feed forward process control.

It has been identified in Section 7.4.5 that whilst the model incorporates a change of conductivity as material changes from powder to solid form, the same is not true of absorptance. Absorptance for a solid is lower than that of a powder.

Absorptance could be calculated at each heat step as a function of density (as conductivity is), but it is believed that a step change from a powder to a solid value would be sufficient. In this work, the facility has been added to manually set values of absorptance per scan in the model, based on the degree of overlap with previous scans (scan spacing). This facility should be tested, and adopted if effective.

To predict the curl and residual stresses occurring in manufactured parts, it would be necessary to couple thermal and stress analyses. As above, parameters could be optimised using the model, to minimise curl and residual stress before manufacturing parts.

Chapters 6 and 7 show that the cross-sectional shape of manufactured parts changes from being circular to being half-moon shaped at low speeds (1mm/s for instance). By contrast, the model always predicts a half-moon shape. The model has no capacity to consider the surface tension effect which drives molten metal into rounded shapes. One solution to this problem is to use a more analytical approach to scanned track morphology, as used by Yevko and Kaplan in Section 2.5.3. The numerical heat model would be used to calculate the length, width, depth and overall volume of scanned tracks. Analytical methods would then decide the track shape, fitting the experimentally-observed form to these dimensions.

The morphological comparisons made in this chapter were based on evaluation of cross-sectional areas, using GSharp and Image Pro software. It may be possible to write a Matlab script which could evaluate the volume and mass of modelled parts, using the 3D density versus position data output by the model. After the initial effort required to write the script, time would be saved in generating manufactured part data for comparison. Weighing manufactured parts would be much quicker than sectioning and analysing them to evaluate area.

CHAPTER EIGHT

8 CONCLUSIONS

Thermal experiments and numerical modelling have been carried out to help develop a direct metal SLS process. The main material considered was stainless steel 314S HC powder, of particle diameter up to 300 microns. Experimental work investigated the thermal situation occurring in the process, incorporating calculations of material conductivity k and absorptance α in a range of representative situations. Modelling involved the development of an existing Fortran finite element model of the process; increasing modelled part size, enhancing ease of use, adding post-processing options and testing the model's output against the SLS manufacturing process output.

Contact and non-contact measurement systems were constructed from existing and custom-designed equipment, to record temperature against time on the surface of and inside the SLS powder bed. When the laser was applied, surface material heated from room to melting temperature in less than 0.5 seconds, then fell back to solidification temperature in under 3 seconds. At 20mm distance from the processed area, temperature rises did not exceed 1°C.

Temperature measurements were used to calculate material k and α. k values found for stainless steel-based powders ranged from 0.07 to 0.25 W/(m.K), depending on atmosphere and particle size. α was measured during the scanning of lines and layers, and for rescanning of lines. α varied from 0.08 to 0.21, and was dependent on the atmosphere and material type. For single lines, α increased with laser scanning speed U, more than four-fold between 0.5 and 10mm/s at power P of 160W. Multiple scans of a single line showed that α reduced when the line was rescanned, due to reduced surface porosity.

A change of scan cross-sectional shape occurring at low U was investigated. Results suggest that the shape change and mass reduction observed was caused by formation of a metal vapour cloud over the processing area.

In modelling work, a spreadsheet was written to automate calculations required when changing mesh sizes. The program was made to report more status information during execution, for performance analysis. Output file size was reduced by 40 percent. Sparse matrix methods introduced by another worker were found to increase running speed 600 times.

Process maps of part quality against inputs P, U and scan spacing s were constructed, to compare the model against the SLS machine and to guide future modelling. At most relevant values of P, U and s, the model ran without problems. The form of process maps for modelling and manufacturing is quite similar.

2D visualisation of model output was enhanced for purpose. 3D visualisation was introduced. 3D views of modelled parts prompted observations of their form. 2D and 3D parts were used to test changes to the model; a deepening of the thermal mesh improved the stability of part depth in the scanning direction. The area, relative density and morphology of manufactured and modelled layer cross-sections were compared. The cross-sectional area of manufactured layers was 30 to 75 percent more than that of modelled layers. Reasons for this difference have been suggested. Modelled scan cross-sections always have a half-moon shape; real SLS-processed metal sections can be circular in shape due to molten material surface tension. The model recognises that k increases as material is processed, but does not recognise that α changes during processing. A method was devised to incorporate variable α per scan into the model.

REFERENCES

[1.] 3D Systems (2002): "SLS Systems/ Production Tooling", *Web-Based DataSheet*, 3D Systems Inc., USA, www.3dsystems.com, Products Section, as 01.07.2002

[2.] Agarwala, M., Bourell, D., Beaman, J., Marcus, H., Barlow, J. (1995a): "Direct Selective Laser Sintering of Metals", *Rapid Prototyping Journal*, MCB University Press, Bradford, UK, Vol.1, No.1, pp.26-36

[3.] Agarwala, M., Bourell, D., Beaman, J., Marcus, H., Barlow, J. (1995b): "Post-Processing of Selective Laser Sintered Metal Parts", *Rapid Prototyping Journal*, MCB University Press, Bradford, UK, Vol.1, No.2, pp.36-44

[4.] Anthony, T.R., Cline, H.E. (1977): "Surface Rippling Induced by Surface-Tension Gradients During Laser Surface Melting and Alloying", *Journal of Applied Physics*, Vol.48, No.9, September 1977, pp.3888-3894

[5.] Auburn (2001): "CF8M Stainless Steel", *Web-Based Properties Table*, Solidification Design Center, Auburn University, USA, metalcasting.auburn.edu/data/CF8M_Stainless_Steel/CF8MSS.html, as 01.01.2003

[6.] Badrinarayan, B., Barlow, J.W. (1994): "Manufacture of Injection Molds Using SLS", *Proceedings of the Solid Freeform Fabrication Symposium 1994*, University of Texas, Austin, Texas, USA, pp.371-378

[7.] Beaman, J.J. et al (1997): "Solid Freeform Fabrication: A New Direction in Manufacturing", Kluwer Academic Publishers, Dordrecht

[8.] Bechtel, J.H. (1974): "Heating of Solid Targets with Laser Pulses", *Journal of Applied Physics*, Vol. 46, No. 4, April 1975, pp.1585-1593

[9.] Benda, J.A. (1994): "Temperature-Controlled Selective Laser Sintering", *Proceedings of the Solid Freeform Fabrication Symposium 1994*, University of Texas, Austin, Texas, USA, pp.277-284

[10.] Berzins, M., Childs, T.H.C., Dalgarno, K.W., Ryder, G.R., Stein, G. (1996): "The Selective Laser Sintering of Polycarbonate", *Annals of CIRP*, Vol. 45 Part 1, pp.187-190

[11.] Boddu, M.R., Thayalan, V.P., Landers, R.G. (2003): "Modelling for the Control of the Laser Aided Manufacturing Process (LAMP)", *Proceedings of the Solid Freeform Fabrication Symposium 2003*, University of Texas, Austin, Texas, USA, pp.186-193

[12.] Boivie, K. (2003): "A Generic System for Homogenous SLS Steel Materials", *Proceedings of the Solid Freeform Fabrication Symposium 2003*, University of Texas, Austin, Texas, USA, pp.632-642

[13.] Bontha, S., Klingbeil, N.W. (2003): "Thermal Process Maps for Controlling Microstructure in Laser-Based Solid Freeform Fabrication", *Proceedings of the Solid Freeform Fabrication Symposium 2003*, University of Texas, Austin, Texas, USA, pp.219-226

[14.] Bourell, D.L. et al (1992): "Selective Laser Sintering of Metals and Ceramics", *International Journal of Powder Metallurgy*, Vol.28, No.4, pp.369-81

[15.] Bugeda, G., Cervera, M., Lombera, G. (1999): "Numerical Prediction of Temperature and Density Distributions in Selective Laser Sintering Process", *Rapid Prototyping Journal*, MCB University Press, Bradford, UK, Vol.5, No.1, pp.21-26

[16.] Bunnel, D.E. et al (1994): "Fundamentals of Liquid Phase Sintering Related to Selective Laser Sintering of Metals", *Proceedings of the Solid Freeform Fabrication Symposium 1994*, University of Texas, Austin, Texas, USA, pp.379-385

[17.] CAD/CAM Publishing (1997): "Rapid Prototyping Report, Jan. 1997", CAD/CAM Publishing, San Diego, California USA

[18.] Calder, N. (2001): "Rapid Manufacturing of Functional Materials", *Time Compression Technology 2001 Proceedings*, Rapid News Publications, UK

[19.] Carslaw, H.S., Jaeger, J.C. (1959): "Conduction of Heat in Solids", Clarendon Press, Oxford, UK

[20.] Carter, W.T., Jones, M.G. (1993): "Direct Laser Sintering of Metals", *Proceedings of the Solid Freeform Fabrication Symposium 1993*, University of Texas, Austin, Texas, USA, pp.51-59

[21.] Castle Island (2002): "The Most Important Commercial Rapid Prototyping Technologies at a Glance", *Web-Based DataSheet*, Castle Island Co., USA, http://home.att.net/~castleisland, Brief Tutorial Section, as 01.01.2003

[22.] Chan, C., Mazumder, J., Chen, M.M. (1984): "A Two Dimension Transient Model for Convection in a Laser Melted Pool", *Metals Transactions A*, Vol.15A, pp.2175-2184

[23.] Chan, C.L., Mazumder, J. (1987): "One-Dimensional Steady-State Model for Damage by Vaporization and Liquid Expulsion Due to Laser-Material Interaction", *Journal of Applied Physics*, Vol.62, 1987, pp.4579-4586

[24.] Chen, I., Lee, S. (1983): "Transient Temperature Profiles in Solids Heated with Scanning Laser", *Journal of Applied Physics*, Vol.54, No.2, February 1983, pp.1062-1066

[25.] Childs, T.H.C., Maekawa, K., Maulik, P. (1988): "Effects of Coolant on Temperature Distribution in Metal Machining", *Materials Science and Technology*, November 1988, Vol.4, pp.1006-1019

[26.] Childs, T.H.C., Cardie, S., Brown, J.S. (1994): "Selective Laser Sintering of Polycarbonate at Varying Powers, Scan Speeds and Scan Spacings", *Proceedings of the Solid Freeform Fabrication Symposium 1994*, University of Texas, Austin, Texas, USA, pp.356-363

[27.] Childs, T.H.C., Ryder, G.R., Berzins, M. (1997a): "Experimental and Theoretical Studies of Selective Laser Sintering", Rapid Product Development, Chapman and Hall, UK, pp.132-141

[28.] Childs, T.H.C. (1997b): "Program sintfeam- Outline Description Version 1", University of Leeds, UK

[29.] Childs, T.H.C. et al (1998): "Selective Laser Sintering of an Amorphous Polymer-Simulations and Experiments", *Proceedings of the Institution of Mechanical Engineers, Part B, Journal of Engineering Manufacture*, UK, Vol.213, No.4, pp.333-349

[30.] Childs, T.H.C., Hauser, C., Tontowi, A.E., Taylor, C. (2000): "Simulation and Experimental Verification of Crystalline Polymer and Metal Selective Laser Sintering", *Proceedings of the Solid Freeform Fabrication Symposium 2000*, University of Texas, Austin, Texas, USA, pp.100-109

[31.] Childs, T.H.C., Tontowi, A.E. (2001): "Selective Laser Sintering of a Crystalline and a Glass-Filled Crystalline Polymer: Experiments and Simulations", *Proceedings of the Institution of Mechanical Engineers*, Vol. 215, Part B, pp.1481-1495

[32.] Choi, D.-S. et al (2001): "Development of a Direct Metal Freeform Fabrication Technique Using CO_2 Laser Welding and Milling Technology", *Journal of Materials Processing Technology*, Vol.113, pp.273-279

[33.] Chung, H., Das, S. (2003): "Level Set Methods for Modelling Laser Melting of Metals", *Proceedings of the Solid Freeform Fabrication Symposium 2003*, University of Texas, Austin, Texas, USA, pp.227-232

[34.] Churchill, S.W. (1986): "The Thermal Conductivity of Dispersions and Packed Beds- an Illustration of the Unexploited Potential of Limiting Solutions for Correlation", *Advances in Transport Processes*, Vol.4, J. Wiley, New York, pp.394-418

[35.] Cline, H.E., Anthony, T.R. (1977): "Heat Treating and Melting Material with a Scanning Laser or Electron Beam", *Journal of Applied Physics*, Vol.48, No.9, pp.3895-3900

[36.] Crafer, R.C., Oakley, P.J. (1993): "Laser Processing in Manufacturing", Chapman and Hall, London, UK

[37.] Crawford, R.H. (1993): "Computer Aspects of Solid Freeform Fabrication", *Proceedings of the Solid Freeform Fabrication Symposium 1993*, University of Texas, Austin, Texas, USA, pp.102-112

[38.] Dai, K. et al (2003a): "Thermal Modelling of Selective Area Laser Deposition (SALD) and SALD Vapour Infiltration of Silicon Carbide", *Rapid Prototyping Journal*, MCB University Press, Bradford, UK, Vol.9, No.4, pp.219-230

[39.] Dai, K. (2003b): "Comparisons Between Thermal Modelling and Experiments in Laser-Densified Dental Powder Bodies", *Proceedings of the Solid Freeform Fabrication Symposium 2003*, University of Texas, Austin, Texas, USA, pp.233-240

[40.] Dalgarno, K.W. et al (1996): "Finite Element Analysis of Curl Development in the Selective Laser Sintering Process", *Proceedings of the Solid Freeform Fabrication Symposium 1996*, University of Texas, Austin, Texas, USA, pp.559-566

[41.] Dalgarno, K.W., Stewart, T.D., Childs, T.H.C. (2000): "Production Tooling for Polymer Components Via the DTM RapidSteel Process", *Proceedings of the Solid Freeform Fabrication Symposium 2000*, University of Texas, Austin, Texas, USA, pp.125-132

[42.] Das, S. et al (1992): "Process Control System for a High Temperature Workstation Performing the Selective Laser Sintering Process", *Proceedings of the Solid Freeform Fabrication Symposium 1992*, University of Texas, Austin, Texas, USA, pp.16-25

[43.] Das, S. (1996a): "Selective Laser Sintering", *Solid Freeform Laboratory Webpage*, University of Texas, Austin, Texas, USA, lff.me.utexas.edu/sls.html, as 01.01.2001

[44.] Das, S. et al (1996b): "Selective Laser Sintering of High Performance High Temperature Materials", *Proceedings of the Solid Freeform Fabrication Symposium 1996*, University of Texas, Austin, Texas, USA, pp.89-95

[45.] Das, S. et al (1997): "Direct Selective Laser Sintering and Containerless Hot Isostatic Pressing for High Performance Metal Components", *Proceedings of the Solid Freeform Fabrication Symposium 1997*, University of Texas, Austin, Texas, USA, pp.81-89

[46.] Das, S. et al (1998): "Direct Laser Freeform Fabrication of High Performance Metal Components", *Rapid Prototyping Journal*, MCB University Press, Bradford, UK, Vol.4, No.3, pp.112-117

[47.] Davis, J.R. (1994): "Stainless Steels", ASM International, Materials Park, Ohio, USA

[48.] Deckard, C. (1986): "Method and Apparatus for Producing Parts by Selective Sintering", *US Patent*, No.4,863,538, 1989. Source: www.uspto.gov, as 01.07.2002

[49.] Deckard, C., Miller, M. (1995): "Improved Energy Delivery for Selective Laser Sintering", *Proceedings of the Solid Freeform Fabrication Symposium 1995*, University of Texas, Austin, Texas, USA, pp.151-158

[50.] Deng, X., Beaman, J.J. (1992): "Application of Factorial Design in Selective Laser Sintering", *Proceedings of the Solid Freeform Fabrication Symposium 1992*, University of Texas, Austin, Texas, USA, pp.154-161

[51.] Dickens, P. et al (1992): "Rapid Prototyping Using 3-D Welding", *Proceedings of the Solid Freeform Fabrication Symposium 1992*, University of Texas, Austin, Texas, USA, pp.280-289

[52.] Dickens, P.M. (1995): "Research Developments in Rapid Prototyping", *Proceedings of the Institution of Mechanical Engineers, Part B, Management and Engineering Manufacture*, London Mechanical Engineering Publications, Vol.209, 1995, pp.261-266

[53.] Dickens, P.M. et al (2000): "Methods of Rapid Tooling Worldwide", *MoldMaking Technology Magazine*, October 2000

[54.] Dowden, J., Davis, M., Kapadia, P. (1983): "Some Aspects of the Fluid Dynamics of Laser Welding", *Journal of Fluid Mechanics*, Vol.126, 1983, pp.123-146

[55.] Dowden, J., Davis, M., Kapadia, P. (1985): "Molten-Region Temperature Distribution in Laser Welding", *Journal of Physics D: Applied Physics*, Vol.18, 1985, pp.1987-1994

[56.] Eane, R.B. (2003): "Metal Powder Effects on Selective Laser Sintering", *PhD Thesis*, School of Mechanical Engineering, University of Leeds, UK

[57.] Equilasers, Inc. (2001): "Laser Micro-Welding for the Photonics Industry", *Business Briefing*. Source: www.wmrc.com, as 01.01.2003

[58.] Eyerer, P. et al (1994): "LAPS- Laser Aided Powder Solidification- Technology for the Direct Production of Metallic and Polymer Parts", *Proceedings of the Solid Freeform Fabrication Symposium 1994*, University of Texas, Austin, Texas, USA, pp.82-93

[59.] Festa, R. et al (1987): "A Comparison Between Models of Thermal Fields in Laser and Electron Beam Surface Processing", *International Journal of Heat and Mass Transfer*, Vol. 31, No.1, 1988, pp.99-106

[60.] Flach, L., Klosterman, D.A., Chartoff, R.P. (1997): "A Thermal Model for Laminated Object Manufacturing (LOM)", *Proceedings of the Solid Freeform Fabrication Symposium 1997*, University of Texas, Austin, Texas, USA, pp.677-688

[61.] Frenkel, J. (1945): "Viscous Flow of Crystalline Bodies Under the Action of Surface Tension", *Journal of Physics*, Academy of Sciences of the USSR, Vol. 9, No.5, 1945, pp.385-391

[62.] Geiger, M. et al (1996): "Advanced Rapid Prototyping by Laser Beam Sintering of Metal Prototypes- Design and Development of an Optimised Laser Beam Delivery System", *SPIE Proceedings Series*, 1996, Vol.2787, pp.103-114

[63.] Geiger, M., Coremans, A. (1997): "Laser-Supported Rapid Tooling- Tools for the Manufacture of Functional Components with Net Shape Properties", *Proceedings of the International Conference on Industrial Tools*, 1997, pp. 5-18

[64.] German, R.M. (1996): "Sintering Theory and Practice", Wiley, New York

[65.] Gibson, I., Shi, D. (1997): "Material Properties and Fabrication Parameters in Selective Laser Sintering Process", *Rapid Prototyping Journal*, MCB University Press, Bradford, UK, Vol.3, No.4, pp.129-136

[66.] Goldsmith, A. (1961): "Handbook of Thermophysical Properties of Solid Materials", MacMillan, New York

[67.] Griffith, M.L. et al (1998): "Thermal Behaviour in the LENS Process", *Proceedings of the Solid Freeform Fabrication Symposium 1998*, University of Texas, Austin, Texas, USA, pp.89-96

[68.] Hauser, C., Childs, T.H.C., Dalgarno, K.W., Eane, R.B. (1999a): "Atmospheric Control During Direct Selective Laser Sintering of Stainless Steel 314S Powder", *Proceedings of the Solid Freeform Fabrication Symposium 1999*, University of Texas, Austin, Texas, USA, pp.265-272

[69.] Hauser, C., Childs, T.H.C., Dalgarno, K.W. (1999b): "Selective Laser Sintering of Stainless Steel 314S HC Processed Using Room Temperature Powder Beds", *Proceedings of the Solid Freeform Fabrication Symposium 1999*, University of Texas, Austin, Texas, USA, pp.273-280

[70.] Hauser, C. (2001): "Process Maps and Cross- Sectional Profiles for Direct SLS Processed Stainless Steel 314S HC Tracks", *Private Communication*

[71.] Ho, J.R., Griporopoulos, C.P., Humphrey, J.A.C. (1995): "Computational Study of Heat Transfer and Gas Dynamics in the Pulsed Laser Evaporation of Metals", *Journal of Applied Physics*, Vol.78, 1995, pp.4696-4709

[72.] Holman, J.P. (1997): "Heat Transfer", 8th Edition, McGraw-Hill, New York/ London

[73.] Hopkinson, N., Dickens, P. (1997): "Thermal Effects on Accuracy in the 3DKeltool™ Process", *Proceedings of the Solid Freeform Fabrication Symposium 1997*, University of Texas, Austin, Texas, USA, pp.267-274

[74.] Hull, C.W. (1984): "Method for Production of Three-Dimensional Objects by Stereolithography", *US Patent*, No.4,575,330, 1986. Source: www.uspto.gov, as 01.01.2003

[75.] Hunt, E.H. (2001): "Towards Rapid Design and Manufacturing- an Evolution of Rapid Prototyping", *Proceedings of Euro RP 2001*, Keynote Speech

[76.] Jacobs, P.F. (1992): "Fundamentals of Stereolithography", *Proceedings of the Solid Freeform Fabrication Symposium 1992*, University of Texas, Austin, Texas, USA, pp.196-206

[77.] Jacobs, P.F., (1996): "Stereolithography and Other RP and M Techniques", ASME Press, New York, USA

[78.] Jenkins, I., Wood, J.V. (1991): "Powder Metallurgy- an Overview", Institute of Metals, London, UK

[79.] Jiang, W., Dalgarno, K.W., Childs, T.H.C.C. (2002): "Finite Element Analysis of Residual Stresses and Deformations in Direct Metal SLS Process", *Proceedings of the Solid Freeform Fabrication Symposium 2002*, University of Texas, Austin, Texas, USA, pp.340-348

[80.] Johnson, D.L., Rusin, R.P. (1992): "Application of a New Sintering Model", *Proceedings of the Powder Metallurgy World Congress*, Vol.3, 1992, San Fransisco, California, USA

[81.] Kahlen, F.-J., Kar, A. (2001): "Tensile Strengths for Laser-Fabricated Parts and Similarity Parameters for Rapid Manufacturing", *Transactions of the ASME*, Vol.123, February 2001, pp.38-44

[82.] Kalpakjian, S. (1997): "Manufacturing Processes for Engineering Materials", Addison-Wesley, Reading, UK

[83.] Kalpakjian, S., Schmid, S.R. (2001): "Manufacturing Engineering and Technology", Prentice-Hall, London, UK

[84.] Kandis, M., Buckley, C.W., Bergman, T.L. (1999): "An Engineering Model for Laser-Induced Sintering of Polymer Powders", *Transactions of the ASME*, Vol.121, Aug. 1999, pp.360-365

[85.] Kaplan, A.F.H., Groboth, G. (2001): "Process Analysis of Laser Beam Cladding", *Journal of Manufacturing Science and Engineering*, Vol.123, November 2001, pp.609-614

[86.] Karapatis, N.P. (1998a): "Direct Rapid Tooling: a Review of Current Research", *Rapid Prototyping Journal*, MCB University Press, Bradford, UK, Vol.4, No.2, pp.77-89

[87.] Karapatis, N.P. (1998b): "Thermal Behaviour of Parts Made by Direct Metal Laser Sintering", *Proceedings of the Solid Freeform Fabrication Symposium 1998*, University of Texas, Austin, Texas, USA, pp.79-87

[88.] Kathuria, Y.P. (1997): "Laser Assisted Rapid Prototyping for Direct Fabrication of Metallic Parts", Rapid Product Development, Chapman and Hall, UK, pp.142-148

[89.] Kaye, G.W.C., Laby, T.H. (1995): "Tables of Physical and Chemical Constants", Longman, London, UK

[90.] Kaysser, W.A. (1991): "Solid State Sintering", *Powder Metallurgy- an Overview*, Institute of Metals, London, Ch.12, pp.168-181

[91.] Khaing, M.W., Fuh, J.Y.H., Lu, L. (2001): "Direct Metal Laser Sintering for Rapid Tooling: Processing and Characterisation of EOS Parts", *Journal of Materials Processing Technology*, Vol.113, pp.269-272

[92.] Kizaki, Y. et al (1992a): "Phenomenological Studies in Laser Cladding. Part I. Time-Resolved Measurements of the Absorptivity of Metal Powder", *Japanese Journal of Applied Physics*, Vol.32, No.1A, Jan. 1993, pp.205-212

[93.] Kizaki, Y. et al (1992b): "Phenomenological Studies in Laser Cladding. Part II. Thermometrical Experiments on the Melt Pool", *Japanese Journal of Applied Physics*, Vol.32, No.1A, Jan. 1993, pp.213-220

[94.] Klocke, F., Wirtz, H., Meiners, W. (1996): "Direct Manufacturing of Metal Prototypes and Prototype Tools", *Proceedings of the Solid Freeform Fabrication Symposium 1996*, University of Texas, Austin, Texas, USA, pp.141-148

[95.] Knights, M. (2001): "Rapid Tooling is Ready for Prime Time", *Plastics Technology Magazine*, Jan. 2001, available online at www.plasticstechnology.com, as 01.01.03

[96.] Kruth, J. –P. (1991): "Material Incress Manufacturing by Rapid Prototyping Technologies", *CIRP Annals*, Vol.40, No.2, pp.603-614

[97.] Kruth, J. –P. et al (1996): "Basic Powder Metallurgical Aspects in Selective Metal Powder Sintering", *CIRP Annals*, Vol.45, No.1, pp.183-186

[98.] Kruth, J.-P. (1997): "Selective Laser Sintering of WC-Co 'Hard Metal' Parts", Rapid Product Development, Chapman and Hall, UK, pp.149-156

[99.] Kruth, J.-P. (1998a): "Progress in Additive Manufacturing and Rapid Prototyping", *CIRP Annals*, Vol.47, No.2, pp.525-540

[100.] Kruth, J.-P. et al (1998b): "Comparison Between CO_2 and Nd:YAG Lasers for Use with Selective Laser Sintering of Steel-Copper Powders", *Revue de CFAO et d'Informatique Graphique*, Vol.13, No.4-6, pp.95-110

[101.] Landers, R.G. (2003): "Process Control of Laser Metal Deposition Manufacturing- a Simulation Study", *Proceedings of the Solid Freeform Fabrication Symposium 2003*, University of Texas, Austin, Texas, USA, pp.246-253

[102.] Laoui, T. et al (2000): "Laser Penetration in a Powder Bed During Selective Laser Sintering of Metal Powders: Simulations Versus Experiments", *Proceedings of the Solid Freeform Fabrication Symposium 2000*, University of Texas, Austin, Texas, USA, pp.453-460

[103.] Lax, M., (1977): "Temperature Rise Induced by a Laser Beam", *Journal of Applied Physics*, Vol.48, No.9, pp.3919-3924

[104.] Livesley, R.K. (1983): "Finite Elements: an Introduction for Engineers", Cambridge University Press, UK

[105.] Lorrison, J.C. et al (2002): "Selective Laser Sintering of Bioactive Glass Ceramics", *Proceedings of the Solid Freeform Fabrication Symposium 2002*, University of Texas, Austin, Texas, USA, published on CD

[106.] Luxon, J.T., Parker, D.E. (1985): "Industrial Lasers and their Applications", Prentice-Hall, New Jersey, USA

[107.] MacKenzie, J.K., Shuttleworth, R. (1949): "A Phenomenological Theory of Sintering", *Proceedings of the Physical Society LXII*, Vol.12, B, pp.833-852

[108.] Magison, E.C. (1990): "Temperature Measurement in Industry", Instrument Society of America, North Carolina, USA

[109.] Matsumoto, M., Shiomi, M., Osakada, K., Abe, F. (2001): "Finite Element Analysis of Single Layer Forming on Metallic Powder Bed in Rapid Prototyping by Selective Laser Processing", *International Journal of Machine Tools and Manufacture*, Pergamon Press, Vol.42, 2002, pp.61-67

[110.] McAlea, K.P. (2000): "DTM's Selective Laser Sintering Technology: New Products, New Benefits, New Manufacturing Horizons", *The 8th International Conference on Rapid Prototyping Technology*, Tokyo, Japan, pp.347-352

[111.] McCrum, N.G., Buckley, C.P., Bucknall, C.B. (1988): "Principles of Polymer Engineering", Oxford University Press, Oxford, UK, Chapter 8

[112.] McMahon, C., Browne, J. (1998): "CADCAM: Principles, Practice and Manufacturing Management", Addison-Wesley, Harlow, UK

[113.] McWilliams, J., Hysinger, C., Beaman, J.J. (1992): "Design of a High Temperature Process Chamber for the Selective Laser Sintering Process", *Proceedings of the Solid Freeform Fabrication Symposium 1992*, University of Texas, Austin, Texas, USA, pp.110-117

[114.] Meiners, W. et al (1999): "Direct Generation of Metal Parts and Tools by Selective Laser Powder Remelting (SLPR)", *Proceedings of the Solid Freeform Fabrication Symposium 1999*, University of Texas, Austin, Texas, USA, pp.655-661

[115.] Melvin III, L.S., Das, S., Beaman, J.J. (1994): "Video Microscopy of Selective Laser Sintering", *Proceedings of the Solid Freeform Fabrication Symposium 1994*, University of Texas, Austin, Texas, USA, pp.34-41

[116.] Miller, D., Deckard, C., Williams, J. (1997): "Variable Beam Size SLS Workstation and Enhanced SLS Model", *Rapid Prototyping Journal*, MCB University Press, Bradford, UK, Vol.3, No.1, pp.4-11

[117.] Morgan, R., Sutcliffe, C.J., O'Neill, W. (2001a): "Experimental Investigation of Nanosecond Pulsed Nd:YAG Laser Re-Melted Pre-Placed Powder Beds", *Rapid Prototyping Journal*, MCB University Press, Bradford, UK, Vol.7, No.3, pp.159-172

[118.] Morgan, R. et al (2001b): "Fabrication of Metal Components by Direct Metal Laser Remelting (DMLR)", *Time Compression Technology 2001 Proceedings*, Rapid News Publications, UK, published on CD

[119.] Murr, L.E. (1975): "Interfacial Phenomena in Metals and Alloys", Addison-Wesley, London, UK

[120.] Nelson, J.C. (1992): "Relating Operating Parameters between SLS Machines which have Different Scanner Geometries and Laser Spot Sizes", *Proceedings of the Solid Freeform Fabrication Symposium 1992*, University of Texas, Austin, Texas, USA, pp.228-236

[121.] Nelson, J.C. (1993a): "Selective Laser Sintering: a Definition of the Process and an Empirical Sintering Model", *PhD Dissertation*, The University of Texas at Austin

[122.] Nelson, J.C. et al (1993b): "Model of the Selective Laser Sintering of Bisphenol-A Polycarbonate", *Industrial & Engineering Chemistry Research*, 1993, Vol.32, No.10, pp.2305-2317

[123.] Nelson, J.C. et al (1995): "Improvements in SLS Part Accuracy", *Proceedings of the Solid Freeform Fabrication Symposium 1995*, University of Texas, Austin, Texas, USA, pp.159-169

[124.] Niu, H.J., Chang, I.T.H. (2000): "Selective Laser Sintering of Gas Atomised M2 High Speed Steel Powder", *Journal of Materials Science 2000*, Kluwer Academic Publishers, pp.31-38

[125.] Norrell, J.L., Kandis, M., Bergman, T.L. (1996): "The Influence of Natural Convection and Radiation Heat Transfer on Sintering of Polycarbonate Powders", *Proceedings of the Solid Freeform Fabrication Symposium 1996*, University of Texas, Austin, Texas, USA, pp.619-627

[126.] Nyrhila, O. et al (1998): "Industrial Use of Direct Metal Laser Sintering", *Proceedings of the Solid Freeform Fabrication Symposium 1998*, University of Texas, Austin, Texas, USA, pp.487-493

[127.] Ohsuga, S. (1989): "Towards Intelligent CAD Systems", *Computer-Aided Design*, Vol.21, No.5, pp.315-337

[128.] O'Neill, W. (1998): "Investigation of Short Pulse Nd:YAG Laser Interaction with Stainless Steel Powder Beds", *Proceedings of the Solid Freeform Fabrication Symposium 1998*, University of Texas, Austin, Texas, USA, pp.147-153

[129.] Osprey (1997): "Particle Size Distribution", *Private Communication*, Osprey Powder Group, Neath, UK

[130.] Ostwald, P.F., Munoz, J. (1997): "Manufacturing Processes and Systems", Wiley, Chichester, UK

[131.] Pahl, G., Beitz, W. (1999): "Engineering Design: a Systematic Approach", Springer-Verlag, Berlin, Germany

[132.] Papadatos, A.L. et al (1997): "On Dimensional Stabilities: Modelling of the Bonus-Z During the SLS Process", *Proceedings of the Solid Freeform Fabrication Symposium 1997*, University of Texas, Austin, Texas, USA, pp.709-715

[133.] Papadatos, A.L. et al (1998): "Enhanced Controlling of the SLS Process During a Build", *Proceedings of the Solid Freeform Fabrication Symposium 1998*, University of Texas, Austin, Texas, USA, pp.47-55

[134.] Pham, D.T., Gault, R.S. (1998): "A Comparison of Rapid Prototyping Technologies", *International Journal of Machine Tools and Manufacture*, No.38, pp.1257-1287

[135.] Pham, D.T., Dimov, S., Lacan, F. (1999): "Selective Laser Sintering: Applications and Technological Capabilities", *Proceedings of the Institution of Mechanical Engineers*, Vol. 213, Part B, pp.435-449

[136.] Poirier, P., Barlier, C. (2001): "Stratoconception: a Complete Family of Stations Dedicated to Rapid Tooling", *Proceedings of Euro RP 2001*, Process Development Session

[137.] Prakash, S., Boddu, M.R., Liou, F. (2003): "Process Control of Laser Metal Deposition Manufacturing- a Simulation Study", *Proceedings of the Solid Freeform Fabrication Symposium 2003*, University of Texas, Austin, Texas, USA, pp.254-261

[138.] Radstok, E. (1999): "Rapid Tooling", *Rapid Prototyping Journal*, MCB University Press, Bradford, UK, Vol.5, No.4, pp.164-168

[139.] Ralston, A., Rabinowitz, P. (1978): "A First Course in Numerical Analysis", McGraw-Hill, New York, USA, Ch.9

[140.] Ready, J.F. (1997): "Industrial Applications of Lasers", Academic Press, San Diego

[141.] Ribeiro, A.F., Norrish, J. (1996): "Rapid Prototyping Process Using Metal Directly", *Proceedings of the Solid Freeform Fabrication Symposium 1996*, University of Texas, Austin, Texas, USA, pp.249-256

[142.] Roark, R.J. (1975): "Formulas for Stress and Strain", McGraw-Hill, New York

[143.] Ryder, G.J., Berzins, M., Childs, T.H.C. (1996): "Modelling Simple Feature Creation in Selective Laser Sintering", *Proceedings of the Solid Freeform Fabrication Symposium 1996*, University of Texas, Austin, Texas, USA, pp.567-574

[144.] Ryder, G.J. (1998): "A Numerical Model of the Selective Laser Sintering Process", *PhD Thesis*, School of Mechanical Engineering, University of Leeds, UK

[145.] Saad, Y., Schultz, M.H. (1985): "Conjugate Gradient-Like Algorithms for Solving Nonsymmetric Linear Systems", *Mathematics of Computation*, Vol.44, No.170, pp.417-424

[146.] Sabourin, E. et al (1996): "Adaptive Slicing Using Stepwise Uniform Refinement", *Rapid Prototyping Journal*, MCB University Press, Bradford, UK, Vol.2, No.4, pp.20-26

[147.] Sachs, E. et al (1999): "Low Shrinkage Metal Skeletons by Three Dimensional Printing", *Proceedings of the Solid Freeform Fabrication Symposium 1999*, University of Texas, Austin, Texas, USA, pp.411-418

[148.] Sanders, D.J. (1984): "Temperature Distributions Produced by Scanning Gaussian Laser Beams", *Applied Optics*, Vol.23, No.1, pp.30-35

[149.] Scherer, G.W. (1976): "Sintering of Low-Density Glasses: I, Theory", *Journal of the American Ceramic Society*, Vol.60, 1977, pp.236-239

[150.] Shellabear, M., Giurcich, M. (2001): "Increasing Precision in Direct Metal Laser Sintering- Recent Improvements in Materials, Hardware and Software", *Time Compression Technology 2001 Proceedings*, Rapid News Publications, UK, published on CD

[151.] Sih, S.S., Barlow, J.W. (1992): "The Measurement of the Thermal Properties and Absorptances of Powders Near Their Melting Temperatures", *Proceedings of the Solid*

Freeform Fabrication Symposium 1992, University of Texas, Austin, Texas, USA, pp.131-140

[152.] Sih, S.S., Barlow, J.W. (1993): "Measurement of the Thermal Conductivity of Powders by Two Different Methods", *Proceedings of the Solid Freeform Fabrication Symposium 1993*, University of Texas, Austin, Texas, USA, pp.370-375

[153.] Sih, S.S., Barlow, J.W. (1994): "Measurement and Prediction of the Thermal Conductivity of Powders at High Temperatures", *Proceedings of the Solid Freeform Fabrication Symposium 1994*, University of Texas, Austin, Texas, USA, pp.321-329

[154.] Sih, S.S., Barlow, J.W. (1995a): "The Prediction of the Thermal Conductivity of Powders", *Proceedings of the Solid Freeform Fabrication Symposium 1995*, University of Texas, Austin, Texas, USA, pp.397-401

[155.] Sih, S.S., Barlow, J.W. (1995b): "Emissivity of Powder Beds", *Proceedings of the Solid Freeform Fabrication Symposium 1995*, University of Texas, Austin, Texas, USA, pp.402-408

[156.] Sindel, M. et al (1994): "Direct Laser Sintering of Metals and Metal Melt Infiltration for Near Net Shape Fabrication of Components", *Proceedings of the Solid Freeform Fabrication Symposium 1994*, University of Texas, Austin, Texas, USA, pp.94-101

[157.] Skorokhod, V.V., Ragulya, A.V. (1999): "Physico-Chemical and Rheological Principles of Selective Laser Sintering", *Science of Sintering*, Vol.31, No.1, 1999, pp.3-15

[158.] Sohlenius, G. (1992): "Concurrent Engineering", *CIRP Annals*, Vol.41, No.2, pp.645-655

[159.] Song, Y.-A. (1997): "Experimental Study of the Basic Process Mechanism for Direct Selective Laser Sintering of Low-Melting Metallic Powder", *CIRP Annals*, Vol.46, No.1, pp.127-130

[160.] Steen, W.M. (2003): "Laser Material Processing", Springer, London, UK

[161.] Steinberger, J. et al (2000): "The Simulation of the SLS Process as the Basis of a Process Optimization", *Proceedings of the Solid Freeform Fabrication Symposium 2000*, University of Texas, Austin, Texas, USA, pp.377-385

[162.] Stultz, T.J. (1981): "The Use of Beam Shaping to Achieve Large-Grain CW Laser-Recrystallized Polysilicon on Amorphous Substrates", *Applied Physics Letters*, Vol.39, No.6, pp.498-500

[163.] Sun, M.M., Beaman, J.J. (1991): "A Three- Dimensional Model for Selective Laser Sintering", *Proceedings of the Solid Freeform Fabrication Symposium 1991*, University of Texas, Austin, Texas, USA, pp.102-109

[164.] Swift, K.G., Booker, J.D. (1997): "Process Selection: from Design to Manufacture", Arnold, London, UK

[165.] Tay, A.O., Stevenson, M.G., de Vahl Davis, G. (1973): "Using the Finite Element Method to Determine Temperature Distributions in Orthogonal Machining", *Proceedings of the Institute of Mechanical Engineers*, Vol.188, No.55, 1974, pp. 627-638

[166.] Taylor, C.M., Childs, T.H.C.C. (2001): "Thermal Experiments in Direct Metal Laser Sintering", *Proceedings of Euro RP 2001*, Process Development Session

[167.] Taylor, C.M., Childs, T.H.C.C. (2002): "Morphology of Direct SLS-Processed Stainless Steel Layers", *Proceedings of the Solid Freeform Fabrication Symposium 2002*, University of Texas, Austin, Texas, USA, published on CD

[168.] Tiziani, A. et al (1989): "Liquid Phase Sintering of AISI 316L Stainless Steel", *Powder Metallurgy*, Vol.32, No.2, 1989, pp. 118-122

[169.] Tolochko, N.K. et al (1999): "The Structure of Sintered Materials Fabricated by a Laser Beam", *Science of Sintering*, Vol.31, No.2, 1999, pp.91-96

[170.] Tolochko, N.K. et al (2000): "Absorptance of Powder Materials Suitable for Laser Sintering", *Rapid Prototyping Journal*, MCB University Press, Bradford, UK, Vol.6, No.3, pp.155-160

[171.] Tolochko, N. et al (2003a): "Selective Laser Sintering of Single- and Two-Component Metal Powders", *Rapid Prototyping Journal*, MCB University Press, Bradford, UK, Vol.9, No.2, pp.68-78

[172.] Tolochko, N. et al (2003b): "Mechanisms of Selective Laser Sintering and Heat Transfer in Ti Powder", *Rapid Prototyping Journal*, MCB University Press, Bradford, UK, Vol.9, No.5, pp.314-326

[173.] Tontowi, A.E., Childs, T.H.C.C. (1999): "A Numerical Model of Selective Laser Sintering of Duraform Polyamide", *Indonesian Students' Scientific Meeting*, pp.128-131

[174.] Tontowi, A.E. (2000): "Selective Laser Sintering of Crystalline Polymers", *PhD Thesis*, School of Mechanical Engineering, University of Leeds, UK

[175.] Tontowi, A.E., Childs, T.H.C.C. (2001): "Density Prediction of Crystalline Polymer Sintered Parts at Various Powder Bed Temperatures", *Rapid Prototyping Journal*, MCB University Press, Bradford, UK, Vol.7, No.3, pp.180-184

[176.] Toolcraft (2000): "Comparison of Materials Used to Make Mould Tools", *Web-Based DataSheet*, Toolcraft Plastics Ltd., UK, www.toolcraftplastics.co.uk/toolsqc7ccht.htm, as 01.01.2003

[177.] Tumer, I.Y., Wood, K.L., Busch-Vishniac, I.J. (1995): "Modelling of Dynamic Effects Caused by the Beam Delivery System in Selective Laser Sintering", *Proceedings of the Solid Freeform Fabrication Symposium 1995*, University of Texas, Austin, Texas, USA, pp.353-361

[178.] Touloukian, Y.S. (1970): "Thermophysical Properties of Matter", Vol.s 1,3,7, IFI Plenum, New York, USA

[179.] Tsai, F.-R., Kannatey-Asibu Jr., E. (2000): "Modeling of Conduction Mode Laser Welding Process for Feedback Control", *Transactions of the ASME*, Vol.122, August 2000, pp.420-428

[180.] Turner, K., Walker, H.F. (1992): "Efficient High Accuracy Solution with GMRES(m)", *SIAM Journal of Scientific and Statistical Computing*, Vol.13, No.3, pp.815-825

[181.] Van der Schueren, B., Kruth, J.–P. (1995a): "Powder Deposition in Selective Metal Powder Sintering", *Rapid Prototyping Journal*, MCB University Press, Bradford, UK, Vol.1, No.3, pp.23-31

[182.] Van der Shueren, B., Kruth, J.–P. (1995b): "Design Aspects of a 'Selective Metal Powder Sintering' Apparatus", *Proc. of 11th Int. Symp. for Electro-Machining (ISEM-XI)*, pp.651-662

[183.] Vasinonta, A., Beuth, J. (1999): "Process Maps for Laser Deposition of Thin-Walled Structures", *Proceedings of the Solid Freeform Fabrication Symposium 1999*, University of Texas, Austin, Texas, USA, pp.383-391

[184.] Vasinonta, A., Beuth, J., Griffith, M. (2000): "Process Maps for Controlling Residual Stress and Melt Pool Size in Laser-Based SFF Processes", *Proceedings of the Solid Freeform Fabrication Symposium 2000*, University of Texas, Austin, Texas, USA, pp.200-208

[185.] Volpato, N. (2001): "Time-Saving and Accuracy Issues in Rapid Tooling by Selective Laser Sintering", *PhD Thesis*, School of Mechanical Engineering, University of Leeds, UK

[186.] Wang, J.C. et al (1978): "Theoretical Analysis of Thermal and Mass Transport in Ion-Implanted Laser-Annealed Silicon", *Applied Physics Letters*, Vol.33, No.5, pp.455-458

[187.] Wang, X. (1999): "Calibration of Shrinkage and Beam Offset in SLS Process", *Rapid Prototyping Journal*, MCB University Press, Bradford, UK, Vol.5, No.3, pp.129-133

[188.] Wang, X. et al (2002): "Direct Selective Laser Sintering of Hard Metal Powders: Experimental Study and Simulation", *The International Journal of Advanced Manufacturing Technology*, Vol.19, pp.351-357

[189.] Weissman, E.M., Hsu, M.B. (1991): "A Finite Element Model of Multi-Layered Laser Sintered Parts", *Proceedings of the Solid Freeform Fabrication Symposium 1991*, University of Texas, Austin, Texas, USA, pp.86-94

[190.] Wilkening, C. (1996): "Fast Production of Technical Prototypes Using Direct Laser Sintering of Metals and Foundry Sand", *Proceedings of the Solid Freeform Fabrication Symposium 1996*, University of Texas, Austin, Texas, USA, pp.133-140

[191.] Williams, J.D. et al (1996): "Selective Laser Sintering Part Strength as a Function of Andrew Number, Scan Rate and Spot Size", *Proceedings of the Solid Freeform Fabrication Symposium 1996*, University of Texas, Austin, Texas, USA, pp.549-557

[192.] Williams, J.D. (1998): "Advances in Modelling the Effects of Selected Parameters on the SLS Process", *Rapid Prototyping Journal*, MCB University Press, Bradford, UK, Vol.4, No.2, pp.90-100

[193.] Wohlers, T. (1999a): "Advances in Rapid Technologies Worldwide", *Proceedings of EuroMold Conference, "Rapid Tooling's Strategic Benefits and Risks"*, Dec. 1999

[194.] Wohlers, T. (1999b): "Rapid Prototyping and Tooling State of the Industry 1999: Executive Summary", *Time-Compression Technologies magazine*, Vol.4, Issue 3, June 1999

[195.] Wohlers, T. (2000): "Rapid Prototyping and Tooling Worldwide: Stalled Growth, Countless Benefits, Vast Confusion", *CATIA Solutions*, Jan/Feb 2000 Edition

[196.] Wojciechowski, K.F. (1999): "Surface Energy of Metals: Theory and Experiment", *Surface Science*, Vol.437, pp.285-288

[197.] Xu, F. (1999): "Considerations and Selection of Optimal Orientation for Different Rapid Prototyping Systems", *Rapid Prototyping Journal*, MCB University Press, Bradford, UK, Vol.5, No.2, pp.54-60

[198.] Xue, S.S., Barlow, J.W. (1991): "Models for the Prediction of the Thermal Conductivities of Powders", *Proceedings of the Solid Freeform Fabrication Symposium 1991*, University of Texas, Austin, Texas, USA, pp.62-69

[199.] Yagi, S., Kunii, D. (1957): "Studies on Effective Thermal Conductivities in Packed Beds", *American Institute of Chemical Engineers Journal*, Vol.3, No.3, 1957, pp.373-381

[200.] Yardimci, M.A. et al (1997): "Thermal Analysis of Fused Deposition", *Proceedings of the Solid Freeform Fabrication Symposium 1997*, University of Texas, Austin, Texas, USA, pp.689-698

[201.] Yevko, V., Park, C.B., Zak, G., Coyle, T.W., Benhabib, B. (1998): "Cladding Formation in Laser-Beam Fusion of Metal Powder", *Rapid Prototyping Journal*, MCB University Press, Bradford, UK, Vol.4, No.4, pp.168-184

[202.] Zong, G. et al (1992): "Direct Selective Laser Sintering of High Temperature Materials", *Proceedings of the Solid Freeform Fabrication Symposium 1992*, University of Texas, Austin, Texas, USA, pp.72-85

APPENDICES

CONTENTS

The following can be found here.

Appendix A Record of Experiments

Table of Thermal Experiments- Thermal Camera 22.08.01 Page 1 of 5

System tests, thermal property measurement series 1.10 (marked "*"), thermal field study

Corresp. Graph No.s	Line / Layer Dim.s (mm), Atmos.	Temp Range ('C)	Measure -ment *z*-Pos'ns (mm) (all near line *x* centre)	Power (W)	Scan Speed (mm/s), Spacing (mm)	Notes
1	-	-	-	-	-	Test
2-8	60 line, air	29.9-1508	Line	21.0	6	6 *T* ranges
9-16	60 line, air	29.9-1508	Line	132.7	6	6 *T* ranges
17,18	40x20 lr, air	26.4-1506	Edge/edge, ctr/ctr	100.6	60, 0.5	2 *T* ranges
19,20*	60 line, air	20.3-203	40/7, 8	38.2	6	2 *T* ranges
21*	60 line, air	20.4-36.7	24/7,40/7,8	38.2	6	*Tvy* proper
22*	60 line, air	25.0-40.8	32/7,40/7,48/7,8	38.2	6	No *Tini*
23*,24*, 25*	60 line, air	26.8-31.0	48/7, 8	38.2	6	Printer jam
26*,27*	60 line, air	27.4-64.4	32/7, 40/7	38.2	6	
28*,29*	60 line, air	27.8-63.6	32/7, 40/7	72.5	6	
30,31, 32*	60 line, air	28.7-134	16/7, 24/7	38.2	6	
33,34*	60 line, air	23.5-1500	16/7, 24/7	38.2	6	Highest dt
35,36,37	-	Evaluating	highest *dt*	-	-	= 0.464s
38*	60 line, air	28.0-29.6	64/7, 72/7	38.2	6	
39,40*, 41*	60 line, air	25.0-335	24/7, 32/7	20.8	6	3 *T* ranges
42*	60 line, air	26.9-34.9	24/7	38.2	6	
43*	60 line, air	27.8-31.8	48/7, 56/7	38.2	6	
44*	60 line, air	29.6-33.5	64/7, 72/7	72.5	6	
45*	60 line, air	28.6-30.2	48/7, 56/7	20.8	6	
46	60x20 layer	30.6-1505	Edge: ctr/edge	20.8	6, 0.5	
47	in air	30.5-1505	Ctr: ctr/edge	20.8	6, 0.5	
48	60x20 layer	29.9-1505	1/4 pos'n,1/4 po'n	20.8	0.5, 0.5	
49	60 line, argn	29.9-203	Line	20.7	6	Diff. atmos.
50	60 line, argn	29.9-203	Line	132.7	6	
51	60 line, argn	29.9-203	Line	20.7	6	
52,53	60 line, argn	29.9-536	Line	132.7	6	2 *T* ranges
54	60 line, argn	29.9-203	Line	38.2	6	
55,56	60 line, argn	29.9-536	Line	72.5	6	2 *T* ranges
57	60 line, argn	29.9-203	Line	38.2	6	
58	60 line, argn	29.9-203	Line	72.5	6	
59	40x20 layer	30.5-1505	Edge, edge	100.6	6	
60	in argon	29.9-1505	Centre, centre	100.6	6	Highest *dt*
61,62,63	60 line, air	29.9-1505	Line	20.8	6	5 spots
64, 65	60 line, argn	29.9-1505	Line	20.8	6	
66, 67	""" + relase	29.9-1505	Line	20.8	6	
68, 69	""",relase2,3	29.9-1505	Line	20.8	6	
70, 71	""",relase4,5	29.9-1505	Line	20.8	6	

Table of Thermal Experiments- Thermocouples 30.03.00 Page **2** of 5

Output Data File Name	Series No/ Atmos, Line Length (mm)	Scan Type	Therm'cpl Pos'ns for T2, 3, 4, 5, 6 Respec'ly (mm)	Power (W)	Scan Speed (mm/s)	Notes
040200n1	Air, 45	10 parallel	10, 20, 30,	40	6	'C o/p
040200n2	Air, 45	scans,	40 height.	58	6	dt about
040200n3	Air, 45	7mm gap.	No T6.	80	6	0.68 secs.
040200n4	Air, 45	1 central	First four	80	6	dt 0.68s
040200n5	Air, 45	scan. Line	mid holes.	80	3	dt 4.2s
090300n1	S1.1, 45	6 chosen out of	41, 42, 43,	80	4	mV DC o/p, dt 9.9s
090300n2	S1.1, 45	plot	44 height.	60	4	dt 8.4s
090300n3	S1.1, 45	lines	No T6.	40	4	dt 8.4s
090300n4	S1.1, 45	1-10	First four	20	4	"
100300n1	S1.1, 45	for central	NC drill	100	4	"
100300n2	S1.1, 45	scan.	holes,	80	8	"
100300n3	S1.1, 45	"	central	100	8	"
100300n4	S1.1, 45	"	column.	120	8	"
160300n1	S1.1, 45	"	47, 46, 45,	20	4	dt 8.4s
160300n2	S1.1, 45	"	44 height.	40	4	Ch3 Out
160300n3	S1.1, 45	"	No T6.	80	4	dt 8.4s
160300n4	S1.1, 45	"	First four	120	4	dt 8.4s
160300n5	S1.1, 45	"	NC holes,	40	8	Ch3 Out
160300n6	S1.1, 45	"	mid col'n.	80	8	Ch3 Out
160300n7	S1.1, 45	"	T/c order:	160	16	Ch3 Out
170300n1	S1.1, 45	"	from left,	5	4	No Power
170300n2	S1.1, 45	"	T3, T2,	10	4	No Power
170300n3	S1.1, 45	"	T5,T4.	160	32	Ch4 Out
170300n4	S1.1, 45	"	48, 46, 49,	10	4	No Power
170300n5	S1.1, 45	"	45 height.	20	4	dt 8.4s
170300n6	S1.1, 45	"	No T6.	40	4	dt 8.4s
170300n7	S1.1, 45	1 central	Order T3,	80	4	Sample dt
170300n8	S1.1, 45	scan	T2, T4, T5	80	8	reduced 4×, 2.1s
170500n1	Air, 60	1 central	50, 48, 46,	20	6	dt 2.1s
170500n2	Air, 60	scan. Line	44, 38	20	6	dt 2.1s
170500n3	Air, 60	14 chosen	height.	40	6	Ch5/6 Out
170500n4	Air, 60	out of	First five.	80	6	", dt 0.6s
170500n5	Air, 60	plot	Order T2,	120	6	", dt 0.6s
170500n6	Air, 60	lines	T3, T4,	160	6	", dt 0.6s
170500n7	Air, 60	11-16	T5, T6.	20	6	", dt 0.6s
170500n8	Air, 60	for central	40mm	60	6	", dt 2.1s
170500n9	Air, 60	scan.	height.	60	6	", dt 8.4s
			NC 2,3,4			
			T2/3/4			Note: all **air** atmos so far.

Table of Thermal Experiments- Thermocouples 17.10.00 Page **3** of 5

Output Data File Name	Series No/ Atmos, Line Length (mm)	Scan Type	Therm'cpl Pos'ns for T2, 3, 4, 5, 6 Respec'ly (mm)	Power (W)	Scan Speed (mm/s)	Notes
120700n1	Argon, 60	1 central	T2/3/4,	120	6	mV DC
120700n2	Argon, 60	scan. Line	46mm h't.	120	6	o/p,
120700n3	Argon, 60	14 chosen	NCs 2,3,4	120	6	dt about
120700n4	Argon, 60	out of	respect'ly.	120	6	0.6 secs.
120700n5	Argon, 60	plot	Position in	120	6	Now using
130700n1	Argon, 60	lines	line dir'n	120	6	t/c
130700n2	Argon, 60	11-16	of	120	6	vacuum
130700n3	Argon, 60	for central	interest.	120	6	feedthro'.
130700n4	S2.1, 60	scan.	46, 48, 50,	80	6	dt 0.6s
130700n5	S2.1, 60	2 rulers	42, 44 h't.	80	6	Re-lase.
130700n6	S2.1, 60	used as	First five	80	6	6 mins of
130700n7	S2.1, 60	spacers	NC drill	80	6	temps
130700n8	S2.1, 60	front to	holes	80	6	recorded.
130700n9	S2.1, 60	back.	respect'ly.	80	6	dt 0.6s
140700n1	Argon, 60	Resulting	46, 48, 50,	20	6	Bed voids.
140700n2	Argon, 60	line about	47, 44 h't.	20	6	dt 0.6s
140700n3	Argon, 60	58mm	First five	40	20	Rapid
140700n4	Argon, 60	long.	NC holes.	30	10	Steel2.
Output Data File Name	**Series No, Line/ Layer Dim.s (mm)**	**Scan Type**	***y* Pos'ns for T3, 4, 5, 6, 7 Respec'ly (mm)**	**Power (W)**	**Scan Speed (mm/s), Spacing (mm)**	**Notes**
121000n3	S1.9, 60	Line 14.	4.9, 2.8,	15.3	350	T/c wires
121000n4	S1.9, 60	New	1.6, 3.7,	19.0	225	b'kwards.
161000n1	S1.9, 60	spacer:	5.7 depth	19.0	225	
161000n2	S1.9, 60	alu plate	(vernier),	19.0	97.1	NI board's
161000n3	S1.9, 60	and tape.	First five	19.0	60.5	Ch2 funny.
161000n4	S1.9, 60		NC holes.	9.8	30.0	Now T3-7.
161000n5	S1.9, 60			15.3	30.0	*dt* 0.6s.
021100n4	S3.1,	Layer,	NCs 2,3,4	121.2	150, 0.2	*dt* 2.1s
021100n5	single	positioned	respect'ly.	121.2	75, 0.4	*dt* 2.1s
021100n6	layer,	directly	Order T4,	121.2	60, 0.5	Ch4 out
021100n7	40x20mm.	over t/cs	T5, T6.	121.2	50, 0.6	
021100n8		(offset=	Various	121.2	43, 0.7	
021100n9	S3.1,	x+2,y-7)	depths,	121.2	33.5, 0.9	
031100n1	single	Ratio	5.2-1.0mm	121.2	43, 0.7	
031100n2	layer,	$P/(U.s)$	(vernier).	121.2	150, 0.2	
031100n3	40x20mm.	constant.		121.2	75, 0.4	
031100n4		Layr takes		121.2	60, 0.5	
031100n5	S3.1,	24 seconds		121.2	50, 0.6	
031100n6	single	to scan.		121.2	43, 0.7	Ch4 out
031100n7	layer,			121.2	33.5, 0.9	
031100n8	40x20mm.			121.2	33.5, 0.9	

Table of Thermal Experiments- Thermocouples 16.11.00 Page **4** of 5

Output Data File Name	Series No/ Atmos, Line/ Layer Dim.s (mm)	Scan Type	*y* Pos'ns for T2, 3, 4, 5, 6 Respec'ly (mm)	Power (W)	Scan Speed (mm/s), Spacing (mm)	Notes
151100n1	Argon, 60	1 central	NCs 2,3,4	121.2	60	mV DC
151100n2	Argon, 60	line 14.plt	respect'ly.	121.2	60	o/p,
151100n3	S3.1,	Directly	Order T4,	121.2	37.5, 0.8	*dt* about
151100n4	single	over t/cs	T5, T6.	121.2	30, 1.0	0.6 secs.
151100n5	layer,	(offset=	Various	121.2	37.5, 0.8	T3 and
151100n6	40x20mm.	x+2,y-7).	depths,	121.2	30, 1.0	T7 used to
151100n7		24 seconds	5.0-1.0	121.2	37.5, 0.8	measure
151100n8	Argon, 60	to scan.	(vernier).	121.2	33.5	air T
010301n1	S3.1,	New offset		121.2	300, 0.1	8 mins of
010301n2	single	of x+14,	NCs 2,3,4	121.2	35.5, 0.85	temps
010301n3	layer,	y-7	respect'ly.	121.2	33.5, 0.9	recorded.
010301n4	40x20mm.	Resulting	Order T4,	121.2	27.5, 1.1	*dt* 0.6s
010301n5	S3.1,	layers	T5, T6.	121.2	35.5, 0.85	
010301n6	single	38x18.	Various	121.2	300, 0.1	
010301n7	layer,		depths,	121.2	35.5, 0.85	n1-n8, T6
010301n8	40x20mm.	Lots of	5.0-1.0	121.2	33.5, 0.9	was out.
010301n9	S3.1,	breakages,	(vernier).	121.2	27.5, 1.1	n9, works.
070301n1	single	ceramic		121.2	300, 0.1	n1-n3, T4
070301n2	layer,	rods.		121.2	35.5, 0.85	& T5 were
070301n3	40x20mm.			121.2	33.5, 0.9	out.
240902n*	S1.5, S1.6,	2 scans,	Spaced	160	Speed 0.5,	α v U
250902n*	S1.7, 60	30mm space	7.0-2.0	160	1.0, 10	for 314.
041002n*	S1.5, S1.6,	Directly	(vernier).	160	Speed 0.5,	5 readings
111002r1	S1.7, 60	over t/cs		160	1.0, 10	per 2 runs.
091002n1	S1.2, 60	2 scans,	Spaced	40 to	Speed	k and α,
to	S1.2, 60	30mm space	6.0-2.5	160	0.5 to 15	314 small
091002nD	S1.2, 60	over t/cs	(vernier).			
111002n*	S1.3, 60	2 scans,	Spaced	40 to	Speed	k and α,
and	S1.3, 60	30mm space	6.0-2.5	160	0.5 to 15	314 med.
161002n*	S1.3, 60	over t/cs	(vernier).			
101002n1	S1.4, 60	2 scans,	Spaced	40 to	Speed	k and α,
to	S1.4, 60	30mm space	6.0-2.5	160	0.5 to 15	314 large
101002nC	S1.4, 60	over t/cs	(vernier).			
161002b1	S1.8, 60	2 scans,	Spaced	40 to	Speed	k and α,
to	S1.8, 60	30mm space	6.0-2.5	160	0.5 to 15	M2 med.
161002bC	S1.8, 60	over t/cs	(vernier).			

Experiments: Single Layer Manufacture 30.01.02 Page **5** of 5

Run No.	Date	No. Scans	Scan Length (mm)	Scan Spacing ($\times d$ /6)	Power (W)	Scan Speed (mm/s)	No. Samples	Notes
1	24.01.02	10	10	3	60	1	3	Manuf-
2	07.02.02	10	10	5	60	1	3	actured
3	07.02.02	10	10	9	60	1	3	for
4	07.02.02	10	10	3	120	6	3	comp-
5	07.02.02	10	10	5	120	6	3	arison
6	07.02.02	10	10	9	120	6	3	with
7	07.02.02	10	10	3	155	12	3	model-
8	07.02.02	10	10	5	155	12	3	-led
9	07.02.02	10	10	9	155	12	3	parts

Appendix B Fortran Program to Extract Data from Thermocouple Logs

```
      PROGRAM LogRead

C     --- BY CHRIS TAYLOR, 11.08.00. MODIFIED NOVEMBER 2000 FOR 5
C        -CHANNEL DIRECTORY, T2 NOT WORKING (IE Tn => Tn+1).

C     --- TAKES SPECIFIED OUTPUT FILE FROM PC RUNNING LABVIEW AND
C         ATTACHED TO A THERMOCOUPLE DATA CARD. READS THROUGH DATA, AND
C         SELECTS OUT INITIAL/ MAXIMUM READINGS WITH CORRESPONDING TIME.
C         HAS TO IGNORE FIRST N LINES, PICK OUT CHARACTER/ REAL
C         VARIABLE TYPES, STORE MAXIMUM VOLTAGE VALUE FOR EACH COLUMN
C         (THERMOCOUPLE). CONVERTS DATA TO TEMPERATURE FORM AND PRINTS
C         ON SCREEN.

C     --- NOTES ON DISCOVERIES MADE WHILST DEBUGGING:
C         LINES MUST BE <=72 CHARACTERS LONG, CARRY OVER WITH AN APPROP
C        -RIATELY PLACED SYMBOL (LIKE HYPHEN SHOWN IN THIS SENTENCE).
C         LINE NUMBERS MUST BE PLACED TO BEGIN IN COLUMN 1.

      REAL VSTART(5), VMAX(5), VCOMP(5), TEINI(5), TEMAX(5)
      CHARACTER LOG*12, DIRFILE*22
      CHARACTER UNWANT*60, DATE*10, TISTRT*12, TICOMP*12, TIPEAK(5)*12
      INTEGER I, J, L

C     DEFINITION/ SETUP OF FILE. NAME INPUT BY USER EACH TIME.
C     INITIALISATION OF MAXIMA TO 0.0.
C     IF NO READING GREATER THAN THIS FOUND, TIME='NONE'.

      PRINT *,'Input text file name (without .log extension): '
      READ(*,100) LOG
      DIRFILE(1:10)='5 Channel\'
      DIRFILE(11:18)=LOG
      DIRFILE(19:22)='.log'
      OPEN(10,FILE=DIRFILE)
C     OPEN(10,FILE='Test.log')
      REWIND 10

      DO 10 I=1,5
            VMAX(I)=0.0
            TIPEAK(I)='NONE'
10    CONTINUE

C     CLEAR ALL UNWANTED DATA AT START OF FILE. PICKS UP ON UNIQUE
C     STRING '(V)' FOUND IN LINE BEFORE NUMBERS OF INTEREST BEGIN.

      DO 20 L=1,8
      READ(10,100) UNWANT
100   FORMAT(A)
20    CONTINUE
30    CONTINUE
      READ(10,100) UNWANT
      IF (UNWANT(52:54).NE.'(V)') THEN
      GO TO 30
      END IF
      CONTINUE

C     READ INITIAL TIME/ VOLTAGE VALUES.
C     REPLACEMENT OF MAXIMUM VOLTAGE AND TIME WHERE READ VALUE LARGER.
C     CHECK FOR SPURIOUS DATA: O/P <0.084V (=2000'C). NOT FOOLPROOF!
C     PROBLEMS WHERE THERMOCOUPLE CIRCUIT BROKEN ETC.
C     APPROXIMATE CONVERSION TO 'C (BASED ON TYPICAL CALIBRATION).

      READ(10,200) DATE, TISTRT, VSTART(1), VSTART(2), VSTART(3),
```

```
     -VSTART(4), VSTART(5)
200   FORMAT(A, 6X, A, 4X,
     -F11.0, 5X, F11.0, 5X, F11.0, 5X, F11.0, 5X, F11.0)
C      WRITE(6,*) DATE, TISTRT, VSTART(1), VSTART(2), VSTART(3),
C     -VSTART(4), VSTART(5)

      DO 210 I=1,5
            TEINI(I)=(23560*VSTART(I))+22.14
            IF ((VSTART(I).GT.VMAX(I)).AND.(VSTART(I).LT.0.084)) THEN
                  VMAX(I)=VSTART(I)
                  TIPEAK(I)=TISTRT
            END IF
210   CONTINUE
      J=2
220   CONTINUE

C     REPEATEDLY READ ROWS OF VALUES UNTIL FILE ENDS

      READ(10,200,END=240) DATE, TICOMP, VCOMP(1), VCOMP(2), VCOMP(3),
     -VCOMP(4), VCOMP(5)
      DO 230 I=1,5
            IF ((VCOMP(I).GT.VMAX(I)).AND.(VCOMP(I).LT.0.084)) THEN
                  VMAX(I)=VCOMP(I)
                  TIPEAK(I)=TICOMP
            END IF
230   CONTINUE
      J=J+1
      GO TO 220

240   CONTINUE

C     PRINT TIMES AND VOLTAGES. CONVERT AND DISPLAY AS TEMPERATURES.

      PRINT *, ' '
      PRINT 300, TISTRT
300   FORMAT(' ', 'Start time: ', A12)
      PRINT *, ' '
      PRINT 400, VSTART(1), VSTART(2), VSTART(3), VSTART(4), VSTART(5)
400   FORMAT(' ', 'Start Voltages: ',
     -F11.7, F11.7, F11.7, F11.7, F11.7)
      PRINT 500, TEINI(1), TEINI(2), TEINI(3), TEINI(4), TEINI(5)
500   FORMAT(' ', '  Temperatures: ',
     -F11.3, F11.3, F11.3, F11.3, F11.3)
      PRINT *, ' '
      DO 510 I=1,5
            PRINT 600, (I+2), TIPEAK(I), VMAX(I)
            TEMAX(I)=(23560*VMAX(I))+22.14
            PRINT 700, (I+2), TIPEAK(I), TEMAX(I)
510   CONTINUE
600   FORMAT(' ', 'Thermocouple T', I1, ' peak time and voltage ',
     -A12, F11.7, ' V')
700   FORMAT(' ', 'Thermocouple T', I1, ' peak time and temp.   ',
     -A12, F11.2, '''C')
      PRINT 100, DATE

            PRINT *, ' '
      PRINT 800, J
800   FORMAT(' ', I4, ' (-2) rows read.')
      PRINT *, ' '

      END
```

Appendix C Modifications to Fortran Program *stmet3d*

```
      PROGRAM STMET3DGMRES_3
c Version of stmet3d with GMRES. 12.12.01

c Version _2: thermal mesh marches on beyond end of scan (testing consistency
compared to static dwell)
c  03.01.02      absorptivity (and therefore power) can be varied from one scan to
the next.

c Version _3: some changes to marching cooldown to save time, and Rhoplot
formatting. 10.02.02

c this version modified 17/10/01 to solve heat equations by ilut preconditioned
gmres.
c the subroutine HSOLVE is totally different from before and calls subroutines
ilut, qsplit,
c pgmres, amux, lusol and daxpy; and functions ddot and dnrm2.
c compared to the previous code, the PARAMETER MNAL is no longer needed and is
removed from the
c parameter list. Two new parameters are needed in HSOLVE - go to HSOLVE to read
more
c
c
c Modified by CMT: in new sparse matrix section, some lines ran beyond
c col 72. Carried these over to next line. Same problems on Salford as
c original THCC program: numbers raised to real power. Modified lines:
c 'Trial=Trial**2.0', 2x '...(TANH(5.0*ALPAVD))**4.0)'.
c
C        TWO NEW OUTPUT FILES ADDED TO MAIN PROGRAM AND SUBROUTINE "OUTPUT"
C        FOR GSHARP COMPATIBILITY, SEPT. 2001. CODE BY NV.
C
C         MODIFIED BY CMT 14.11.01 TO MAKE RHOPLOT X/Z MATLAB FRIENDLY (TOOK TEXT
OUT).
C        ACTUALLY EASIER TO READ VALUES INTO MATLAB FROM RHOPLOT:
C        MODIFIED OUTPUTTING OF RHOPLOT TO PUT A LINE AT THE START, TELL MATLAB
C        HOW MANY X, Y, Z POINTS; DEC. 2001.
C
C        ** am_2

C         Modified, CMT 03.01.02: decided to have thermal mesh carry on marching
after scanning,
C         with no further power being input into bed. The previous system had the
thermal mesh
C            dwell at the end of the scan until all temperatures fell below
solidification point.
C        This is inconsistent with how the rest of the scan is processed- provides
much more
C         time for diffusion of heat into scan's end region, meaning much wider,
deeper geometry
C         (big lump on end of scan). Now thermal mesh marches on for it's entire
length once
C        scanning ceases, before moving to start position of next scan.
C
C          At the same time, added a new 10x10 array ABSORBSCAN (rather than 1
ABSORB value).
C         Surface laser power profile is modified in magnitude for each separate
scan, through
C        values in ABSORBSCAN which dictate absorptance. Two purposes for this: to
model the
C        difference in average absorptance between 1st and nth scans (scanning raw
powder as
C         opposed to partially scanning dense and shiny processed powder); and to
simulate
C           boosting laser power to counter this effect/ heat sink effect from
adjacent previously
C        processed (higher conductivity) material ("Adaptive Manufacture" method).

C        **

C         Modified, CMT 31.01.02: some more diagnostic info. Full heat/ cool step
ID (layer,
C        scan, step), reporting processor start/ end time, time elapsed.
```

```
C        ** am_3

C         Modified, CMT 10.02.02: decided to amend marching cooldown phase- mesh
will continue
C        to march with P=0 for MGXMAX steps, UNLESS following condition is met. At
each cool
C         step, maximum of thermal mesh nodal temperatures is found, compared to
TDWELL. If
C          lower, it is deemed that material has cooled enough to be completely
solid. Program
C        execution moves onto next scan. This should reduce program run time. Some
new
C         integer variables are also added, to record the maximum number of cool
steps
C           executed for a scan, and identify corresponding scan. If any scan
requires MGXMAX
C        cool steps and still has not fully solidified, this is reported.
C
C              A second change made at the same time, relating to output of
x,y,z,RHO,DTAV data.
C           Values have been output to text file at 6 S.F. in a field of 16
characters (by
C         default). Spaces between values can account for Mb of storage space in
output files.
C        Formatting of data now applied in subroutine OUTPUT when writing Rhoplot,
Rhoplotx/z.

C        **

C         --- MODEL STARTED 06/03/97- THIS VERSION FOR ISOMORPHOUS MELTING OF
CRYSTALLINE
C         POLYMERS IN 2D STARTED 6/11/98, CONVERSION TO 3D METALS STARTED 6/14/99
C             GREATER USE OF COMMON BLOCKS THAN SINTCR3D2.F, TO TRY TO MAKE BETTER
USE OF MEMORY
C         AND VARIABLE Z-SPACING IN THERMAL MESH STARTED 26/9/99
C     --- CALCN. OF NEW VARIABLE DTGLOB ADDED 22/04/01
```

[Break in code]

```
C
      COMMON  /BLOCKO/ISTORX,ISTORZ,NXLAST,NYLAST,NZLAST
        COMMON  /BLOCKO/NXMIN,NXMAX,NYMIN,NYMAX,NZMIN,NZMAX
C
C       Added ABSORBSCAN. CMT, Jan.02. TEXT1, TEXT2, Feb.02.

        DIMENSION NSCAN(10),SINSTT(10,20),ABSORBSCAN(10,10),ZSTART(10)
        DIMENSION DTEND(MNODT3),ALPEND(MNODT3)
        CHARACTER(LEN=39) TEXT1
        CHARACTER(LEN=28) TEXT2
C
C this version calculates temperature / time histories through an fe mesh.
C data is entered through reading from a data file in which the order is
C (line 0, inside program gives nmq = 7 - this is the number of nodes over the
beam diameter
C   and must not be changed)
C line 1: global powder bed size, defined as n10 nodes long(X),n11 layers depth(Y)
C         and n12 wide(Z) (but also depends on nmq)
C line 2: thermal mesh parameters n1 nodes long(x), (historically the x-length was
n1+n5 nodes)
C         n4 deep(y) and n6 wide(z)
C line 3: a list of thermal mesh relative spacings in horizontal direction (placed
in nthermx)
C line 4: a list of thermal mesh relative depth spacings,in groups multiplying to
6 (i.e 6x1,3x2 or 2x3)
C         placed in nthermy
C line 5: a list of thermal mesh relative spacings in width (placed in nthermz)
C line 6: surface element position in x-dirn, 10 in all, where the heat source is,
C         otherwise enter 0, in nheatx
C line 7: surface element positions in z-dirn, 10 in all, where the heat source
is,
C         otherwise enter 0, in nheaty
C line 8: laser power(W), scan speed(mm/s),spot diameter (mm)
C line 9: layer thickness, bed temperature (deg C),
C density of powder solid and max.density in sintering law,in kg/m3
C line 10: min. temperature for sintering (C).
```

```
C line 11: conductivity law consts. (w/m/c) and sp. ht.consts. (j/kg)
C       and heat loss in W/m2/c.
C line 12: latent heat and liquidus and solidus temperatures;
C line 13: coefficients in heat absorption with depth law
C line 14: coefficients in law for dependence of k on porosity
C line 15: fe calculation number THETA
C line 16: start layer of build and number of layers (up to 10 for now);
C (cont.) and scan spacing, entered as the integral number of 1/6ths of the beam
diameter
C line 17: for each layer, the number of scans per layer - at moment up to 10.
C line 18: for each layer, z position (slice) of first scan in that layer.
C lines 19 and following: - 2 sets of values.
C       1 line for each layer; start and end point x-value of each scan vector in
layer (10x20).
C       1 line for each layer; power absorptance (fraction) per scan - at moment up
to 10x10.
C

C Added lines to report processor time at start. CMT, 31.01.02

      CALL CPU_TIME(TIME1)
      PRINT *,'PROCESSOR TIME AT START, ',TIME1

C DEFINITION OF FILES. FILES 15 AND 16 NEW FOR GSHARP OUTPUT, SEPT. 2001
      OPEN(10,FILE='STME3DAT')
      OPEN(12,FILE='SINTPROD')
      OPEN(14,FILE='RHOPLOT')
      OPEN(15,FILE='RHOPLOTZ')
      OPEN(16,FILE='RHOPLOTX')
      REWIND 10
      REWIND 12
      REWIND 14
      REWIND 15
      REWIND 16
CC
                DO 10 I=1,10
                NSCAN(I)=0
C               Zeroing ABSORBSCAN. Added Jan.02, CMT

                DO 5 J=1,10
                ABSORBSCAN(I,J)=0
 5              CONTINUE

                DO 10 J=1,20
                SINSTT(I,J)=0
 10             CONTINUE
      NMQ=7
      READ(10,*) N10,N11,N12
        READ(10,*) N1,N4,N6
        READ(10,*) (NTHERMX(I),I=1,N1-1)
        READ(10,*) (NTHERMY(I),I=1,N4-1)
        READ(10,*) (NTHERMZ(I),I=1,N6-1)
        READ(10,*) (NHEATX(I),I=1,N1-1)
        READ(10,*) (NHEATZ(I),I=1,N6-1)
      READ(10,*) PR,VSPEED,DIAMETER
      READ(10,*) TLAYER,TDEGO,RHOPOW,RHOSOL,RMAX
      READ(10,*) TDWELL
      READ(10,*) CONDO,CONDV,CAPO,CAPV,HLOSS
      READ(10,*) TLAT,TMELT,TSOL
        READ(10,*) DPA,DPN
      READ(10,*) SIGV1,SIGV2
      READ(10,*) THETA
      READ(10,*) LAYER, NBER,ISCAN
        READ(10,*) (NSCAN(I), I=1,NBER)
        READ(10,*) (ZSTART(I),I=1,NBER)
        READ(10,*) ((SINSTT(I,J),J=1,2*NSCAN(I)),I=1,NBER)

C     New multiple absorptance values read in, 1 per scan. CMT, Jan.02
        READ(10,*) ((ABSORBSCAN(I,J),J=1,NSCAN(I)),I=1,NBER)

C       WRITE(6,*) (NSCAN(I), I=1,NBER)
C       WRITE(6,*) (ZSTART(I),I=1,NBER)
C       WRITE(6,*) ((SINSTT(I,J),J=1,2*NSCAN(I)),I=1,NBER)
C
C * NLAYER is the last layer sintered, when LAYER is the first one:
```

```
      NLAYER=LAYER-NBER+1
C
C * the next lines work out how many global MGZ AND MGX elements from origin of
thermal mesh to centre
C * of the heat source, assuming that the heat source covers 10 x 10 global
elements - it links to
C * calculation of NELSTRT in DO 610 loop. they also sum up max. no. of x, y,z
global elements in thermal mesh
C * and store these in MGXMAX, etc. ISTORZ and ISTORX also give which thermal
element is at centre of heat source
C
      MGZ=0
        MGZMAX=0
        IGZ=0
        DO 15 I=1,N6-1
        MGZMAX=MGZMAX+NTHERMZ(I)
        IF(IGZ.GT.6) GO TO 15
        ISTORZ=I
        IGZ=IGZ+NHEATZ(I)
        MGZ=MGZ+NTHERMZ(I)
 15   CONTINUE
C
      MGX=0
        MGXMAX=0
        IGX=0
        DO 20 I=1,N1-1
        MGXMAX=MGXMAX+NTHERMX(I)
        IF(IGX.GT.6) GO TO 20
        ISTORX=I
        IGX=IGX+NHEATX(I)
        MGX=MGX+NTHERMX(I)
 20   CONTINUE
C
      MGYMAX=0
        DO 30 I=1,N4-1
        MGYMAX=MGYMAX+NTHERMY(I)
 30   CONTINUE
C
C * thermal property calculations and conversions
      CONDO=CONDO/1000.0
      CONDV=CONDV/1000.0
      CAPO=CAPO/1000000000.0
      CAPV=CAPV/1000000000.0
      HLOSS=HLOSS/1000000.0
      TLAT=TLAT/1000000000.0
        TGAP=TMELT-TSOL
C
      QLAS = PR/DIAMETER**2.0
C
C     Removed ABSORB term, different value to be applied each scan. CMT, Jan. 02
C     QLAS = ABSORB*PR/DIAMETER**2.0 (Original statement).
C
C
C start by creating powder bed model, to contain initial coordinates
C of nodes and initial values of density of elements, also data on
C connectivity of nodes
C *** VALUES  OF N10, N11, N12 DESCRIBE GLOBAL BRICK MODEL.
C *** N10 IS NUMBER OF NODES IN X-DIRN (PARALLEL TO SURFACE), N11
C *** IS NUMBER OF POWDER LAYERS IN THE BED; I.E. EACH TLAYER THICK.
C *** THE PROGRAM ASSUMES THAT EACH LAYER HAS 6 STREAM TUBES.
C *** N12 IS NUMBER OF NODES IN SURFACE PERPENDICULAR TO X
C *** THE VALUE OF NMQ , THE NUMBER OF NODES DEFINING HEAT SOURCE WIDTH
C *** MUST ALSO BE ENTERED AT THIS STAGE.
C
        NODTG=N10*(N11*6+1)*N12
        NELTG=(N10-1)*(N11*6)*(N12-1)
C
      CALL PDERBED(N10,N11,N12,NMQ,DIAMETER,TLAYER,RHOPOW,TDEGO,XLNTH1,
     &RHOSOL)
C
C* the thermal model is a discrete number of powder bed layers thick, its mesh
divided into
C* sixths, thirds or halves, etc., of powder bed thickness depending on depth
below surface.
C* its mesh dimensions are multiples of powder bed mesh, as defined in input file.
```

```
C* in early versions of program, n1 was number of nodes ahead of heat source and
nmq was the
C* nodes covering the heat source, lying on top of the first nodes of n5. but this
restriction has
C* since been removed. there is a case for replacing n1 and n5 as separate
variables by a single n1,
C* - that has been done in this version.
C
C * the time step should be chosen to relate to element size (see after INPUT)
C
C ** START TO CREATE THERMAL MODEL - NODT3 AND NELT3 ARE NUMBERS OF NODES,
ELEMENTS IN 3D,
C ** NODT, NELT ARE NUMBERS OF NODES, ELEMENTS IN A SINGLE LAYER
C
        NLINE1=N4
        NLINE2=N1
C
      NODT= N4*NLINE2
        NODT3=(N6*NODT)
      NELT= 6*((N4-1)*(NLINE2-1))
        NELT3=(N6-1)*NELT
C
C
C * mesh generates the element connectivities and boundary conditions of the
C * finite element thermal model, including over which elements the laser acts
C * it also creates the mapping from the powderbed dataset to the thermal model.
C * and finally sets up thermal condensed matrix and index variables
C
      CALL MESH(N10,N11)
C
C
C * start of transient thermal analysis, based on crank-nicolson  time steps
C * first set time step; and also various counters to zero (use explained later)
C
C    New variables introduced and set: to identify which scan takes longest to
cool.
C   Integers MAXCOOL, ICOOLED. CMT, 10.02.02
      MAXCOOL=0
      ICOOLED=1
      DTIME=XLNTH1/VSPEED
        ILAY=0
      KYMAX=0
        KYMIN=N11*6
        KXMAX=0
        KXMIN=N10-1
        KZMAX=0
        KZMIN=N12-1
C
      DO 600 I=LAYER,NLAYER,-1
C set top layer powder thickness to merge with next layer down
            MSTART=(I-1)*6+1
            DO 350 ISLICE=1,N12
            N3=LINEGL(MSTART,1,ISLICE)
            YTOP=XGLOB(2*N3)
            DO 400 J=1,N10
            NTEMP=MSTART+6
            N2=LINEGL(NTEMP,J,ISLICE)
            YBOT=XGLOB(2*N2)
            DY=(YBOT-YTOP)/6.0
            DO 450 K=1,5
            NTEMP=MSTART+K
            N2=LINEGL(NTEMP,J,ISLICE)
            XGLOB(2*N2)=YTOP+K*DY
 450     CONTINUE
 400     CONTINUE
 350     CONTINUE
C * The next lines work out integer values KY, KZ, KX, to place in MFEG to
establish global element
C * number at the origin of the thermal mesh. It includes using MGZ and MGX to
shift from centre of
C * heat source to origin of thermal mesh. The maximimum and minimum values of KY,
KZ, KX are also worked
C * out throughout the program and are used to select global data for display in
OUTPUT.
C
```

```
      KY=(I-1)*6+1
      IF (KY.GT.KYMAX) KYMAX=KY
        IF (KY.LT.KYMIN) KYMIN=KY
C
      ILAY=ILAY+1
        KZ=ZSTART(ILAY)/XLNTH1-MGZ+ISCAN
C
      DO 610 ISLICE=1,NSCAN(ILAY)
C * next line shifts thermal mesh origin ISCAN global stream tubes towards global
origin every x-scan;
C * and after that< max> and min> values of kz continue to be stored
        KZ=KZ-ISCAN
      IF (KZ.GT.KZMAX) KZMAX=KZ
        IF (KZ.LT.KZMIN) KZMIN=KZ
      PRINT *,'STARTING LAYER  ', I, '   SCAN NUMBER = ',ISLICE
      INUM=ISLICE*2
      INS=INUM-1
C set counters to determine limits of laser movement -
        NLAST=SINSTT(ILAY,INS)/XLNTH1
        NBIT=SINSTT(ILAY,INUM)/XLNTH1

C New lines: if laser start and stop "x" position have been given the same value,
program assumes
C that the scan is to be skipped. Moves straight to next scan- saves 1 heat step
and MGXMAX cool
C steps (about 10 minutes' worth). CMT, 05.02.02.
        IF (NLAST.EQ.NBIT) THEN
        PRINT *,'SKIPPING LAYER  ', I, '   SCAN NUMBER = ',ISLICE
        GO TO 610
        ENDIF

        NLIMIT=NBIT-NLAST+1
          KX=NBIT-MGX+1
C set temperatures to ambient and laser heating values for HEAT
            DO 100 J=1,NODT3
 100        DT(J)=TDEGO
            DO 200 M=1,NELT3
            GU(M,1)=VSPEED
            GU(M,2)=0.0
              GU(M,3)=0.0
            ETP(M)=TDEGO
 200        CONTINUE
C -square pyramid approximation of gaussian heat source follows

C Changes in magnitude of QMAX accorded to ABSORBSCAN, changes scan to scan. CMT,
Jan. 02.
        ABSORB=ABSORBSCAN(ILAY,ISLICE)
        QMAX=ABSORB*QLAS*1.126
        PRINT *,'ABSORB= ',ABSORB

        DO 210 J=1,(NMQ+3)
        DO 210 K=1,(NMQ+3)
        HFRIC(J,K)=0.082*QMAX
 210  CONTINUE
        DO 212 J=2,(NMQ+2)
        DO 212 K=2,(NMQ+2)
        HFRIC(J,K)=0.223*QMAX
 212  CONTINUE
        DO 214 J=3,(NMQ+1)
        DO 214 K=3,(NMQ+1)
        HFRIC(J,K)=0.472*QMAX
 214  CONTINUE
        DO 216 J=4,(NMQ)
        DO 216 K=4,(NMQ)
        HFRIC(J,K)=0.779*QMAX
 216  CONTINUE
        DO 218 J=5,(NMQ-1)
        DO 218 K=5,(NMQ-1)
        HFRIC(J,K)=QMAX
 218  CONTINUE

C
C -setting material as all solid state before start of heating
       DO 540 J=1,NODT3
       ALPOLD(J)=1.0
       ALPHA(J)=1.0
```

```
 540   CONTINUE
C
C start of transient temperature calculation - and also estimating max. and min KX
(for OUTPUT)
      WRITE(6,*)'NLIMIT IS....',NLIMIT
         DO 550 J=1,NLIMIT
           KX=KX-1
       IF (KX.GT.KXMAX) KXMAX=KX
         IF (KX.LT.KXMIN) KXMIN=KX
            NELSTRT=MFEG(KY,KX,KZ)
            NSTART=MCNGLB(NELSTRT,1)
C          NSTART=NSTART-1
C          NELSTRT=NELSTRT-1

C Added layer/ scan number variables to printout per heat step, for diagnosis.
CMT, 31.01.02
      WRITE(6,2610)'STARTING HEAT STEP    ',I,'  \',ISLICE,'  \',J
2610  FORMAT(A,I4,A,I4,A,I4)

C* time step set so that movement in one time step is element spacing
      CALL RETRIEVE(NSTART,NELSTRT,NLINE1,NLINE2,N6)
C
C store previous time step temperatures for use in sintering calculation
      DO 580 JJ=1,NODT3
 580  DTOLD(JJ)=DT(JJ)
C
C  * the next line sets up a flag to print data in OUTPUT if negative volume
generated in HEAT
      IFAIL =0
      CALL HEAT(THETA,DTIME,NLINE1,NLINE2,NMQ,TDEGO,RMAX,
     1TGAP,TSOL,TMELT,TLAT,IFAIL,DPA,DPN)
C
C the sintering step is empirical for metals.
      CALL SINTER(NELSTRT,DTIME,RMAX)
C
C NOW STORE ALPHA IN ALPHAOLD FOR NEXT TIME STEP CYCLE and include convection
effect
      DO 581 KK=1,N6
         DO 581 JJ=1,N4
         DO 581 II=2,NLINE2
         DIV=1.0/NTHERMX(II-1)
         ITRIAL =(KK-1)*NODT+(JJ-1)*NLINE2+II
         ALPOLD(ITRIAL)=ALPHA(ITRIAL-1)*DIV+ALPHA(ITRIAL)*(1-DIV)
 581  CONTINUE
C
C calculate shrinkage associated with densification
      CALL SHRINKAGE(KZ,KX,KY,MGZMAX,MGXMAX,MGYMAX)
C
C
 550  CONTINUE
C
 551  CONTINUE
C store last time step temperature and state of melting as a record for OUTPUT
      DO 555 JJ=1,NODT3
        ALPEND(JJ)=ALPHA(JJ)
 555  DTEND(JJ)=DT(JJ)
C
C Have exchanged static dwell period (below) for a marching one. QLAS=0. Thermal
mesh moves
C it's whole length (MGXMAX) in x direction after heating, well beyond end of
line. CMT, Jan.02

C Can have a dwell period here; i.e. timesteps but zero heat in until the
C model has cooled down enough to stop sintering - also stop thermal mesh marching
over surface
C - possibility of jumping dwell by going straight to 600 - CURRENTLY INACTIVATED
C        GO TO 610
C -also set a counter IDWELL so the time spent in dwell can be estimated

           DO 590 J =1,(NMQ+3)
                DO 591 JJ=1,(NMQ+3)
 591       HFRIC(J,JJ)=0.0
 590       CONTINUE

C ** "No heat in" marching stage, section 1 **
```

```
C Laser power off, thermal mesh continues on for MGXMAX more elements in x
direction.
C CMT, Jan.02.

C UNLESS all nodal temperatures in thermal mesh are below solidification level, in
which case
C calculation moves on to next scan. Time saver. CMT, Feb.02.

C Stop recording change in KX, most new material will remain unsintered. CMT,
Jan.02.

      WRITE(6,*)'MARCHING COOLDOWN PHASE. MGXMAX IS....',MGXMAX
         DO 595 J=1,MGXMAX

C New lines to save some fruitless time in marching cooldown phase.

            TMAX=0.0
            DO 597 JJ=1,NODT3
            IF(DT(JJ).GT.TMAX) TMAX=DT(JJ)
597    CONTINUE
            IF(TMAX.LT.TDWELL) THEN
               IF(J.GT.MAXCOOL) THEN
                  MACOSCAN=ISLICE
                  MACOLAY=I
                  MAXCOOL=J
               END IF
               TEXT1='ALL THERMAL MESH TEMPERATURES LIE BELOW'
               TEXT2=' TDWELL. MOVING TO NEXT SCAN'
               WRITE(6,*)TEXT1,TEXT2
               WRITE(6,*)' '
               GO TO 610
            END IF
            IF(J.EQ.MGXMAX) ICOOLED=0

C End of new lines.

            KX=KX-1
            NELSTRT=MFEG(KY,KX,KZ)
            NSTART=MCNGLB(NELSTRT,1)
C           NSTART=NSTART-1
C           NELSTRT=NELSTRT-1

C Added layer/ scan number variables to printout per cool step, for diagnosis.
CMT, 31.01.02
      WRITE(6,2620)'STARTING COOL STEP    ',I,'  \',ISLICE,'  \',J
2620  FORMAT(A,I4,A,I4,A,I4)

C ** "No heat in" marching stage, end of section 1 **

C ** Dwell stage code, section 1 **

C           DO 592 J=1,NELT3
C             GU(J,1)=0.0
C592        CONTINUE
C           IDWELL=-1
C increase the time step here - reduce it again before exit at 610 CONTINUE
C           DTIME=2*DTIME
C595        CONTINUE
C             IDWELL=IDWELL+1

C ** Dwell stage code, end of section 1 **
C
      CALL RETRIEVE(NSTART,NELSTRT,NLINE1,NLINE2,N6)
C
      DO 596 JJ=1,NODT3
 596  DTOLD(JJ)=DT(JJ)
C
      IFAIL=0
      CALL HEAT(THETA,DTIME,NLINE1,NLINE2,NMQ,TDEGO,RMAX,
     &TGAP,TSOL,TMELT,TLAT,IFAIL,DPA,DPN)
C
C
      CALL SINTER(NELSTRT,DTIME,RMAX)
C NOW STORE ALPHA IN ALPHAOLD FOR NEXT TIME STEP CYCLE
      DO 587 JJ=1,NODT3
 587  ALPOLD(JJ)=ALPHA(JJ)
```

```
C
      CALL SHRINKAGE(KZ,KX,KY,MGZMAX,MGXMAX,MGYMAX)
C ** "No heat in" marching stage, section 2 **
 595  CONTINUE
C ** "No heat in" marching stage, end of section 2 **
C ** Dwell stage code, section 2 **
C      TMAX=0.0
C      DO 597 JJ=1,NODT3
C      IF(DT(JJ).GT.TMAX) TMAX=DT(JJ)
C597   CONTINUE
C      IF(TMAX.GT.TDWELL) GO TO 595
C        TMDWELL=DTIME*IDWELL
C      WRITE(6,*)'TIME (SEC) IN DWELL STAGE IS    ',TMDWELL
C      DTIME=0.5*DTIME
C
C ** Dwell stage code, end of section 2 **
 610  CONTINUE
 600  CONTINUE
C
C * establishing ranges of global powder bed elements to be displayed in output
routines. Earlier, the variables
C * KXMAX, KXMIN and similarly for y and z have established extreme global element
numbers at origin of thermal
C * mesh. Extreme values of the centre of the heat source are then KXMAX/MIN+MGX,
KYMAX/MIN,  KZMAX/MIN+MGZ. The
C * range of global data to print out/visualise may span from say KXMIN to
KXMAX+MGXMAX, from KYMIN to
C * KYMAX+MGYMAX, from KZMIN to KZMAX+MGZMAX
      NXMIN=KXMIN
        NXMAX=KXMAX+MGXMAX
      NYMIN=KYMIN
        NYMAX=KYMAX+MGYMAX
      NZMIN=KZMIN
        NZMAX=KZMAX+MGZMAX
C
C * global element numbers of the heat source centre at the last time step are
      NXLAST=KX+MGX
        NYLAST=KY
        NZLAST=KZ+MGZ

      CALL OUTPUT(N1,N4,N6,DTEND,ALPEND,TLAYER,IFAIL)

C Added lines to report on maximum number of cool steps required before moving to
next scan.
C CMT, 10.02.02

      IF(ICOOLED.EQ.0) THEN
         WRITE(6,*)'ONE OR MORE SCANS DID NOT FULLY SOLIDIFY, EVEN IN'
         WRITE(6,*)'MGXMAX COOL STEPS'
      END IF
      IF(ICOOLED.EQ.1) THEN
         WRITE(6,*)'MAXIMUM NO. OF COOL STEPS BEFORE'
         WRITE(6,2650)'FULL SOLIDIFICATION: ',MAXCOOL
         WRITE(6,2655)'FOR SCAN I.D. ',MACOLAY,'  \',MACOSCAN
      END IF

2650  FORMAT(A,I4)
2655  FORMAT(A,I4,A,I4)

C Added lines to report processor time at end, elapsed program time. CMT, 31.01.02

      CALL CPU_TIME(TIME2)
      PRINT *,'PROCESSOR TIME AT END, ',TIME2
      ELAPSED=(TIME2-TIME1)/60
      PRINT *,'PROGRAM TIME ELAPSED WAS ',ELAPSED,' MINS'

 650  CONTINUE
C
      STOP
      END
```

```
C
```

[Break in code]

```
C-----------------------------------------------------------------
C
      SUBROUTINE OUTPUT(N1,N4,N6,DTEND,ALPEND,TLAYER,IFAIL)
C
C *** OUTPUTS  NODAL & ELEMENT SOLUTIONS ***
C

C creation of output from global data, for plotting: for each global element,
C calculate its centre of volume and relate its density to that point; also
calculate
C average global element temperature (it could have been done alreasdy for TELGLOB
but
C hasn't been.

C     ADDED THE 4 LINES OF CODE BELOW. TELLS MATLAB HOW TO READ RHOPLOT DATA.
C     NXX, NYY, NZZ ARE NO. OF NODES FOR WHICH DATA IS STORED. 0.0,0.0 AIDS MATLAB
IMPORT.
C     CMT, 06.12.01.

C       NEW FORMAT LINES- 2660,2670,2680. DESIGNED TO REDUCE SIZE OF RHOPLOT,
RHOPLOTX/Z FILES.
C     CMT, 10.02.02.

      NZZ=NZMAX-NZMIN+1
      NYY=NYMAX-NYMIN+1
      NXX=NXMAX-NXMIN+1
C
      WRITE(14,*) NXX,NYY,NZZ,0.0,0.0

        DO 40 K=NZMIN,NZMAX
        DO 50 I=NYMIN,NYMAX
        DO 60 J=NXMIN,NXMAX
        M3=MFEG(I,J,K)
        NODE1=MCNGLB(M3,1)
        NODE2=MCNGLB(M3,2)
        NODE3=MCNGLB(M3,3)
        NODE4=MCNGLB(M3,4)
        NODE5=MCNGLB(M3,5)
        NODE6=MCNGLB(M3,6)
        NODE7=MCNGLB(M3,7)
        NODE8=MCNGLB(M3,8)
C
      XSUM=XGLOB(2*NODE1-1)+XGLOB(2*NODE2-1)+XGLOB(2*NODE3-1)
        XSUM=XSUM+XGLOB(2*NODE4-1)+XGLOB(2*NODE5-1)+XGLOB(2*NODE6-1)
        XAV=(XSUM+XGLOB(2*NODE7-1)+XGLOB(2*NODE8-1))/8.0
      YSUM=XGLOB(2*NODE1)+XGLOB(2*NODE2)+XGLOB(2*NODE3)
        YSUM=YSUM+XGLOB(2*NODE4)+XGLOB(2*NODE5)+XGLOB(2*NODE6)
        YAV=(YSUM+XGLOB(2*NODE7)+XGLOB(2*NODE8))/8.0
      ZSUM=ZGLOB(NODE1)+ZGLOB(NODE2)+ZGLOB(NODE3)
        ZSUM=ZSUM+ZGLOB(NODE4)+ZGLOB(NODE5)+ZGLOB(NODE6)
        ZAV=(ZSUM+ZGLOB(NODE7)+ZGLOB(NODE8))/8.0
      RHOAV=RHOGLOB(M3)
      DTSUM=DTGLOB(NODE1)+DTGLOB(NODE2)+DTGLOB(NODE3)
        DTSUM=DTSUM+DTGLOB(NODE4)+DTGLOB(NODE5)+DTGLOB(NODE6)
        DTAV=(DTSUM+DTGLOB(NODE7)+DTGLOB(NODE8))/8.0
      WRITE(14,2660) XAV,YAV,ZAV,RHOAV,DTAV
  60  CONTINUE
  50  CONTINUE
  40  CONTINUE
C
2660  FORMAT(F6.3,F7.4,F7.3,F7.1,F6.0)
C
C
C ***************************************************
C
C NEW SECTION WRITTEN BY NV FOR BLADE VERSION, GSHARP-COMPATIBLE OUTPUT
C creation of output from global data, for plotting: for each global element,
C calculate its centre of volume and relate its density to that point
C
      PRINT *,'WRITING FILE RHOPLOTZ'
C
```

```
      NZZ=NZMAX-NZMIN+1
      NYY=NYMAX-NYMIN+1
      NXX=NXMAX-NXMIN+1
C
      WRITE(15,*) NXX,NYY,NZZ
      NZIDEN=0
      DO 43 K=NZMIN,NZMAX
        DO 53 I=NYMIN,NYMAX
          DO 63 J=NXMIN,NXMAX
           M3=MFEG(I,J,K)
           NODE1=MCNGLB(M3,1)
           NODE2=MCNGLB(M3,2)
           NODE3=MCNGLB(M3,3)
           NODE4=MCNGLB(M3,4)
           NODE5=MCNGLB(M3,5)
           NODE6=MCNGLB(M3,6)
           NODE7=MCNGLB(M3,7)
           NODE8=MCNGLB(M3,8)
C
           XSUM=XGLOB(2*NODE1-1)+XGLOB(2*NODE2-1)+XGLOB(2*NODE3-1)
           XSUM=XSUM+XGLOB(2*NODE4-1)+XGLOB(2*NODE5-1)+XGLOB(2*NODE6-1)
           XAV=(XSUM+XGLOB(2*NODE7-1)+XGLOB(2*NODE8-1))/8.0
           YSUM=XGLOB(2*NODE1)+XGLOB(2*NODE2)+XGLOB(2*NODE3)
           YSUM=YSUM+XGLOB(2*NODE4)+XGLOB(2*NODE5)+XGLOB(2*NODE6)
           YAV=(YSUM+XGLOB(2*NODE7)+XGLOB(2*NODE8))/8.0
           ZSUM=ZGLOB(NODE1)+ZGLOB(NODE2)+ZGLOB(NODE3)
           ZSUM=ZSUM+ZGLOB(NODE4)+ZGLOB(NODE5)+ZGLOB(NODE6)
           ZAV=(ZSUM+ZGLOB(NODE7)+ZGLOB(NODE8))/8.0
           RHOAV=RHOGLOB(M3)
C
           IF(NZIDEN.EQ.K)GOTO 5551
             WRITE(15,*) ZAV,' 0.0 0.0'
             NZIDEN=K
 5551     CONTINUE
C
           WRITE(15,2670) XAV,YAV,RHOAV
   63    CONTINUE
   53   CONTINUE
   43  CONTINUE
C
C
      PRINT *,'WRITING FILE RHOPLOTX'
C
      WRITE(16,*) NZZ,NYY,NXX
      NXIDEN=0
      DO 64 J=NXMIN,NXMAX
        DO 54 I=NYMIN,NYMAX
          DO 44 K=NZMIN,NZMAX
           M3=MFEG(I,J,K)
           NODE1=MCNGLB(M3,1)
           NODE2=MCNGLB(M3,2)
           NODE3=MCNGLB(M3,3)
           NODE4=MCNGLB(M3,4)
           NODE5=MCNGLB(M3,5)
           NODE6=MCNGLB(M3,6)
           NODE7=MCNGLB(M3,7)
           NODE8=MCNGLB(M3,8)
C
           XSUM=XGLOB(2*NODE1-1)+XGLOB(2*NODE2-1)+XGLOB(2*NODE3-1)
           XSUM=XSUM+XGLOB(2*NODE4-1)+XGLOB(2*NODE5-1)+XGLOB(2*NODE6-1)
           XAV=(XSUM+XGLOB(2*NODE7-1)+XGLOB(2*NODE8-1))/8.0
           YSUM=XGLOB(2*NODE1)+XGLOB(2*NODE2)+XGLOB(2*NODE3)
           YSUM=YSUM+XGLOB(2*NODE4)+XGLOB(2*NODE5)+XGLOB(2*NODE6)
           YAV=(YSUM+XGLOB(2*NODE7)+XGLOB(2*NODE8))/8.0
           ZSUM=ZGLOB(NODE1)+ZGLOB(NODE2)+ZGLOB(NODE3)
           ZSUM=ZSUM+ZGLOB(NODE4)+ZGLOB(NODE5)+ZGLOB(NODE6)
           ZAV=(ZSUM+ZGLOB(NODE7)+ZGLOB(NODE8))/8.0
           RHOAV=RHOGLOB(M3)
C
           IF(NXIDEN.EQ.J)GOTO 5552
             WRITE(16,2680)'SLICE X = ',XAV
             NXIDEN=J
 5552     CONTINUE
C
           WRITE(16,2670) ZAV,YAV,RHOAV
   44    CONTINUE
```

```
  54    CONTINUE
  64   CONTINUE
C
2670   FORMAT(F6.3,F7.4,F7.1)
2680   FORMAT(A,F6.3)
C
C END OF NV SECTION
C ***************************************************
C
C
C * 110 should be (n1-1F5.0)
  110 FORMAT (21F5.0)
C * 111 should be (n6-1F5.0)
  111 FORMAT(18F5.0)
C * 115 should be (n1F6.0)
  115 FORMAT (22F6.0)
C * 116 should be (n6F6.0)
  116 FORMAT(19F6.0)
C * 117 should be (n1F6.2)
  117 FORMAT(22F6.2)
C * 118 should be (n6F6.2)
  118 FORMAT(19F6.2)
C  120 FORMAT (20F6.3)
C * 121 should be (n6F6.3)
  121 FORMAT (19F6.3)
C * 130 should be (n1F6.2)
  130 FORMAT (22F6.2)
C
      RETURN
```

Appendix D Modified GSharp 2D Visualisation Script

```
# d:/Program Files/Gsharp/bin/Gsharp.exe
# ... Neri Volpato, Date:22/05/00
# ... Converted by Chris Taylor, starting 24/09/01
# ... Version for 1 x slice, x_165_1mesh5

# ... "1mesh4" as opposed to "1mesh2/3": less contour colours (only 3
# ...  greyscale, for easy counting of squares), and use of "xmesh_b"/
# ...  "ymesh_b"- used for counting squares.
# ...  Also changed x, y, aspect to 1.0: need x and y
# ... pixels-per-millimetre ratio (jpegs) to be the same, acheived with z=0.178.

# ... "1mesh" version has a custom mesh superimposed, to see dimensions
# ... more clearly. Good for reporting and for first estimates of track depth etc.
# ... Mesh line positions set using "xmesh_b"/" ymesh_b" .dat files in "Output\".
# ... CMT, 18.12.01.

# ... New push: get contour colour limits set in more relevant manner.
# ... Want 1 limit just above powder density (4356), the rest around 7500.
# ... Considered removing myclas (slice density max./ min. split into 10
# ... via RANGE), replacing with my own n density values. Once this was
# ... working, it proved the best method.
#
# ... Also tried using XuNCalculationMode/ XuMaxLimit/ XuLimitStep.
# ... For more on these, see GSharp User's Guide pdf (help section).
# ... OK for constant class intervals. New method more flexible however.
#
# ... Easiest thing to do was override myclas values, by using
# ... command "XuNclassLimits[1]=4358.0000" (for example).
# ... But, only seems to work if specified values are approx. what they would
# ... be if set automatically (i.e. approx. evenly spaced between 4356/7850).
# ... Tried setting limits 4358,7100,7200,... Wouldn't work, "Not ascending".
# ... CMT, 16.01.02.

# ..................................................

# ... Enter data file name and location; Slice numbers  ...
# ... to be plotted; Set 'myclas' to layer 1 (only relevant layer).

# ... If changing slice plane (YZ/ ZY):          ...
# ... Change fname and filesource below, e.g. 0nnRhoplotx/z;  ...
# ...( Rhoplotx = YZ plane, Rhoplotz = XY plane.)     ...
# ... Set 'legendx' text, and also x/z Limits  ...

# ..................................................

# *****  Reset GSharp ****************

reset all;

# *****  Enter data file name and location, graph title ****************

fname="E:/Fortran/Output Files/165Rhoplotx";

filesource="165Rhoplotx";

#fname="E:/Fortran/THCC Mod/Output Files/016bRhoplotz";

#filesource="016bRhoplotz";

# *****  Enter the X (Z) slice numbers to be plotted (2 and 3 irrelevant here) ***

#44: found to be centre of sections in x direction (using 3-section script)

n1=44;

n2=24;
n3=69;

# **********  Enter limits for slice Z (ZY)   ************
lxMin=3.0;
lxMax=21.0;
```

```
# **********  Enter limits for slice X (XY)  ***************
#lxMax=5.0;
#lxMin=2.2;

lyMax=0.6;
lyMin=2.0;



# *******  Choose 'legendx' text according to the case  ***

legendx = "z (Length) mm";
#legendx = "x (Length) mm";


# ****   Lines added for more spaced graph mesh, CMT 17.12.01
# ****   Change these two files to get a different overlaid mesh.
# ****   Could have a mesh specific to each slice (e.g. 050xmesh).

import_report("E:/Fortran/Output Files/xmesh_b.dat");
import_report("E:/Fortran/Output Files/ymesh_b.dat");


# .........  Read the Data from 'fname'  ...................

# .........  "nx ny nz" is first line of rhoplotx/z, tells how many nodes  .....

import_ascii(fname,1,1,,,,"nx ny nz");

# .........  "t" is no. of nodes in 1 x/z slice ..................

t=(nx*ny);

# .........  "linest/ linend": where to start and stop reading for x/z slice ...

linend=(t*n1)+n1+1;
linest=linend-t+1;

# .........  Importing title ...................

import_ascii(fname,(linest-1),(linest-1),,,,"slicez1","text");

# .........  Importing slice data  ...................

import_ascii(fname,linest,linend,,,,"x1 y1 density1","real",,,,"vertical");

linend=(t*n2)+n2+1;
linest=linend-t+1;

import_ascii(fname,(linest-1),(linest-1),,,,"slicez2","text");

import_ascii(fname,linest,linend,,,,"x2 y2 density2","real",,,,"vertical");

linend=(t*n3)+n3+1;
linest=linend-t+1;

import_ascii(fname,(linest-1),(linest-1),,,,"slicez3","text");

import_ascii(fname,linest,linend,,,,"x3 y3 density3","real",,,,"vertical");


# .............  New lines added to clip X and Y data .............

y1 = if(x1>lxMax ,undef, y1);
density1 = if(x1>lxMax ,undef,density1);
x1 = if(x1>lxMax ,undef, x1);


y1 = if(x1<lxMin ,undef, y1);
density1 = if(x1<lxMin ,undef,density1);
x1 = if(x1<lxMin ,undef, x1);


x1 = if(y1>lyMin ,undef, x1);
density1 = if(y1>lyMin ,undef,density1);
```

```
y1 = if(y1>lyMin ,undef, y1);


newx1 = mask(x1, x1<>undef and y1<>undef);
newy1 = mask(y1, x1<>undef and y1<>undef);
ndensity1 = mask(density1, x1<>undef and density1<>undef);


y2 = if(x2>lxMax ,undef, y2);
density2 = if(x2>lxMax ,undef,density2);
x2 = if(x2>lxMax ,undef, x2);


y2 = if(x2<lxMin ,undef, y2);
density2 = if(x2<lxMin ,undef,density2);
x2 = if(x2<lxMin ,undef, x2);


x2 = if(y2>lyMin ,undef, x2);
density2 = if(y2>lyMin ,undef,density2);
y2 = if(y2>lyMin ,undef, y2);


newx2 = mask(x2, x2<>undef and y2<>undef);
newy2 = mask(y2, x2<>undef and y2<>undef);
ndensity2 = mask(density2, x1<>undef and density2<>undef);


y3 = if(x3>lxMax ,undef, y3);
density3 = if(x3>lxMax ,undef,density3);
x3 = if(x3>lxMax ,undef, x3);


y3 = if(x3<lxMin ,undef, y3);
density3 = if(x3<lxMin ,undef,density3);
x3 = if(x3<lxMin ,undef, x3);


x3 = if(y3>lyMin ,undef, x3);
density3 = if(y3>lyMin ,undef,density3);
y3 = if(y3>lyMin ,undef, y3);


newx3 = mask(x3, x3<>undef and y3<>undef);
newy3 = mask(y3, x3<>undef and y3<>undef);
ndensity3 = mask(density3, x1<>undef and density3<>undef);

# .............  End, lines added to clip X and Y data .............


# ****** Set 'myclas' as n values between min./max. density for slice.  *******

# myclas=range(ndensity1,10);
myclas = 4358//7550;

set displayoption
   ( XuNautoApply = false,
     XuNautoRepaint = true,
     XuNgraphPicking = true
   );


#xgrid1 = range(x1,200);
#ygrid1 = range(y1,100);
#grid1 = bilinear(x1,y1,density1,xgrid1,ygrid1);
xgrid1 = range(newx1,200);
ygrid1 = range(newy1,100);
grid1 = bilinear(newx1,newy1,ndensity1,xgrid1,ygrid1);
grid1b  = bilinear(newx1,newy1,ndensity1,xmesh_b,ymesh_b);

#xgrid2 = range(x2,200);
#ygrid2 = range(y2,100);
#grid2 = bilinear(x2,y2,density2,xgrid2,ygrid2);
xgrid2 = range(newx2,200);
ygrid2 = range(newy2,100);
grid2 = bilinear(newx2,newy2,ndensity2,xgrid2,ygrid2);
```

```
#xgrid3 = range(x3,200);
#ygrid3 = range(y3,100);
#grid3 = bilinear(x3,y3,density3,xgrid3,ygrid3);
xgrid3 = range(newx3,200);
ygrid3 = range(newy3,100);
grid3 = bilinear(newx3,newy3,ndensity3,xgrid3,ygrid3);

set page_1
   ( XuNsize = (164.775,63.3219) mm
   );
#create Viewport page_1.Density
#    ( XuNangleInXYPlane = 236 deg,
#      XuNdistanceFactor = 6.53378,
#      XuNelevationPlane = 14.37 deg,
#      XuNfirstDiagonalPoint = (5,8) %,
#      XuNfocusHeight = 47.2973,
#      XuNframeWidth = 0.1 mm,
#      XuNsecondDiagonalPoint = (92,90) %,
#      XuNxRatio = 1.16,
#      XuNyRatio = 1.63,
#      XuNzRatio = 0.347
#    );
create Viewport page_1.Density
   ( XuNangleInXYPlane = 180 deg,
     XuNdistanceFactor = 5.5,
     XuNelevationPlane = 0.0 deg,
     XuNfirstDiagonalPoint = (6,8) %,
     XuNfocusHeight = 51.0,
     XuNframeWidth = 0.0 mm,
     XuNsecondDiagonalPoint = (93,92) %,
     XuNxRatio = 1.0,
#     XuNyRatio = 1.63,
     XuNyRatio = 1.0,
     XuNzRatio = 0.178
   );


# .............  FIRST GRAPH  ........................

create Domain page_1.Density.domain_1
   ( XuNpriority = 0,
     XuN3DPlane = true,
     XuNclassType = "limits",

# Set number of contour boundaries, and "myclas" (set manually above).
     XuNnumValues = 2,
     XuNclassData = "myclas",

#     XuNcalculationMode = "maxStep",
#     XuNmaxLimit = 7800.0,
#      XuNlimitStep = 100.0,   (Good for regular intervals, but now have a better
way.)

#     XuNclassLimits[1]=4358.0000,  (Won't work when "maxStep" set, & obsolete!)

     XuNgraphClipping = true,
     XuNlevel = 0.635135,
     XuNlocation = "top",
     XuNmirrorX = true,
     XuNplane = "yz",

# RGB values from 0 to 100. Didn't like interval 4 default colour.
    XuNrgbValues[1]=(50,50,50),
    XuNrgbValues[2]=(80,80,80),
    XuNrgbValues[3]=(100,100,100),

     XuNxMaximum = lxMax,
     XuNxMinimum = lxMin,
     XuNyMaximum = lyMax,
     XuNyMinimum = lyMin
   );
set page_1.Density.domain_1.legend
#    ( XuNentryHeight = 5.61538 %,
   ( XuNentryHeight = 4.11538 %,
     XuNlegendOrigin = (0.0,0.0) %,
     XuNobjectEnabled = true
```

```
   );

create Graph page_1.Density.domain_1.graph_1
   ( XuNcolorDataGrid = "grid1",
     XuNgraphType = "2DContour",
     XuNregionBorderCells = "contoured",
     XuNxData = "xgrid1",
     XuNyData = "ygrid1"
   );
create Note page_1.Density.domain_1.note_1
   ( XuNexpansion = 1.55405,
     XuNfont = "cart",
     XuNheight = 5.0 %,
     XuNhorizontalJustification = "left",
     XuNposition = (68.0,128.0) %,
#     XuNrotation = 0.0 deg,
     XuNrotation = 0.0 deg,
     XuNskewing = 90.0 deg,
     XuNtext = "slicez1"
   );


set page_1.Density.domain_1.xaxis1
   (XuNaxle = false
   );
set page_1.Density.domain_1.yaxis1
   (XuNaxle = false
   );
set page_1.Density.domain_1.xaxis2
   ( XuNaxisLabelsHeightActual = 7.0 %,
     XuNaxisTextHeight = 8.5 %,
     XuNaxisTextText = "legendx",
     XuNaxle = true
   );
set page_1.Density.domain_1.yaxis2
   ( XuNaxisLabelsHeightActual = 7.0 %,
     XuNaxisLabelsScale = "fine",
     XuNaxisLabelsTrailingZeros = "truncated",
     XuNaxisTextHeight = 6.0 %,
     XuNaxisTextText = "y (Depth) mm",
     XuNaxle = true
   );


# .............  OVERLAID GRAPH  .........................
#   ****   Overlay a less intense grid pattern than original graph provides.
#   ****   CMT, 17.12.01

create Domain page_1.Density.domain_2
   ( XuN1st2DXAxis = false,
     XuN1st2DYAxis = false,
     XuNpriority = 0,
     XuN3DPlane = true,
     XuNclassData = "myclas",
     XuNclassType = "limits",
     XuNgraphClipping = true,
     XuNlevel = 0.635135,
     XuNlocation = "top",
     XuNmirrorX = true,
     XuNplane = "yz",
#     XuNrgbValues[2]=(0.00,41.64,100.00),
     XuNxMaximum = lxMax,
     XuNxMinimum = lxMin,
     XuNyMaximum = lyMax,
     XuNyMinimum = lyMin
   );

create Graph page_1.Density.domain_2.graph
   ( XuNgraphType = "2DContour",
     XuNcontourShading  = false,
     XuNcolorDataGrid = "grid1b",
     XuNmesh = true,
     XuNxData = "xmesh_b",
     XuNyData = "ymesh_b"
   );
```

```
# **********   Title for Graphs   **************

create Note page_1.Density.domain_1.note_2
   ( XuNheight = 8.0 %,
     XuNposition = (50,-15)%,
     XuNtext = "Density v Position in YZ Plane"
   );
create Note page_1.Density.domain_1.note_3
   ( XuNheight = 8.0 %,
     XuNposition = (50,-30)%,
     XuNtext = "filesource"
   );

# ...................
#create Title page_1.Density.title_1
#    ( XuNheight = 4 %,
#      XuNjustification = "right",
#      XuNtitleText = "slicez1",
#      XuNverticalBase = (350.494,79.3113) %
#    );
#create Title page_1.Density.title_2
#    ( XuNheight = 4 %,
#      XuNjustification = "right",
#      XuNtitleText = "slicez2",
#      XuNverticalBase = (94.7,92.513) %
#    );
#create Title page_1.Density.title_3
#    ( XuNheight = 4 %,
#      XuNjustification = "right",
#      XuNtitleText = "slicez3",
#      XuNverticalBase = (19.194,85.3113) %
#    );

# ..................

#8888888888888
```

Appendix E Matlab 3D Visualisation Script

```
% Read DTAV from Rhoplot into vectors for plotting
% IsoTemp reads x,y,z, size from Rhoplot, modification of IsoSurf
% Chris Taylor, 12.01.02

% ____________________________________________________________
%
% 1 number to change each time: RhoNo. Graph title changes automatically.
% ____________________________________________________________

clear;

% Change RhoNo each run
RhoNo=173;

RhoplotNo = Int2str(RhoNo);
echo;
PlotData = [RhoplotNo 'Rhoplot']
echo;

Graphtitle = ['stmed3dgmres Temperature Plot, Source Rhoplot' RhoplotNo];

% Set file path
load c:\temp\Rhoplot -ascii;
% e.g. c:\temp\035Rhoplot -ascii

%CarryThrough = [PlotData '(1,1)'];
xtot = Rhoplot(1,1);
ytot = Rhoplot(1,2);
ztot = Rhoplot(1,3);

x = zeros(xtot,ytot,ztot);
y = zeros(xtot,ytot,ztot);
z = zeros(xtot,ytot,ztot);
temperature = zeros(xtot,ytot,ztot);

for k = 1:ztot
    for j = 1:ytot
        for i = 1:xtot
           n = ((k-1)*ytot*xtot)+((j-1)*xtot)+i+1;
           x(i,j,k) = Rhoplot(n,1);
           y(i,j,k) = Rhoplot(n,2);
           z(i,j,k) = Rhoplot(n,3);
%           rho(i,j,k) = Rhoplot(n,4);
           temperature(i,j,k) = Rhoplot(n,5);
        end
    end
end

clear Rhoplot;

%smoothrho = smooth3(rho,'box',5);

structure1=isosurface(x,y,z,temperature,-800.0);

%structure=isosurface(x,y,z,rho,7500.0);
%pat=
patch(structure1,'FaceColor','red','EdgeColor','none');
%alpha(0.5);

structure2=isosurface(x,y,z,temperature,1000.0);
%pat=
patch(structure2,'FaceColor','yellow','EdgeColor','none');
%alpha(0.2);
```

```
%isonormals(x,y,z,rho,pat);
%set(pat,'FaceColor','red','EdgeColor','none');

%colormap hot;
daspect([1 1 1]);
axis tight;
box on;
view(300,340)
%view(90,180);
%view(135,315);
camzoom(1.0);
camproj perspective;
camlight;
lighting gouraud;
lightangle(120,120);

title(Graphtitle,'FontSize',16);
xlabel('x Axis (Scan Direction)','FontSize',10);
ylabel('y Axis (Depth)','FontSize',10);
zlabel('z Axis (Rastering Direction)','FontSize',10);
```

Appendix F Record of Fortran Model Parameters

Table of Fortran Model Parameters 17.01.02 Page **1** of 3

Testing and process mapping. Parts for display purposes are not tabulated.

Run No.	No. Scans	Scan Length (mm)	Scan Spacing ($\times d/6$)	Power (W)	Scan Speed (mm/s)	Absorptance (Range)	Run Time (min)	Notes
01	2	2	10	125	2	0.92	-	Initial
02	2	2	10	125	2	0.2	-	tests
03	2	2	10	125	2	0.6	-	
04	2	2	10	125	2	0.4	-	
05	2	2	5	125	2	0.4	-	
07	1	2	5	125	2	0.4	-	
08	1	1	5	125	2	0.4	-	
09	1	0.5	5	125	2	0.4	-	
13	1	0.5	5	125	2	0.4	-	
14	1	0.5	5	125	2	0.4	-	
16	2	2	5	125	2	0.4	-	
17	1	0.8	5	125	2	0.4	-	
23	2	2	5	125	2	0.4	-	GMRES
24	2	2	5	125	2	0.4	-	modifi-
25	2	2	5	125	2	0.4	-	cation
26	2	2	5	125	2	0.4	-	
31	1	3	5	60	6	1.0	-	Single
32	2	2	5	125	2	0.4	-	line version
37	10	10	3	125	2	0.4	-	_am mesh
39	10	10	3	125	2	0.4	-	shape
40	10	15	3	125	2	0.4	-	
47	5	4	5	125	2	0.4	-	
48	5	4	3	125	2	0.4	-	
49	10	5	3	125	2	0.4	-	
50	10	5	5	125	2	0.4	-	
51	10	5	3	112.5	2	0.4	-	
54	10	5	3	125	2	0.4	-	$2\times y$
55	10	5	3	112.5	2	0.4	-	definition
56	10	5	3	112.5	2	0.4-0.5	-	Marching
57	10	5	3	112.5	2	0.4-0.6	-	cooldown,
58	10	10	3	112.5	2	0.1-0.9	-	variable α
59	10	10	3	37.5	6	0.1-0.9	-	(_am2)
60	10	10	3	75	12	0.1-0.9	-	Thermal
65	10	10	3	75	12	0.1-0.9	-	mesh
66	10	5	5	125	2	0.4	-	deepened
72	10	5	5	40	0.5	0.2-0.4	-	by 2 layers

Table of Fortran Model Parameters 30.01.02 Page **2** of 3

Testing and process mapping. Parts for display purposes are not tabulated.

Run No.	No. Scans	Scan Length (mm)	Scan Spacing (× *d*/6)	Power (W)	Scan Speed (mm/s)	Absorptance (Range)	Run Time (min)	Notes
73	10	10	5	40	0.5	0.2-0.4	-	layers
74	10	10	3	40	0.5	0.2-0.4	-	
75	10	10	3	100	1.0	0.2-0.4	-	
76	10	10	3	40	0.5	0.4-0.5	-	2 more
77	10	10	5	40	0.5	0.4-0.5	-	thermal
80	10	10	5	58	0.5	0.4-0.5	-	*x* nodes,
81	10	10	3	58	0.5	0.4-0.5	-	in front
82	10	10	3	190	4.0	0.4-0.5	-	of laser
83	10	10	3	85	1.0	0.2-0.3	-	beam
84	10	10	3	120	6.0	0.2-0.3	-	
85	10	10	3	155	12.0	0.2-0.3	-	4 more
86	10	10	3	120	6.0	0.4-0.5	296	*y*
87	10	10	3	155	12.0	0.4-0.5	267	thermal
88	10	10	3	200	18.0	0.4-0.5	258	mesh
89	10	10	3	200	12.0	0.4-0.5	287	nodes,
90	10	10	3	120	18	0.4-0.5	168	12
91	10	10	3	240	6	0.4-0.5	350	spaced
92	10	10	3	72	1	0.4-0.5	367	
93	10	10	3	240	6	0.4-0.5	348	Process
94	10	10	3	280	12	0.4-0.5	302	mapping
95	10	10	3	44	1	0.86-1.0	381	activity
96	10	10	5	38	1	0.68-1.0	352	begins
97	10	10	5	100	6	0.5-1.0	316	
98	10	10	5	100	12	0.55-1.0	248	
99	7	10	9	100	4	0.55-1.0	238	
101	7	10	9	100	4	0.55-1.0	153	Conditional
102	7	10	9	120	6	0.4-1.0	140	marching
103	7	10	9	120	12	0.5-1.0	120	cooldown,
104	10	10	3	40	2	0.75-1.0	197	formatted
105	10	10	3	100	1	0.4-0.5	255	Rhoplot,
106	10	10	9	120	6	0.2-0.5	148	Rhoplot
107	10	10	3	80	1	0.75-1.0	295	*x*/*z*
108	10	10	3	50	4	0.4-1.0	141	
109	10	10	3	100	1	0.7-1.0	315	
110	10	10	3	20	2	0.5-1.0	104	
111	10	10	3	80	2	0.75-1.0	234	
112	10	10	3	40	4	0.75-1.0	172	
113	10	10	3	90	2	0.278-1.0	508	
114	10	10	3	120	18	0.583-1.0	159	
115	10	10	5	20	1	0.75-1.0	151	
116	10	10	3	50	0.5	0.8-1.0	397	
117	10	10	9	80	2	0.75-0.99	245	
118	10	10	9	100	12	0.8-1.0	187	
119	10	10	9	40	2	0.5-1.0	159	
120	10	10	9	100	6	0.8-1.0	215	

Table of Fortran Model Parameters 25.05.02 Page **3** of 3

Testing and process mapping. Parts for display purposes are not tabulated.

Run No.	No. Scans	Scan Length (mm)	Scan Spacing (× *d*/6)	Power (W)	Scan Speed (mm/s)	Absorptance (Range)	Run Time (min)	Notes
121	10	10	9	60	1	0.666-1.0	272	
122	10	10	9	60	1	0.75-0.92	270	
123	10	10	9	90	4	0.778-1.0	221	
124	10	10	5	40	2	0.75-1.0	200	
125	10	10	5	20	2	0.5-1.0	104	
126	10	10	5	40	6	0.75-1.0	128	
127	10	10	5	80	1	0.75-1.0	293	
128	10	10	5	80	2	0.75-1.0	240	
131	10	10	3	140	50	0.71-1.0	91	
132	10	10	3	240	100	0.75-1.0	80	
133	10	10	3	200	50	0.75-1.0	147	
134	10	10	3	140	30	0.71-1.0	153	
135	10	10	3	200	30	0.8-1.0	193	
136	10	10	3	150	40	0.8-1.0	135	
137	10	10	3	125	6	0.8-1.0	224	
138	10	10	3	200	75	0.8-1.0	84	
139	10	10	3	184	50	0.902-1.0	160	
140	10	10	5	53	1	0.868-1.0	277	
141	10	10	3	126	30	0.905-1.0	155	
142	10	10	3	200	60	0.85-1.0	129	
143	10	10	3	200	12	0.85-1.0	231	
144	10	10	3	200	9	0.5-1.0	224	
145	10	10	3	140	40	0.929-1.0	145	
146	10	10	3	190	60	0.947-1.0	141	
147	10	10	3	180	7	0.75-1.0	229	
148	10	10	3	142	7	0.915-1.0	229	
149	10	10	5	53	1	0.868-1.0	274	
150	10	10	5	85	12	0.824-1.0	174	
151	10	10	5	200	2	0.43-0.47	238	
152	10	10	3	200	7	0.15-0.25	152	
174	10	10	3	100	30	0.8-0.9	93	
175	10	10	5	160	6	0.813-1.0	236	
176	10	10	5	40	4	0.625-1.0	140	
177	10	10	5	60	9	0.667-1.0	154	
178	10	10	9	50	12	0.8-1.0	116	
179	10	10	9	40	4	0.75-1.0	174	
180	10	10	9	35	1	0.857-1.0	243	
181	10	10	9	200	4	0.65-0.67	254	
182	10	10	9	40	6	0.75-1.0	132	
183	10	10	9	24	1	0.75-1.0	168	
184	10	10	9	25	4	0.8-1.0	116	
185	10	10	5	200	50	0.8-1.0	143	
186	10	10	9	200	50	0.8-1.0	143	
189	10	10	9	200	25	0.8-1.0	205	
190	10	10	5	200	60	0.8-1.0	111	

THESIS CONTAINS

VIDEO CD DVD TAPE CASSETTE